広島大学学位請求論文

Experimental study on QCD phase transition by measuring charged particle density correlations in Au+Au collisions at $\sqrt{s_{NN}}$ =200GeV

（核子対あたりの重心系衝突エネルギー200GeV の金・金原子核衝突における荷電粒子密度相関の測定による QCD 相転移の実験的研究）

２００９年

広島大学大学院理学研究科

物理科学専攻

中村　智昭

（理化学研究所　仁科加速器研究センター　延與放射線研究室）

目　次

別紙

共著者リスト①

S. S. Adler, S. Afanasiev, C. Aidala, N. N. Ajitanand, Y. Akiba, J. Alexander, R. Amirikas, L. Aphecetche, S. H. Aronson, R. Averbeck, T. C. Awes, R. Azmoun, V. Babintsev, A. Baldisseri, K. N. Barish, P. D. Barnes, B. Bassalleck, S. Bathe, S. Batsouli, V. Baublis, A. Bazilevsky, S. Belikov, Y. Berdnikov, S. Bhagavatula, J. G. Boissevain, H. Borel, S. Borenstein, M. L. Brooks, D. S. Brown, N. Bruner, D. Bucher, H. Buesching, V. Bumazhnov, G. Bunce, J. M. Burward-Hoy, S. Butsyk, X. Camard, J.-S. Chai, P. Chand, W. C. Chang, S. Chernichenko, C. Y. Chi, J. Chiba, M. Chiu, I. J. Choi, J. Choi, R. K. Choudhury, T. Chujo, V. Cianciolo, Y. Cobigo, B. A. Cole, P. Constantin, D. dEnterria, G. David, H. Delagrange, A. Denisov, A. Deshpande, E. J. Desmond, A. Devismes, O. Dietzsch, O. Drapier, A. Drees, K. A. Drees, A. Durum, D. Dutta, Y. V. Efremenko, K. El Chenawi, A. Enokizono, H. Enyo, S. Esumi, L. Ewell, D. E. Fields, F. Fleuret, S. L. Fokin, B. D. Fox, Z. Fraenkel, J. E. Frantz, A. Franz, A. D. Frawley, S.-Y. Fung, S. Garpman, T. K. Ghosh, A. Glenn, G. Gogiberidze, M. Gonin, J. Gosset, Y. Goto, R. Granier de Cassagnac, N. Grau, S. V. Greene, M. Grosse Perdekamp, W. Guryn, H.-A°. Gustafsson, T. Hachiya, J. S. Haggerty, H. Hamagaki, A. G. Hansen, E. P. Hartouni, M. Harvey, R. Hayano, N. Hayashi, X. He, H. W. van Hecke, M. Heffner, T. K. Hemmick, J. M. Heuser, M. Hibino, J. C. Hill, W. Holzmann, K. Homma, B. Hong, A. Hoover, T. Ichihara, V. V. Ikonnikov, K. Imai, D. Isenhower, M. Ishihara, M. Issah, A. Isupov, B. V. Jacak, W. Y. Jang, Y. Jeong, J. Jia, O. Jinnouchi, B. M. Johnson, S. C. Johnson, K. S. Joo, D. Jouan, S. Kametani, N. Kamihara, J. H. Kang, S. S. Kapoor, K. Katou, S. Kelly, B. Khachaturov, A. Khanzadeev, J. Kikuchi, D. H. Kim, D. J. Kim, D. W. Kim, E. Kim, G.-B. Kim, H. J. Kim, E. Kistenev, A. Kiyomichi, K. Kiyoyama, C. Klein-Boesing, H. Kobayashi, L. Kochenda, V. Kochetkov, D. Koehler, T. Kohama, M. Kopytine, D. Kotchetkov, A. Kozlov, P. J. Kroon, C. H. Kuberg, K. Kurita, Y. Kuroki, M. J. Kweon, Y. Kwon, G. S. Kyle, R. Lacey, V. Ladygin, J. G. Lajoie, A. Lebedev, S. Leckey, D. M. Lee, S. Lee, M. J. Leitch, X. H. Li, H. Lim, A. Litvinenko, M. X. Liu, Y. Liu, C. F. Maguire, Y. I. Makdisi, A. Malakhov, V. I. Manko, Y. Mao, G. Martinez, M. D. Marx, H. Masui, F. Matathias, T. Matsumoto, P. L. McGaughey, E. Melnikov, F. Messer, Y. Miake, J. Milan, T. E. Miller, A. Milov, S. Mioduszewski, R. E. Mischke, G. C. Mishra, J. T. Mitchell, A. K. Mohanty, D. P. Morrison, J. M. Moss, F. M¨uhlbacher, D. Mukhopadhyay, M. Muniruzzaman, J. Murata, S. Nagamiya, J. L. Nagle, T. Nakamura, B. K. Nandi, M. Nara, J. Newby, P. Nilsson, A. S. Nyanin, J. Nystrand, E. OBrien, C. A. Ogilvie, H. Ohnishi, I. D. Ojha, K. Okada, M. Ono, V. Onuchin, A. Oskarsson, I. Otterlund, K. Oyama, K. Ozawa, D. Pal, A. P. T. Palounek, V. Pantuev, V. Papavassiliou, J. Park, A. Parmar, S. F. Pate, T. Peitzmann, J.-C. Peng, V. Peresedov, C. Pinkenburg, R. P. Pisani, F. Plasil, M. L. Purschke, A. K. Purwar, J. Rak, I. Ravinovich, K. F. Read, M. Reuter, K. Reygers, V. Riabov, Y. Riabov, R. du Rietz, G. Roche, A. Romana, M. Rosati, P. Rosnet, S. S. Ryu, M. E. Sadler, N. Saito, T. Sakaguchi, M. Sakai, S. Sakai, V. Samsonov, L. Sanfratello, R. Santo, H. D. Sato, S. Sato, S. Sawada, Y. Schutz, V. Semenov, R. Seto, M. R. Shaw, T. K. Shea, T.-A. Shibata, K. Shigaki, T. Shiina, C. L. Silva, D. Silvermyr, K. S. Sim, C. P. Singh, V. Singh, M. Sivertz, A. Soldatov, R. A. Soltz, W. E. Sondheim, S. P. Sorensen, I. V. Sourikova, F. Staley, P. W. Stankus, E. Stenlund, M. Stepanov, A. Ster, S. P. Stoll, T. Sugitate, J. P. Sullivan, E. M. Takagui, A. Taketani, M. Tamai, K. H. Tanaka, Y. Tanaka, K. Tanida, M. J. Tannenbaum, P. Tarj´an, J. D. Tepe, T. L. Thomas, A. Toia, J. Tojo, H. Torii, R. S. Towell, I. Tserruya, H. Tsuruoka, S. K. Tuli, H. Tydesj¨o, N. Tyurin, J. Velkovska, M. Velkovsky, V. Veszpr´emi, L. Villatte, A. A. Vinogradov, M. A. Volkov, E. Vznuzdaev, X. R.Wang, Y.Watanabe, S. N. White, F. K.Wohn, C. L.Woody, W. Xie, Y. Yang, A. Yanovich, S. Yokkaichi, G. R. Young, I. E. Yushmanov, W. A. Zajc, C. Zhang, S. Zhou, S. J. Zhou, L. Zolin.

共著者リスト②

S. S. Adler, S. Afanasiev, C. Aidala, N. N. Ajitanand, Y. Akiba, J. Alexander, R. Amirikas, L. Aphecetche,
S. H. Aronson, R. Averbeck, T. C. Awes, R. Azmoun, V. Babintsev, A. Baldisseri, K. N. Barish,
P. D. Barnes, B. Bassalleck, S. Bathe, S. Batsouli, V. Baublis, A. Bazilevsky, S. Belikov, Y. Berdnikov,
S. Bhagavatula, J. G. Boissevain, H. Borel, S. Borenstein, M. L. Brooks, D. S. Brown, N. Bruner,
D. Bucher, H. Buesching, V. Bumazhnov, G. Bunce, J. M. Burward-Hoy, S. Butsyk, X. Camard, J.-S. Chai,
P. Chand, W. C. Chang, S. Chernichenko, C. Y. Chi, J. Chiba, M. Chiu, I. J. Choi, J. Choi,
R. K. Choudhury, T. Chujo, V. Cianciolo, Y. Cobigo, B. A. Cole, P. Constantin, D. G. dEnterria, G. David,
H. Delagrange, A. Denisov, A. Deshpande, E. J. Desmond, O. Dietzsch, O. Drapier, A. Drees, R. du Rietz,
A. Durum, D. Dutta, Y. V. Efremenko, K. El Chenawi, A. Enokizono, H. Enyo, S. Esumi, L. Ewell,
D. E. Fields, F. Fleuret, S. L. Fokin, B. D. Fox, Z. Fraenkel, J. E. Frantz, A. Franz, A. D. Frawley,
S.-Y. Fung, S. Garpman, T. K. Ghosh, A. Glenn, G. Gogiberidze, M. Gonin, J. Gosset, Y. Goto,
R. Granier de Cassagnac, N. Grau, S. V. Greene, M. Grosse Perdekamp, W. Guryn, H.-Å. Gustafsson,
T. Hachiya, J. S. Haggerty, H. Hamagaki, A. G. Hansen, E. P. Hartouni, M. Harvey, R. Hayano, X. He,
M. Heffner, T. K. Hemmick, J. M. Heuser, M. Hibino, J. C. Hill, W. Holzmann, K. Homma, B. Hong,
A. Hoover, T. Ichihara, V. V. Ikonnikov, K. Imai, D. Isenhower, M. Ishihara, M. Issah, A. Isupov,
B. V. Jacak, W. Y. Jang, Y. Jeong, J. Jia, O. Jinnouchi, B. M. Johnson, S. C. Johnson, K. S. Joo, D. Jouan,
S. Kametani, N. Kamihara, J. H. Kang, S. S. Kapoor, K. Katou, S. Kelly, B. Khachaturov, A. Khanzadeev,
J. Kikuchi, D. H. Kim, D. J. Kim, D. W. Kim, E. Kim, G.-B. Kim, H. J. Kim, E. Kistenev, A. Kiyomichi,
K. Kiyoyama, C. Klein-Boesing, H. Kobayashi, L. Kochenda, V. Kochetkov, D. Koehler, T. Kohama,
M. Kopytine, D. Kotchetkov, A. Kozlov, P. J. Kroon, C. H. Kuberg, K. Kurita, Y. Kuroki, M. J. Kweon,
Y. Kwon, G. S. Kyle, R. Lacey, V. Ladygin, J. G. Lajoie, A. Lebedev, S. Leckey, D. M. Lee, S. Lee,
M. J. Leitch, X. H. Li, H. Lim, A. Litvinenko, M. X. Liu, Y. Liu, C. F. Maguire, Y. I. Makdisi, A. Malakhov,
V. I. Manko, Y. Mao, G. Martinez, M. D. Marx, H. Masui, F. Matathias, T. Matsumoto, P. L. McGaughey,
E. Melnikov, M. Mendenhall, F. Messer, Y. Miake, J. Milan, T. E. Miller, A. Milov, S. Mioduszewski,
R. E. Mischke, G. C. Mishra, J. T. Mitchell, A. K. Mohanty, D. P. Morrison, J. M. Moss, F. Mühlbacher,
D. Mukhopadhyay, M. Muniruzzaman, J. Murata, S. Nagamiya, J. L. Nagle, T. Nakamura, B. K. Nandi,
M. Nara, J. Newby, P. Nilsson, A. S. Nyanin, J. Nystrand, E. OBrien, C. A. Ogilvie, H. Ohnishi, I. D. Ojha,
K. Okada, M. Ono, V. Onuchin, A. Oskarsson, I. Otterlund, K. Oyama, K. Ozawa, D. Pal,
A. P. T. Palounek, V. S. Pantuev, V. Papavassiliou, J. Park, A. Parmar, S. F. Pate, T. Peitzmann,
J.-C. Peng, V. Peresedov, C. Pinkenburg, R. P. Pisani, F. Plasil, M. L. Purschke, A. K. Purwar, J. Rak,
I. Ravinovich, K. F. Read, M. Reuter, K. Reygers, V. Riabov, Y. Riabov, G. Roche, A. Romana, M. Rosati,
P. Rosnet, S. S. Ryu, M. E. Sadler, N. Saito, T. Sakaguchi, M. Sakai, S. Sakai, V. Samsonov,
L. Sanfratello, R. Santo, H. D. Sato, S. Sato, S. Sawada, Y. Schutz, V. Semenov, R. Seto, M. R. Shaw,
T. K. Shea, T.-A. Shibata, K. Shigaki, T. Shiina, C. L. Silva, D. Silvermyr, K. S. Sim, C. P. Singh, V. Singh,
M. Sivertz, A. Soldatov, R. A. Soltz, W. E. Sondheim, S. P. Sorensen, I. V. Sourikova, F. Staley,
P. W. Stankus, E. Stenlund, M. Stepanov, A. Ster, S. P. Stoll, T. Sugitate, J. P. Sullivan, E. M. Takagui,
A. Taketani, M. Tamai, K. H. Tanaka, Y. Tanaka, K. Tanida, M. J. Tannenbaum, P. Tarján, J. D. Tepe,
T. L. Thomas, J. Tojo, H. Torii, R. S. Towell, I. Tserruya, H. Tsuruoka, S. K. Tuli, H. Tydesjö, N. Tyurin,
H. W. van Hecke, J. Velkovska, M. Velkovsky, L. Villatte, A. A. Vinogradov, M. A. Volkov, E. Vznuzdaev,
X. R. Wang, Y. Watanabe, S. N. White, F. K. Wohn, C. L. Woody, W. Xie, Y. Yang, A. Yanovich, S. Yokkaichi,
G. R. Young, I. E. Yushmanov, W. A. Zajc, C. Zhang, S. Zhou, S. J. Zhou, L. Zolin.

A. Adare, S. S. Adler, S. Afanasiev, C. Aidala, N. N. Ajitanand, Y. Akiba, H. Al-Bataineh, J. Alexander, A. Al-Jamel, K. Aoki, L. Aphecetche, R. Armendariz, S. H. Aronson, J. Asai, E. T. Atomssa, R. Averbeck, T. C. Awes, B. Azmoun, V. Babintsev, G. Baksay, L. Baksay, A. Baldisseri, K. N. Barish, P. D. Barnes, B. Bassalleck, S. Bathe, S. Batsouli, V. Baublis, F. Bauer, A. Bazilevsky, S. Belikov, R. Bennett, Y. Berdnikov, A. A. Bickley, M. T. Bjorndal, J. G. Boissevain, H. Borel, K. Boyle, M. L. Brooks, D. S. Brown, N. Bruner, D. Bucher, H. Buesching, V. Bumazhnov, G. Bunce, J. M. Burward-Hoy, S. Butsyk, X. Camard, S. Campbell, J.-S. Chai, P. Chand, B. S. Chang, W. C. Chang, J.-L. Charvet, S. Chernichenko, J. Chiba, C. Y. Chi, M. Chiu, I. J. Choi, R. K. Choudhury, T. Chujo, P. Chung, A. Churyn, V. Cianciolo, C. R. Cleven, Y. Cobigo, B. A. Cole, M. P. Comets, P. Constantin, M. Csan´ad, T. Cs¨orgo, J. P. Cussonneau, T. Dahms, K. Das, G. David, F. De´ak, M. B. Deaton, K. Dehmelt, H. Delagrange, A. Denisov, D. dEnterria, A. Deshpande, E. J. Desmond, A. Devismes, O. Dietzsch, A. Dion, M. Donadelli, J. L. Drachenberg, O. Drapier, A. Drees, A. K. Dubey, A. Durum, D. Dutta, V. Dzhordzhadze, Y. V. Efremenko, J. Egdemir, F. Ellinghaus, W. S. Emam, A. Enokizono, H. Enyo, B. Espagnon, S. Esumi, K. O. Eyser, D. E. Fields, C. Finck, M. Finger Jr., M. Finger, F. Fleuret, S. L. Fokin, B. Forestier, B. D. Fox, Z. Fraenkel, J. E. Frantz, A. Franz, A. D. Frawley, K. Fujiwara, Y. Fukao, S.-Y. Fung, T. Fusayasu, S. Gadrat, I. Garishvili, F. Gastineau, M. Germain, A. Glenn, H. Gong, M. Gonin, J. Gosset, Y. Goto, R. Granier de Cassagnac, N. Grau, S. V. Greene, M. Grosse Perdekamp, T. Gunji, H.-A°. Gustafsson, T. Hachiya, A. Hadj Henni, C. Haegemann, J. S. Haggerty, M. N. Hagiwara, H. Hamagaki, R. Han, A. G. Hansen, H. Harada, E. P. Hartouni, K. Haruna, M. Harvey, E. Haslum, K. Hasuko, R. Hayano, M. Heffner, T. K. Hemmick, T. Hester, J. M. Heuser, X. He, P. Hidas, H. Hiejima, J. C. Hill, R. Hobbs, M. Hohlmann, M. Holmes, W. Holzmann, K. Homma, B. Hong, A. Hoover, T. Horaguchi, D. Hornback, M. G. Hur, T. Ichihara, V. V. Ikonnikov, K. Imai, M. Inaba, Y. Inoue, M. Inuzuka, D. Isenhower, L. Isenhower, M. Ishihara, T. Isobe, M. Issah, A. Isupov, B. V. Jacak, J. Jia, J. Jin, O. Jinnouchi, B. M. Johnson, S. C. Johnson, K. S. Joo, D. Jouan, F. Kajihara, S. Kametani, N. Kamihara, J. Kamin, M. Kaneta, J. H. Kang, H. Kanou, K. Katou, T. Kawabata, T. Kawagishi, D. Kawall, A. V. Kazantsev, S. Kelly, B. Khachaturov, A. Khanzadeev, J. Kikuchi, D. H. Kim, D. J. Kim, E. Kim, G.-B. Kim, H. J. Kim, Y.-S. Kim, E. Kinney, A. Kiss, E. Kistenev, A. Kiyomichi, J. Klay, C. Klein-Boesing, H. Kobayashi, L. Kochenda, V. Kochetkov, R. Kohara, B. Komkov, M. Konno, D. Kotchetkov, A. Kozlov, A. Kr´al, A. Kravitz, P. J. Kroon, J. Kubart, C. H. Kuberg, G. J. Kunde, N. Kurihara, K. Kurita, M. J. Kweon, Y. Kwon, G. S. Kyle, R. Lacey, Y.-S. Lai, J. G. Lajoie, A. Lebedev, Y. Le Bornec, S. Leckey, D. M. Lee, M. K. Lee, T. Lee, M. J. Leitch, M. A. L. Leite, B. Lenzi, H. Lim, T. Liska, A. Litvinenko, M. X. Liu, X. Li, X. H. Li, B. Love, D. Lynch, C. F. Maguire, Y. I. Makdisi, A. Malakhov, M. D. Malik, V. I. Manko, Y. Mao, G. Martinez, L. Masek, H. Masui, F. Matathias, T. Matsumoto, M. C. McCain, M. McCumber, P. L. McGaughey, Y. Miake, P. Mikes, K. Miki, T. E. Miller, A. Milov, S. Mioduszewski, G. C. Mishra, M. Mishra, J. T. Mitchell, M. Mitrovski, A. K. Mohanty, A. Morreale, D. P. Morrison, J. M. Moss, T. V. Moukhanova, D. Mukhopadhyay, M. Muniruzzaman, J. Murata, S. Nagamiya, Y. Nagata, J. L. Nagle, M. Naglis, I. Nakagawa, Y. Nakamiya, T. Nakamura, K. Nakano, J. Newby, M. Nguyen, B. E. Norman, A. S. Nyanin, J. Nystrand, E. OBrien, S. X. Oda, C. A. Ogilvie, H. Ohnishi, I. D. Ojha, H. Okada, K. Okada, M. Oka, O. O. Omiwade, A. Oskarsson, I. Otterlund, M. Ouchida, K. Oyama, K. Ozawa, R. Pak, D. Pal, A. P. T. Palounek, V. Pantuev, V. Papavassiliou, J. Park, W. J. Park, S. F. Pate, H. Pei, V. Penev, J.-C. Peng, H. Pereira, V. Peresedov, D. Yu. Peressounko, A. Pierson, C. Pinkenburg, R. P. Pisani, M. L. Purschke, A. K. Purwar, J. M. Qualls, H. Qu, J. Rak, A. Rakotozafindrabe, I. Ravinovich, K. F. Read, S. Rembeczki, M. Reuter, K. Reygers, V. Riabov, Y. Riabov, G. Roche, A. Romana, M. Rosati, S. S. E. Rosendahl, P. Rosnet, P. Rukoyatkin, V. L. Rykov, S. S. Ryu, B. Sahlmueller, N. Saito, T. Sakaguchi, S. Sakai, H. Sakata, V. Samsonov, L. Sanfratello, R. Santo, H. D. Sato, S. Sato, S. Sawada, Y. Schutz, J. Seele, R. Seidl, V. Semenov, R. Seto, D. Sharma, T. K. Shea, I. Shein, A. Shevel, T.-A. Shibata, K. Shigaki, M. Shimomura, T. Shohjoh, K. Shoji, A. Sickles, C. L. Silva, D. Silvermyr, C. Silvestre, K. S. Sim, C. P. Singh, V. Singh, S. Skutnik,

M. Slunecka, W. C. Smith, A. Soldatov, R. A. Soltz, W. E. Sondheim, S. P. Sorensen, I. V. Sourikova, F. Staley, P. W. Stankus, E. Stenlund, M. Stepanov, A. Ster, S. P. Stoll, T. Sugitate, C. Suire, J. P. Sullivan, J. Sziklai, T. Tabaru, S. Takagi, E. M. Takagui, A. Taketani, K. H. Tanaka, Y. Tanaka, K. Tanida, M. J. Tannenbaum, A. Taranenko, P. Tarj´an, T. L. Thomas, M. Togawa, A. Toia, J. Tojo, L. Tom´asek, H. Torii, R. S. Towell, V.-N. Tram, I. Tserruya, Y. Tsuchimoto, S. K. Tuli, H. Tydesj¨o, N. Tyurin, T. J. Uam, C. Vale, H. Valle, H. W. van Hecke, J. Velkovska, M. Velkovsky, R. Vertesi, V. Veszpr´emi, A. A. Vinogradov, M. Virius, M. A. Volkov, V. Vrba, E. Vznuzdaev, M. Wagner, D. Walker, X. R. Wang, Y. Watanabe, J. Wessels, S. N. White, N. Willis, D. Winter, F. K. Wohn, C. L. Woody, M. Wysocki, W. Xie, Y. L. Yamaguchi, A. Yanovich, Z. Yasin, J. Ying, S. Yokkaichi, G. R. Young, I. Younus, I. E. Yushmanov, W. A. Zajc, O. Zaudtke, C. Zhang, S. Zhou, J. Zim´anyi, L. Zolin, X. Zong.

共著者リスト④

M. Allen, M. J. Bennett, M. Bobrek, J. B. Boissevain, S. Boose, E. Bosze, C. Britton, J. Chang, C. Y. Chi, M. Chiu, R. Conway, R. Cunningham, A. Denisov, A. Deshpande, M. S. Emery, A. Enokizono, N. Ericson, B. Fox, S.-Y. Fung, P. Giannotti, T. Hachiya, A. G. Hansen, K. Homma, B. V. Jacak, D. Jaffe, J. H. Kang, J. Kapustinsky, S. Y. Kim, Y. G. Kim, T. Kohama, P. J. Kroon, W. Lenz, N. Longbotham, M. Musrock, T. Nakamura, H. Ohnishi, S. S. Ryu, A. Sakaguchi, R. Seto, T. Shiina, M. Simpson, J. Simon-Gillo, W. E. Sondheim, T. Sugitate, J. P. Sullivan, H. W. van Hecke, J. W. Walker, S. N. White, P. Willis, N. Xu.

主論文

Experimental study on QCD phase transition
by measuring charged particle density correlations
in Au+Au collisions at $\sqrt{s_{NN}} = 200$ GeV

Tomoaki Nakamura

Department of Physical Science, Graduate School of Science
Hiroshima University
Kagamiyama 1-3-1, Higashi-Hiroshima, 739-8526, Japan

January 2009

Abstract

Theoretical studies of Quantum Chromodynamics (QCD), which is the underlying theory of strong interactions, indicate that QCD matter has rich phase structures in non-perturbative regimes. The phase diagram can be parametrized by temperature T and baryo-chemical potential μ_B. Based on the phase diagram, one can obtain perspectives on how the vacuum structure of the early universe evolved in extremely high temperature states after the Big Bang. We expect the phase diagram to exhibit at least two distinct regions. One is the quark-gluon phase, and the other is the hadron phase. There is a first order phase boundary at $\mu_B > 0$ and $T = 0$. At $\mu_B = 0$ and $T > 0$, a smooth crossover transition is expected due to finite masses of quarks. Logically we can then expect that a critical end-point (CEP) exists at the end of the first order phase transition line. The location of the CEP would be a landmark in understanding the whole structure of the phase diagram. Although numerical calculations using lattice gauge theory as well as model calculations predict the existence of the CEP, none of them have reached a quantitative agreement on the location at the present precision. Therefore experimental investigations are indispensable to pin down the location, and to understand properties of the phase point based on fundamental observables. The high energy heavy ion experiment at the Relativistic Heavy Ion Collider (RHIC) at Brookheaven National Laboratory (BNL) is one of the unique opportunities to access such a high temperature state as well as studying the properties of the QCD matter.

In this thesis, an experimental result on longitudinal density correlations of produced matter in Au+Au collisions at $\sqrt{s_{NN}} = 200$ GeV has been reported to search for the critical phase boundary of QCD. The density correlation, which is one of the basic observables in the most simplest thermodynamical treatment of the matter based on Ginzburg-Landau phenomenology, is extracted from inclusive charged particle multiplicity distributions in various pseudorapidity interval sizes $\delta\eta$ measured by the PHENIX detector within the total pseudorapidity coverage of $|\eta| < 0.35$. The measured multiplicity distributions are fit by Negative Binomial Distributions (NBD), and the NBD parameters μ (mean) and k^{-1} (deviation from a Poissonian width) are determined in various collision centralities. The corresponding range in the average number of participant nucleons (N_{part}) at the nucleus-nucleus collision is from 29.8 to 352.2. The product of the correlation strength α and the correlation length ξ, which has a monotonic correspondence to a susceptibility, is extracted from a known relation between the NBD k parameter and $\alpha\xi$ as a function of $\delta\eta$. A local maximum of $\alpha\xi$ is seen at $N_{part} \sim 90$. The corresponding energy density based on the Bjorken picture is $\epsilon_{Bj}\tau \sim 2.4$ GeV/(fm$^2\cdot c$) with a transverse area size of 60 fm^2. This behavior may suggest a critical phase boundary based on the Ginzburg-Landau framework.

Contents

Chapter 1

Introduction

1.1 QCD phase transition

One of the most important subjects in physics is to investigate the origin and evolution of our universe. According to the Big Bang cosmology [1], it is considered that the universe was expanding with decreasing temperature and changing the state of matter characterized by each energy scale *i.e.* phase transitions. In the process of the evolution of the early universe, elementary particles; quarks, leptons and massive gauge bosons obtained their masses by the spontaneous symmetry breaking of scalar potential via Higgs mechanism [2] at a critical temperature of electro-weak energy scale around 250 GeV followed by the energy scale of Grand Unified Theory (GUT) immediately after the inflation [3]. As a result of further expansion of the universe, hadrons are produced at the critical temperature $T_c < 200$ MeV and obtain those effective masses by the spontaneous chiral symmetry breaking with formations of the quark pair condensate $\langle \bar{q}q \rangle$. Figure 1.1 shows a conceptual drawing of the matter consisting of quarks and gluons, which is the gauge particle of the strong interaction between quarks and gluons, at higher and lower temperature compared to the T_c.

In other words, the state of matter can be separated by the T_c or the corresponding singularity on some proper thermodynamic variables. In fact, various singular effects are often observed as critical phenomena when matter pass through phase boundaries like critical opalescence at the phase transition to superconductivity phases in the field of condensed matter physics at low temperature [4]. These phenomena have been understood by the phenomenological theory of V. L. Ginzburg and L. D. Landau [5] based on the thermodynamical treatment of matter. Therefore, those theories developed in the low temperature physics will be of assistance to understand the state of matter even in higher temperature, if we apply the concept of the phase transitions to the process of evolution of the universe.

If one focuses on the phase transitions from the quarks and gluons (called

a) quark and gluon phase
T > T_c

b) hadron phase
T < T_c
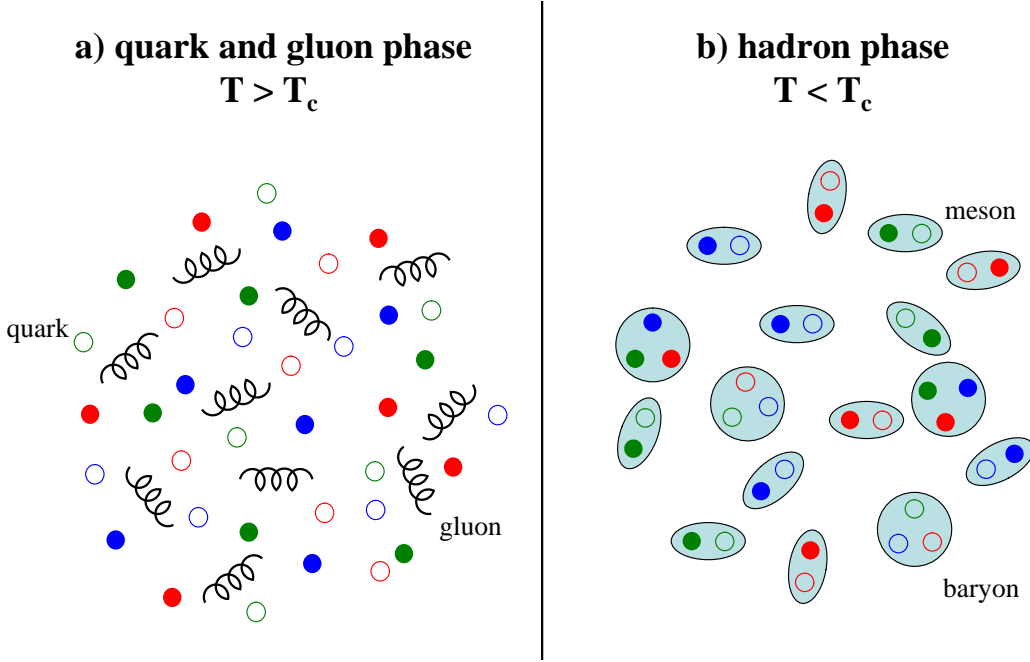
Figure 1.1: Conceptual drawing of matter that consist of quarks and gluons. a) Matter is in $T > T_c$. b) Matter is in $T < T_c$, quarks are confined in hadrons.

together partons) phase to the hadrons phase, it should be treated based on the quantum chromodynamics (QCD) [6], which describes the strong interaction between the quarks and gluons. The QCD is the first principle theory for the strong interaction, and it well describes many experimental results of the particle production and the structure of the proton by using the perturbative approach. On the other hand, the phenomena regarding to the phase transition are often related with low momentum (soft) particles. This means the QCD phase transition belongs to the non-perturbative regime. However, since QCD is a non-Abelian gauge theory, it is difficult to derive the correct answers for the non-perturbative regions analytically without introducing any phenomenological models.

Y. Nambu and G. Jona-Lasinio (NJL) introduced a model for a dynamical mechanism of the chiral phase transition inspired by the phase transition of the superconductivity [7, 8]. It is expressed by a Lagrangian as

$$\mathcal{L} = \bar{q}i\gamma \cdot \partial q + \frac{1}{2}g[(\bar{q}q)^2 + (\bar{q}i\gamma^5\tau q)^2], \tag{1.1}$$

where γ^5 is the chirality operator and the first and second term correspond to kinetic energy and potential term, respectively. For simplicity, considering only u and d quarks with zero masses, this Lagrangian can be rewritten by the linear
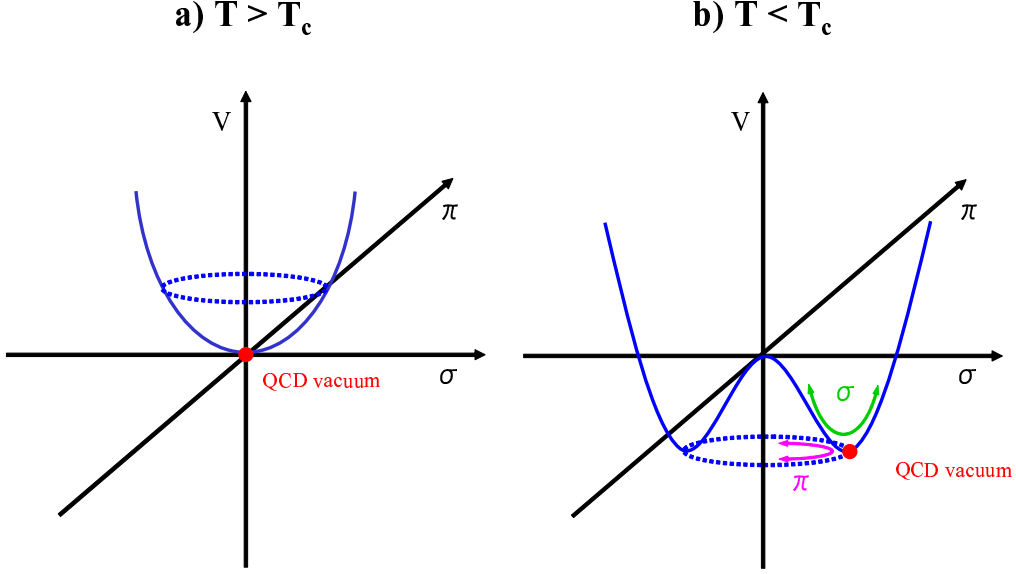
Figure 1.2: Potential of the linear sigma model in Equation (1.2). a) QCD vacuum in $T > T_c$. b) QCD vacuum in $T < T_c$.

sigma model (LSM) which is expressed as

$$\mathcal{L} = \frac{1}{2}[(\partial_\mu \sigma)^2 + (\partial_\mu \pi)^2] + V(\sigma^2 + \pi^2), \qquad (1.2)$$

where σ and π meson's field are defined by

$$\begin{aligned} \sigma &= \bar{q}q, \\ \pi &= \bar{q}i\gamma^5\tau q, \end{aligned} \qquad (1.3)$$

respectively. Figure 1.2 indicates the potential shape in Equation (1.2) and the position of the QCD vacuum. The chiral symmetry is broken in the case of choosing a direction of the QCD vacuum $\langle \bar{q}q \rangle$ for $\pi = 0$ at $T < T_c$ as shown in Figure 1.2 b). Since the QCD vacuum has a finite vacuum expectation value at $T < T_c$, a meson obtains the large effective mass as compared to the quark current mass. Masses of dynamical particles are described by the excitation of the vacuum as shown in the arrows inside the figure. Since the arrow in π direction indicates zero potential gradient, π meson is created as zero mass particles named as Nambu-Goldstone boson as a result of this spontaneous chiral symmetry breaking. It is supported by the small mass of π meson as compared to the other hadrons. Thus, the $\langle \bar{q}q \rangle$ condensation become a proper order parameter in the case of the chiral phase transition. Many phenomenological models of the

Figure 1.3: Theoretical QCD phase diagram for two massless quarks, up and down, as a function of temperature T and baryo-chemical potential μ [14]. Solid and dashed line corresponds to the first and second order phase boundary, respectively. The phase tagged with 2SC is a color superconductor phase in which up and down quarks with two out of three colors pair and form a condensate.

QCD phase transition have been developed based on the NJL model in modern nuclear physics.

There is the another theoretical approaches for the QCD phase transition. It is considered that two phases can exist in the many-body system separated by the critical temperature T_c. One is the hadronic phase and the other is quark deconfined phase namely quark-gluon-plasma (QGP) [9–11]. This concept has been developed as an extension of hadron bag models [12]. The hadron bag models are phenomenological theories to describe the quark confinement in a hadron by introducing tensions from color electric flux between quarks as a bag pressure of the hadron [13]. In this concept, quarks are free from the confined state with increasing temperature or baryo-chemical potential of the system as shown in Figure 1.1 a).

The lattice gauge theory is the only way to calculate quantitative value of the transition temperature based on the first principle of QCD. 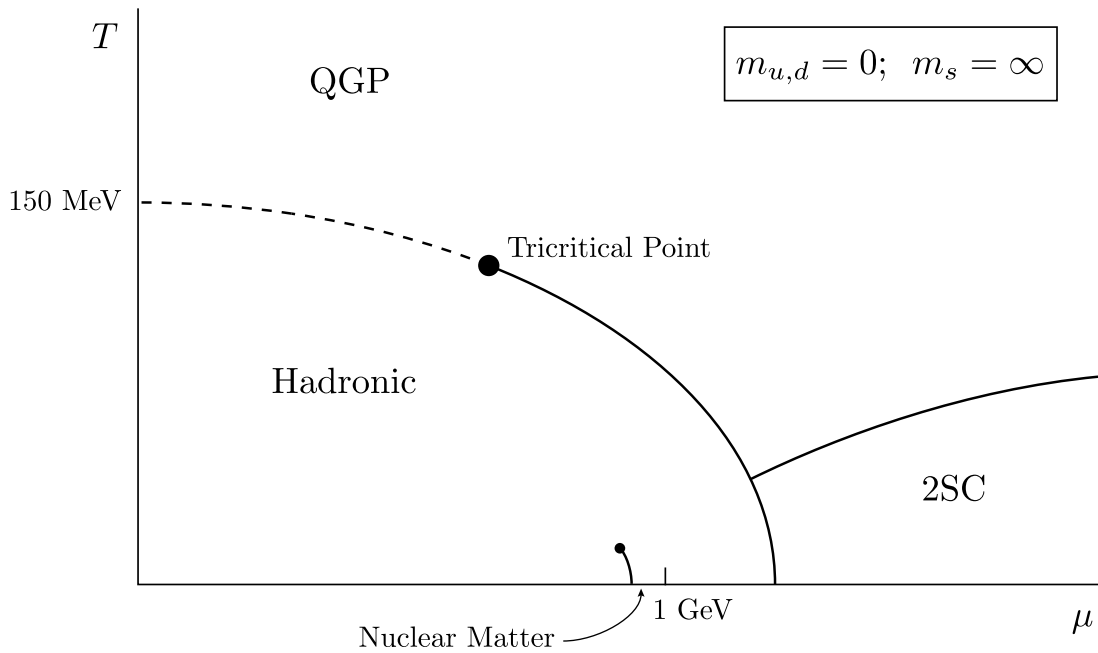Figure 1.3 shows the QCD phase diagram for two massless quarks as a function of temperature T and baryo-chemical potential μ [14]. Since the μ corresponds to the energy of the system per baryon number, the normal nuclear matter at zero temperature indicates 1 GeV. According to the numerical lattice gauge simulation, two phases

in Figure 1.3 are separated by the line from $150 < T < 200$ GeV at $\mu = 0$ [15]. Although the chiral phase transition and the phase transition to the quark deconfined state are different concepts in the QCD energy scale, the lattice gauge simulation indicates the coincidence of the transition temperature at $\mu = 0$ in both cases [16]. However, it is known that there are several difficulties to obtain the accurate values for the region of the large finite μ in the numerical calculations [17]. Therefore, it is crucial for both theoretical and experimental studies to develop new methods to understand the phase structure quantitatively.

The motivation of this study is to investigate the QCD phase transition and the structure of the phase boundary by creating hot and dense QCD matter experimentally.

1.2 Theoretical approaches on the QCD phase diagram

Before explaining experimental methods for the study of QCD matter, several theoretical knowledge of the QCD phase diagram are reviewed in this section. The theoretical studies of QCD in the non-perturbative regimes indicate that QCD matter has the rich phase structure. The phase diagram can be parametrized by temperature T and baryo-chemical potential μ.

The second order phase transition is predicted at $\mu = 0$ and $T > 0$ by the lattice QCD calculation [15] at zero mass, $m = 0$. If one added one more dimension of quark mass m to the phase diagram, it can be depicted as Figure 1.4. Figure 1.4 shows the three dimensional QCD phase diagram based on the NJL model [18]. The first order phase boundaries extend to the mass direction as hatched area in the figure. Since actual quarks have been thought having a finite current mass, a smooth crossover transition is expected due to the finite masses of quarks [19] at $\mu = 0$ and $T > 0$ and $m \neq 0$. The crossover transition is also predicted by the lattice QCD calculation in $\mu = 0$ [20]. Thus, logically one can expect that a critical end-point (CEP) exists at the end of the first order phase transition line [21]. According this picture, the CEP is defined by the connecting point of the two second order lines and one first order line in $m = 0$ plane. Consequently, the location of the CEP would be the landmark in understanding the whole structure of the phase diagram. Figure 1.5 shows the predictions of the CEP locations based on the lattice QCD calculations, the NJL models, the linear sigma model and the other phenomenological models. Dashed line is the expected second order phase boundary obtained by connecting two CEP in the different lattice QCD calculations and the transition temperature at $\mu = 0$. Although numerical calculations using the lattice gauge theory as well as model calculations predict the existence of the CEP, none of them have reached a quantitative agreement on the location at the present precision [22].
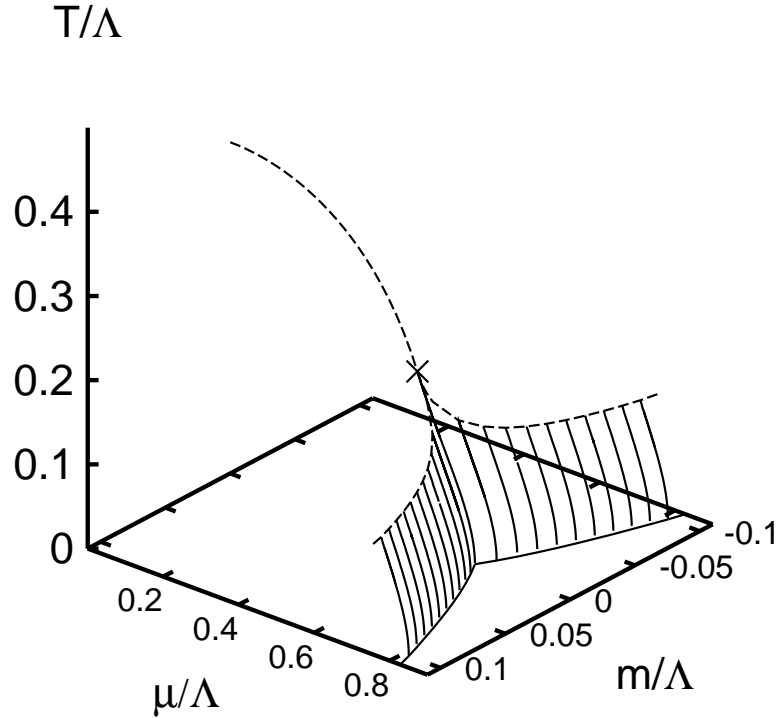
Figure 1.4: Three dimensional QCD phase diagram based on the NJL model as a function of temperature T, baryon chemical potential μ and quark mass m in [18].

The phase transition to the quark-gluon deconfinement phase derived by the several hadron bag models is the different concept from the QCD chiral phase transition as explained in Section 1.1. Since the bag models does not assume the second order phase transition, the first order line obtained by this model does not include the CEP as shown in the solid line in Figure 1.5. However, those models do not indicate any quantitative phase boundaries.

Therefore, experimental investigations are indispensable to pin down the location of the CEP and phase boundary to investigate properties of the phase stricture in the QCD energy scale based on fundamental observables.
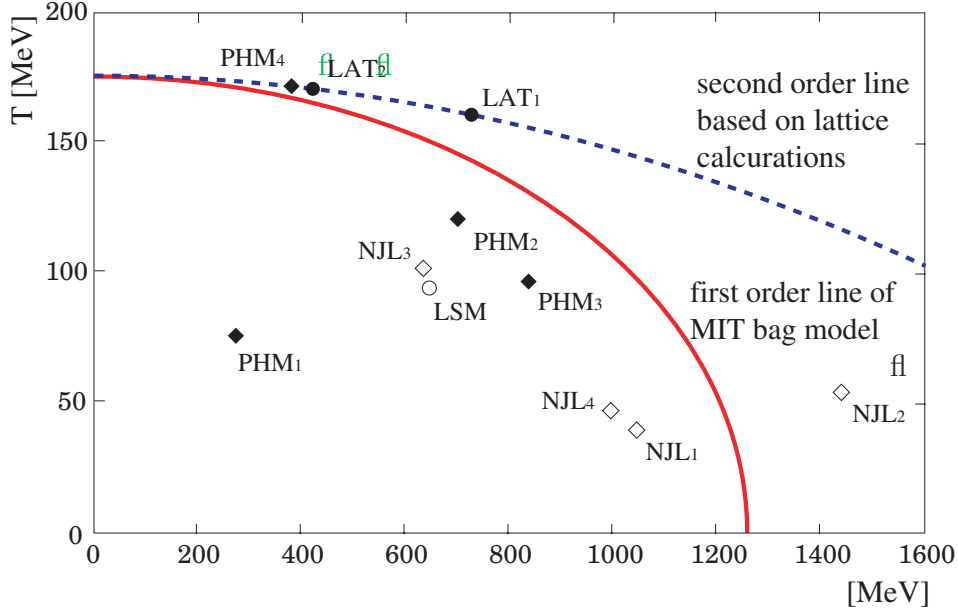
Figure 1.5: Theoretical predictions of the QCD phase boundary and critical end-point summarized in [22]. Dashed line is expected second order phase boundary connecting end-points of lattice QCD calculations in [15, 23, 24]. Markers indicate critical end-points obtained by several theoretical calculations; filled circles are lattice QCD calculations (LAT$_1$ in [23] and LAT$_2$ in [24]), the open circle is based on Linear Sigma Model (LSM in [25]), open diamonds are based on Nambu and Jona-Lasinio model (NJL$_1$, NJL$_2$ in [26], NJL$_3$ in [27], NJL$_4$ in [25]), and the filled diamonds are based on other phenomenological models (PHM$_1$ in [28], PHM$_2$ in [29], PHM$_3$ in [30], PHM$_4$ in [31]). The solid line corresponds to the first order phase boundary by the MIT bag model [13].

1.3 High energy heavy ion experiment

It is necessary to create the extremely hot and dense matter in order to verify whether the QCD phase transition can occur and the new state of matter QGP is formed in nature or not. In this case the hot and dense matter must have large energy density beyond the normal nucleon energy density. One of the methods to make it is colliding accelerated nucleus with high momentum to gain the energy density. For the purpose of producing a large size of the interaction region, heavy ion collisions, $A + A$ is effective compared to proton (anti-proton)-proton,

$p\,(\bar{p}) + p$ collisions, because former one has a larger radius and can collide many incoming number of nucleons at the same time. There are many experiments to search for the QGP by using heavy ion accelerators in the past two decades as follows. Firstly the beam energy of 2.1 GeV per nucleons (A GeV) was used in Bevalac at Lawrence Berkeley Laboratory (LBL, 1975-1985), 15 A GeV heavy ion beam became available by Alternating Gradient Synchrotron (AGS, 1987-1995) at Brookhaven National Laboratory (BNL), and then the beam energy was achieved at 400 A GeV in Super Proton Synchrotron (SPS, 1987-present) at European Organization for Nuclear Research (CERN). These were all fixed target experiments at the extraction beam line. Relativistic Heavy Ion Collider (RHIC, 2000-present) at BNL has accomplished to collide 100 A GeV of gold ions (Au) by using two opposed circular beam line as the world's first heavy ion collider experiment. RHIC enabled us to study the QCD matter by the circumstance of center of mass energy of 200 GeV per colliding nucleus pairs denoted as $\sqrt{s_{NN}}$.

It was already considered that the high temperature and high energy density matter, like a fire ball, could be produced through the high energy nucleus-nucleus collisions which explains observed multiple hadron productions in cosmic ray experiments by E. Fermi and L. D. Landau around in 1950. J. D. Bjorken has introduced a picture of the evolving matter in the intervening region of the incoming nuclei to estimate its energy density, which is independent of inertial reference frame [32]. Figure 1.6 shows the schematic diagram of the head-on colliding nuclei with respect to before and after the collisions based on the Bjorken picture. The longitudinal width of the accelerated nuclei near the light velocity in the beam direction z become less than 1 fm by the Lorentz contraction before the collision as shown in Figure 1.6 a). The volume of the region of interest for the produced matter after the collision in Figure 1.6 b) can be obtained as $\pi R^2 dz$, where R and dz is the transverse radius of the nucleus and the longitudinal gap between the outgoing nuclei, respectively. The dz can be substituted with $\tau_f dy$ by introducing a concept of a proper formation time τ_f for the produced matter, where y is longitudinal rapidity expressed as

$$y = \frac{1}{2}ln\left(\frac{E + q_L}{E - q_L}\right), \tag{1.4}$$

where E is energy and q_L is longitudinal momentum for the accelerated nucleus. The relations of the E, q_L and y are

$$\begin{aligned} E &= m_T \cdot \cosh(y), \\ q_L &= m_T \cdot \sinh(y), \end{aligned} \tag{1.5}$$

where m_T is the transverse mass defined by $m_T^2 \equiv m^2 + q_T^2 = E^2 - q_L^2$. Although partons start interactions immediately after the collisions, a finite time is needed for the achievement of the thermal equilibrium. The volume of the system with this concept of the proper formation time τ_f is appropriate for the estimation of
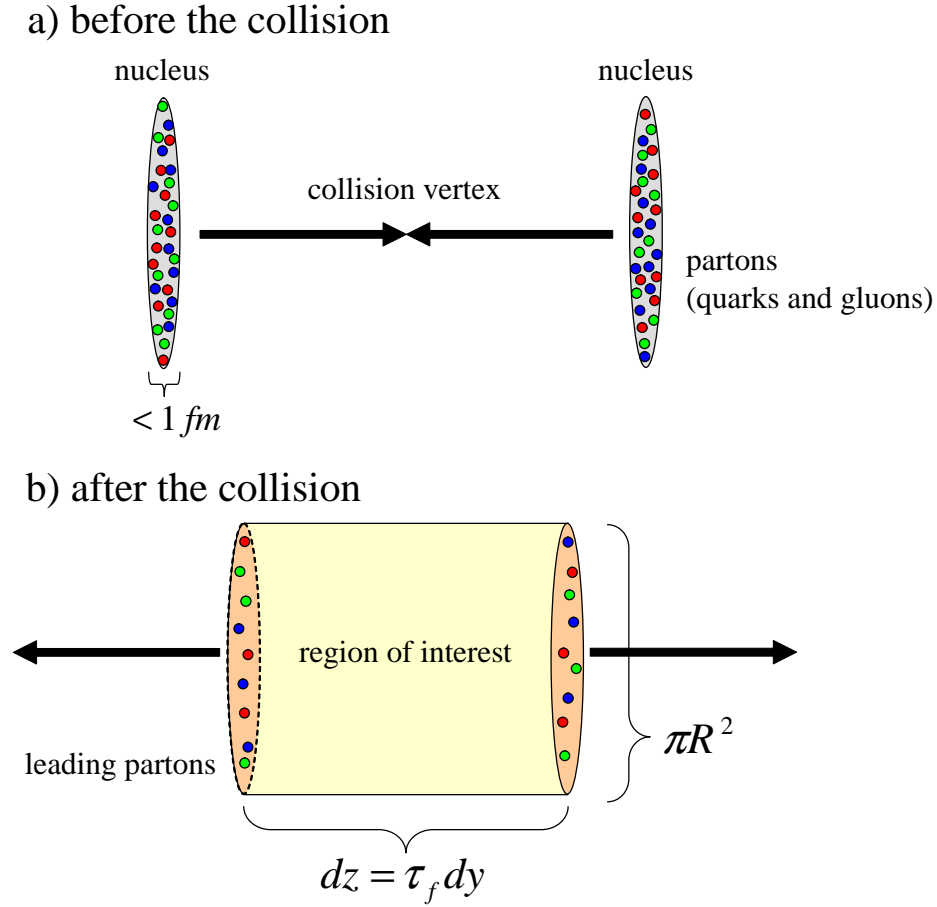
Figure 1.6: Schematic diagram of the head-on colliding nuclei. a) The width of accelerated nucleus becomes < 1 fm by the Lorentz contraction before the collision. b) The region of interest for the particle production is indicated by the filled area after the collision.

the energy density, if QGP is defined as a thermalized and partonic deconfined phase. The rapidity y after the collision can be represented by a time t and a longitudinal space point z as

$$y = \frac{1}{2} ln \left(\frac{t + z}{t - z} \right), \tag{1.6}$$

where a proper time τ is expressed as $\tau = \sqrt{t^2 - z^2}$. According to the relation, t and z become

$$\begin{aligned} t &= \tau \cdot \cosh(y), \\ z &= \tau \cdot \sinh(y), \end{aligned} \tag{1.7}$$
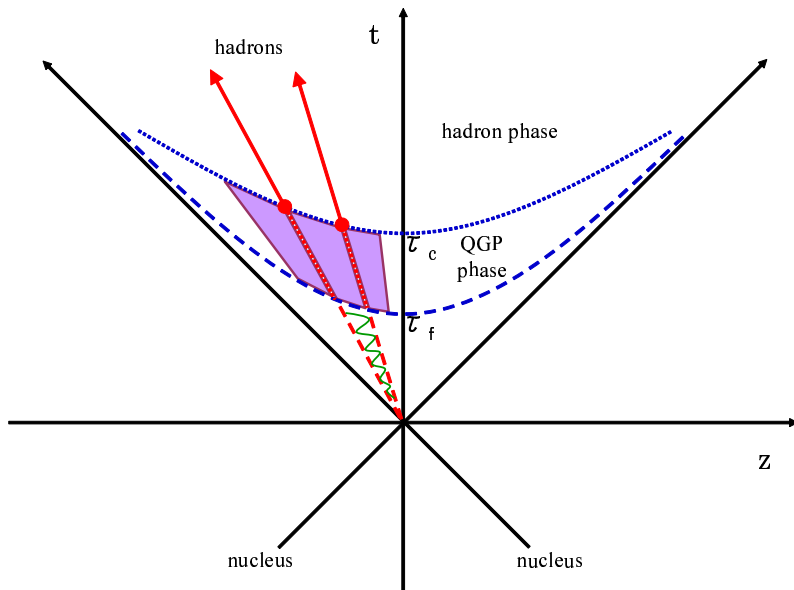
Figure 1.7: Longitudinal Space (z) vs. time (t) diagram of a nucleus-nucleus collision. Produced matter is thermalized at the proper time τ_f plane. Hadornizations occur at the τ_c plane.

where the longitudinal velocity $\beta = z/\tau$ in the laboratory frame is same as the center of mass frame. Figure 1.7 shows the space time evolution after the nucleus-nucleus collision as a function of t and z. The beam of colliding nuclei, which are accelerated near the light velocity, is indicated by the light cone. The hypersurfaces at τ_f (dashed line) and τ_c (dotted line) correspond to the proper formation time and the hadornization time, respectively. The system achieves thermal equilibrium above the hypersurface of τ_f followed by parton-parton interactions after the nucleus-nucleus collision. The temperature decreases with the expansion of the system, and then the thermal hadornization occurs at the critical hypersurface of τ_c. The area surrounded by those two hypersurfaces corresponds to the expected QGP phase. Since this phase is considered to achieve the thermalization, hydrodynamical treatments are possible. The filled area in the Figure 1.7 indicates a hydrodynamical volume element. According to this estimation of the volume on the region of interest and an assumption that N particles produced at τ_f as $\langle m_T \rangle = (q_L^2 + m^2)^{1/2}$ contribute to the energy production, the energy density can be obtained as a function of τ_f,

$$\langle \varepsilon(\tau_f) \rangle = \frac{\langle m_T \rangle dN(\tau_f)}{\pi R^2 dz} = \frac{\langle m_T \rangle}{\pi R^2 \tau_f} \frac{dN(\tau_f)}{dy}. \tag{1.8}$$

Table 1.1: Bjorken energy density ε_{Bj} at $\tau_f = 1$ fm/c.

Accelerator	Colliding nucleus	$\sqrt{s_{NN}}$ (GeV)	ε_{Bj} (GeV/fm^3)	Reference
AGS	Au + Au	5	1.5	[33]
SPS	Pb + Pb	17	2.9	[34–36]
RHIC	Au + Au	200	5.4	[35, 37]

With the relation of

$$\frac{dE_T}{dy} = \langle m_T \rangle \frac{dN}{dy}, \qquad (1.9)$$

where E_T is the total transverse energy of produced particles, the energy density is also expressed as

$$\langle \varepsilon(\tau_f) \rangle = \frac{1}{\pi R^2 \tau_f} \frac{dE_T(\tau_f)}{dy}. \qquad (1.10)$$

This is referred to as the Bjorken energy density ε_{Bj} [32]. The ε_{Bj} can be obtained in each accelerator beam energy as shown in Table 1.1, if one puts $\tau_f = 1$ fm/c into the Equation (1.10), which is not based on any particular justifications but based on Bjorken's order estimate with respect to the particle production [32], and measured final state dE_T/dy by the experiments [33–37]. These estimations contain some ambiguities due to the several assumptions, for instance, the assumption of τ_f and using the measured value of E_T/dy in the final state, which is not in the formation stage. It will be discussed in Section 4.1.4. However, as long as one refers to the Bjorken estimation of the energy density as a lower limit, the matter with a sufficiently high energy density for the QCD phase transition are produced in the RHIC energy compared to the normal nuclear mater.

1.4 Motivation of this study

The direct indication of the dynamical chiral symmetry breaking is difference of masses between light mesons *e.g.* σ (scalar) and π (pseudoscalar) as a result of nondegeneracy [11]. Therefore, observations of those meson's mass shift are considered to be a signature of the chiral phase transition [38]. However, it is expected that the life time of those mesons are too long as compared to the produced matter in heavy ion collisions. Since those mesons decay after the cooling of produced mater, their masses are not affected by the QCD medium. Low mass vector mesons, ρ, ω and ϕ, have a possibility to keep the value of the shifted mass in the medium at the final state, because they have short life times ($\sim 10^{-22}$ second). However, measurements of the low mass vector mesons

are experimentally difficult due to the huge background of decay products from
the other particles.

On the other hand, the suppression of the J/ψ production cross section, which
is a bound state of charm quarks, has been predicted as a direct signature on the
phase transition to the quark deconfined state [39]. This is based on a mechanism
of the Debye screening of the quark color charge. In this model, the screening ra-
dius becomes smaller than the binding radius between two quarks, and it results
in the J/ψ suppression. However, this model has ambiguities on the unknown
production mechanism of the normal J/ψ production as a reference of the pro-
duction cross section.

Therefore, it is necessary to investigate the QCD phase transition by the
other complementary observables in a basic thermodynamic treatment of the
matter. In this study, an analysis result of density correlations measured by
the PHENIX [40] detector at RHIC, which is potentially sensitive to both chiral
and deconfinement phase transitions as explained in Chapter 2, will be discussed
under the experimental situation described in Section 1.3.

Chapter 2

Experimental observable

2.1 Thermodynamic singularity

In general, phase transitions are discussed with order parameters which characterize phases in many body systems. The transition point is defined by discontinuities of an extensive variables Φ as a function of intensive variables h, for example temperature T, in thermodynamics. In this case, both Φ and h are thermodynamic variables. This Φ is defined by partial differential coefficient of Gibbs free energy G with respect to the h. For instance, entropy S and specific heat C_h correspond to the first order and second order derivative of G as indicated in Equation (2.1) and Equation (2.2), respectively. The second order derivatives, isothermal compressibility [41] and correlation length, are called susceptibility χ collectively.

$$\Phi(T, h) = -\left(\frac{\partial G}{\partial h}\right)_T, \quad S = -\left(\frac{\partial G}{\partial T}\right)_h. \tag{2.1}$$

$$\chi = \left(\frac{\partial \Phi}{\partial h}\right)_T = -\left(\frac{\partial^2 G}{\partial h^2}\right)_T, \quad C_h = -T\left(\frac{\partial^2 G}{\partial T^2}\right)_h. \tag{2.2}$$

Thus, the discontinuous or divergent behavior of the derivatives of G as functions of thermodynamic variables determines not only the transition point but also the transition order [4]. This is the thermodynamic singularity.

Here is one of the most obvious examples of phase transitions. Figure 2.1 shows the phase diagram of He^4 as a function of pressure and temperature [42]. The phase indicated by "Liquid He II" is the known super fluidity phase. Figure 2.2 shows the measured specific heat of the liquid He^4 as a function of $T - T_\lambda$, where T_λ is the critical temperature to the super fluidity phase [43, 44]. This figure is made by changing the resolutions to T_c. The specific heat in Figure 2.2, which corresponds to the second order derivative as noted in Equation (2.2), indicates the divergence at $T = T_\lambda$. Therefore, the line with triangles in Figure 2.1 corresponds to the second order phase transition line.

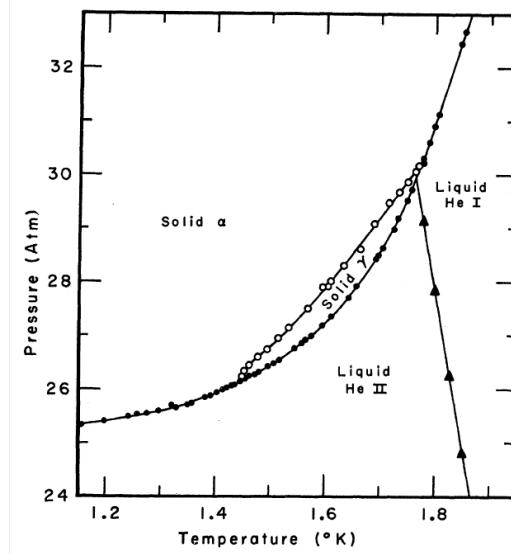Figure 2.1: The phase diagram of He^4 as a function of pressure and temperature [42]. Liquid He II indicated inside the figure is the super fluidity phase. The line with triangles corresponds to the second order transition line.
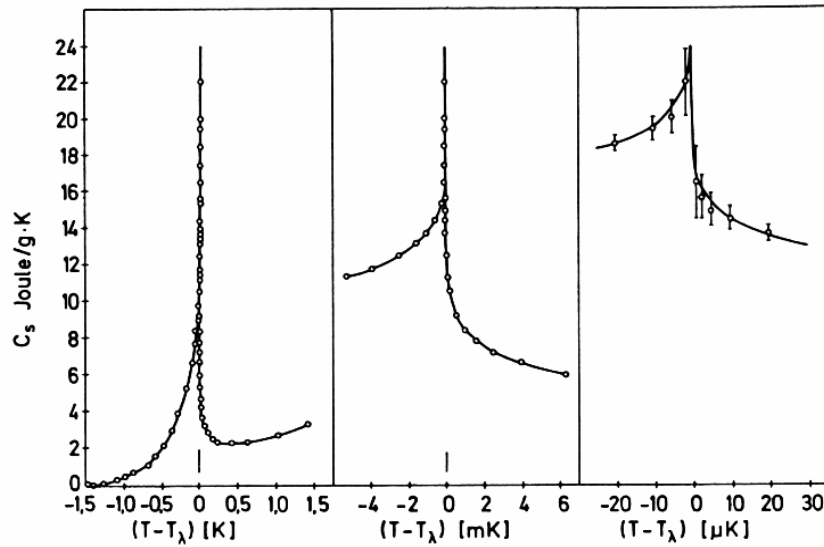

Figure 2.2: The specific heat of liquid He^4 as a function of $T - T_\lambda$ measured by various resolutions [43, 44], where T_λ is the critical temperature for the super fluidity phase.

The singular behaviors in the derivatives of G as in the specific heat of He^4 are often seen when matter go through the phase boundary. That is to say, the critical phenomena are not dependent on details of the local interactions among the constituent particles in the matter but dependent on the global property of the matter such as susceptibility of the thermodynamic variables. Several global properties; the number of dimensions of a system or the number of components of the order parameter and so on, can be considered to characterize the phase transition. It is referred to as the Universality Hypothesis [45–47], which was proven by using the renormalization group theory by K. G. Wilson [48, 49] in the special case of the second order phase transition. Therefore, the thermodynamic fluctuations of an order parameter or the singular behaviors of the susceptibility become signatures of the phase transition even in the case of QCD phase transition. In Section 2.2, relations between an order parameter and the susceptibility are explained based on the Ginzburg-Landau framework [5].

2.2 Density fluctuation and susceptibility

The relation between the thermodynamic fluctuations of order parameter and the susceptibility is expressed by the Fluctuation-Dissipation theorem [4] more precisely. In this section, however, it is explained based on the phenomenological Ginzburg-Landau (GL) [5, 50] framework for a scalar order parameter to understand its essence easily.

GL describes the relation between a free energy density f and an order parameter ϕ as a function of the system temperature T. By adding a spatially inhomogeneous term $A(T)(\nabla\phi)^2$ and an external field h, the general form is described as follows

$$
\begin{aligned}
f(T, \phi, h) = f_0(T) + \frac{1}{2}A(T)(\nabla\phi)^2 + \\
\frac{1}{2}a(T)\phi^2 + \frac{1}{4}b\phi^4 + \cdots - h\phi,
\end{aligned} \tag{2.3}
$$

where f_0 is the equilibrium value of the free energy density, terms with odd powers are neglected due to the symmetry of the order parameter introduced in this analysis, and the sign of b is used to classify the transition orders: $b < 0$ for the first order, $b > 0$ for the second order and $b = 0$ at the critical point. Since the order parameter should vanish above a critical temperature T_c, it is natural for the coefficient $a(T)$ to be expressed as $a(T) = a_0|T - T_c|$, while b is usually assumed to be constant in the vicinity of T_c. Figure 2.3 shows the free energy density up to the fourth order therm as a function of the order parameter ϕ with respect to the different signs of a, where the sign of $a > 0$, $a = 0$ and $a < 0$ corresponds to the case at $T > T_c$, $T = T_c$ and $T < T_c$, respectively. In the following, the higher order terms beyond the second order term is neglected. This
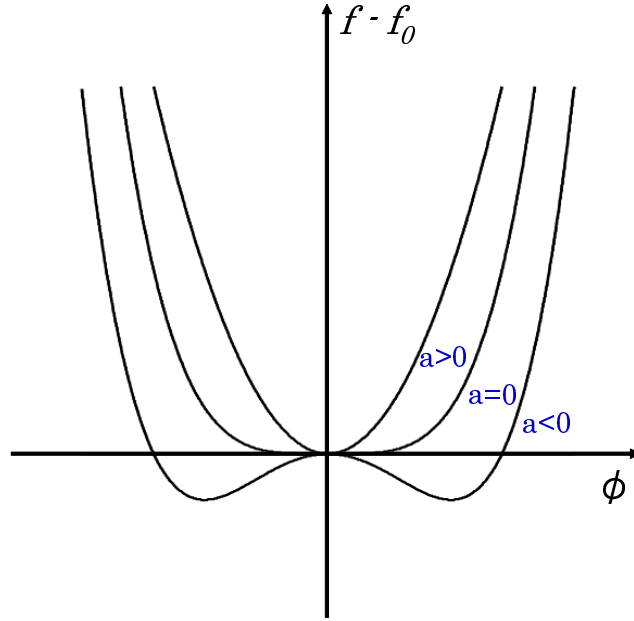
Figure 2.3: The free energy density as a function of scalar order parameter ϕ with the different signs of $a(T)$ in Equation (2.3). Lines with $a > 0$, $a = 0$ and $a < 0$ corresponds to $T > T_c$, $T = T_c$ and $T < T_c$, respectively.

approximation corresponds to a picture where a system approaches to the phase boundary far from the boundary, since ϕ introduced in the following analysis is close to zero in the regions far from T_c. In this sense, the approximation is insensitive to the details of the phase transition order, *i.e.* higher order terms, but only sensitive to the behaviors near the T_c.

The order parameter in this analysis corresponds to the density fluctuation as a function of spacial point r, which is defined as

$$\phi(r) = \rho(r) - \langle \rho(r) \rangle, \tag{2.4}$$

where the pair of brackets indicates an operator to take the average. With the Fourier expansion of the density fluctuation in r, $\phi(r) = \sum_k \phi_k e^{ikr}$ where k is a wave number, one can express the deviation of the free energy density due to spatial fluctuations from the equilibrium value f_0

$$\begin{aligned} \Delta F/Y &= \frac{1}{Y} \int (f - f_0) dr \\ &= \frac{1}{2} \sum_k |\phi_k|^2 (a(T) + A(T)k^2), \end{aligned} \tag{2.5}$$

where Y is the total range corresponding to a volume and up to the second order terms are taken into account as an approximation in the vicinity of the critical

point in Equation (2.3). Given the free energy deviation, one can obtain the statistical weight W for fluctuation $\phi(r)$ to occur in a given temperature T as

$$W(\phi(r)) = Ne^{-\Delta F/T}. \tag{2.6}$$

Therefore the statistical average of the square of the density fluctuation with the wave number k is described as

$$\begin{aligned}
\langle |\phi_k|^2 \rangle &= \int_{-\infty}^{+\infty} |\phi_k|^2 W \left(\sum_k \phi_k e^{ikr} \right) d\phi_k \\
&= \frac{NT}{Y} \frac{1}{a(T) + A(T)k^2}.
\end{aligned} \tag{2.7}$$

An experimentally observable two point density correlation function can be related to the statistical average of the square of the density fluctuation. With a density $\rho(r_i)$ for a given sub-volume dr_i, the two point density correlation G_2 is expressed in the case of $\langle \rho(r_1) \rangle = \langle \rho(r_2) \rangle = \langle \rho \rangle$ as

$$G_2(r_1, r_2) = \langle (\rho(r_1) - \langle \rho \rangle)(\rho(r_2) - \langle \rho \rangle) \rangle, \tag{2.8}$$

where case 1 coinciding with case 2 is excluded to simplify the following discussion. Multiplying both sides of Equation (2.8) by $e^{-ikr} \equiv e^{-ik(r_2 - r_1)}$ and integrating over sub-volume dr_1 and dr_2 gives

$$\begin{aligned}
Y \int G_2(r)e^{-ikr}dr &= \langle | \int (\rho(r) - \langle \rho \rangle)e^{-ikr}dr|^2 \rangle \\
&= \langle |\phi_k|^2 \rangle.
\end{aligned} \tag{2.9}$$

From Equation (2.7) and Equation (2.9), G_2 can be related to the inverse Fourier transformation of the statistical average of $|\phi_k|^2$. This integral can be evaluated by the Ornstein-Zernike formula [51, 52] as

$$G_2(r) \propto \begin{cases} |r|^{-(d-1)/2} e^{-|r|/\xi} & (T > T_c) \\ |r|^{-d+2} & (T = T_c) \end{cases}, \tag{2.10}$$

where d corresponds to the number of dimensions of the system. Therefore in the one dimensional case G_2 is described as

$$G_2(r) = \frac{NT}{2Y^2 A(T)} \xi(T)e^{-|r|/\xi(T)}, \tag{2.11}$$

where the correlation length $\xi(T)$ is introduced, which is defined as

$$\xi(T)^2 = \frac{A(T)}{a_0 |T - T_c|}. \tag{2.12}$$

In general, a singular behavior of $\xi(T)$ as a function of T indicates the critical temperature of the phase transition.
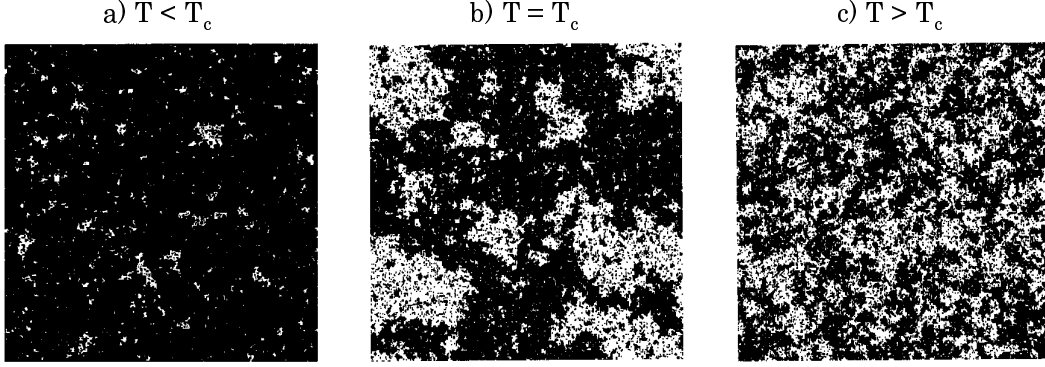
a) T < T$_c$ b) T = T$_c$ c) T > T$_c$

Figure 2.4: The coordination of spin obtained by a simulation of two dimensional Ising model [53] in a) $T < T_c$, b) $T = T_c$, and c) $T > T_c$. Black and white corresponds to upward and downward spin, respectively.

The wave number dependent susceptibility can also be defined from the expansion of the GL free energy density based on Equation (2.3) and Equation (2.5) as follows,

$$
\begin{aligned}
\chi_k &= -\left(\frac{\partial^2 f}{\partial h^2}\right) = \left(\frac{\partial h}{\partial \phi_k}\right)^{-1} \\
&= \left(\frac{\partial^2 (\Delta F/Y)}{\partial \phi_k^2}\right)^{-1} \\
&= \frac{1}{a_0 |T - T_c|(1 + k^2 \xi(T)^2)}.
\end{aligned}
\tag{2.13}
$$

In the case of the long wavelength limit, which correspond to $k = 0$, the susceptibility can be expressed as

$$
\chi_{k=0} = \frac{1}{a_0 |T - T_c|} = \frac{2Y^2}{NT} \xi(T) G_2(0).
\tag{2.14}
$$

In this framework, the ξ and $\chi_{k=0}$ diverge at the same temperature. This is the relation between the fluctuations of order parameter (density fluctuation) and the correlation length ξ and the susceptibility $\chi_{k=0}$.

The correlation length ξ is useful to understand the order of the phase intuitively. It also have an advantage for the application to the correlations among dynamically produced particles. Figure 2.4 show coordinations of spin in a two dimensional Ising model simulation [53]. Figure 2.4 a) indicates the ordered state in $T < T_c$. Most of the directions of spins are lined up to upward in this phase. A typical size of the domains itself corresponds to the correlation length ξ. Figure 2.4 b) is the coordination at $T = T_c$. One can find various sizes of domains

exist together and the typical scale in $T < T_c$ vanishes at $T = T_c$. This is the origin of the divergence of ξ. Figure 2.4 c) shows the spin coordinate of disordered phase in the $T > T_c$. In this case, the ξ decreases with increasing T.

2.3 Application to the phase transition

The first attempt to apply the free energy discussion to $A + A$ collisions can be found in [54], and the application to the case of the QCD phase transition is indicated in [55]. Theoretically, further prospects have been suggested with respect to derivations of the critical exponents [55] and to detecting the critical opalescence [56] at the phase transition of the QCD matter based on the chiral condensate.

The GL framework is applicable to the density correlations in the longitudinal space coordinate z in the heavy ion collisions based on the picture that the system dynamically evolves. A common proper time frame should be introduced as shown in Figure 1.7 for each hydrodynamical sub volume element in this study for the purpose of the application. Therefore, the differential length dz between the neighboring hydrodynamical volume elements at the common proper
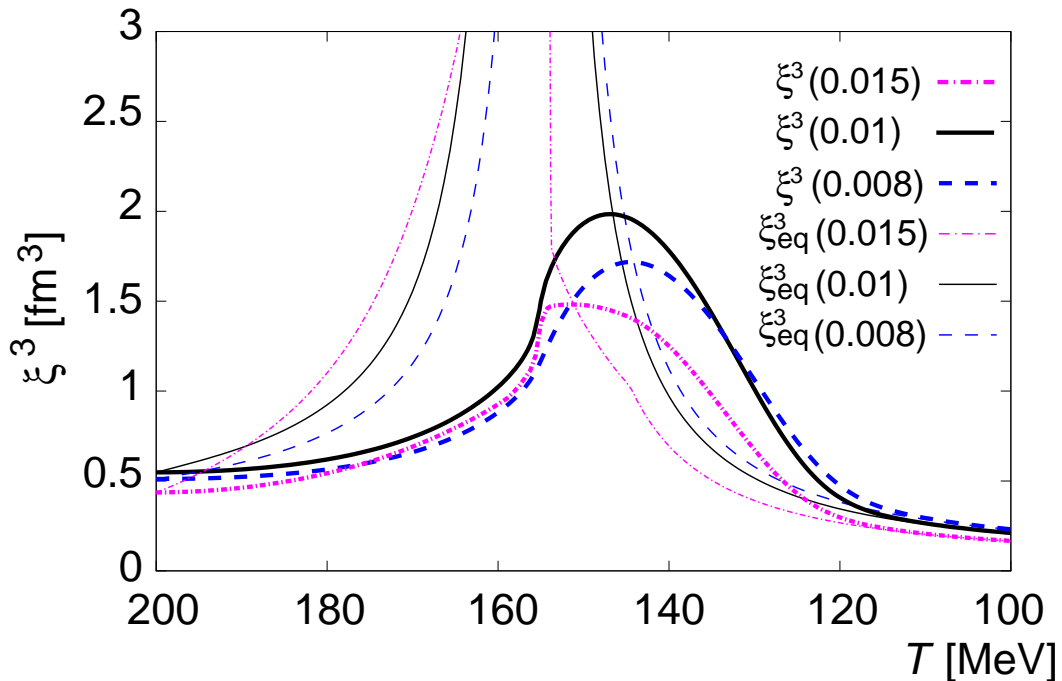
Figure 2.5: Cube of the equilibrium correlation length (thin lines) and non-equilibrium correlation length (thick lines) as a function of temperature [60].

time $\tau = \sqrt{t^2 - z^2}$ is expressed as $dz = \tau \cdot \cosh(y)dy$, where y is rapidity, as
introduced in [57]. The matter produced in the collision expands longitudinally
from its earliest time, which leads to cooling after the initial thermalization. If
the system's evolution takes it near a critical phase boundary as it cools, then
the large correlated density fluctuations will appear as T approaches T_c from
above. If the expansion after that point is rapid enough then these fluctuations
can potentially survive into the final state [58]. One might have a question on
a possible incompleteness of the thermal equilibrium for the produced matter
in heavy ion collisions. Nevertheless, it is indicated that the universal singular
effects can survive on the final state observables such as correlation length and
fluctuations [59] originating from the critical phase boundary according to a hy-
drodynamical calculation [60]. Figure 2.5 shows the correlation length for the
equilibrated fluid (thin line) and non-equilibrated fluid (thick line) as a function
of critical temperature in the hydrodynamical calculation.

Experimentally, spatial density fluctuations in longitudinal space z in the
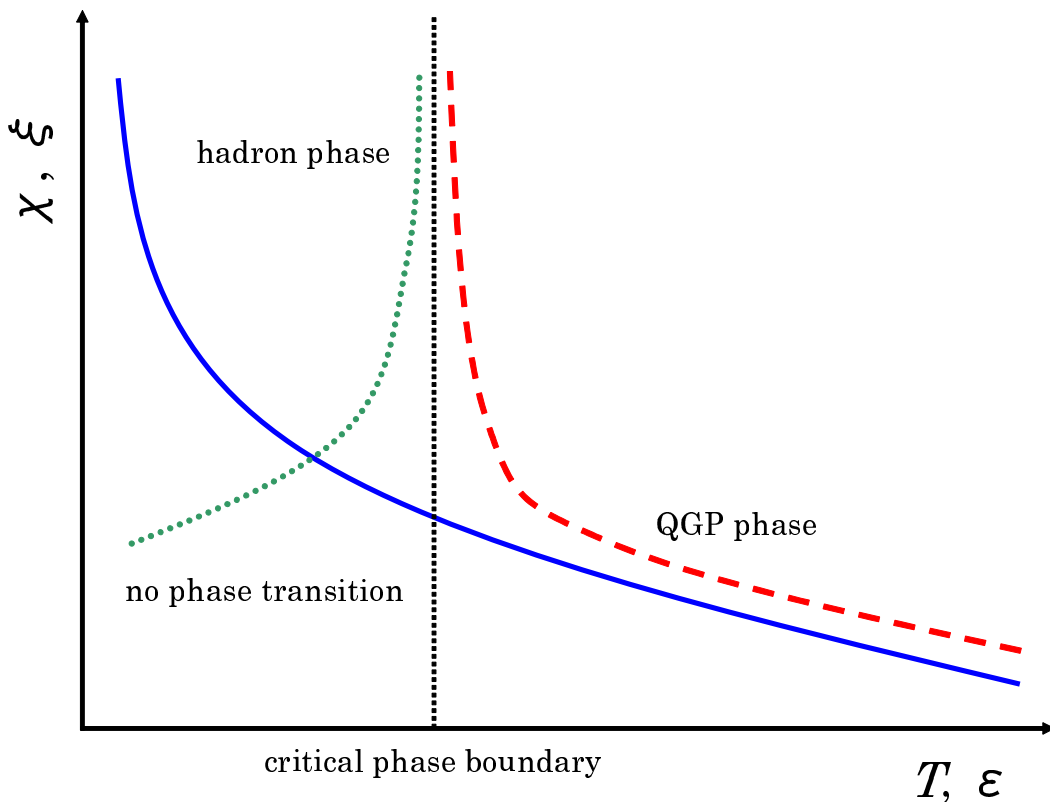
Figure 2.6: Schematic diagram of susceptibility χ or correlation length ξ as a
function of temperature T or energy density ε of the system. Perpendicular
dashed line indicates the hypothetical QCD phase boundary.

early stage of an $A + A$ collision can be measured in rapidity or pseudorapidity space in the final state. The order parameter, in this case, corresponds to the multiplicity density fluctuation for identified or inclusive particles from the mean density. If the study was limited to only a narrow region around mid-rapidity, then $dz \sim \tau dy$ is valid with the approximation of $\cosh(y) \sim 1$. Therefore one can observe density fluctuations in the z coordinate as being mapped onto density fluctuations in rapidity space. In this study, a survey on the susceptibility χ and correlation length ξ have been reported as a function of initial energy density ε of produced matter in Au + Au collisions at $\sqrt{s_{NN}} = 200$ GeV. It is the study to search for the phase boundary between the hadrons and QCD matter by targeting the thermodynamic singularity. Figure 2.6 shows a qualitatively expected behavior of ξ and χ as a function of temperature T or energy density ε of the system. Basically, ξ and χ are expected to smoothly decrease as power law with increasing T or ε as described in Equation (2.12) and Equation (2.14) in $T \gg T_c$, respectively. Therefore, if no phase boundary is contained in the surveying range, there is no divergent behavior as shown in solid line of Figure 2.6. However, if there is transition point in the surveying range, χ and ξ could diverge as shown in dashed and dotted line in Figure 2.6. Although the χ and ξ in the QCD matter are expected to decrease as a function of T and ε in $T > T_c$ side, there is no reason to expect the same values on them over partonic and hadronic matter phases. In Section 2.4, the concrete analysis method will be explained for the extraction of χ and ξ from the multiplicity fluctuations.

2.4 Correlation and fluctuation

In this study, the density fluctuation will be discussed by measuring inclusive charged particle multiplicity distributions as a function of the various pseudorapidity η window size of $\delta\eta$. In the region around mid-rapidity used in this analysis, one can approximate rapidity y by pseudorapidity η for the inclusive charged particles, since the mean transverse momentum $\langle p_T \rangle$ observed in $\sqrt{s_{NN}} = 200$ GeV collisions is so high ($\langle p_T \rangle = 0.57$ GeV/c $\gg m_\pi$) as explained in Section 4.2.

2.4.1 Multiplicity distribution

It is known that the charged particle multiplicity distributions in hadronic processes are well described by the Negative Binomial Distribution (NBD) [61] empirically and it is confirmed in $p\ (\bar{p}) + p$ [62], $A + A$ [63] collisions and even in e^+e^- annihilations [64] as shown in Figure 2.7 through Figure 2.9. The distribution is expressed as

$$P(n) = \frac{\Gamma(n + k)}{\Gamma(n + 1)\Gamma(k)} \frac{(\mu/k)^n}{(1 + \mu/k)^{n+k}} \tag{2.15}$$
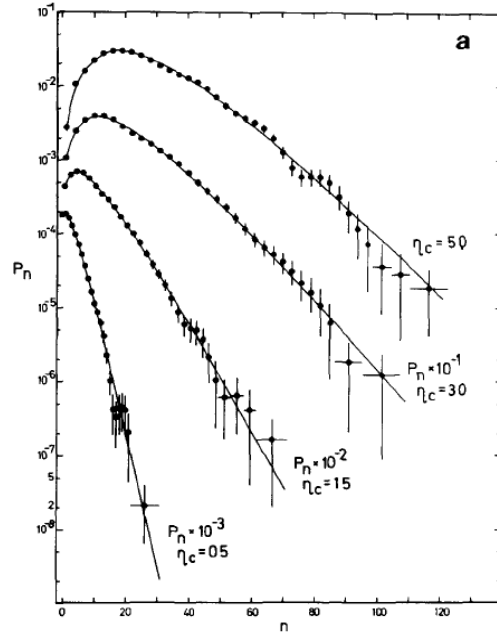
Figure 2.7: Charged particle multiplicity distributions in $\bar{p} + p$ collisions at $\sqrt{s} = 540$ GeV and NBD fits (solid line) [62]. Pseudorapidity intervals η_c are indicated inside the figure.
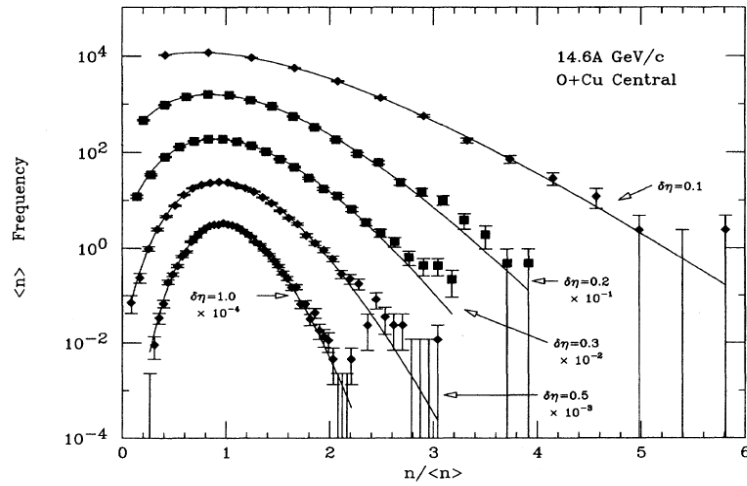
Figure 2.8: Charged particle multiplicity distributions in central O + Cu collisions at 14.6 A GeV/c and NBD fits (solid line) [63]. Markers inside the figure correspond to the differences of pseudorapidity η interval.
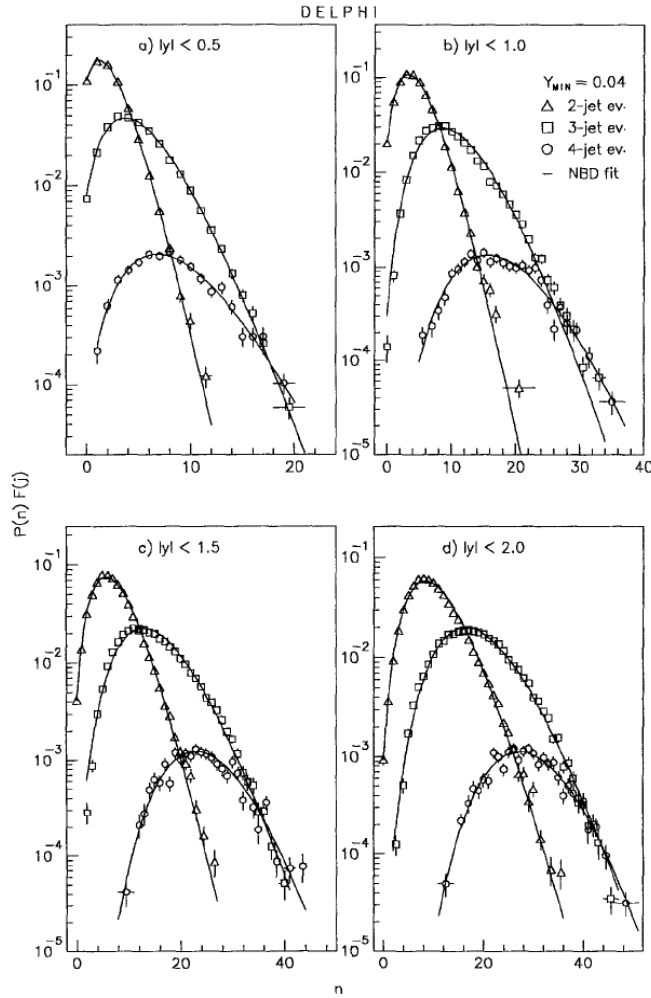
Figure 2.9: Charged particle multiplicity distributions in hadronic Z^0 decays at $e^+ + e^-$ annihilations for various rapidity gaps $|y|$ [64]. a) $|y| < 0.5$, b) $|y| < 1.0$, c) $|y| < 1.5$, d) $|y| < 2.0$. Markers inside the figures correspond to the number of required jets. Solid lines indicate the NBD fits.

where μ is the mean of the distribution *i.e.* $\mu = \langle n \rangle$, and k corresponds to the difference between its width and that of a Poisson with that mean.

$$\text{Poissonian} \quad : \quad P(n) = e^{-\mu}\mu^n / \Gamma(n-1). \tag{2.16}$$

$$\text{BED} \quad : \quad P(n) = \mu^n / (1+\mu)^{n+1}. \tag{2.17}$$

Thus the NBD coincides with the Poisson distribution in Equation (2.16) and the Bose-Einstein distribution (BED) in Equation (2.17), in the case of $k = \infty$ and $k = 1$, respectively. It should be notified that in all cases of above distributions, gamma functions are used instead of factorial functions for the statistical

data analysis. This is proven by using generating function [65] and familiar in Quantum Optics, but one can easily understand by looking the relation between the k parameter and standard deviation σ of the NBD,

$$\frac{\sigma^2}{\mu^2} = \frac{1}{\mu} + \frac{1}{k}. \tag{2.18}$$

This is the reason why NBD is called as the generalized Bose-Einstein distribution. Hence multiple BED are convoluted in NBD and the multiplicity of BED is expressed by the k parameter.

Here, considering the normalized factorial moment (NFM) with respect to a distribution is convenient to figure out the property of the multiplicity distribution [66–69]. The q-th order NFM (F_q), which is defined as

$$F_q \equiv \frac{\langle n(n-1) \cdots (n-q+1) \rangle}{\langle n \rangle^q}, \tag{2.19}$$

represents the strength of correlations among q particles. The second order NFM can be deformed with the standard deviation $\sigma^2 \equiv \langle n^2 \rangle - \langle n \rangle^2$ as

$$
\begin{aligned}
F_2 &= \frac{\langle n(n-1) \rangle}{\langle n \rangle^2} = \frac{\langle n^2 \rangle - \langle n \rangle}{\langle n \rangle^2} = \frac{\sigma^2 + \langle n \rangle^2 - \langle n \rangle}{\langle n \rangle^2} \\
&= 1 + \frac{\sigma^2}{\mu^2} - \frac{1}{\mu}.
\end{aligned}
\tag{2.20}
$$

As a bottom line, the relation between F_2 and NBD k can be obtained with Equation (2.18) as

$$k^{-1} = F_2 - 1. \tag{2.21}$$

Thus the inverse of k parameter in NBD, which corresponds to called as cumulant moment [70, 71] of the second order, directly reflects the degree of correlation between any two particles produced into an experimental window. In other words, NBD is good approximation for the multiplicity distribution in the case of two particle correlation is dominant in the distribution. This is why the multiplicity distribution is agree with NBD in the past high energy experiments.

2.4.2 Extraction of correlation

At the first setout, the normalized factorial moment (NFM) is transformed for the purpose of extractions of density correlation from multiplicity fluctuations by introducing q particle density ρ_q in the given pseudo rapidity window size $\delta\eta$ as

$$F_q(\delta\eta) \equiv \frac{1}{M} \sum_{m=1}^{M} \frac{\langle n_m(n_m-1) \cdots (n_m-q+1) \rangle}{\langle n_m \rangle^q}$$

$$
\begin{aligned}
&= \frac{1}{M} \sum_{m=1}^{M} \frac{\int^{\delta\eta} \rho_q(\eta_1, \cdots, \eta_q) \Pi_{i=1}^{q} d\eta_i}{(\int^{\delta\eta} \rho(\eta) d\eta)^q} \\
&= \frac{1}{M} \sum_{m=1}^{M} \frac{\int^{\delta\eta} \rho_q(\eta_1, \cdots, \eta_q) \Pi_{i=1}^{q} d\eta_i}{(\bar{\rho}_m)^q},
\end{aligned}
\tag{2.22}
$$

where the full pseudo rapidity interval ΔY is divided into M equal bins *i.e.* $\Delta Y = M\delta\eta$. Using this bin divided $F_2(\delta\eta)$, the mathematical connection between the $F_2(\delta\eta)$ and the two particle correlation function C_2 [72–74] can be expressed as

$$
\begin{aligned}
F_2(\delta\eta) &= \frac{\langle n(n-1) \rangle}{\langle n \rangle^2} = \frac{\iint^{\delta\eta} \rho_2(\eta_1, \eta_2) d\eta_1 d\eta_2}{\{\int^{\delta\eta} \rho_1(\eta) d\eta\}^2} \\
&= \frac{1}{(\delta\eta)^2} \frac{\iint^{\delta\eta} C_2(\eta_1, \eta_2) + \rho_1(\eta_1)\rho_1(\eta_2) d\eta_1 d\eta_2}{\bar{\rho}_1{}^2} \\
&= \frac{1}{(\delta\eta)^2} \iint^{\delta\eta} \frac{C_2(\eta_1, \eta_2)}{\bar{\rho}_1{}^2} d\eta_1 d\eta_2 + 1
\end{aligned}
\tag{2.23}
$$

where n is the number of produced particles and $\delta\eta$ is the pseudorapidity window size inside which the multiplicities are measured. In Equation (2.23) one and two particle inclusive multiplicity densities ρ_1 and ρ_2 will be introduced based on the inclusive differential cross section relative to the total inelastic cross section $\sigma_{inelastic}$ [61] as follows

$$
\begin{aligned}
\frac{1}{\sigma_{inelastic}} d\sigma &= \rho_1(\eta) d\eta, \\
\frac{1}{\sigma_{inelastic}} d^2\sigma &= \rho_2(\eta_1, \eta_2) d\eta_1 d\eta_2.
\end{aligned}
\tag{2.24}
$$

Here $\bar{\rho}_1$ is the average density per unit length within $\delta\eta$ which is defined as

$$
\bar{\rho}_1 = \frac{1}{\delta\eta} \int^{\delta\eta} \rho_1(\eta) d\eta.
\tag{2.25}
$$

With these densities, the two particle density correlation function is defined as

$$
C_2(\eta_1, \eta_2) \equiv \rho_2(\eta_1, \eta_2) - \rho_1(\eta_1)\rho_1(\eta_2).
\tag{2.26}
$$

Instead of measuring C_2 or F_2 directly, in this analysis the NBD k parameter as a measure of particle correlations over η are extracted. This is partly for historical reasons [63], but also because, as shown in Section 4.4, the measured k can be corrected for the detector imperfections in a very robust way by using a statistical property of NBD, while the same correction made at the level of F_2 would require additional information on the parent distribution.

The normalized two particle correlation function C_2 in the experiment can be parametrized based on the one dimensional functional form obtained in the GL framework (see Equation (2.11)) as

$$\frac{C_2(\eta_1, \eta_2)}{\bar{\rho}_1{}^2} = \alpha e^{-|\eta_1 - \eta_2|/\xi} + \beta, \tag{2.27}$$

where $\bar{\rho}_1$ is proportional to the mean multiplicity, and the scale factor α is the strength of the correlations at the zero separation. The constant term β arises from any kind of experimental and physical correlations which are independent of the pseudorapidity separation, such as the residual effect on the finite resolution for event characterizations in heavy ion collisions. One has to take into account the fact that the damping behavior in Equation (2.11) is caused only by the spatial inhomogeneity of the system at a fixed temperature. In realistic heavy ion collisions and event samples, there is no single relevant temperature.

Finally, the relation between the NBD k parameter and the pseudorapidity window size $\delta\eta$ can be obtained by the substitution of Equation (2.27) into Equation (2.23) and the integration over the range $0 < \eta_1 < \delta\eta$ and $0 < \eta_2 < \delta\eta$ as

$$k^{-1}(\delta\eta) = F_2 - 1 = \frac{2\alpha\xi^2(\delta\eta/\xi - 1 + e^{-\delta\eta/\xi})}{\delta\eta^2} + \beta. \tag{2.28}$$

In the limit of $\xi \ll \delta\eta$, Equation (2.28) can be approximated as

$$k(\delta\eta) = \frac{1}{2\alpha\xi/\delta\eta + \beta} \quad (\xi \ll \delta\eta), \tag{2.29}$$

where experimentally it can not be resolved α and ξ separately, but the product $\alpha\xi$ can be directly determined. The product is related to the susceptibility in the long wavelength limit, $\chi_{k=0} \propto |T - T_c|^{-1}$ for a given temperature T based on Equation (2.14). Combined with the parametrization in Equation (2.27), the $\alpha\xi$ product should then follow

$$\alpha\xi \propto \bar{\rho}_1{}^{-2} \frac{1}{|1 - T_c/T|}. \tag{2.30}$$

Since $\bar{\rho}_1$ can be expected as a monotonic function of T in the limit of T far from T_c, $\alpha\xi$ should vary monotonically as a function of T. However, if T approaches T_c, the $\alpha\xi$ product will show a singular behavior. Therefore, any non-monotonic increase of $\alpha\xi$ could be an indication of $T \sim T_c$ near a critical point. If the experimental bias term β is excluded in Equation (2.29), the slope in k vs. $\delta\eta$ thus contains crucial information on the phase transition.

It is worth mentioning that in this method, correlations on scales even smaller than the minimum $\delta\eta$ window can be meaningfully discussed based on the differences of the NBD k as a function of $\delta\eta$ window sizes, since the correlations are always integrated from the limit of the detector resolution to $\delta\eta$ window size.

Chapter 3

Experimental setup

3.1 Relativistic heavy ion collider (RHIC)

The relativistic heavy ion collider (RHIC), which is started the operation in 2000, at Brookhaven National Laboratory is the world first collider that can accelerate heavy ions such as gold ion to one hundred GeV/c order of the beam momentum. The heavy ion sources are made at the Tandem Van de Graaff facility. The facility consists of two 15 million volt electrostatic accelerators. It can provide more than 40 different types of ion beams. The produced heavy ions are sent to the Booster synchrotron and accumulated to increase the beam intensity, and then the beam is injected to the Alternating Gradient Synchrotron (AGS). At the AGS, the heavy ion beam is further accelerated to 9 GeV/c to inject the RHIC ring. After the injection to the RHIC ring, the beam is finally accelerated to the maximum energy of 100 GeV/c.

The RHIC ring has 3.82 km length of two beam pipes, which is arranged to accelerate the beam in the opposite direction each other. The beam in each ring can be collided at 6 collision points. Since at the maximum 120 beam bunch can be stored at the same time, its designed luminosity corresponds to 2×10^{26}cm$^{-2}s^{-2}$ for gold ions. Figure 3.1 shows the path of the heavy ion beam from the Tandem Van de Graaff facility to the RHIC.

3.2 PHENIX detector overview

The Pioneering High Energy Nuclear Interaction eXperiment (PHENIX) is one of the four experiments operating at RHIC [40]. The detector of PHENIX is a multi purpose detector, which is constructed to address for the measurements of a lot of possible observables in the heavy ion physics and spin physics. Therefore, the PHENIX detector consists of more than 15 sub systems. Figure 3.2 shows the schematic view of PHENIX detector.

The PHENIX sub systems can be categorized as follows. The first category is
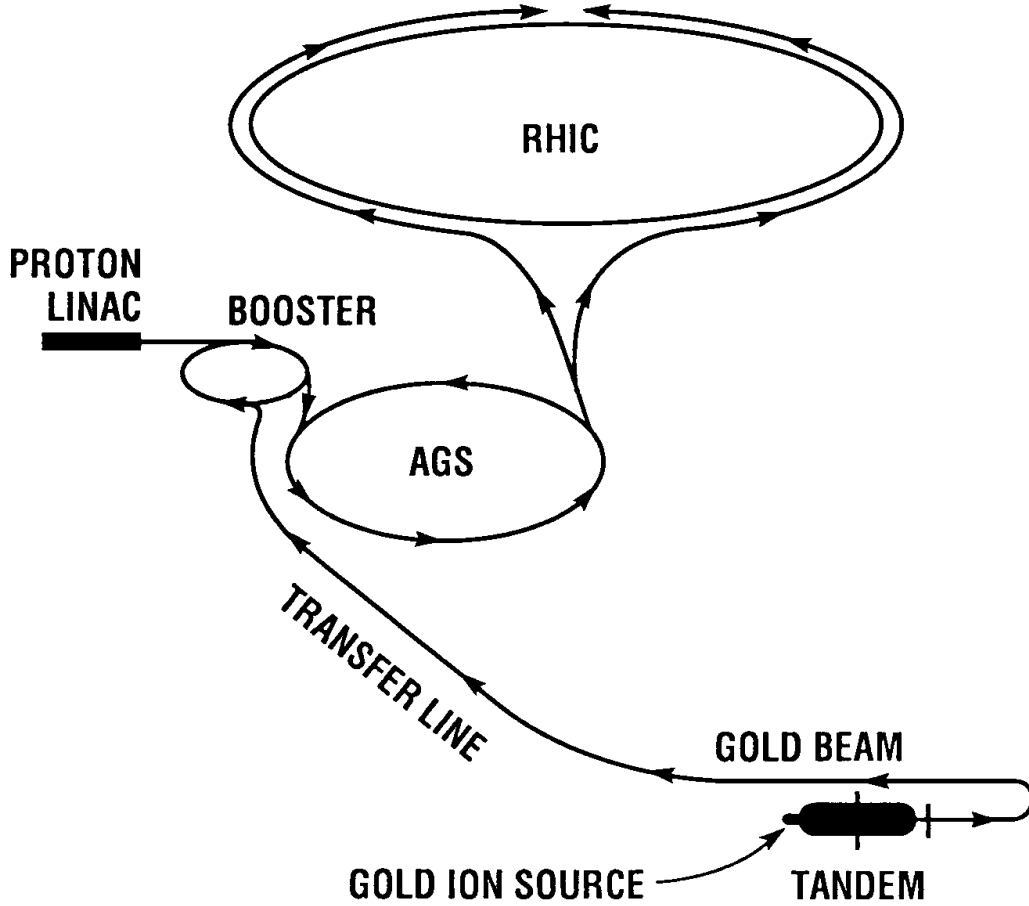
Figure 3.1: Schematic diagram for path of heavy ion beam at RHIC.

the global detectors, which are placed at the forward region from the intersecting point of nucleus beams for the purpose of beam measurements and triggers of nucleus-nucleus collision. There are two types of detectors named as the zero degree calorimeter (ZDC) and the beam-beam counter (BBC) [75]. The ZDC and BBC are designed to measure the number of spectator neutrons in the colliding nucleus and particles from the collision participant, respectively. A detailed descriptions of the global detectors can be found in Section 3.3.

The second category is the central arm spectrometer for the measurement of produced particles by the nucleus-nucleus collisions at the midrapidity region. The PHENIX detector has two central spectrometer arms, denoted as East and West. Each central arm covers the pseudorapidity range $|\eta| < 0.35$ and sub-
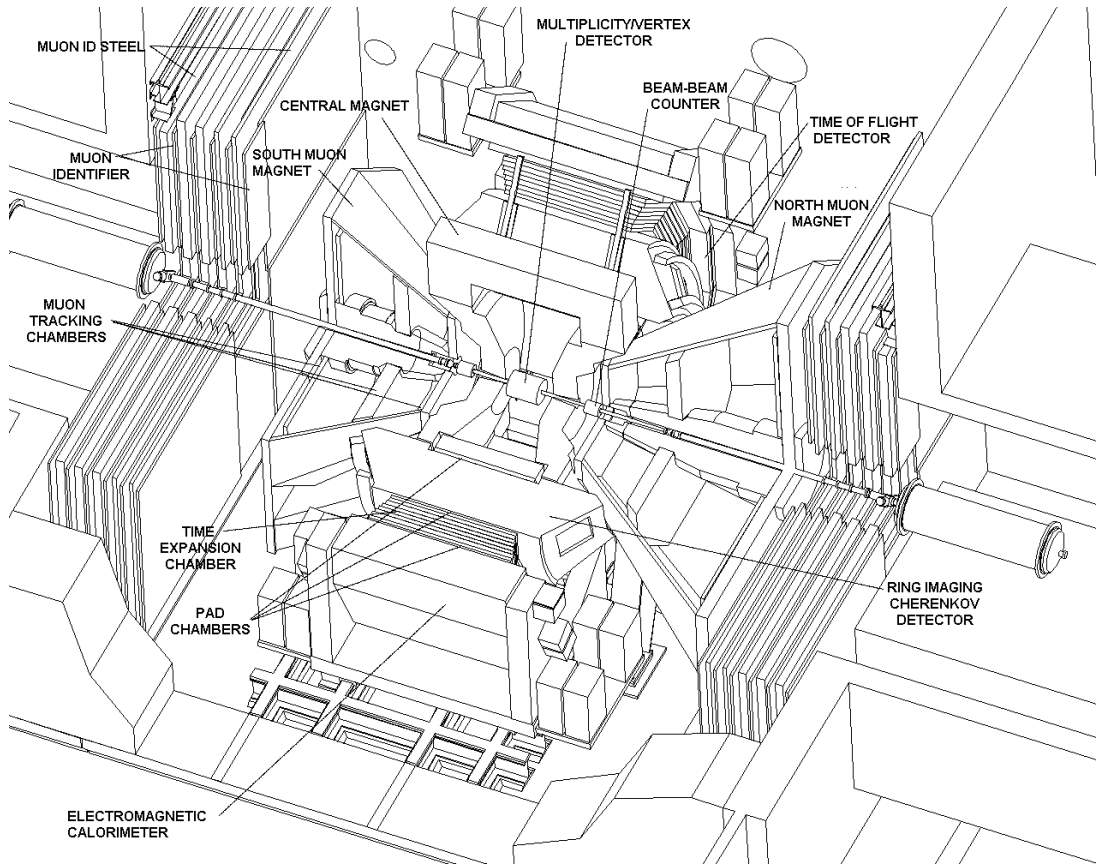
Figure 3.2: Schematic view of PHENIX detector.

tends an azimuthal angle range $\Delta\phi$ of $\pi/2$ around the beam axis (z direction). The nominal integrated magnetic field of 0.7 T·m can be applied for the gap region between the beam pipe and the central arm spectrometer by the central magnet system (CM) [76]. It enables the momentum measurement of charged particles and particle identifications (PID) with the following tracking detectors and PID detectors. A drift chamber (DC) and multi wire chambers with pad readout (PC) [77] are used for the charged particle tracking and momentum measurement. The particle identification with respect to the charged hadrons can be done by the time of flight counter in wide momentum range [78]. At the end of the central arm spectrometer, two type of electro magnetic calorimeter (EM-Cal) [79] are placed to observe neutral particles and for the energy measurement of neutral and charged particles. Details of these detectors will be explained in Section 3.4. There are the other types of PID detectors in the central arm spectrometer. Electrons and positrons are identified by the ring imaging Čerenkov counter (RICH) [78]. The time expansion chamber (TEC) is placed at the backward of RICH from the beam pipe for the purpose of high p_T electron positron

identifications by using the energy loss information (dE/dx). Since this analysis only focuses on the inclusive charged particles, mainly charged hadron, the RICH and TEC were not used. Figure 3.3 shows the layout of these detectors above.
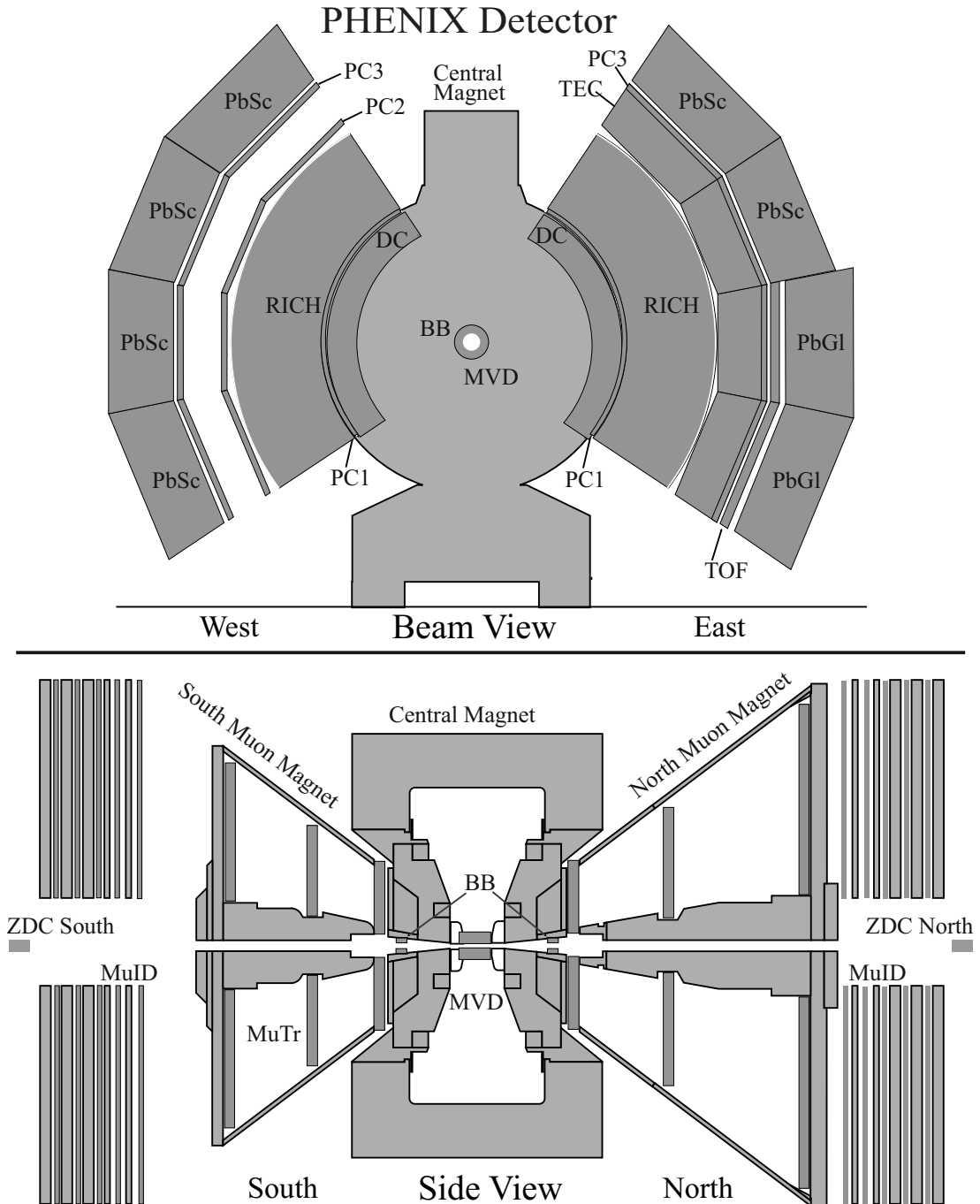
Figure 3.3: PHENIX detector layout in beam view (top) and side view (bottom).

The final category of the subsystems is the data acquisition system and online trigger system as described in Section 3.5. One can find detailed descriptions in [80, 81].

The detector subsystems relevant for this analysis will be briefly summarized below. The Au + Au minimum bias trigger and collision centrality were provided by combining information from both BBC and ZDC. The collision vertex point in each event, which is measured by BBC, is used not only for the charged particle tracking but also for the purpose of event selections due to the fiducial volume of the central arm spectrometer. The tracks of charged particles are measured by the DC by requiring the two PC (PC1 and PC3) hit association in the East arm. Cluster positions in EMCal made by charged particles are partly used for the selection of charged tracks to optimize the several parameters, which are related with track associations. The EMCal is also used for the measurement of total transverse energy E_T in each collision centrality. Since this analysis has been done at the condition of no magnetic filed to enhance the low p_T statistics of the inclusive charged particles as described in Section 4.2.2, CM and PID detectors are not used directly. However, the measured p_T spectra of charged hadrons by using those detectors are used for the estimation of background contributions in this analysis.

3.3 Global detectors

PHENIX has two types of global detectors, which are placed at the forward region at the intersection point of the nucleus beams provided from RHIC, for the purpose of collision triggers and determinations of event characterization. One is the zero degree calorimeter (ZDC) and the other is the beam-beam Counter (BBC). Both BBC and ZDC have the same type of front-end electronics (FEM) modules for their readout. The FEM consists of discriminators, shaping amplifiers, time-to-voltage converters (TVC) and flash ADC's (FADC). The time and pulse height information are digitized at the FEM's, and the digitized values are stored in digital buffer memories for the time of 40 beam bunch crossings to wait for the event trigger decisions. The basic specifications of them are introduced in this section, and their actual performances will be explained in Section 4.1.

3.3.1 Zero degree calorimeter (ZDC)

The zero degree calorimeter (ZDC) [82] in the PHENIX detector is a pair of hadron calorimeters that are placed at a distance of 18.25 m from the intersection point of nucleus beams. Figure 3.4 shows a schematic layout of the ZDC, (A) and (B) correspond to the top view and the view along with the beam direction, respectively. Since the ZDC is mounted on the backward of the bending magnet between two RHIC beam pipes, almost of the charged particles produced by
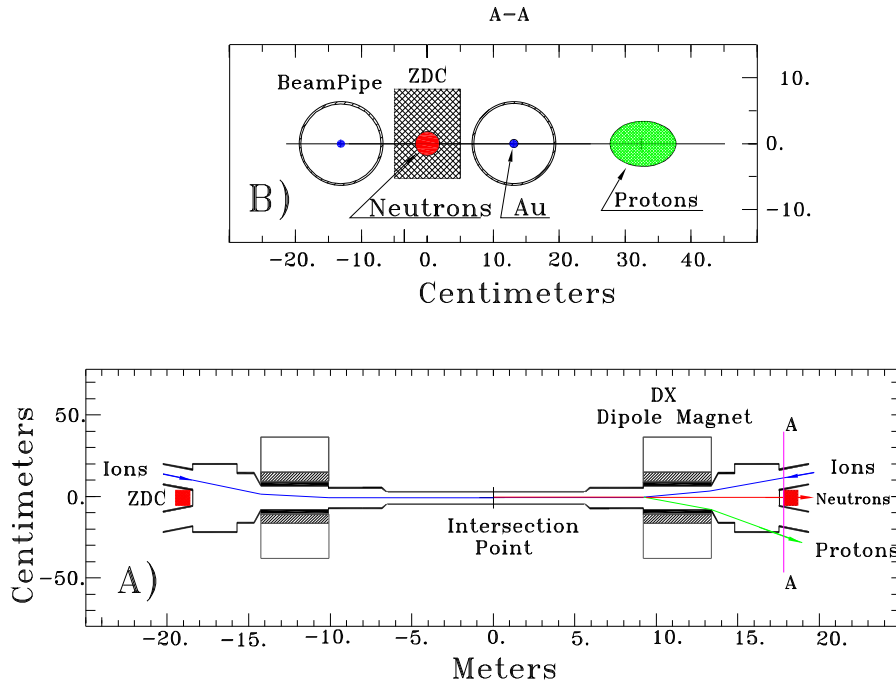
Figure 3.4: Schematic view of the ZDC layout for the top view (A) and the view along with the beam direction (B).

nucleus-nucleus collisions are swept out before the ZDC. The ZDC is composed of the tungsten absorber and layers of optical fibers to collect Čerenkov light, and its dynamic range of energy deposits is optimized for the neutron response *i.e.* it is adjusted by the single neutron peak. Therefore, the signal can be used for the minimum bias level 1 collision trigger by requiring the coincidence hits of both side of the ZDC without the beam-gas background events, where beam-gas background means collisions between the nucleus in the beam and residual gases in the RHIC beam pipe. A method of the estimation of the trigger efficiency used in this analysis will be explained in Section 4.1.2. In fact, the ZDC can count the number of spectator neutrons in nucleus, which are not come from the nucleus-nucleus inelastic collision. Combined with the information from the beam-beam Counter (see Section 3.3.2), event characters of heavy ion collisions related with impact parameter is determined. More details of the collision centrality measurement will be described in Section 4.1.3.

3.3.2 Beam-beam counter (BBC)

The beam-beam counter (BBC) [75, 83], which is one of the timing detectors in PHENIX, plays several roles to provide basic information of the nucleus-nucleus collisions. The first role is to provide the minimum bias trigger of the collisions, second one is the determination of the collision centrality. The vertex point of the nucleus-nucleus collision in beam direction V_z and its collision timing T_0 can be derived by the hit timing information of the BBC. The V_z is used for the track association of the charged particles, which is reconstructed by the central arm tracking detector (see Section 3.4.1). The T_0 value is used for the start timing of the time of flight measurement of the charged particle with the PHENIX time of flight counter (see Section 3.4.3). In this section, the method of the derivation of event information from the measured values is described with explanations of the BBC components.

The pair of BBC's is placed at a distance of 1.44 m from the nominal intersection point of the nucleus beam along with the beam axis *i.e.* forward and backward regions. One is called as North side of the BBC and the other is called as South side of the BBC. The pseudorapidity (η) coverage and acceptance in azimuth (ϕ) corresponds to $3.1 < |\eta| < 4.1$ and 2π rad, respectively. Each BBC assembly has 64 elements consisting three cm quartz Čerenkov radiator and photo multiplier tube (PMT). Figure 3.5 shows the mount position of the BBC in PHENIX and its element. Since the BBC is placed at the position within the magnetic field, a mesh dynode PMT is chosen to be made less subject to the amplification of signals [83]. The Čerenkov quartz radiator is adopted to achieve a good timing resolution, because the coincidence hits information are used for the level 1 trigger. The intrinsic timing resolution is known as ~ 40 psec by the test beam experiment [83]. The method to make the minimum bias trigger and haw to estimate the trigger efficiency will be explained in Section 4.1.2. The actual dynamic range of the charge measurement in each element of the BBC is adjusted to be able to measure at maximum 30 incident minimum ionizing particles. Therefore, in total $\sim 4,000$ particles from a nucleus-nucleus inelastic collision can be measured by the BBC. Using this information the collision centrality is determined with count of spectator neutrons measured by the ZDC as described in Section 4.1.3.

The vertex point V_z and collision timing T_0 can be calculated by the average hit timing over all elements in each side as follows

$$
\begin{aligned}
V_z &= \frac{T_S - T_N}{2} \cdot c, \\
T_0 &= \frac{T_S + T_N - 2L/c}{2},
\end{aligned}
\tag{3.1}
$$

where T_S and T_N corresponds to the average hit timing in South and North side, respectively. L is the distance between the two BBC sides. This primary collision point V_z is used for the charged particle tracking with central arm tracking
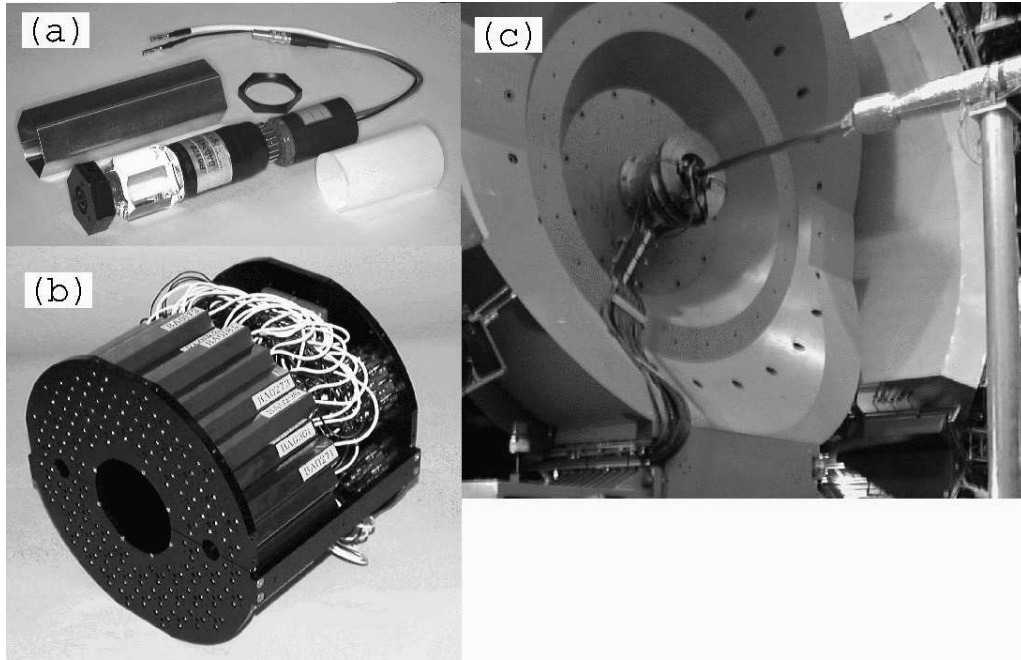
Figure 3.5: (a) One of the BBC elements consisting a mesh dynode PMT with three cm quartz radiator. (b) The BBC assembly has 64 elements. (c) The BBC is mounted on the PHENIX detector surrounding the RHIC beam pipe.

detectors (see Section 3.4.1). The resolution of V_z corresponds to 0.5 cm at the central Au + Au collisions at $\sqrt{s_{NN}} = 200$ GeV, which was evaluated by the collision data [75]. The longitudinal size of beam bunch at RHIC Au + Au collisions is designed to be 25 cm RMS. However, there is a finite fiducial range for the collision vertex in beam direction for the central arm spectrometer. For this reason, a finite range of acceptable V_z is also set for the level 1 trigger. The T_0 value is used as the start timing of the time of flight measurement as described in Section 3.4.3. The resolution of T_0 corresponds to 20 psec in the case of the central Au + Au collisions $\sqrt{s_{NN}} = 200$ GeV.

3.4 Central arm spectrometer

Several detectors in PHENIX central arm spectrometer, which is used in this analysis, are focused on in this section. This section is organized as follows; tracking detectors for charged particles are described in Section 3.4.1 and 3.4.2, a detector for charged hadron identification is explained in Section 3.4.3 and a electro-magnetic calorimeter for the total transverse energy measurement at midrapidity is introduced in Section 3.4.4.

3.4.1 Drift chamber (DC)

The PHENIX drift chambers (DC) [77] are placed in the region from 2 to 2.4 m from the beam axis (z direction) and 2 m along the z direction as shown in Figure 3.3. Figure 3.6 shows the construction of the DC frame. Each DC measures
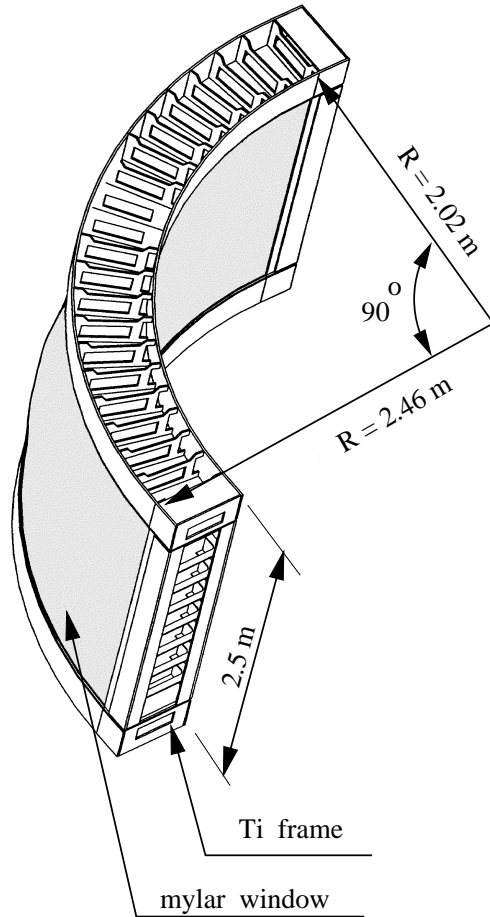
Figure 3.6: Construction of DC frame.

charged particle trajectories in the r - ϕ direction to determine the transverse momentum p_T of each particle. The single wire resolution is designed to better than 150 μm and 2 mm in r - ϕ and z direction, respectively. Two tracks can be separated whose distance at the reference plane is greater than 1.5 mm by the single wire with 99% efficiency.

The DC frame is divided in 20 equal sectors. Each sector has six types of wire modules named as X1, U1, V1, X2, U2 and V2. Figure 3.7 shows the layout of these wires in one sector. The X1 and X2 wires run in parallel to the beam axis to determine the azimuthal angle of charged particles. Since U1, V1, U2
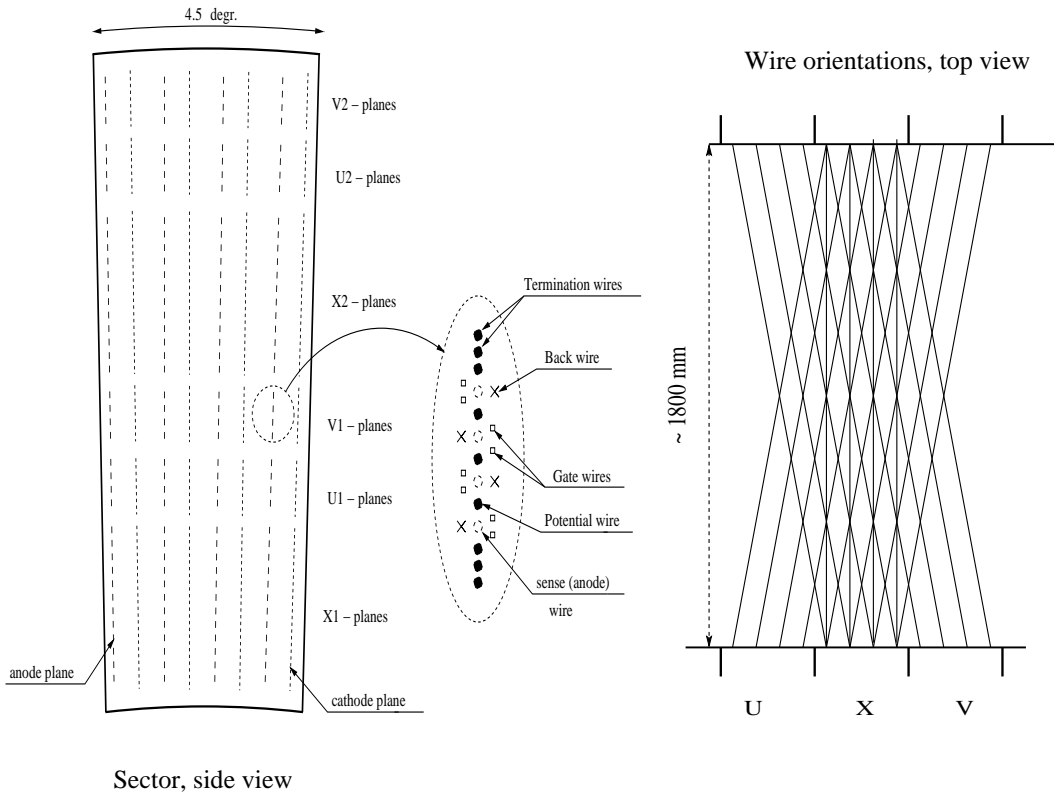
Figure 3.7: DC wire components. The layout of the wire position for one sector inside the anode plane (left). The schematic diagram of wires in top view (right).

and V2 wires are for the pattern recognition of the tracks and to measure the z coordinate, they have stereo angle of 6° relative to the X wires.

The charged tracks selected in this analysis are reconstructed by all type of the DC wires. The DC track resolution of 2 mm in the z direction at a reference radius of 220 cm from the beam axis corresponds to 1.0×10^{-3} in η. The resolution in ϕ is 1 mrad, but the maximum drift length in DC corresponds to 0.012 rad. In this analysis, the two track separation cut for the rejection of fake tracks at the circumstance of high multiplicity is optimized based on these parameters.

3.4.2   Pad chamber (PC)

The PHENIX pad chamber (PC) is a cluster of multi wire proportional chambers. The PC consists of three layers depending on their positions in r direction. The purpose of the PC is pattern recognitions in charged particle tracking with DC vectors and determinations of the location of z coordinate for the tracks. There are three layers in the West arm but only two layers in the East arm as shown in
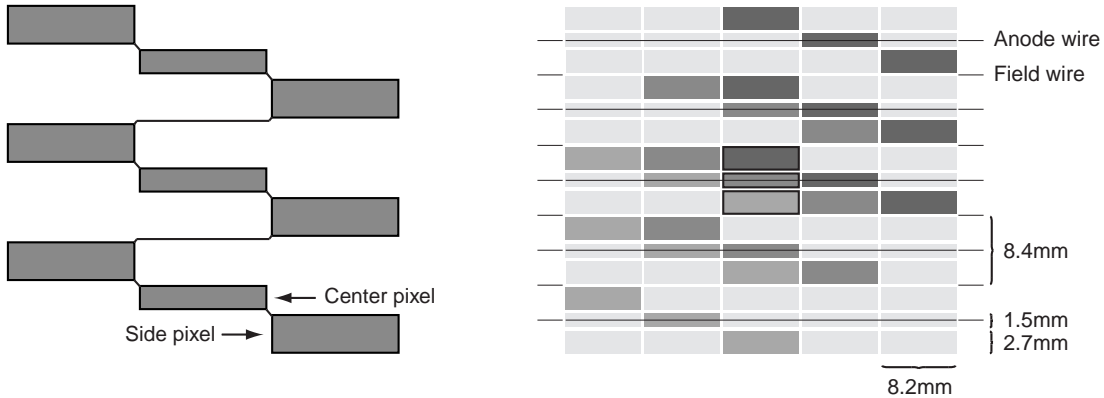
Figure 3.8: The PC pixel geometry (left). A cell defined by three pixels (right).

Figure 3.3. Since selected tracks in this analysis are measured by the East arm, only two layers are used in this analysis. The used layers are named as PC1 and PC3 placed at 2.5 m and 5 m from the beam axis, respectively.

A special pad design was invented to bring down the cost. Each layer contains a single plane of wires inside a gas volume bounded by two cathode planes. One cathode is finely segmented into an array of pixels. Figure 3.8 shows the geometrical configuration of the pixels. Each cell contains three pixels and an avalanche must be sensed by all three pixels to form a valid hit in the cell, and nine pixels are connected to a common readout channel. However, the hit information can be broken down by the requirement of identifying pattern of triplets of the pixels.

The PC1 and PC3 have the same solid angle each other, and these pixel sizes are 8.4 mm and 14.7 mm, respectively. These pixel sizes are greater than the requirement of two-track separation cuts used in this analysis as described in Section 4.2.1, and these resolutions are 1.7 mm and 3.6 mm for PC1 and PC3 respectively in z direction, and these values also correspond to 1.0×10^{-3} in η.

3.4.3 Time of flight counter (TOF)

One of the basic observables to examine the property of the QCD matter by produced particles in the heavy ion collisions is transverse momentum spectrum with particle identification. The particle identification for the charged hadrons in PHENIX has been done [84, 85] by the combined information from the tracking detectors and timing detectors. The tracking detectors (see Section 3.4.1 and 3.4.2) provide the particle trajectory and momentum information for each charged particle. Time of flight information for each track can be measured as the time difference between the BBC (see Section 3.3.2) start timing, and stop timing measured by the PHENIX time of flight counter (TOF). Using those information,

mass square value for each particle species can be derived as

$$m^2 = \frac{p^2}{c^2} \left[\left(\frac{t_{TOF}}{L/c} \right)^2 - 1 \right], \tag{3.2}$$

where p is the momentum, t_{TOF} is the time of flight and L is a flight path length.

The TOF [78] is designed to have the timing resolution of ~ 85 psec to achieve pion/kaon and kaon/proton separation up to 2.4 GeV/c and 4.0 GeV/c with 4σ, respectively. It is placed at a distance of 5.1 m from the collision vertex, in between the Pad Chamber (see 3.4.2) and the Electro-magnetic Calorimeter (see 3.4.4) in the East arm of the PHENIX. The geometrical acceptance corresponds to $70° \leq \theta \leq 110°$ in the longitudinal direction and $30°$ in azimuth. The TOF
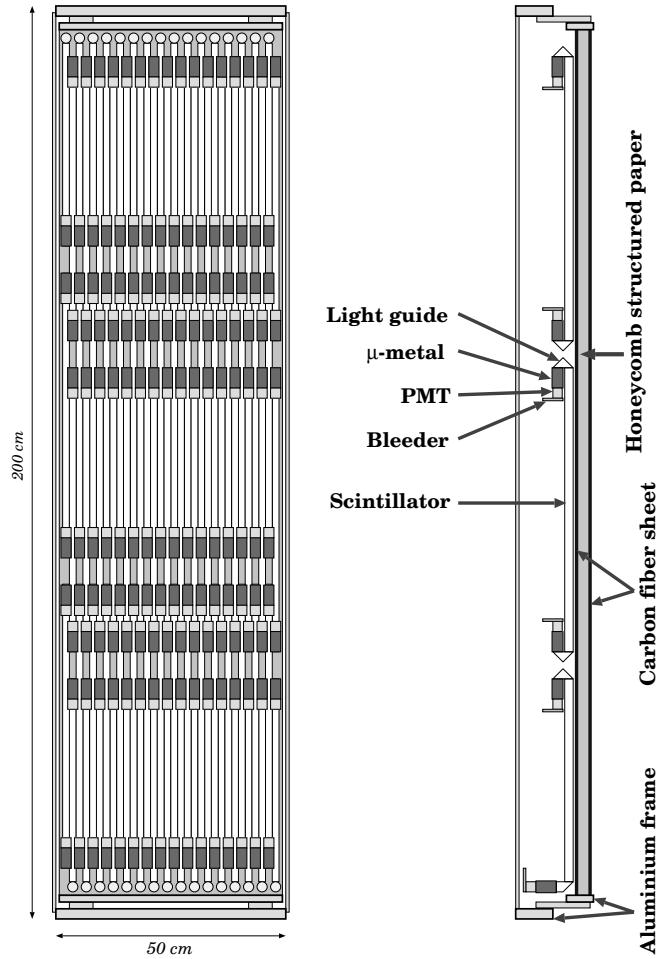
Figure 3.9: The TOF panel (left). A panel have 96 segments of plastic scintillator modules (right).

counter consists of 10 panels of the TOF walls. One TOF wall, called panel, consists of 96 segments equipped with a plastic scintillator slat and photomultiplier tube readouts at both ends. The slat is oriented along the r - ϕ direction and provides time and longitudinal position information of particles that hit the slat. Figure 3.9 shows the schematic view of one panel of the TOF counter. In total 10 TOF panels, 960 slats of scintillators and 1920 channels of PMT's have been used for the measurement of the time of flight.

3.4.4 Electro-magnetic calorimeter (EMCal)
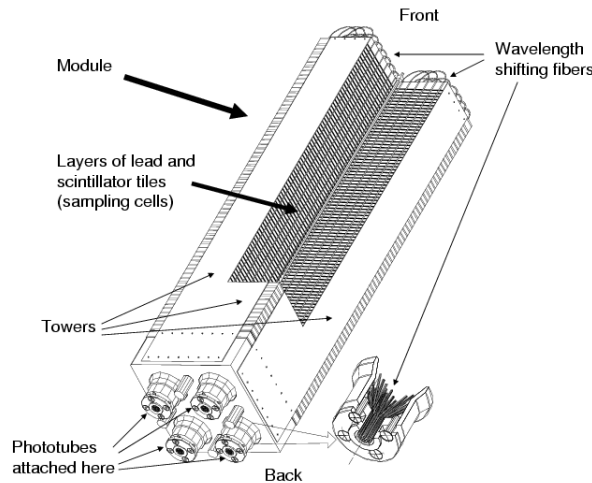
Figure 3.10: A module of lead scintillator type electro-magnetic calorimeter.

The primary role of the PHENIX electro-magnetic calorimeter (EMCal) [79] is to provide measurements of energies and spatial positions of photons and electrons produced in the heavy ion collisions. The measurements of the neutral pion production cross section have been done with the $\pi^0 \rightarrow 2\gamma$ decay channel measured by this EMCal system [86]. Although the charged hadron identification is available only up to 4 GeV/c in the transverse momentum by the TOF counter, the results of p_T distribution of π^0 enable us to discuss behaviors of the hadron productions in high p_T regions greater than 4 GeV/c.

There are two kinds of calorimeters in the PHENIX detector. One is a shashlik type lead scintillator sampling calorimeter (PbSc) [87] and the other is a Čerenkov lead glass calorimeter (PbGl). Six PbSc sectors and two PbGl sectors have been installed and each sector covers $1/8$ π rad in azimuth. They cover the same acceptance as tracking detectors in PHENIX central arms as shown in Figure 3.3. The total E_T measurement [35] have been done by using the PbSc

type calorimeter, which can be used for the event characterization in heavy ion collisions as described in Section 4.1.4. Therefore, the specifications of this PbSc type EMCal is explained in this section. A sector of PbSc is composed of 18 super modules and it covers a 2 m × 4 m plane area approximately which includes 108 PbSc super modules in total. Since a super module has 12×12 readout channels by the PMT, there are 15552 PbSc readout channels in total. Figure 3.10 shows the schematic view of a PbSc module, which has four readout channels. The PbSc calorimeter has a nominal energy resolution of 8.1% $\sqrt{E}$ GeV $\oplus$ 2.1% and an intrinsic timing resolution better than 200 ps for electro-magnetic showers.

3.5 Data acquisition system (DAQ)

The interaction rate at design luminosity of RHIC varies from a few kHz for Au + Au central collisions to approximately 500 kHz for minimum bias $p + p$ collisions. The PHNEIX data acquisition system (DAQ) [80] was designed to accommodate improvements in the design luminosity. The DAQ consists of several types of electronics modules. Since all of them are pipelined and synchronized with the RHIC beam clock, the system has deadtimeless features. Figure 3.11 shows the connections between all modules and detectors.

Figure 3.12 shows the block diagram of the PHENIX timing system. The RHIC beam clocks are distributed to the PHENIX detector system via optical serial links through a VME board called the v124 broad in the PHENIX counting house. We can set the global timing delay from the RHIC clock to all of the PHENIX subsystems to adjust the collision timing at this board. The adjusted clock are transferred to the Master Timing Modules (MTM). The MTM has two roles as follows. One is to provide the clock to the Granule Timing Module (GTM), which is allocated for each detector subsystem and the trigger system to absorb the difference of timing offsets among the subsystems and send the clock to the Front End Module (FEM). The clocks are converted from a 20 bit parallel stream being clocked at 9.4 MHz of RHIC clock rate up to 4 times the beam clock rate and then serialized into a 900 MHz stream at the GTM. Second is to provide the Global level-1 trigger (GL1) decisions synchronized with the clock. The definition of the minimum bias trigger at the GL1 for the Au + Au collisions and its trigger efficiency are explained in Section 4.1.2.

The analog data taken by each detector are transferred by cables to the FEM, which is located near the detectors in the beam intersecting region. The transferred data are buffered in each FEM for the time of 40 beam bunch crossings to wait for the decision of GL1, where the beam crossing rate corresponds to 106 ns at RHIC. There are two different types of buffering methods, one is buffering the digitized data in each beam crossing, and the other is buffering the analog data from detector in Analog Memory Unit (AMU) and then digitized when it received the trigger decision. The ZDC, BBC, DC, PC and TEC adopt former

type. The TOF, RICH and EMCal adopt the later type of the buffering method. Figure 3.13 shows the block diagram for a typical FEM with AMU. What kind of data are buffered *e.g.* pulse height and timing, depends on the purpose of each detectors and more detailed descriptions are elsewhere in [40].

The triggered data are transferred to the Data Collection Modules (DCM) via the optical fiber. The maximum average level-1 trigger (LVL1) rate is 25 KHz and the RHIC beam crossing clock runs at 9.4 MHz. At the maximum LVL1 trigger rate, the FEM's send over 100 GBytes of data per second. The DCM are designed to receive this large uncompressed event fragment data volume. Firstly, the DCM provide data buffering up to five LVL1 events, and perform zero suppression for all detector subsystems. At the same time, the data are performed error checking and formatting. The formatted data are compressed and send to the PHENIX Event Builder (EvB).

The two primary functions of the PHENIX EvB are to perform the final stage of event assembly in the PHENIX DAQ and to provide an environment in which level-2 (LVL2) trigger processing is performed. The EvB receives many parallel data streams from the PHENIX DCM's. The fragments from each data stream
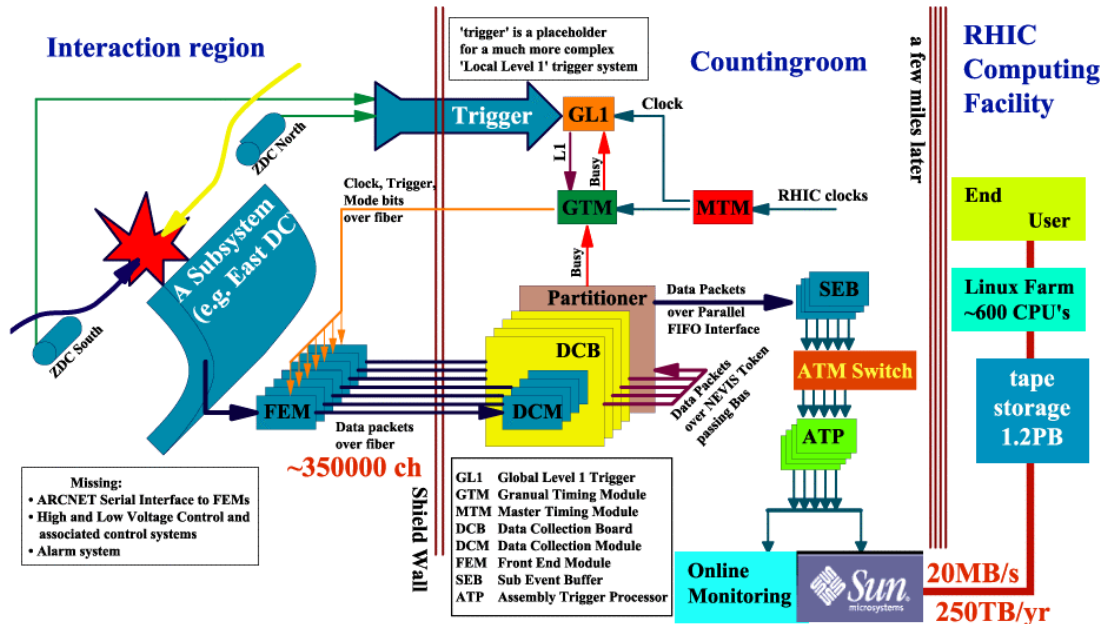
Figure 3.11: Schematic diagram of the PHENIX data stream.

PHENIX Timing System
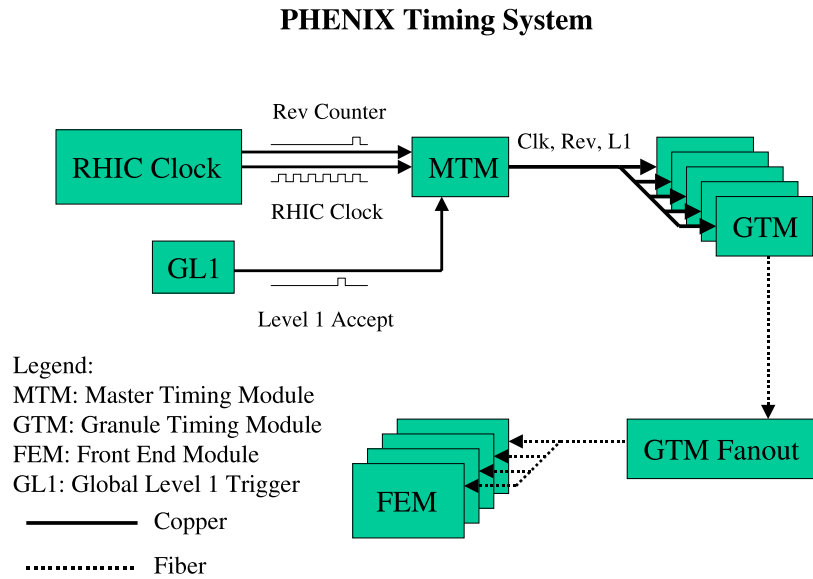
Figure 3.12: Block diagram of the PHENIX timing system.
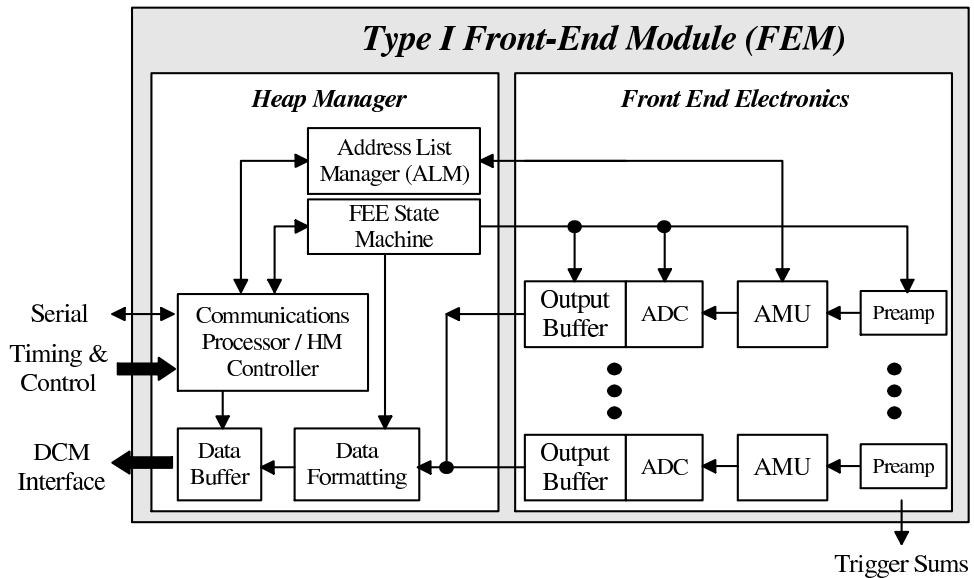
Figure 3.13: Block diagram of the typical FEM with AMU.

are assembled into complete events and performed LVL2 trigger processing on
the events. The accepted events are transmitted to the PHENIX Online Control
System (ONCS) for logging and distribution to monitoring processes. Figure 3.14
shows the block diagram of PHENIX EvB. The fragmented data in each subsys-
tems are once stored to sub event buffer (SEB), and they are distributed by the
Asynchronous Transfer Mode (ATM) technology to the Assembly/Trigger Pro-
cessors. In the case of Au + Au collisions, the total data size of the event is
all different depending on the collision centrality and the number of produced
particles. Therefore, the order of event in real time dose not correspond to the
order in the data file by this parallel processing. The performance of the baseline
EvB were to process events at an input rate of 12.5 kHz and to handle aggregate
data rates as high as 500 MByte/s.
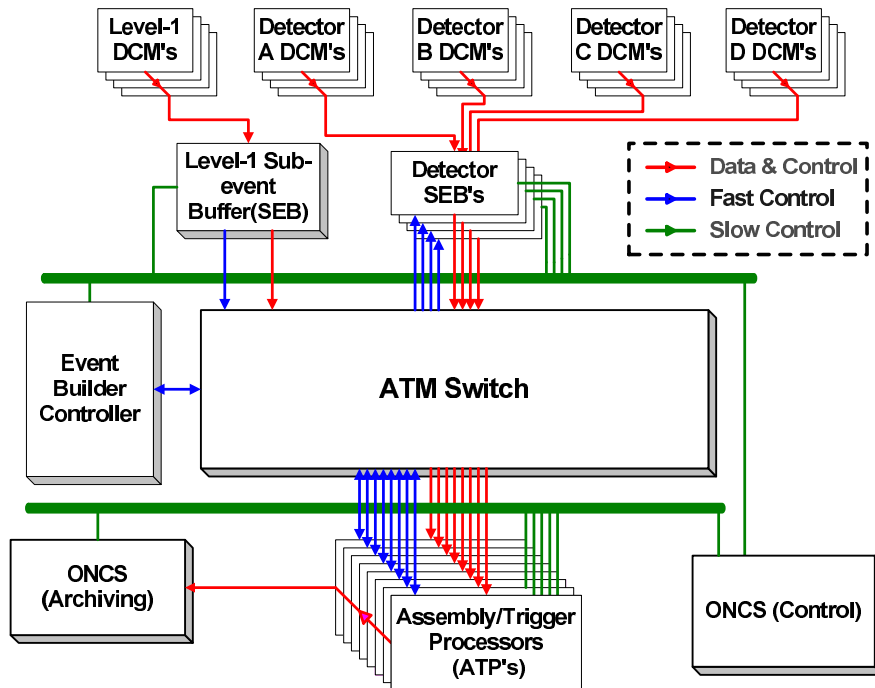
Figure 3.14: Block diagram of PHENIX Event builder.

Chapter 4

Analysis

4.1 Event selections

4.1.1 Data set

This analysis was performed using a data set collected by the PHENIX detector during the run period of gold ion beam operation with 100 GeV/c beam momentum per nucleons from 2001 to 2002. Figure 4.1 shows the integrated luminosity delivered by RHIC as a function of days in the run period. In this period, 24 μb^{-1} were collected at the PHENIX experiment out of the delivered integrated machine luminosity of 85 μb^{-1}. The data were collected by the minimum bias trigger selections as described in Section 4.1.2 with no magnetic filed condition for the PHENIX central arm tracking detectors (see Section 4.2.1). This trigger condition includes the collision vertex cuts of 30 cm from the center of the PHENIX detector. Out of this data set, this analysis was targeted in total 1.5 million events. These event samples were imposed to pass the rigorous data quality assurance with respect to the detector stability as described in the Section 4.1.5.

4.1.2 Trigger selection

The heavy ion physics aims to investigate the production of the QGP by colliding many nucleons as much as possible at high energy. Therefore, estimations of the minimum bias collision trigger efficiency for the total inelastic cross section in the nucleus-nucleus collision is one of the most important issues, because almost of physics results focus on the event characteristics as compared to the single nucleon collisions $i.e.$ $(\bar{p})p + p$ interactions.

The minimum bias collision trigger used in this analysis was made by referring the two forward global detector's information from the BBC and ZDC, and the global level 1 electric logic board. The definition of the minimum bias event to take the data demands coincident hits of two PMT's for each side of the BBC
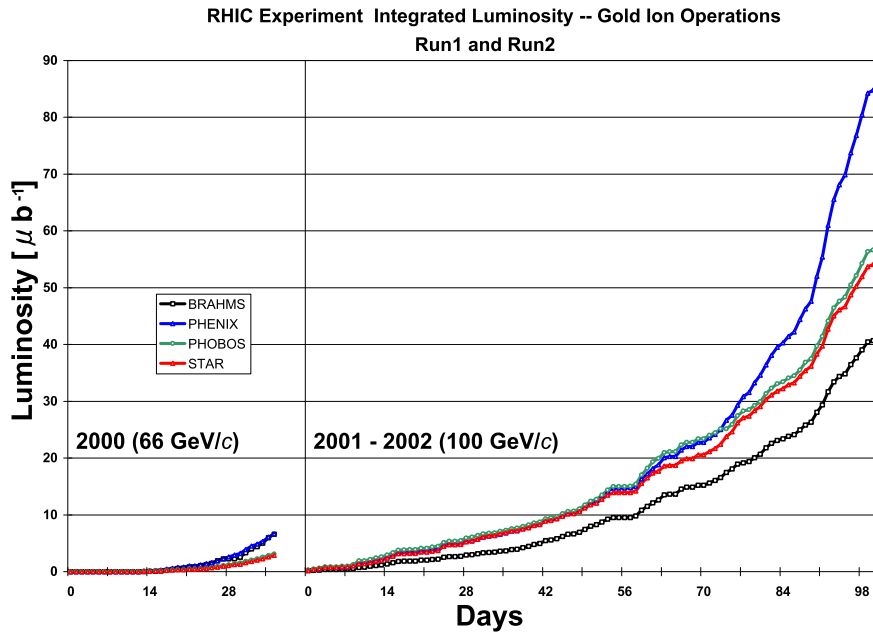
Figure 4.1: Integrated luminosity delivered by RHIC as a function of days. The RHIC was operated with gold ion beam in this term. The beam momentum is 66 GeV/c (left) per nucleons in 2000 and 100 GeV/c (right) per nucleons from 2001 to 2002. Markers correspond to delivered luminosity for four experiments indicated in the legend.

and coincident hits of single neutron energy deposit for each side of the ZDC within beam bunch crossing time. The sides correspond to the forward and backward from collision vertex along with the beam axis. The BBC measures relativistic charged particles from participating nucleons in a Au + Au collision, and the ZDC measures the spectator neutrons, which are not participating to the Au + Au interaction. Therefore, these two detectors take complementary roles to detect Au + Au collisions. It was also required that information of collision vertex positions in the minimum bias trigger definition is to optimize the acceptance of the central arm tracking detectors. In this analysis, a collision vertex cut of $z < \pm 5$ cm was applied on the event selections at the offline data analysis. It is to avoid discrepancies on the geometrical acceptance of the PHENIX central arm in event-by-event basis. Total 256 k events in Au + Au collisions at $\sqrt{s_{NN}} = 200$ GeV were used to obtain the final results.

The flow to make trigger decisions is explained as follows. The hit time in each PMT of the BBC is digitized in the front-end electronics module (FEM) and sent to the BBC local level 1 (BBCLL1) electric logic board with bit reductions for the fast judgment of the BBCLL1 trigger decision. The valid range of the hit time and the time offset for each PMT are applied to the FEM a priori. In the

BBCLL1 logic board, the number of hit PMT's and collision vertex positions are calculated from the reduced bit time information, and then it is sent to the global level 1 board. In the global level 1 broad, using the predefined valid range of the collision vertex and the number of hit PMT's of the BBC *i.e.* two coincident hits in each side, the minimum bias trigger is made associated with ZDC coincidence hits for each side. The trigger decisions are sent to the other subsystems to take the data for the buffered data in each FEM.

The trigger efficiency of the BBCLL1 with respect to the total inelastic cross section of Au + Au collisions was estimated by the GEANT [88] based Monte Carlo simulation with respect to HIJING 1.35 [89] event generator input. In the GEANT based MC simulation, all material information of the PHENIX detector system are implemented to reflect the effects of realistic particle interactions. The realistic BBC responses are applied with calibration constants obtained by the collision data to reproduce the digitized value, for instance, charge and time distributions and the threshold values for each PMT. An software, which is to emulate the BBCLL1 logic board, is applied to reproduce the digitized values to estimate the effects on the bit reduction and the online z vertex cut. According to the simulation, the trigger efficiency of the BBCLL1 for the valid range of z vertex is defined as

$$\varepsilon_{\mathrm{BBCLL1}} \equiv \int_{-z}^{z} \varepsilon(z) \cdot w(z) dz, \tag{4.1}$$

where the efficiency $\varepsilon(z)$ as an input-output ratio and weight $w(z)$ for the z vertex distribution in each z vertex position are defined as

$$
\begin{aligned}
\varepsilon(z) &\equiv \frac{N_{(\mathrm{on\ \&\ off})}(z_{\mathrm{rec}})}{N_{\mathrm{inp}}(z_{\mathrm{true}})}, \\
w(z) &\equiv \frac{1/N_{\mathrm{inp}}(z_{\mathrm{true}})}{\int_{-z}^{z} 1/N_{\mathrm{inp}}(z_{\mathrm{true}}) dz},
\end{aligned}
\tag{4.2}
$$

respectively. $N_{(\mathrm{on\ \&\ off})}$ is the number of reconstructed events by applying the online and offline z vertex cut. The online z vertex cut in the BBCLL1 board corresponds to 75 cm, and the offline z vertex cut in the reconstructed z is 30 cm for the offline analysis. N_{inp} means the number of generated events within the generated z vertex position. Figure 4.2 shows the obtained BBC trigger efficiency as a function of reconstructed z vertex positions. Several things have to be taken into account here for the systematic error estimations in this method. Although the number of produced particles as an input is adjusted to the measured value, this method depends on the model of the event generator *e.g.* particle composition and momentum distributions of produced particles. Furthermore, the obtained trigger efficiency depends on the vertex distributions itself. As an instrumental ambiguity, variations of applied threshold values for each FEM channel should be reflected to the trigger efficiency. Combining all ambiguities mentioned above,
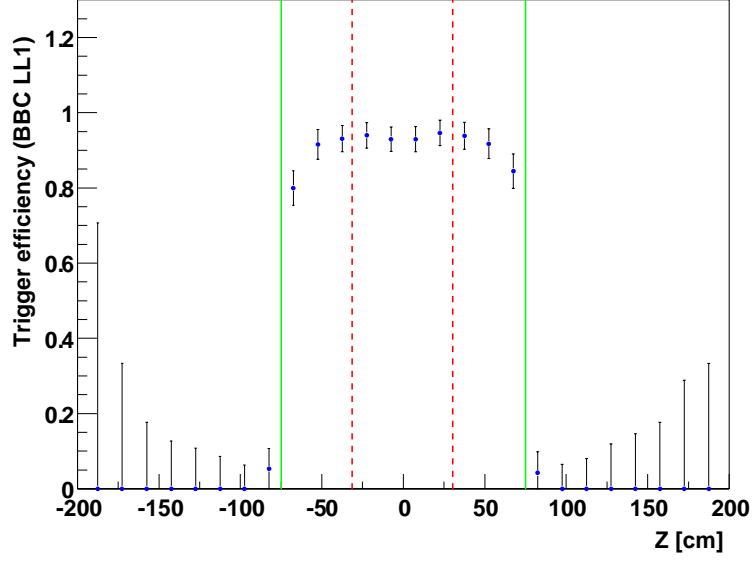
Figure 4.2: Trigger efficiency of BBC local level 1 trigger as a function of z vertex measured by BBC. This trigger efficiency is defined for the offline analysis. Solid lines ($|z| = 75$ cm) and dashed lines ($|z| = 30$ cm) correspond to online and offline vertex cuts, respectively.

the BBC trigger efficiency for the selected trigger condition is finally obtained as

$$\varepsilon_{\mathrm{BBCLL1}} = 92.3\% \pm 0.4\% \text{ (statistical error)} \pm 1.6\% \text{ (systematic error)}. \quad (4.3)$$

The trigger efficiency of ZDC is estimated by the relative trigger rate with respect to the BBC triggered events represented as

$$R = \frac{N_{\mathrm{BBCLL1}} \ \& \ N_{\mathrm{ZDCNS}}}{N_{\mathrm{BBCLL1}}}, \quad (4.4)$$

where N_{ZDCNS} is the number of events with coincident hits in the North and South ZDC sides. Figure 4.3 shows a transit of the relative trigger rate, which is obtained by requiring the BBC offline z vertex cut of 30 cm, for a sampled period. The average value of the rate was obtained by the 97.5%. The dropping to the lower value is due to the increase of background events *e.g.* beam-gas collision and beam halos. The BBCLL1 trigger rate as the denominator in Equation (4.4) is increased by the increase of the accidental coincidence hits in this case. Since 40% of BBCLL1 triggered events withouout ZDCNS triggered events correspond to the ZDC inefficiency, eventually, the ZDC trigger efficiency with respect to the BBCLL1 can be obtained as

$$\varepsilon_{(\mathrm{ZDCNS \ | \ BBCLL1})} = 99.0\% + 1.0\% - 1.6\% \text{ (systematic error)}. \quad (4.5)$$
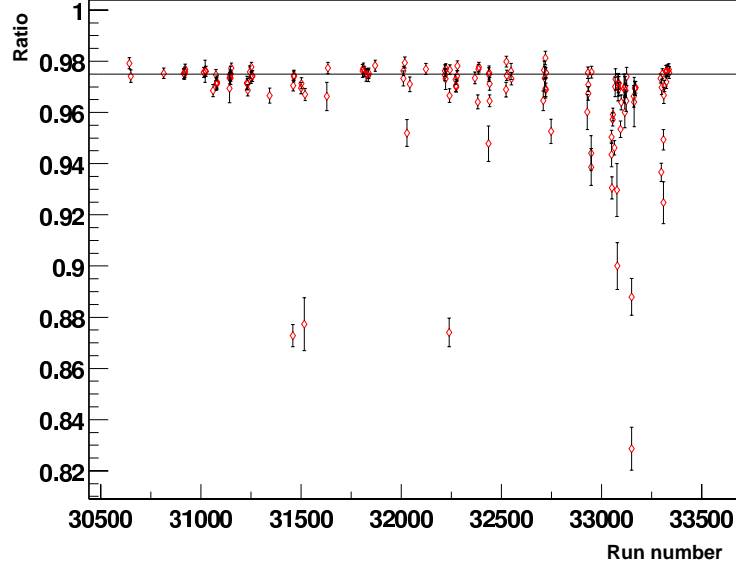
Figure 4.3: Relative counts of the ZDC triggered events with respect to the BBCLL1 triggered events as a function of the run number. The horizontal solid line corresponds to 97.5%.

Finally, the minimum bias collision trigger efficiency for the total inelastic cross section in Au + Au collision at $\sqrt{s_{NN}} = 200$ GeV in this trigger selection can be obtained by Equation (4.3) and Equation (4.5) as

$$
\begin{aligned}
\varepsilon_{(\text{BBCLL1 \& ZDCNS})} &= \varepsilon_{\text{BBCLL1}} \times \varepsilon_{(\text{ZDCNS} \mid \text{BBCLL1})} \\
&= 91.4\% + 2.5\% - 3.0\% \text{ (systematic error)}, \quad (4.6)
\end{aligned}
$$

with all of the systematic errors explained so far.

4.1.3   Collision centrality and number of participant nucleons

$A + A$ collisions have event-by-event characteristics for the particle productions depending on the impact parameter in each event. The parameter is defined by the distance between the center of two colliding nuclei as shown in Figure 4.4. The basic idea to classify the event characteristics is based on a simple geometrical picture named as Glauber model [9]. In this model, nucleons in nucleus which are distributed as black disks within the finite size of the nucleus are distributed with the nuclear density profile. The profile is parametrized by a Woods-Saxon function as a function of the distance from the center of the nucleus r as

$$
\rho(r) = \rho_0 \cdot \frac{1}{1 + e^{(r-R)/a}}, \quad (4.7)
$$
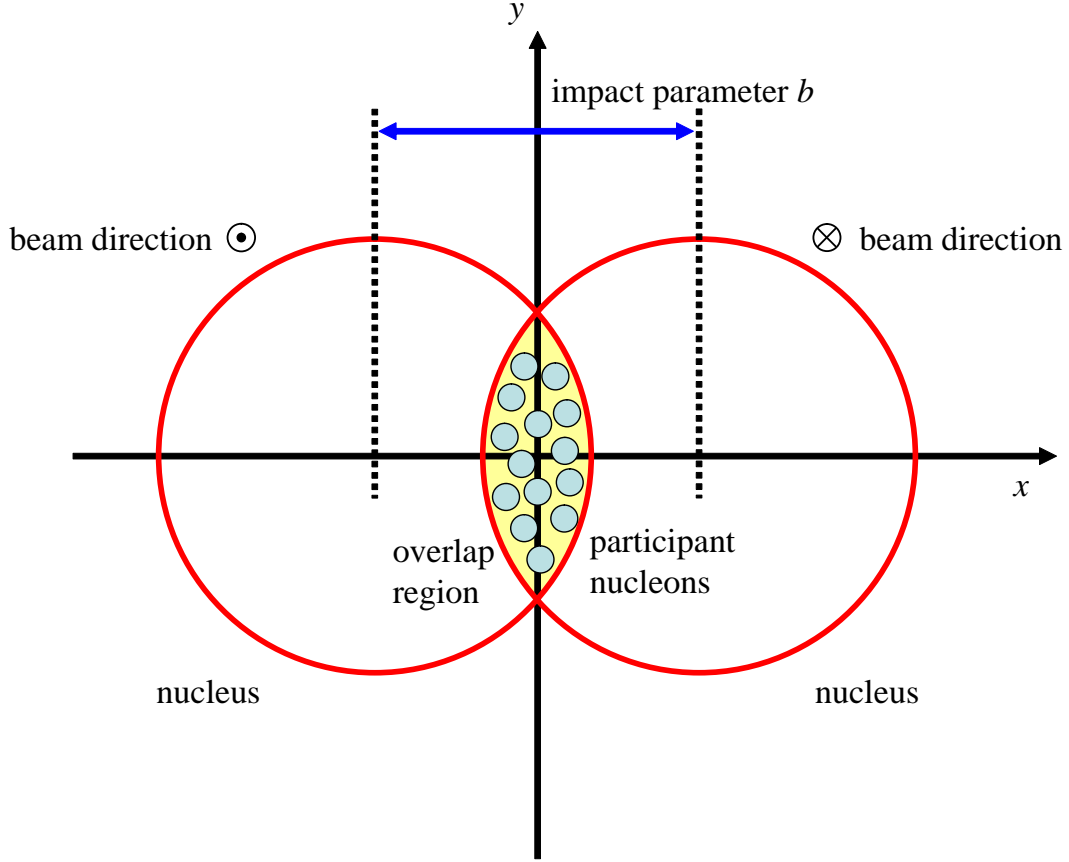
Figure 4.4: Collision geometry of two colliding nuclei. The impact parameter is defined by the distance between the center of two colliding nuclei.

where R and a corresponds to the diameter of the nucleus and the diffusion parameter for the outer surface of the nucleus, respectively. A collision for each nucleon pair in the nucleus takes place if their distance is less than $(\sigma_{NN}/\pi)^{1/2}$, where σ_{NN} is the nucleon-nucleon inelastic cross section at the collision energy. According to this model, the total inelastic cross section with respect to the $A + A$ collisions can be calculated by integrating the individual inelastic cross section over all of possible pairs for a given impact parameter, which can be obtained by a Monte Carlo (MC) simulation with several ambiguities of the model. In the case of Au + Au collision at $\sqrt{s_{NN}} = 200$ GeV, the model parameters in Equation (4.7) correspond to $R = 6.38$ fm, and $a = 0.54$ fm [90] and the nucleon-nucleon cross section $\sigma_{NN} = 42$ mb as the central value for the MC simulation. Figure 4.5 shows the result of differential Au + Au inelastic cross section $d\sigma_{\text{Au+Au}}/db$ at $\sqrt{s_{NN}} = 200$ GeV as a function of the impact parameter b obtained by the MC simulation.
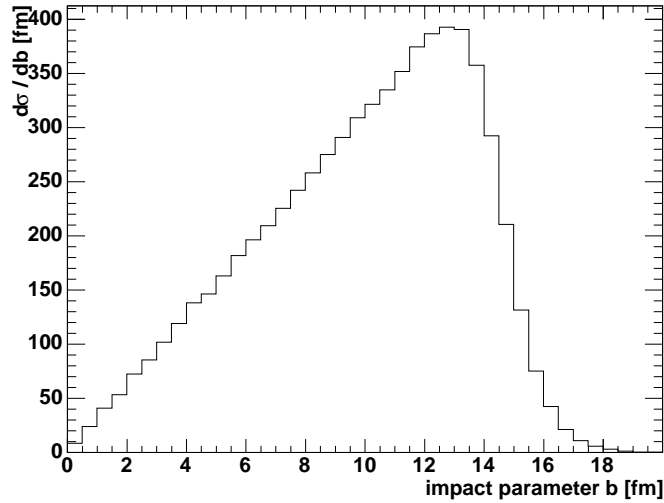
Figure 4.5: Differential Au + Au inelastic cross section at $\sqrt{s_{NN}} = 200$ GeV as a function of impact parameter b.

Although the event characteristics in Au + Au collisions are clearly dependent on the impact parameter b, the direct measurement of the impact parameter is very difficult such as in the circumstance of collider experiment. Nevertheless, it can be estimated indirectly as a collision centrality percentile by the multiplicity or energy measurement for the produced particles, because a monotonic relation between the impact parameter and total multiplicity or total energy can be expected owing to the result of the impact parameter dependence of differential cross section in the Glauber model MC simulation as shown in Figure 4.5.   In the case of the PHENIX experiment, the collision centrality is determined in the anti-correlation of multiplicity distributions between the two forward detector's information (ZDC and BBC) because these two detectors take complementary role to detect the Au + Au collisions as described in Section 4.1.2. Figure 4.6 shows the reproduced anti-correlation between the normalized energy sum in the ZDC and charge sum at the BBC obtained by the MC simulation. The energy resolution of the ZDC ($\sigma_E/E = 218\%/\sqrt{E/GeV}$) is applied, and the charged particle multiplicity distribution and fluctuation in the BBC are adjusted to calibrated collision event by the parameters of Negative Binomial Distribution (NBD) for the MC simulation. Areas filled by the different colors are obtained by choosing the range of impact parameter so that each event fraction equals 5% out of all generated events. Since the BBC measures the charged particle multiplicity from the collision, it is increased with increasing collision centrality. Meanwhile, the ZDC energy sum decreases with increasing collision centrality because it measures the deposit energy of neutrons comes from the spectator part of hadronic inter-
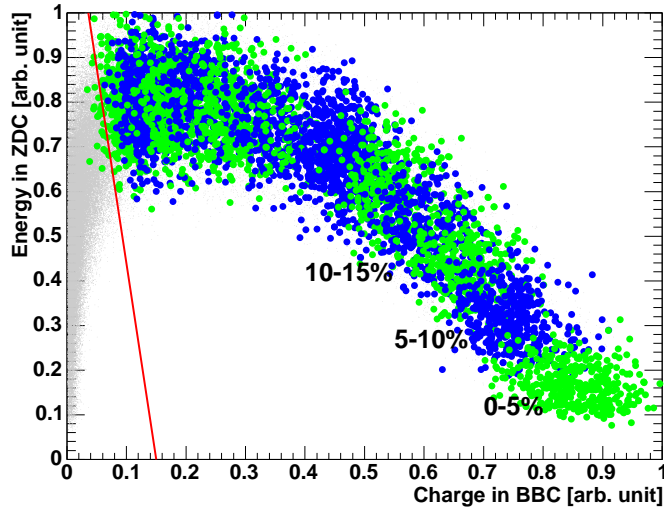
Figure 4.6: BBC charge vs. ZDC energy calculated by a Monte Carlo simulation based on Glauber model [9]. Areas filled by colors are obtained by choosing the range of impact parameter so that each event fraction equals 5% out of all generated events. The solid line indicates the limit of the most peripheral sample used for this analysis.

action *i.e.* they do not participated in the Au + Au collisions. This is the reason why Figure 4.6 indicates the anti-correlation in the region of the BBC charge sum above around 0.2. For the low central region, which is called as peripheral collision, the correlation between the BBC and ZDC can be understood as the dominant effect of mutual Coulomb dissociation [91] in place of hadronic interaction. The number of produced neutrons increases in this collision centrality (BBC charge sum < 0.1) with increasing the centrality due to the increase of electromagnetically dissociated neutrons from both colliding gold ions as compared to the decrease of neutrons in hadronic process. According to the event classification based on the impact parameter in Glauber model MC simulation (see Figure 4.6), the real event samples are separated by the lines from 0.15 in the BBC charge and 0 in ZDC energy in a radial pattern. Figure 4.7 shows the definition of the event classification with respect to the collision centrality in the real event samples with 5% event fraction. The solid line indicates the limit of the most peripheral event sample used for this analysis, and most right hand side region tagged as 5% inside the figure corresponds to the most central 5% event samples.

The number of participant nucleons N_{part} at $A + A$ collisions, which almost corresponds to the number of colliding nucleons existed interior side of the overlap region in Figure 4.4, is often used to represent the collision centrality classification instead of the impact parameter b. This representation is useful in the case that
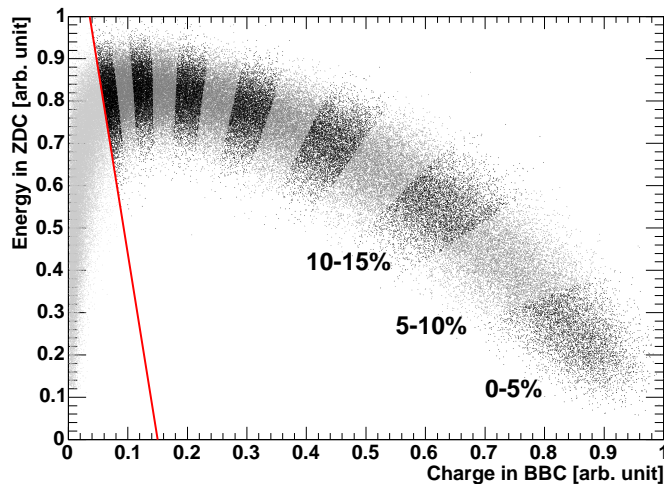
Figure 4.7: Definition of collision centrality, BBC charges versus ZDC energy. Event samples with 5% bin width are plotted from 0 - 5% (central) to 60 - 65% (peripheral). The solid line indicates the limit of the most peripheral sample used for this analysis.

one wants to compare the events with $p(\bar{p}) + p$ collision events at the same collision energy. It can be also extracted from the MC simulation in event-by-event basis and average values of $\langle N_{part} \rangle$ are calculated with respect to the corresponding centrality classes defined in Figure 4.7. The obtained values are summarized in Table 4.1.

At the same time, several systematic error sources on the estimation of the $\langle N_{part} \rangle$ in the MC simulation have been taken into account for both ambiguities originating from the model parameters and adjustment with experimental data due to the centrality classification as follows. Since the most dominant sources of the systematic errors are ambiguities on the nucleus-nucleus cross section and Woods-Saxon parameters, σ_{NN}, R and a are varied by 7% from the central values at maximum in the simulation. In general, nuclei have a hard core component, it means there is restricted area for the nucleus overlapping around the center of nucleus. This effects is estimated by changing requirement of minimum distance between the center of two nucleons at the nucleon-nucleon collisions as greater than 0.4 fm. Due to the formation of the deuteron by the coalescence process [92] in the forward region, a fraction of detectable number of neutrons is reduced compared to the number of spectator neutrons. It is described by a neutron loss function in the MC simulation and also evaluated for the systematic error estimation. The assumption of black disk is evaluated by varying the interaction probability distribution as the following two perspectives. In this case, the black disk corresponds to 100% necleon-nucleon interaction probability

Table 4.1: Average of the number of participant nucleon $\langle N_{part} \rangle$ with the impact parameter $\langle b \rangle$ for each collision centrality class by the Glauber model MC simulation.

Centrality class (%)	$\langle b \rangle$ (fm)	systematic error of $\langle b \rangle$	$\langle N_{part} \rangle$	systematic error of $\langle N_{part} \rangle$
0 - 5	2.3	0.1	351.4	2.9
5 - 10	4.1	0.2	299.0	3.8
10 - 15	5.2	0.3	253.9	4.3
15 - 20	6.2	0.2	215.3	5.3
20 - 25	7.0	0.4	181.6	5.6
30 - 35	8.4	0.3	125.7	4.9
35 - 40	9.1	0.4	102.7	4.3
40 - 45	9.7	0.4	82.9	4.3
45 - 50	10.2	0.4	65.9	3.4
50 - 55	10.7	0.4	51.6	3.2
55 - 60	11.2	0.4	39.4	3.5
60 - 65	11.7	0.5	29.8	4.1

independent of the distance between the nucleons. One is using a reduced interaction probability (gray disk) by taking the ratio between the total and inelastic nucleon-nucleon cross section as $\sigma_{\text{inelastic}}/\sigma_{\text{total}}$. The other is assuming the interaction probability as Gauss distribution depending on the nucleon-nucleon impact parameter, which is same method as in an event generator FRITOF 7.0 [93].

For the estimation of systematic errors of $\langle N_{part} \rangle$, which depend on the experimental conditions, following items are considered. The charged particle multiplicity fluctuation in the BBC are varied to evaluate the smearing effect on the detector resolutions. Basically, the anti-correlation between the BBC charge and ZDC energy indicates a linear relation for the central event samples in the MC simulation. However, Figure 4.7 shows bending behavior due to the saturation effect of the BBC charge in each PMT for the small fraction of events. In fact, Figure 4.6 is made by the MC simulation with this artificial saturation effect. It affects the centrality classification defined by the radial lines as shown in Figure 4.7. This effect is verified by changing the central point of the radial lines from 0.5 to 2.0. Since the event classification depends on the event fraction, errors of the minimum bias trigger efficiency (see Section 4.1.2) affects the difference of selected event fraction between the MC simulation and real event samples. It has been considered by changing the value of the trigger efficiency within the systematic error of it. The statistics of the real event samples also affects the event classifications. It is evaluated as the systematic error by looking at the stability of the fraction in the real data samples taken at the different run range.
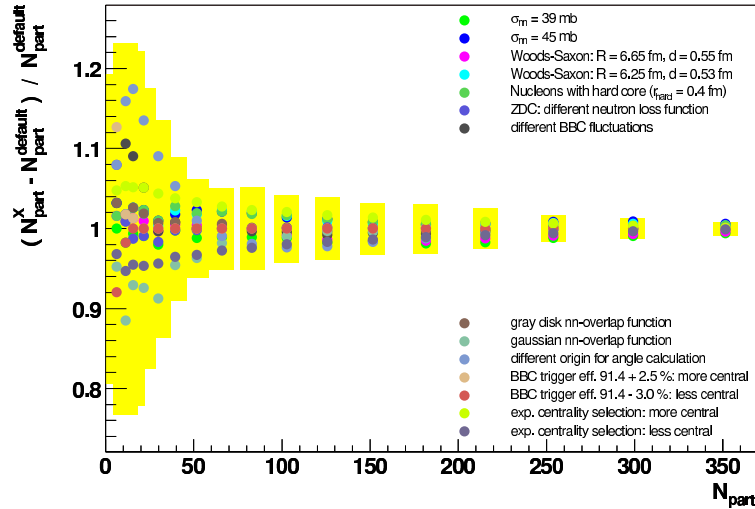
Figure 4.8: Summary of the verification on model ambiguities described in the legend for the systematic error estimation of the $\langle N_{part} \rangle$. Shaded bands indicate the total systematic errors.

Figure 4.8 shows the summary of the systematic error sources and their values explained above as a function of the N_{part}. The total systematic errors for the $\langle N_{part} \rangle$ are obtained by the quadratic sum of all in above sources as shown in the shaded band in Figure 4.8 and the values are listed in Table 4.1. Finally, the total inelastic cross section for Au + Au collision at $\sqrt{s_{NN}} = 200$ GeV was obtained with the systematic error as

$$\sigma_{\mathrm{Au+Au}} = 6847 \pm 542 \text{ mb.} \tag{4.8}$$

An analysis on the measurement of the density correlations was performed by using this event sample with the collision centrality classification. Furthermore detailed event selection criteria, which are related to the charged track reconstructions and multiplicity fluctuation measurements, will be explained in Section 4.2.

4.1.4   Energy density estimation

One of the methods to characterize events in $A + A$ collisions without aid of any models like the Glauber model described in Section 4.1.3 is to characterize the events by the total measured energy for all produced particles. Although PHENIX does not cover whole the acceptance (4π) to measure the all produced particles, the electro-magnetic calorimeter (EMCal [79]) in PHENIX has sufficient capability to measure the total transverse energy in midrapidity region by the sampled data in the limited acceptance. The total transverse energy E_T is defined
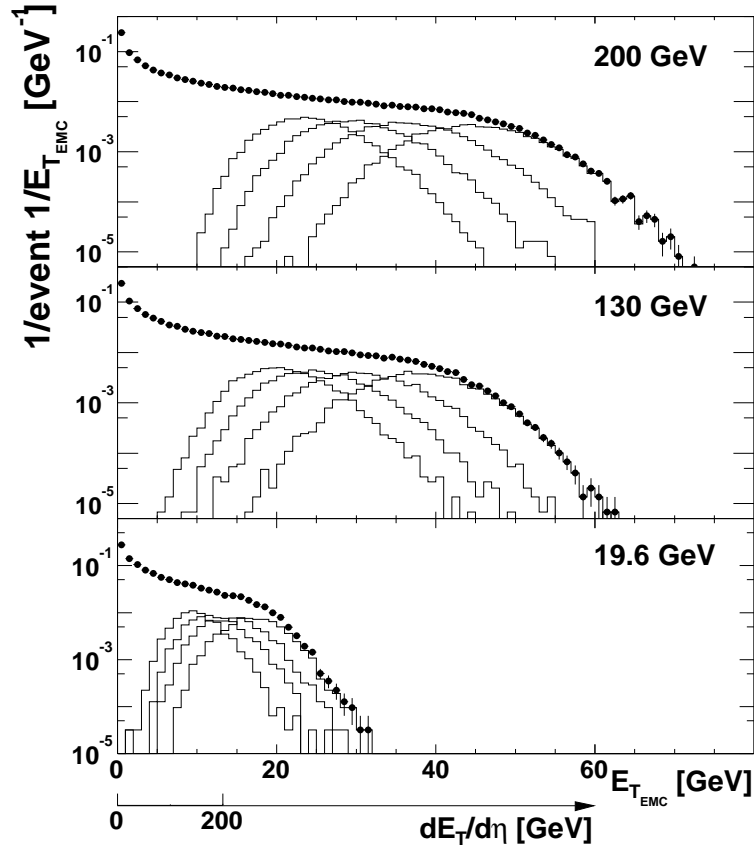
Figure 4.9: The raw E_T distribution in two EMCal sectors measured in Au +Au collisions at three beam energy described in the legend. The lowest axis correspond to the value of $dE_T/d\eta$ for the midrapidity $\eta =0$. Distributions of four 5% centrality bins, which are described in Section 4.1.3, are shown in each plot.

as

$$E_T = \sum_i E_i \, \sin\theta_i, \tag{4.9}$$

where θ_i is polar angle from the beam axis. The sum is taken over all particles emitted into a fixed solid angle per event. The E_T measurement was performed by the PbSc type electro-magnetic calorimeter whose energy resolution is $8.1\% / \sqrt{E \ (\mathrm{GeV})} \oplus 2.1\%$ by the test beam electron as described in Section 3.4.4. Figure 4.9 shows the uncorrected E_T distributions in two EMCal sectors measured in Au +Au collisions at three beam energies of 200 GeV, 130 GeV and 19.6 GeV in $\sqrt{s_{NN}}$ [35].

The correction factors for the raw E_T values have been obtained by the GEANT based MC simulation [88] with HIJING [89] inputs, which is tuned to reproduce the measured data in PHENIX with respect to the particle compo-
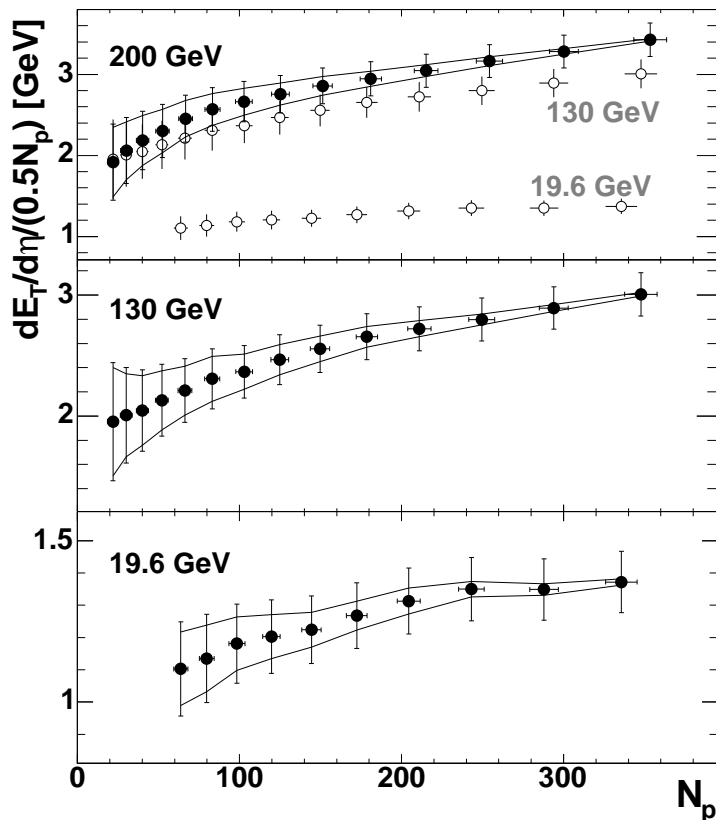
Figure 4.10: Corrected $dE_T/d\eta$ divided by the number of participant pairs (0.5 N_{part}) as a function of N_{part} in Au +Au collisions at three beam energy described in the legend. The vertical errors indicate the full systematic errors.

sition. The systematic error on the geometrical acceptance corrections has been estimated as 2.0% by the MC simulation. At the same time, several study on the systematic error estimations about the E_T measurement for the Au + Au collisions at $\sqrt{s_{NN}} = 200$GeV have been done, and these are summarized as follows. It is known by the energy calibrations that there is 1.5% uncertaintiy in the absolute energy scale for the electro magnetic particles. Meanwhile, the uncertainty in the EMCal response for hadrons give the 3% error to the total E_T, because this EMCal is too thin to detect the total energy deposit from hadrons. It is estimated by a comparison of the energy deposit values with respect to the hadrons between the MC simulation and the test beam data [79]. This comparison was made by varying momenta of the hadrons. Since this estimation depends on the input of MC simulation, an additional error of 1.3% comes from the ambiguities of the particle compositon and momentum distributions. The reconstructed energy deposit has finite energy loss at the edge of the EMCal detector, because for each particle reconstructed by a clustering method [87]. The loss is estimated as
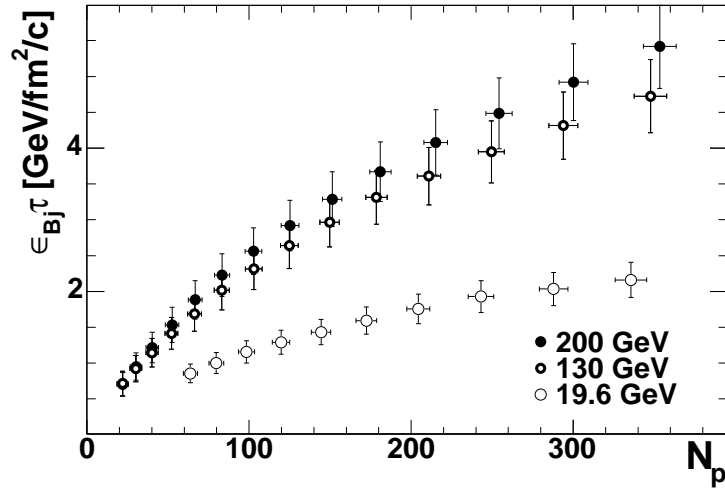
Figure 4.11: Bjorken energy density $\varepsilon_{Bj} \cdot \tau$ as a function of N_{part} in Au + Au collisions at there energy as indicated in the legend.

1.5% of absolute uncertainty. The total systematic error on the EMCal response for both electro magnetic particles and hadrons, which is obtained by taking the quadratic sum in above, corresponds to 3.9%. The systematic errors from background particles and noise in the detector readout system are estimated as from 0.2% to 6.0% with the real event samples in peripheral collisions by selecting the events that have no activity in the midrapidity region corresponding to the EMCal acceptance. Since the EMCal has a finite acceptance, the following two things should be taken into account for the corrections. One is the lost energy or outflow contributions for the total E_T by missing particles due to the decay products, which is originally in the EMCal acceptance at the primary collision point. The other is the inflow contributions coming from the outside of the EMCal acceptance as a sum of the deposit energy from the decay products and the background particles originating from the detector materials. The relative amount of the outflow and inflow contributions with respect to the total E_T are estimated as ~10% and ~24%, respectively, with 3.0% systematic errors based on the MC simulation. Figure 4.10 shows the corrected $dE_T/d\eta$ divided by the number of participant pairs (0.5 N_{part}) as a function of N_{part} in Au +Au collisions at $\sqrt{s_{NN}}$ equal 200 GeV, 130 GeV and 19.6 GeV with full systematic errors. It is obtained by taking the quadratic sum of the errors described in above.

The event samples are classified by the collision centralities, and the definition of the centrarities are based on the Glauber model as described in Section 4.1.3. This is the reason why the collision centrality is often expressed by the average number of participant nucleons $\langle N_{part} \rangle$ over an event sample in the experiment of heavy ion collisions. However, since the measured total E_T values are also

obtained by the event classification, the event classification can be represented by the total E_T instead of N_{part}. If one shows any results as a function of the total E_T, one can obtain the dependencies of collision centrality only by the measurement independently on any models. This is an advantage of the event characterization by the total E_T. However, this concept on the event characterization is implicitly based on an idea that the mechanism of particle productions are linearly related with the total energy. It is a natural assumption, since the aim of the heavy ion experiment is to explore the property of the thermalized QGP by the measurements of produced particles, event samples should be classified by values directly connected to the thermodynamic variables. In this sense, the event samples should not be characterized by the geometrical values like the N_{part}, because the N_{part} is only regarded to the collision dynamics and depends on the collision system and energy. The energy density is more meaningful rather than the total energy, because the particle productions depend not only on the total energy but also on the system size. The energy density based on the Bjorken's picture ε_{Bj}, which is described in Section 1.3, can be calculated through the E_T measurement as

$$\varepsilon_{Bj} = \frac{1}{A_\perp \tau} \frac{dE_T}{dy}, \qquad (4.10)$$

where τ and $A_\perp$ corresponds to the formation time of the thermalized QGP and the nuclei transverse overlap area, respectively. The transverse overlap area of two colliding nuclei $A_\perp$ is estimated by a MC simulation based on the Glauber model. Comparing Equation (4.10) and Equation (1.10), the normalization to πR^2 should be considered, where R is in the Woods-Saxon parameter in Equation (4.7). This estimation has been done for the impact parameter $b = 0$ in the MC simulation. Additionally, for the transformation from $dE_T/d\eta|_{\eta=0}$ to $dE_T/dy|_{y=0}$, which are the values with respect to the midrapidity region, a scale factor of 1.25 ± 0.05 is applied. Figure 4.11 shows the obtained $\varepsilon_{Bj} \cdot \tau$ as a function of N_{part} in Au + Au collisions at $\sqrt{s_{NN}}$ equal 200 GeV, 130 GeV and 19.6 GeV. Since the formation time τ is unknown by the measurement, it is indicated by the product of the ε_{Bj} and τ. Although the observable in this analysis will be shown as a function of N_{part}, it can be transformed by the energy density by using this relation between N_{part} and $\varepsilon_{Bj} \cdot \tau$. The ε_{Bj} monotonically increases with increasing N_{part} in Au + Au collisions at $\sqrt{s_{NN}} = 200$ GeV as shown in Figure 4.11 in the case of the formation time τ is not dependent on the N_{part}. Therefore, it can be said that a scan for the energy density is possible by the scan for N_{part}. This implies that the change of N_{part} at a fixed collision energy can provide a finer scan over the initial temperature compared to changing the collision energy density.

4.1.5 Data quality assurance

It is very important to guarantee that the detector conditions are surely stable to perform the analysis on the event-by-event fluctuation. The data quality assurance was made for the collected 1.5 million events under no magnetic filed conditions by the minimum bias trigger selections, which is described in Section 4.1.2. The status and stability of the detectors is based on the following points of view;

- Whether large dead areas in the acceptance exist or not.

- Whether reasonable correlations on the multiplicity between the number of charged tracks reconstructed by DC and the number of photon like clusters counted by EMCal are seen or not.

- Whether stable multiplicity are seen in the calibrated BBC charge sum, the number of DC tracks and the number of EMCal clusters or not.

These items were confirmed as a function of collected time for the subdivided data segments, each of which contains typically 2,000 to 3,000 events. Figure 4.12 a) and b) show the segment number dependence of the calibrated BBC charge sum a) and the number of reconstructed DC tracks in an event, respectively. The photon like PbSc clusters c) and PbGl clusters d) were counted by requiring not to associate with charged tracks with reasonable time of flight cut. The error bars associated with the points are the statistical errors. All segments deviated from the band, which correspond to 2% fluctuation as indicated by the dashed lines in the figure, were all rejected from the data analysis described in the following sections.

4.2 Measurement of charged particles

4.2.1 Track selection criteria

In this analysis, charged tracks detected in the East arm (see Section 3.2), which covers $|\eta| < 0.35$ and $\Delta\phi < \pi/2$, were used. As charged track selection criteria, we required that each straight-line track reconstructed by a DC hit pattern associated with a PC1 hit be aligned with a PC3 hit and the collision vertex point measured by BBC. Figure 4.13 shows the positional relation for each detectors and alignment of the hit positions with a DC track. The DC has six types of wire modules; two of them are used for the track reconstruction for the azimuthal angle and others are used for the pattern recognition. Selected tracks were reconstructed by using all wire modules of DC. We required associations between DC tracks and PC3 hits to be within 10 cm in the distance of closest approach (DCA), which was determined to minimize the random associations
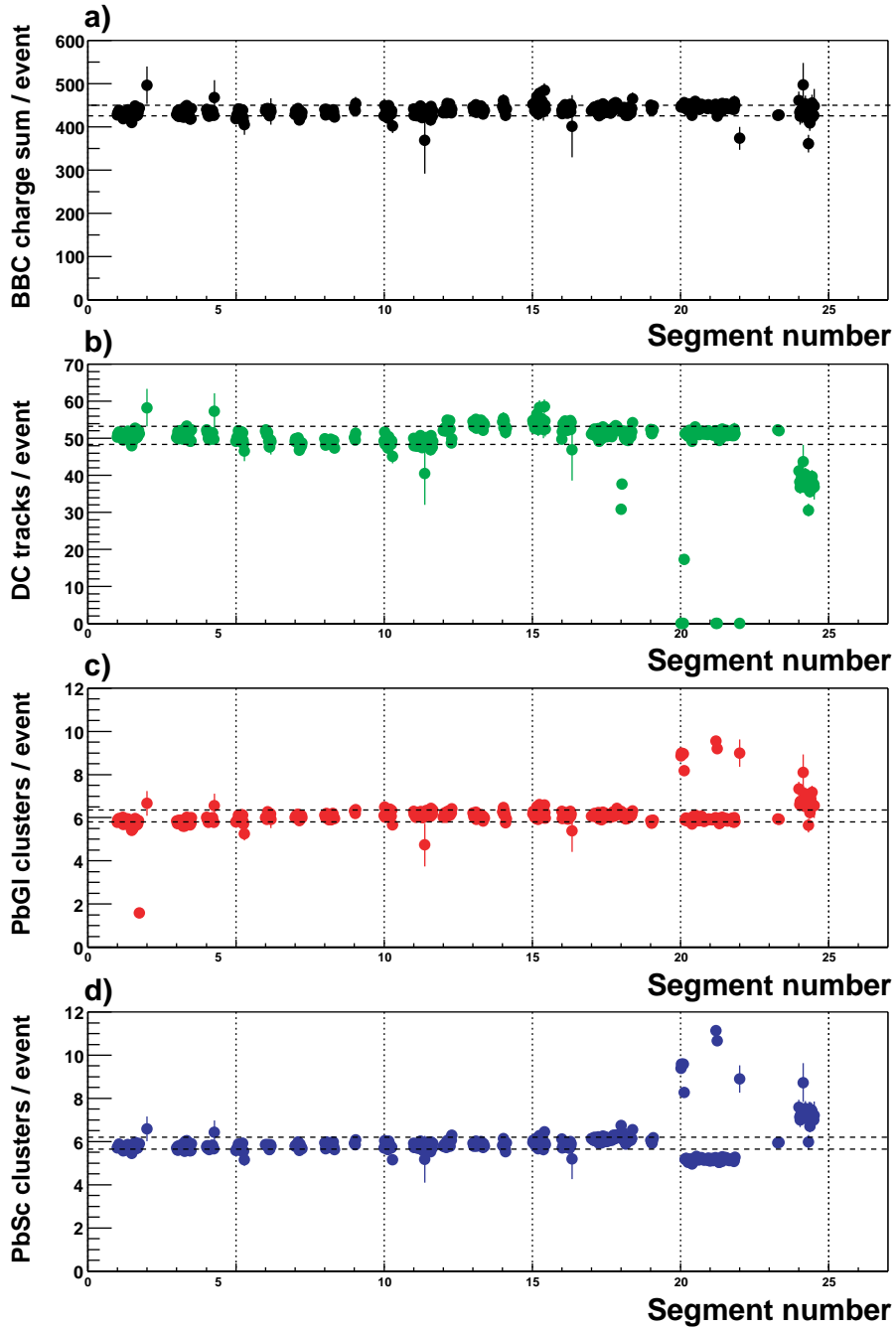
Figure 4.12: Detector stability on the hit multiplicity. a) Average charge sum in BBC. b) Average reconstructed DC tracks. c) Average number of photon like clusters in PbSc. d) Average number of photon like clusters in PbGl.

without losing track detection efficiency unnecessarily. Figure 4.14 a) shows the DCA from all DC tracks to the hit position of PC3. The Filled histogram in this figure was made by flipping the sign of z axis on PC3 hit position intentionally to estimate the amount of random associations. By applying to the cut value, 90% of radamly associated DC tracks with PC3 hit positions can be removed. Figure 4.14 b) shows the DCA from all DC tracks to the collision vertex measured by BBC. Filled histogram was obtained after applying the association cut for the DC tracks and PC3 hit positions. Although almost of fake DC tracks, which is not aligned with collision vertex, have already removed by the association cuts, we have applied 28 cm of association cut with the collision vertex to reject obvious fake track made by miss reconstructions. Since PbSc type calorimeter (Section 3.4.4) in PHENIX has sensitivity on the charged particles, clear peak made by minimum ionizing particles (MIP) can be seen in the cluster energy distributions. The validity of the selected charged tracks with this association cut have been confirmed by the MIP peak.

In addition to the single track selection, we required a minimum two-track separation in order to minimize effects from fake tracks and associated secondary par-
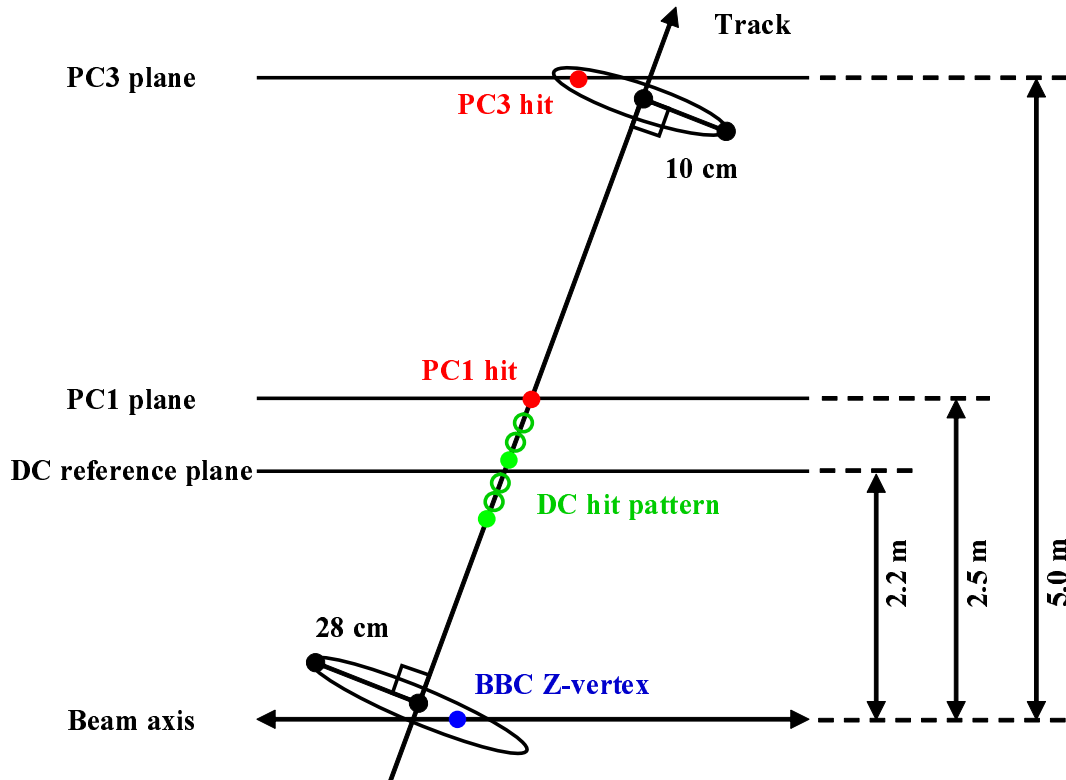
Figure 4.13: Requirements of charged track association.
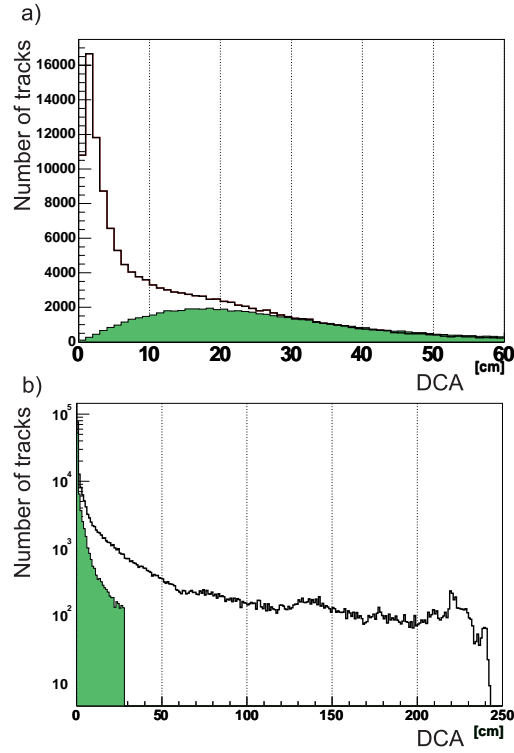
Figure 4.14: a) Distance of closest approach from DC tracks to PC3 hit position. Filled histogram was made by flipping the sign of z axis on PC3 hit position intentionally to estimate the amount of random associations. b) Distance of closest approach from DC tracks to the collision vertex measured by BBC. Filled histogram was obtained after applying the association cut for the DC tracks and PC3 hit positions.
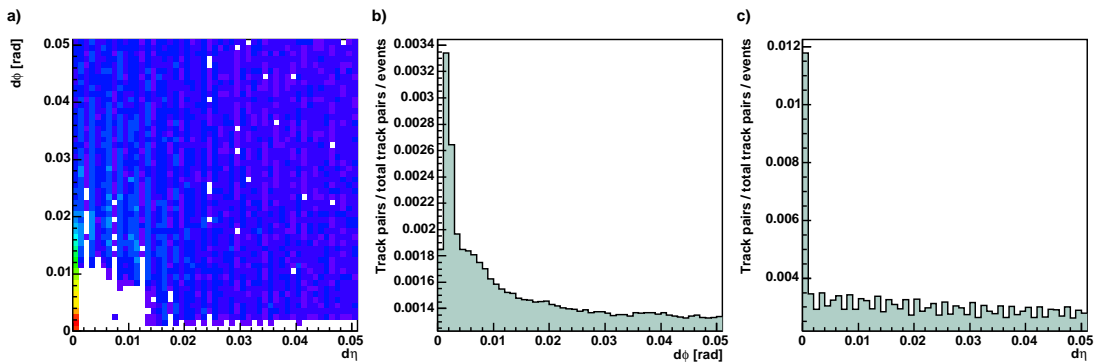
Figure 4.15: a) Distance between any two tracks in $\eta - \phi$ plane. b) and c) is the projection of the distance to the η and ϕ, respectively.

ticles. When we find tracks within the minimum separation window of $\delta\eta < 0.001$ and $\delta\phi < 0.012$ rad, we count them as one track independent of the number of reconstructed tracks in the window. These cut values were determined by looking at $\delta\eta$ and $\delta\phi$ distributions on the $\eta - \phi$ plane of any two track pairs in the real data sample as shown in Figure 4.15. The DC track resolution of 2 mm in the z direction at a reference radius of 220 cm from the beam axis corresponds to 1.0×10^{-3} in η. PC1 and PC3, which are used for the track association, have the same solid angle each other, and these pixel sizes are 8.4 mm and 14.7 mm, respectively. These pixel sizes are greater than the requirement of two-track separation cuts, however, these resolutions are 1.7 mm and 3.6 mm for PC1 and PC3 respectively in z direction, and these values also corresponds to 1.0×10^{-3} in η. The resolution in ϕ is 1 mrad, but the maximum drift length in DC corresponds to 0.012 rad. Therefore the two-track separation window size in η and ϕ is consistent with what is expected.

4.2.2 Magnetic field condition

In the case of normal magnetic field condition at the PHENIX detector, which is used to identify the charged particles, the threshold transverse momenta p_T correspond to 0.2 GeV/c, 0.4 GeV/c and 0.6 GeV/c for charged pions $\pi^{\pm}$, charged kaons $K^{\pm}$ and protons p ($\bar{p}$), respectively [84]. Figure 4.16 shows the measured p_T spectra in Au + Au collisions at $\sqrt{s_{NN}} = 200$ GeV for these particles in the 0 - 5% (central) and 60 - 92% centrality bins.

Since this analysis used the data taken without magnetic field in order to optimize acceptance for the low p_T charged particles, the threshold transverse momenta p_T can be lowered. It is estimated by the GEANT based Monte Carlo (MC) simulation [88] by requiring the equivalent single track selection criteria, which are described in Section 4.2.1. Empirical functions are used to make the input p_T distributions for the MC simulations based on the measured p_T distributions. Figure 4.17 shows the p_T distributions for $(\pi^+ + \pi^-)/2$, $(K^+ + K^-)/2$ and $(\bar{p} + p)/2$ in 0 - 70% centrality bin. Curves in the figures are the fit results by the empirical functions. Following fit functions are chosen as triple exponential, single exponential and exponential with the fourth order polynomial exponent for π, K and p, respectively. For the generation of those particles, the known ratio between the different sign of charge, which is independent on the centrality [84] class, are taken into account as 0.97, 0.93 and 0.75 for π^-/π^-, K^-/K^+ and $\bar{p}/p$, respectively. Figure 4.18 shows the number of generated particles (black) based on the empirical functions and survived particle (red) with the track selection criteria in real data analysis as a function of p_T. Vertical lines indicate the p_T threshold for each particle species as 0.1 GeV/c, 0.25 GeV/c and 0.35 GeV/c for $\pi^{\pm}$, $K^{\pm}$ and $p(\bar{p})$, respectively.

According to this MC simulation, the detectable charged particle compositions in the no magnetic field condition with the same selection criteria as the real data

analysis are estimated as 94% for charged pions, 4% for charged kaons and 2% for proton and antiproton in 0 - 70% centrality. The average p_T for the detected inclusive charged particles are also estimated as 0.57 GeV/c in this MC study. It means the difference of the rapidity and pseudorapidity is at most 3% at the edge of the PHENIX acceptance by assuming the mass of charged pion.

4.3   Measurement of multiplicity distributions

Multiplicity distributions of charged particles were measured while changing the pseudorapidity window size $\delta\eta$ from 0.066 to 0.7 with a step size of $0.7/2^5 = 0.022$. For a given pseudorapidity window size, the window position in the pseudorapidity axis was shifted by a step of $0.7/2^8 = 0.0027$ as long as the window is fully contained within the PHENIX acceptance of $|\eta| < 0.35$. For each window position NBD fits were performed to the multiplicity distributions. Biases originating from inefficient detector areas were corrected with the procedure explained
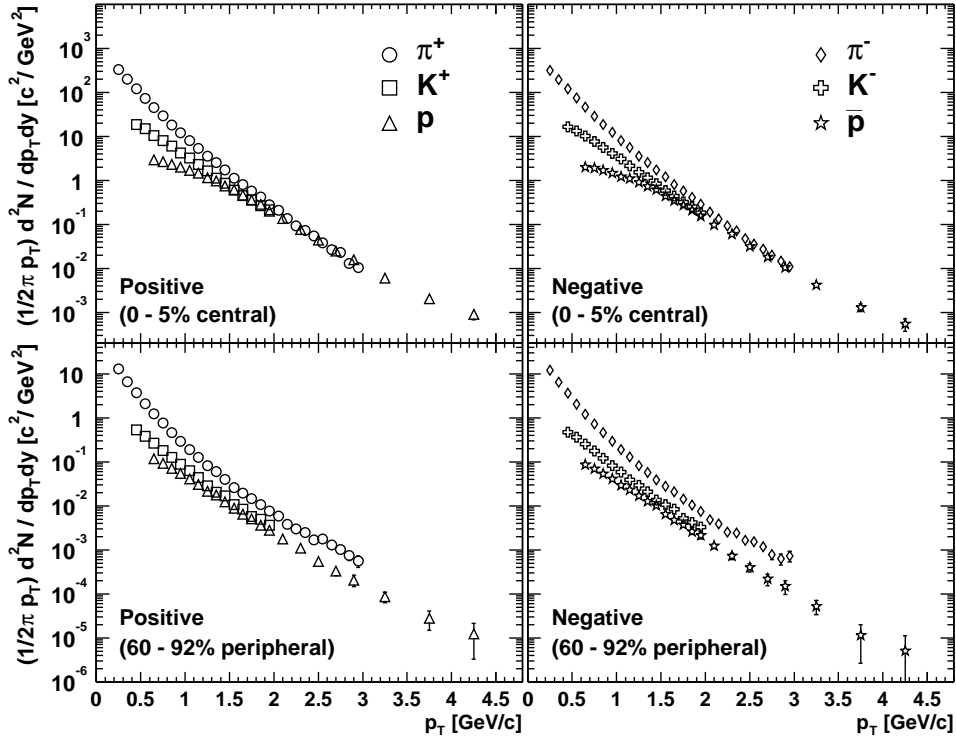
Figure 4.16: Differential cross sections as a function of p_T for π^+ (circle), π^- (diamond), K^+ (square), K^- (cross), p^+ (triangle), and p^- (star). Upper and lower figures correspond to 0 - 5% and 60 - 92% centrality bins, respectively.

in Section 4.4.1. Since even corrected NBD k parameters are not necessarily equal in the case of extremely inefficient window positions, the window positions have been truncated where the reconstruction efficiency is below 50%. This truncation is mainly to exclude biases from the largest hole in the middle of the charged particle detector as shown in Figure 4.19 (a) and (c). After the truncation, it is obtained that the weighted mean of corrected NBD parameters ($\langle \mu_c \rangle$, $\langle k_c \rangle$) for a
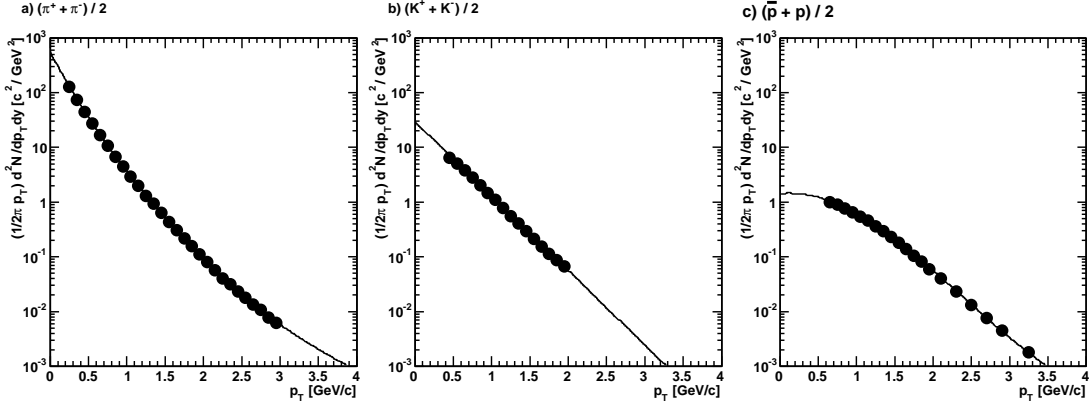
Figure 4.17: Differential cross sections as a function of p_T for $(\pi^+ + \pi^-)/2$ a), $(K^+ + K^-)/2$ b) and $(\bar{p}+p)/2$ c) in centrality 0 - 70%. Curves corresponds to the fits with several empirical functions for the input of MC simulation (see text).
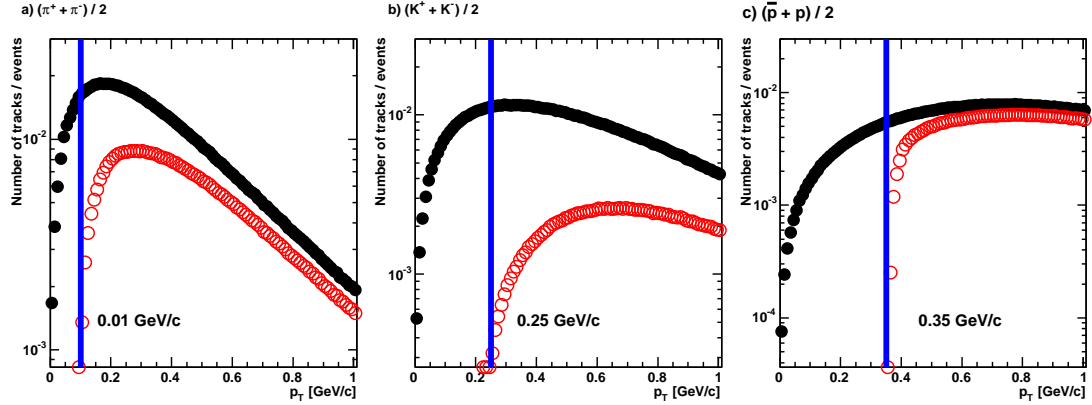
Figure 4.18: The number of generated particles (closed) and survived particle (open) as a function of p_T in the MC simulation. a), b) and c) corresponds to $(\pi^+ + \pi^-)/2$, $(K^+ + K^-)/2$ and $(\bar{p}+p)/2$, respectively. Vertical lines indicate the p_T threshold in the no magnetic field condition.
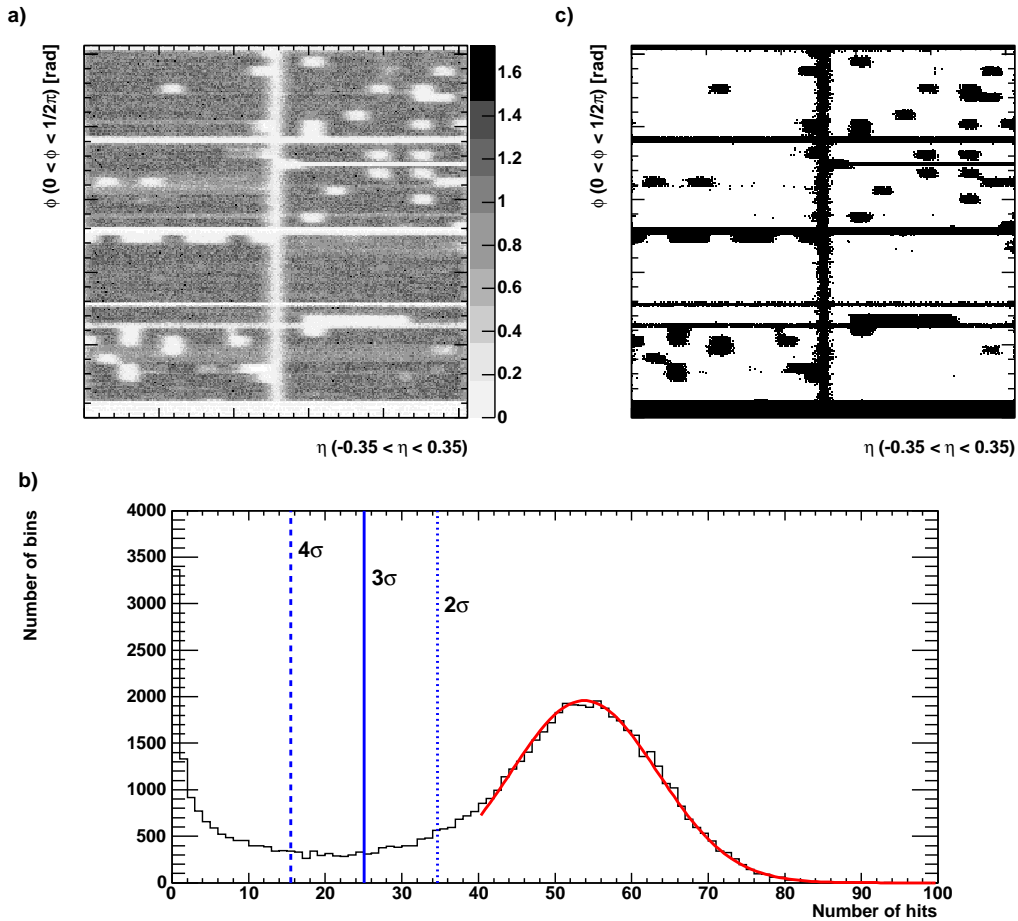
Figure 4.19: 2-dimensional dead map definitions. a) Track projection points onto the η - ϕ plane in the data after all track selections. The scale is normalized to the mean number of hits in the peak position in b). b) The number of bins among subdivided $2^8 \times 2^8$ bins as a function of the accumulated number of hits over the total event sample. c) Definition of the central dead map by excluding the detector region below 3 σ, where black parts are identified as dead areas.
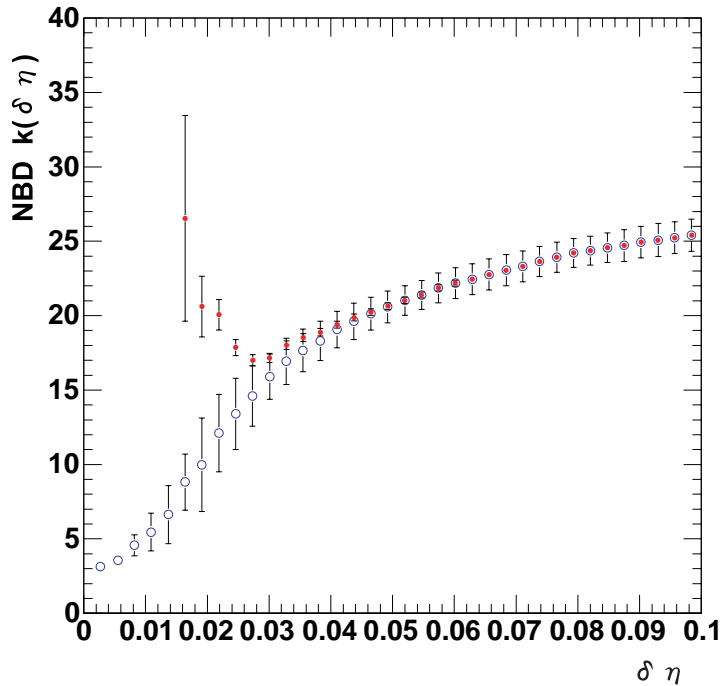
Figure 4.20: Uncorrected NBD k as a function of $\delta\eta$ in the small $\delta\eta$ regions at a typical centrality bin. Closed and open data points were obtained with and without rejection on the inefficient detector areas, respectively.

given window size, which are defined as

$$
\begin{aligned}
\langle \mu_c \rangle &\equiv \sum_{i=1}^{n} \delta\mu_{ci}^{-2}\mu_{ci} / \sum_{i=1}^{n} \delta\mu_{ci}^{-2}, \\
\langle k_c \rangle &\equiv \sum_{i=1}^{n} \delta k_{ci}^{-2}k_{ci} / \sum_{i=1}^{n} \delta k_{ci}^{-2},
\end{aligned}
\tag{4.11}
$$

where n is the number of valid window positions after the truncation and δ indicates errors on fitting parameters by the MINUIT program [94] in each window position i. This procedure have been performed in each centrality bin with 5% and 10% centrality bin width, respectively.

The lower limit of 0.066 was determined so that small window sizes, where corrected NBD k was seen to depend heavily on window position, are all excluded. Figure 4.20 shows the uncorrected NBD k as a function of window size $\delta\eta < 0.1$ in a typical centrality bin. Closed and open data points were obtained with and without rejection on the bad window position, which includes large amount of inefficient detector areas, respectively. One can find a discrepancy between the two type of data points in the small $\delta\eta$ regions. It is an effect on the fail of NBD

fit due to the lack of the number of degree of freedom. Therefore, the lower limit of 0.066 was set to obtain the final results. The lower limit is common for all centrality bins.

4.4   Corrections and error estimations

4.4.1   Correction method

Any dead or inefficient areas in the detector have been identified and the bias on the NBD parameters has been corrected based on a suitable statistical property of NBD. Maps of dead areas were produced from the track projection points onto the η - ϕ plane in the data after the track selections, as shown in Figure 4.19 a), where the detector acceptance is divided into $2^8 \times 2^8$ bins in the η - ϕ plane. The accumulated number of hits over the total event sample in each bin is shown by a gray scale reflecting the statistical weights. The scale is normalized to the mean number of hits in the peak position shown in Figure 4.19 b). Figure 4.19 b) shows the number of bins among subdivided $2^8 \times 2^8$ bins as a function of the accumulated number of hits over the total event sample in each $1/2^8 \times 1/2^8$ acceptance. If there were no dead or inefficient area, a binomial distribution is expected with a probability of $1/2^8 \times 1/2^8$ to the total acceptance. For the binomial part, a $\pm$ 3 σ region are taken. On the other hand, if there are any dead or inefficient areas they tend to contaminate the lower tail of the binomial distribution. A central dead map are defined by excluding detector region below 3 σ as shown in Figure 4.19 c) where black indicates regions that are identified as dead areas. The fraction of good area corresponds to 78% of the total acceptance. This map was used to completely suppress particles which hit the dead areas in the real data.

As long as the baseline distribution is approximated as an NBD, which is certainly true as observed in E802 experiment [63] and in the present analysis, one can estimate the relation between true k values of the NBD and biased k values due to dead or inefficient areas based on the convolution theorem of NBD. For two independent NBD's with (μ_1, k_1) and (μ_2, k_2), it is known that the convolution of the two NBD's is an NBD with (μ_c, k_c), which satisfies relations as

$$
\begin{aligned}
k_c &= k_1 + k_2, \\
\mu_c &= \mu_1/k_1(k_1 + k_2),
\end{aligned}
\tag{4.12}
$$

where $\mu_1/k_1 = \mu_2/k_2$ holds [65, 95]. Therefore the correction can be applied by multiplying a ratio of the total number of η - ϕ bins in a given η window size to the number of bins excluding dead area, as the geometrical acceptance corrections can be applied.

Strictly speaking one can not completely reproduce the original k by this correction, since NBD's in different positions are not completely independent. However, except for the large hole which is already excluded by the truncation, small holes are scattered rather uniformly in azimuthal direction for any position of the $\delta\eta$ windows. As the simplest overall correction to each window position, the convolution theorem [65, 95] was applied by assuming collection of independent NBD sources. As long as the correction is applied in the same manner for all the azimuthal holes, it does not greatly affect the differential measurement to the pseudorapidity space. If the correction is accurate enough, one can expect a constancy of the corrected k values which should be independent of the fraction of dead areas. Based on the degree of constancy of corrected k as a function of the fraction of dead areas in each window position for a given $\delta\eta$ window size, the incompleteness of the correction in each window size has been checked. As briefly mentioned in the last paragraph of Section 4.3, the window sizes to be analyzed were determined so that systematic error bands on $\langle k_c \rangle$ explained in Section 4.4.2, can contain the most of the corrected k values independently of the fraction of dead areas in each window position.

4.4.2 Statistical and systematic errors

As a convolution of statistical errors, errors were adopted on weighted mean values $(\delta\langle\mu_c\rangle, \delta\langle k_c\rangle)$ on corrected NBD parameters after the window truncation mentioned in Section 4.3, which are defined as

$$
\begin{aligned}
\delta\langle\mu_c\rangle^2 &\equiv \frac{\bar{\delta\mu}_{ci}^2}{n_{ind}}, \\
\delta\langle k_c\rangle^2 &\equiv \frac{\bar{\delta k}_{ci}^2}{n_{ind}},
\end{aligned} \tag{4.13}
$$

where $\bar{\delta\mu}_{ci}$ and $\bar{\delta k}_{ci}$ are respectively defined as $\sum_{i=1}^{n} \delta\mu_c/n$ and $\sum_{i=1}^{n} \delta k_c/n$ with the number of valid window positions n after the truncation and $n_{ind} \equiv 0.75/\delta\eta$ is the number of statistically independent window positions for a given $\delta\eta$ window size. This statistical error on $\delta\langle k_c \rangle$ is referred to as $\delta\langle k_c \rangle$ (stat).

The dominant sources of systematic errors for the correlation length measurement are the correction procedure with dead maps and the two-track separation cuts, since both introduce unphysical correlations. 2% fluctuation have been allowed on the average multiplcity of measured number of charged tracks as a run selection. This fluctuation is also originated by the dead channels of the tracking detectors in Section 4.2.1. In order to estimate this, two more patterns of dead maps were defined with the definition of $3\,\sigma \pm 0.5\,\sigma$ as indicated in Figure 4.19 c). The deviation of $\langle k_c \rangle$ from the central dead map definition is referred to as $\delta\langle k_c \rangle$ (dead), which corresponds to 3.4% typically.

As for the two-track separation case, the main purpose is to reject fake track effects, which is dominantly observed in ϕ direction rather than in η, since the PC1 hit requirement can fix z positions along the beam axis as shown in Figure 4.15. Therefore, the effect of the $\delta\phi$ cut was estimated as ± 0.002 rad around the central cut value of 0.012 rad with a fixed cut value on $\delta\eta$ of 0.001. The deviation of $\langle k_c \rangle$ from the central definition on the fake track rejection is referred to as $\delta\langle k_c \rangle$ (fake). This systematic error increases at higher centrality bins, which was estimated as 5.8% and 0.3% at 0 - 5% and 60 - 65% centrality bins, respectively.

The $\langle k_c \rangle$ (stat) is related to agreements between multiplicity distributions and NBD. The $\langle k_c \rangle$ (dead) and $\langle k_c \rangle$ (fake) depends on the position of the window and the average multiplicity in a selected centrality bin, respectively. By treating these contributions as independent systematic error sources, the total systematic error $\delta\langle k_c \rangle$ (total) on $\langle k_c \rangle$ in each $\delta\eta$ in each centrality, was obtained by the quadratic sum over $\delta\langle k_c \rangle$ (stat), $\delta\langle k_c \rangle$ (dead) and $\delta\langle k_c \rangle$ (fake).

Chapter 5

Results

In this chapter the results of the NBD fits are first tabulated. Then the measured NBD k as a function of the pseudorapidity window sizes in various centrality bins are shown in Figure 5.3. Finally, the N_{part} dependences of extracted $\alpha\xi$ product in Equation (2.29) are presented.

5.1 Multiplicity distributions and NBD fits

NBD fit results in all window sizes in all centrality bins are summarized in Appendix Table A.1 through Table A.25 where $\langle\mu_c\rangle$ and $\langle\mu\rangle$ are weighted means of corrected and uncorrected μ over all window positions respectively, $\langle k_c\rangle$ and $\langle k\rangle$ are weighted means of corrected and uncorrected k over all window positions, respectively. The $\langle\mu_c\rangle$ are corrected only for the effect of the detector dead areas as described in Section 4.4.1. The mean multiplicities were confirmed to be consistent with the result of the independent analysis by the different method using only PC1 and PC3 [35], after known additional correction factors were taken into account. These consit of 15 % of correction for finite double hit resolutions in PC1 and 24 % of correction for the energy loss in the detector materials with respect to the $\langle\mu_c\rangle$. Statistical errors on weighted means $\delta\langle k_c\rangle$ (stat) are obtained as explained in Section 4.4.2. $\langle\chi^2/NDF\rangle$ is the average of reduced χ^2 of NBD fits over all window positions. $\langle NDF\rangle$ is the average of the degree of freedom of NBD fits over all window positions, and the systematic errors $\delta\langle k_c\rangle$ (dead), $\delta\langle k_c\rangle$ (fake) and $\delta\langle k_c\rangle$ (total) are already explained in Section 4.4.2. The mean and r.m.s. of the reduced χ^2 values in the NBD fit over all window positions and all $\delta\eta$ sizes and all centrality bins were obtained as 0.75 and 0.33 respectively as shown in Figure 5.1. The mean value corresponds to typically 80% confidence level. Therefore, it is good enough to assume NBD as a baseline multiplicity distribution to obtain the integrated correlation function via the k parameter.

As a demonstration to show how well the NBD fits work, Figure 5.2 shows the charged particle multiplicity distributions in each pseudorapidity window
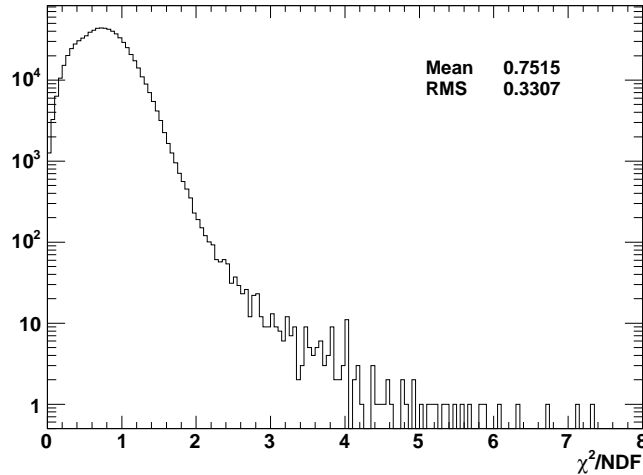
Figure 5.1: Reduced χ^2 values in the NBD fit over all window positions and all $\delta\eta$ sizes and all centrality bins.

size in 1/8 fractions of the full rapidity coverage of $|\eta| < 0.35$ with 0 - 10% events in the collision centrality, where the uncorrected multiplicity distributions within the total error bands on $\langle k_c \rangle$ in Appendix Table A.1 are all merged. The distributions are shown as a function of the number of tracks n normalized to the mean multiplicity $\langle n \rangle$ in each window. The error bars show the statistical errors on the merged distributions. The solid curves are fit results with NBD only for the demonstration purpose. The fit results in Appendix Table A.1 through Table A.25 are not obtained from these convoluted distributions whose accuracies are degraded by the convolutions with different μ values due to different detector biases depending on the window positions.

5.2 $\delta\eta$ dependence of NBD k

Figure 5.3 a) and b) show $\langle k_c \rangle$ as a function of pseudorapidity window size with 10% and 5% centrality bin width, respectively. Centrality classes are indicated inside the figures. The error bars show $\delta\langle k_c \rangle$ (total) defined in Section 4.4.2.

An upper limit on the absolute scale of ξ was obtained as $\xi < 0.035$ with respect to the all centrality bins by the free parameter fits based on Equation (2.28). Since the upper limit of ξ is small enough compared to the fitting region of $\delta\eta$ ($\xi \ll \delta\eta$), Equation (2.29) can be applied for the fits to the NBD k as a function of $\delta\eta$. More discussions on the small ξ can be found in Section 6.1.1.

The solid lines in Figure 5.3 indicate the fit results based on Equation (2.29). The fits were performed in the $\delta\eta$ region from 0.066 to 0.7, which is explained in
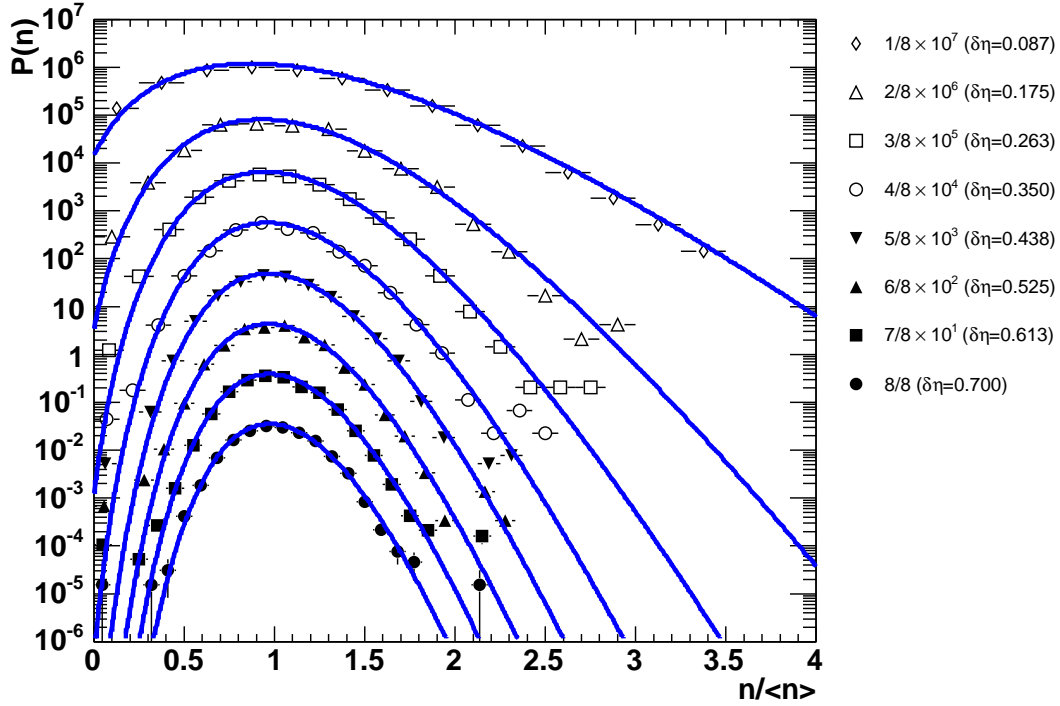
Figure 5.2: Uncorrected charged particle multiplicity distributions in each pseudorapidity window size, as indicated in the legend, at 0 - 10% collision centrality. The distributions are shown as a function of the number of tracks n normalized to the mean multiplicity $\langle n \rangle$ in each window. The error bars show the statistical errors. The solid curves are fit results of NBD.

Section 4.2.1. The typical χ^2/NDF in the fit based on Equation (2.29) is 0.132, which corresponds to 99% confidence level.

As explained in Section 2.4 for Equation (2.29), in the limit of $\beta = 0$, the slopes in k vs. $\delta\eta$ have crucial information on the phase transition. In Figure 5.3, one can identify different behaviors in slopes around 40-50% centrality region even without fit curves.

5.3 N_{part} dependence of β and $\alpha\xi$

Figure 5.4 a) and b) show the obtained fit parameters β and $\alpha\xi$ with Equation (2.29) as a function of the N_{part}, where results for both the 5% and 10% centrality bin width cases are plotted as filled and open circles, respectively. The smooth solid and dotted curves are provided to guide the eye. The horizontal error bars correspond to ambiguities on the mean value of N_{part} as explained
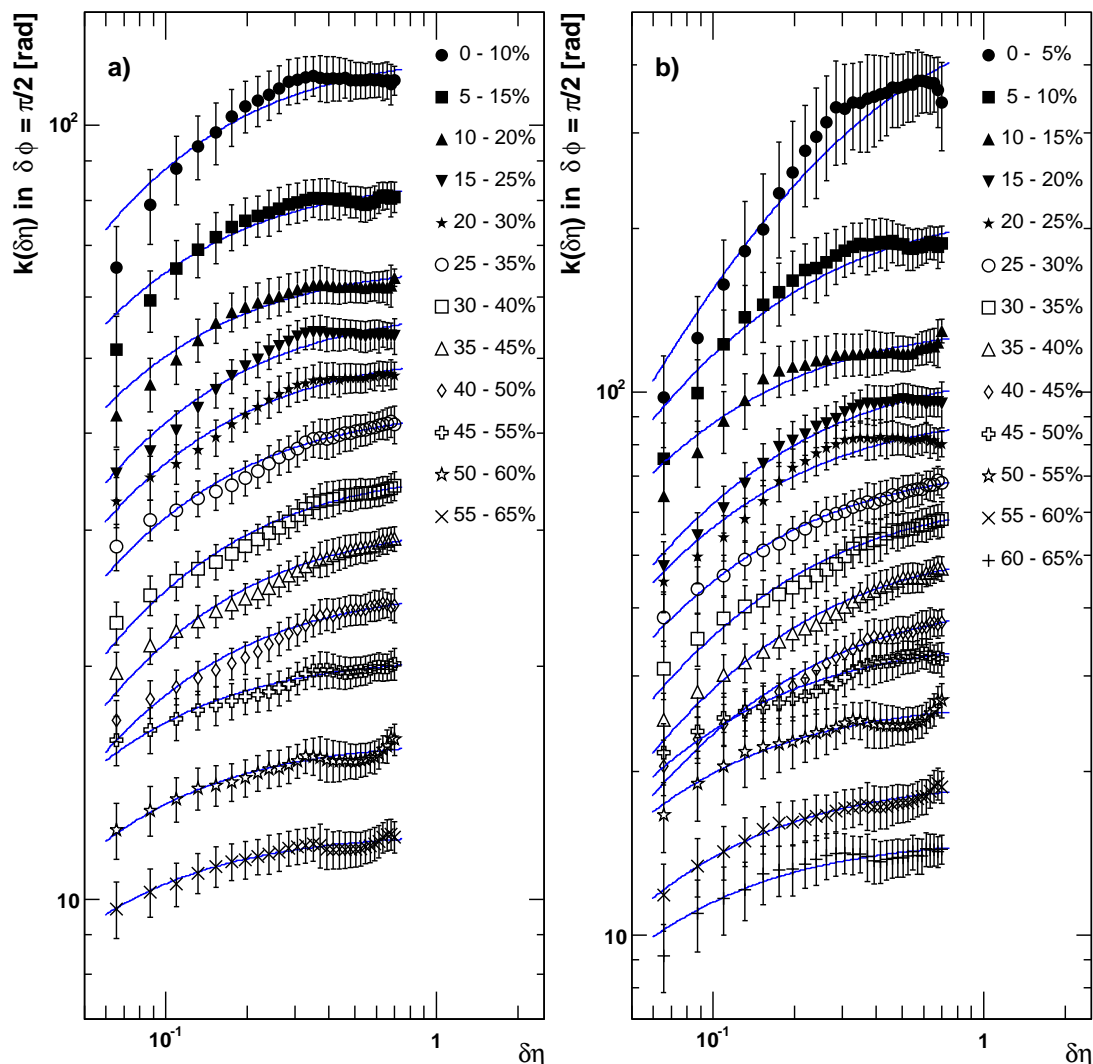
Figure 5.3: Weighted mean of corrected NBD k, $\langle k_c \rangle$ as a function of pseudorapidity window size with a) 10% and b) 5% centrality bin widths. Centrality classes are indicated in the figure legend. The error bars show $\delta\langle k_c \rangle$ (total), as explained in Section 4.4.2. The solid lines indicate the fit curves of Equation (2.29).

in Section 4.1.3. The vertical error bars are obtained from errors on the fitting parameter by the MINUIT program [94]. Table 5.1 summarizes the fit results where centrality bins, corresponding N_{part}, $\alpha\xi$, β and χ^2/NDF obtained by the fit with Equation (2.29) are shown for 10% and 5% centrality bin width cases, respectively.

The β parameter is necessary to absorb any effects independent of pseudorapidity space correlations as explained in Section 2.4.2. For a wider centrality bin,
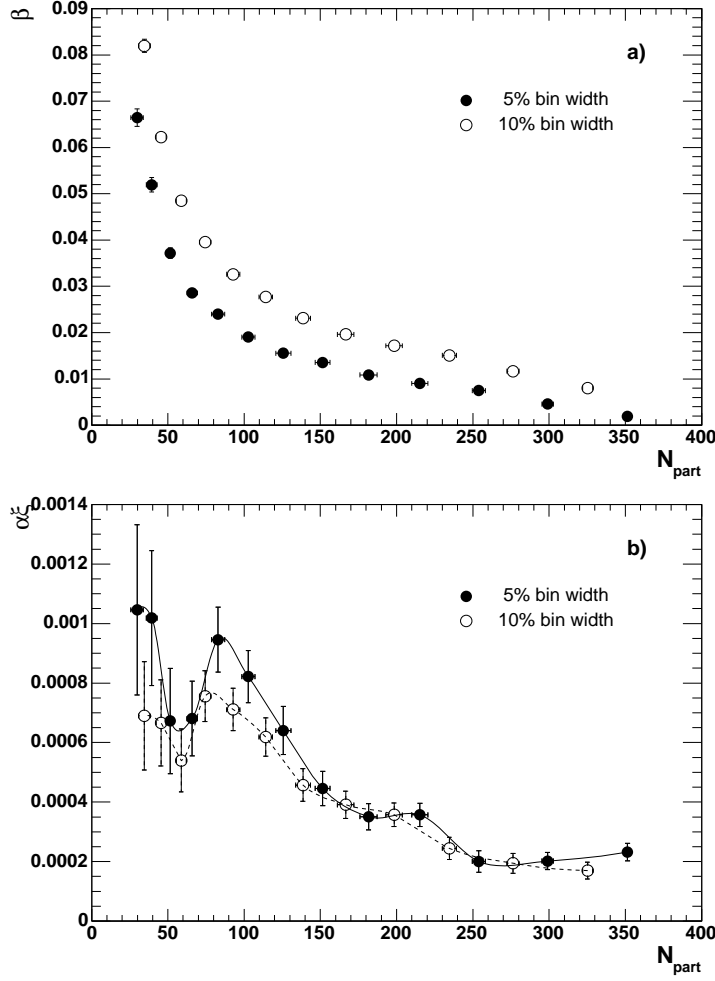
Figure 5.4: Fit results based on Equation (2.29). a) is β and b) is products of $\alpha\xi$ as a function of N_{part}. The horizontal error bars correspond to ambiguities in the mean value of N_{part} as explained in Section 4.1.3. The vertical error bars are obtained from errors on the fitting parameter.

the width of multiplicity distribution becomes broader, since events with wider range of centrality bins are included in the bin. As the result, the systematic difference of β in the 5% and 10% centrality data sets is shown in Figure 5.4 a). It will be discussed in more detail for the exploit of β term at Section 6.2.

The $\alpha\xi$ product in the correlation function, which is monotonically related to susceptibility in the long wavelength limit $\chi_{k=0}$ as explained in Section 2.4.2, indicates the non-monotonic behavior as a function of N_{part}. This is originated in the different behaviors of slopes as shown in Figure 5.3 with respect to the corresponding centrality bins $i.e.$ 40 - 50% and 40 - 45% centrality bins. Since this behavior is one of the main result of this analysis, its significance of the local

Table 5.1: The $\alpha\xi$ and β in Equation (2.29) obtained by the fits to $\langle k_c \rangle$ vs. $\delta\eta$. Upper and lower column corresponds to 10% and 5% centrality bin width cases, respectively.

Centrality (%)	$\langle N_{part} \rangle$	$\alpha\xi$ ($\propto \chi_{k=0}$)	β	χ^2/NDF ($NDF = 27$)
$0-10$	325.2 ± 3.3	$0.17 \times 10^{-3} \pm 0.03 \times 10^{-3}$	$0.80 \times 10^{-2} \pm 0.02 \times 10^{-2}$	0.24
$5-15$	276.4 ± 4.0	$0.19 \times 10^{-3} \pm 0.03 \times 10^{-3}$	$1.17 \times 10^{-2} \pm 0.02 \times 10^{-2}$	0.16
$10-20$	234.6 ± 4.7	$0.24 \times 10^{-3} \pm 0.04 \times 10^{-3}$	$1.51 \times 10^{-2} \pm 0.03 \times 10^{-2}$	0.14
$15-25$	198.4 ± 5.4	$0.36 \times 10^{-3} \pm 0.04 \times 10^{-3}$	$1.72 \times 10^{-2} \pm 0.03 \times 10^{-2}$	0.26
$20-30$	166.6 ± 5.4	$0.39 \times 10^{-3} \pm 0.05 \times 10^{-3}$	$1.96 \times 10^{-2} \pm 0.03 \times 10^{-2}$	0.09
$25-35$	138.6 ± 4.9	$0.46 \times 10^{-3} \pm 0.06 \times 10^{-3}$	$2.31 \times 10^{-2} \pm 0.04 \times 10^{-2}$	0.09
$30-40$	114.2 ± 4.4	$0.62 \times 10^{-3} \pm 0.06 \times 10^{-3}$	$2.77 \times 10^{-2} \pm 0.05 \times 10^{-2}$	0.13
$35-45$	92.8 ± 4.3	$0.71 \times 10^{-3} \pm 0.07 \times 10^{-3}$	$3.26 \times 10^{-2} \pm 0.05 \times 10^{-2}$	0.14
$40-50$	74.4 ± 3.8	$0.76 \times 10^{-3} \pm 0.09 \times 10^{-3}$	$3.96 \times 10^{-2} \pm 0.07 \times 10^{-2}$	0.14
$45-55$	58.8 ± 3.3	$0.54 \times 10^{-3} \pm 0.11 \times 10^{-3}$	$4.85 \times 10^{-2} \pm 0.08 \times 10^{-2}$	0.05
$50-60$	45.5 ± 3.3	$0.67 \times 10^{-3} \pm 0.14 \times 10^{-3}$	$6.22 \times 10^{-2} \pm 0.11 \times 10^{-2}$	0.11
$55-65$	34.6 ± 3.8	$0.69 \times 10^{-3} \pm 0.18 \times 10^{-3}$	$8.19 \times 10^{-2} \pm 0.14 \times 10^{-2}$	0.05
$0-5$	351.4 ± 2.9	$0.23 \times 10^{-3} \pm 0.03 \times 10^{-3}$	$0.19 \times 10^{-2} \pm 0.02 \times 10^{-2}$	0.18
$5-10$	299.0 ± 3.8	$0.20 \times 10^{-3} \pm 0.03 \times 10^{-3}$	$0.46 \times 10^{-2} \pm 0.02 \times 10^{-2}$	0.27
$10-15$	253.9 ± 4.3	$0.20 \times 10^{-3} \pm 0.04 \times 10^{-3}$	$0.75 \times 10^{-2} \pm 0.02 \times 10^{-2}$	0.17
$15-20$	215.3 ± 5.3	$0.36 \times 10^{-3} \pm 0.04 \times 10^{-3}$	$0.90 \times 10^{-2} \pm 0.03 \times 10^{-2}$	0.18
$20-25$	181.6 ± 5.6	$0.35 \times 10^{-3} \pm 0.04 \times 10^{-3}$	$1.08 \times 10^{-2} \pm 0.03 \times 10^{-2}$	0.32
$25-30$	151.5 ± 4.9	$0.45 \times 10^{-3} \pm 0.06 \times 10^{-3}$	$1.35 \times 10^{-2} \pm 0.04 \times 10^{-2}$	0.02
$30-35$	125.7 ± 4.9	$0.64 \times 10^{-3} \pm 0.08 \times 10^{-3}$	$1.55 \times 10^{-2} \pm 0.05 \times 10^{-2}$	0.09
$35-40$	102.7 ± 4.3	$0.82 \times 10^{-3} \pm 0.09 \times 10^{-3}$	$1.90 \times 10^{-2} \pm 0.05 \times 10^{-2}$	0.08
$40-45$	82.9 ± 4.3	$0.95 \times 10^{-3} \pm 0.11 \times 10^{-3}$	$2.40 \times 10^{-2} \pm 0.07 \times 10^{-2}$	0.06
$45-50$	65.9 ± 3.4	$0.68 \times 10^{-3} \pm 0.13 \times 10^{-3}$	$2.86 \times 10^{-2} \pm 0.08 \times 10^{-2}$	0.08
$50-55$	51.6 ± 3.2	$0.67 \times 10^{-3} \pm 0.18 \times 10^{-3}$	$3.72 \times 10^{-2} \pm 0.11 \times 10^{-2}$	0.11
$55-60$	39.4 ± 3.5	$1.02 \times 10^{-3} \pm 0.23 \times 10^{-3}$	$5.19 \times 10^{-2} \pm 0.16 \times 10^{-2}$	0.06
$60-65$	29.8 ± 4.1	$1.05 \times 10^{-3} \pm 0.29 \times 10^{-3}$	$6.64 \times 10^{-2} \pm 0.19 \times 10^{-2}$	0.08

maximum of $\alpha\xi$ will be discussed at Section 6.4. One can find the absolute value of $\alpha\xi$ products were aliened to the same scale for the different centrality bin width cases owing to the β parameter as described in above. The difference on the $\alpha\xi$ value between the 5% and 10% around the local maximum centrality bin width cases can be understood as smearing effects around a peak-like shape, and it is confirmed by a toy model MC calculation.

Chapter 6

Discussions

6.1 Absolute scale of the correlation length

6.1.1 Small correlation length

As long as reliable NBD k in $\delta\eta \sim 0$ can be obtained, which corresponds to $\delta\eta \ll \xi$, α can be treated as a free parameter by Equation (2.28) to extract the absolute value of correlation length ξ in each centrality. If this is not the case, the absolute ξ can not be obtained without any constraints due to the anti-correlations between α and ξ. Under this situation, the correlation lengths have
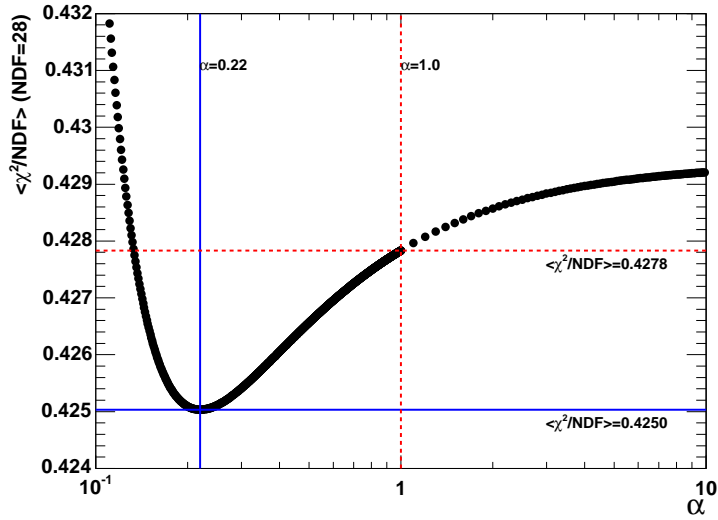
Figure 6.1: Average χ^2/NDF ($NDF = 28$) over all centrality bins at the fits to the integrated correlation function Equation (2.28) as a function of fixed α. The minimum average χ^2/NDF (0.425) at $\alpha = 0.22$ is indicated as solid line. Average χ^2/NDF (0.428) obtained with $\alpha = 1.0$ is indicated as dashed line.

been obtained by fixing the parameter α in Equation (2.28) to 0.22, which was chosen so that the average χ^2/NDF over all centrality bins is minimized in the fit results for the relation between NBD k and $\delta\eta$. Figure 6.1 shows the average χ^2/NDF ($NDF = 28$) over all centrality bins as a function of fixed α value. One can find the minimum average χ^2/NDF (0.425) at $\alpha = 0.22$ as indicated by the solid line. Figure 6.2 shows fit parameters of β and ξ as a function of N_{part} with this fixed parameter $\alpha = 0.22$. A physical reasoning to motivate the parameter α are fixed will be explained in Section 6.1.2.

The obtained ξ indicate very small value as shown in Figure 6.2, and the method of extraction of ξ with fixed α can not be justified enough only by the
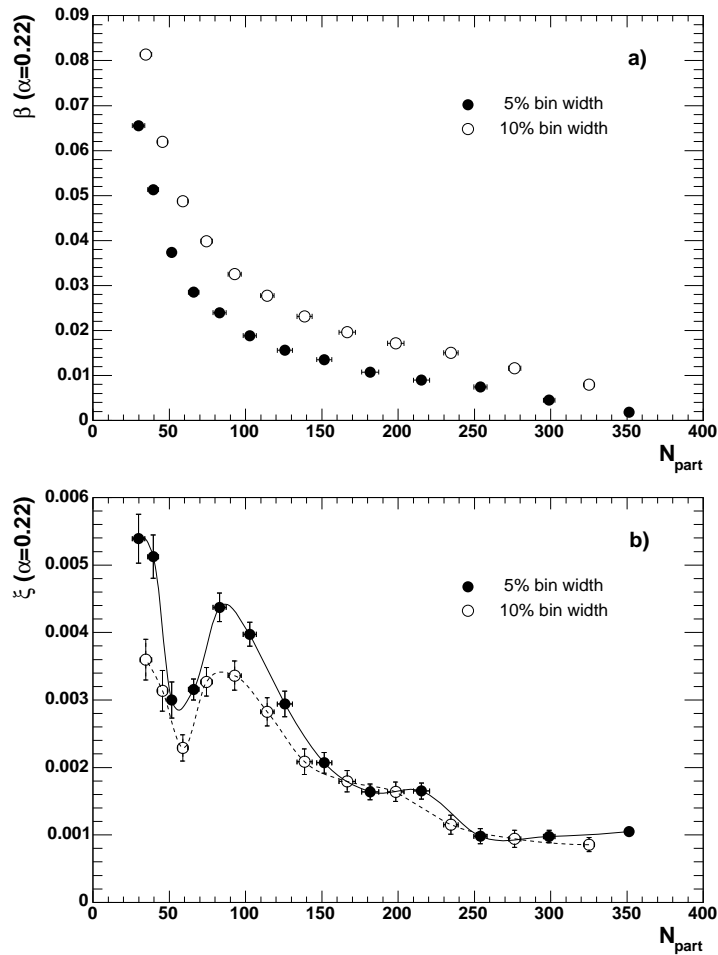
Figure 6.2: Fit results based on Equation (2.28) with fixed $\alpha = 0.22$. a) is β and b) is ξ as a function of N_{part}. The horizontal error bars correspond to ambiguities in the mean value of N_{part} as explained in Section 4.1.3. The vertical error bars are obtained from errors on the fitting parameter.

minimum reduced χ^2 value in Figure 6.1. However, at least the upper limit of the absolute scale of ξ was obtained as $\xi < 0.035$ by the free parameter fits in Equation (2.28). It is qualitatively consistent with expectation from numerical calculations [96] that the correlation lengths become smaller in the RHIC energy than the $(\bar{p})$ $p + p$ collisions [61] and low energy $A + A$ collisions [63]. Since the upper limit of ξ is small enough compared to the fitting region of $\delta\eta$ ($\xi \ll \delta\eta$), Equation (2.29) can be applied for the fits to the NBD k as a function of $\delta\eta$. In this case, the $\alpha\xi$ product, which is proportional to the susceptibility at the static limit as defined in Equation (2.14), can be obtained by the fits without any physical assumptions. The typical χ^2/NDF in the fit based on Equation (2.29) is 0.132, which corresponds to 99 % confidence level as described in Section 5.2. Therefore, the small correlation length is confirmed as below the minimum $\delta\eta$ window sizes of 0.066 based on the validity of the approximated function for the small ξ of Equation (2.29).

6.1.2 Relation with Bose-Einstein correlation

If the observed correlation were to originate only from the effect of Bose-Einstein correlation (HBT), then the α is expected to be directly related with the chaoticity parameter λ in HBT analysis which is measured in relative momentum space q. A similar measurement in pseudorapidity space based on Equation (2.27) without β term in low energy $A + A$ collision systems [97] indicates the direct relation between λ and α quantitatively. The observed two particle correlation strength α in pseudorapidity space is weaker than λ measured in q space and essentially becomes zero for the particle pairs selected in the higher q region where HBT effect also becomes zero. This indicates that the observed pseudorapidity correlations in the lower energy $A + A$ collisions are essentially explained purely by the HBT effect.

In Au + Au collisions at $\sqrt{s_{NN}} = 200$ GeV, measured λ shows the constant behavior as a function of N_{part} within 12 % of its systematic errors [98, 99]. Figure 6.3 shows one dimensional HBT radius parameter R_{inv} (bottom) and chaoticity parameter λ (top) as a function of N_{part} with respect to the correlations of identified pions in same charge. According to the correspondence between α and λ, α can be rephrased as a fraction of correlated particles in the chaotic source. Therefore, the maximum α of 1.0, which is indicated by the dashed line in Figure 6.1, is a physical limit. This means 100 % correlation for the produced particles. In this sense, obtained α of 0.22 by the fit is not contrived with the HBT measurement. This is the reason why the constant α was assumed in Section 6.1.1.

However, obtained parameters for both $\alpha\xi$ in Figure 5.4 and ξ in Figure 6.2 indicates the non-monotonic behavior as a function of N_{part}, where its non-monotonicity will be discussed in Section 6.4, in spite of the fact that λ and R_{inv} indicates the constant behavior. This implies that the non-monotonic be-
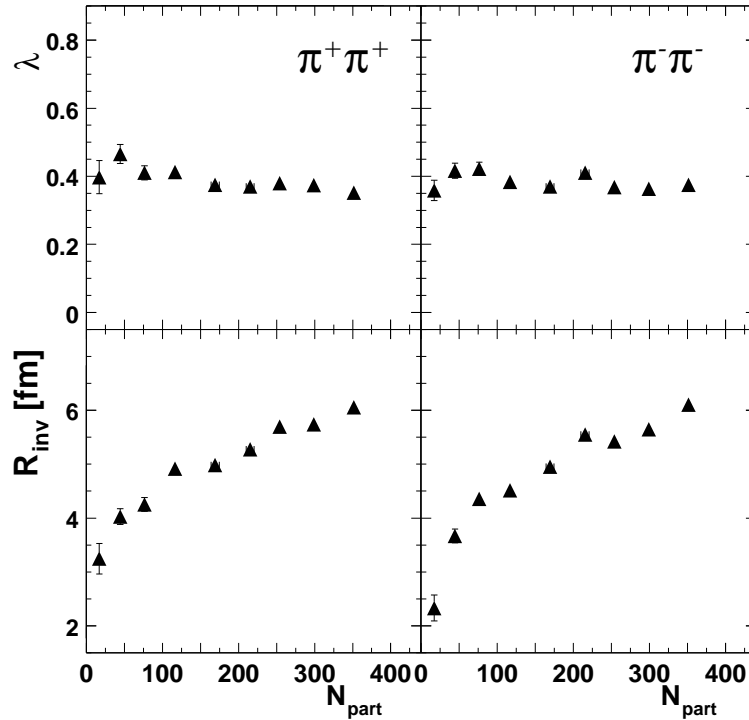
Figure 6.3: One dimensional HBT radius parameter R_{inv} (bottom) and chaoticity parameter λ (top) as a function of N_{part} for $\pi^+ \pi^+$ (left) and $\pi^- \pi^-$ (right) correlations [99].

havior of the $\alpha\xi$ product can not be explained solely as a result of the known HBT effect, because $\alpha \propto \lambda$ is expected to be constant for any N_{part} and ξ which would be related with the HBT source radii is expected to be monotonic, if the known HBT effect is the only source of the correlation.

6.2   Pseudorapidity independent correlation

It should be emphasized that the parametrization in Equation (2.27) is practically necessary. The β parameter can absorb any effects independent of pseudorapidity space correlations. For a wider centrality bin, the width of multiplicity distribution becomes broader, since events with wider range of centrality bins are included in the bin. This causes the systematic difference of β in the 5% and 10% centrality data sets as shown in Figure 5.4 a). The systematic shift of β parameters to smaller values in the smaller centrality bin width, suggests that β dominantly contains fluctuations on N_{part}.

The ambiguity on N_{part} measured by PHENIX is not large compared, for example, to NA49 experiment at SPS where a non-monotonic behavior on scaled

variance of multiplicities was seen as a function of the number of projectile participant nucleons N_{proj} [100,101]. In NA49, only spectators from the projectile nucleus are measurable and it causes an increase of scaled variance of multiplicity distributions in peripheral collisions due to dominantly large N_{proj} fluctuations in the target nucleus [102]. This is due to the partial sampling with respect to the total number of nucleons in two colliding nuclei. Since both projectile and target nuclei in both sides can be measured by BBC and ZDC at PHENIX, this kind of large ambiguities on N_{part} is more suppressed even in peripheral collisions. However, even though the N_{part} fluctuation is still remaining, β parameter can absorb this kind of offset parts of fluctuations and the N_{part} fluctuation is not harmful for the measurement of the $\alpha\xi$ products, since they are based on the differential values of fluctuations for a given centrality bin.

In addition, β is expected to absorb effects from azimuthal correlations. Since the PHENIX detector does not cover the full azimuthal range, fluctuations of low p_T particles caused by event reaction plane rotations and elliptic flow [103] should contribute to the two particle correlation function even in the pseudorapidity direction as an offset in principle. Owing to the β parameter, the non-monotonic behavior of the measured $\alpha\xi$ in the pseudorapidity direction cannot be biased by elliptic flow nor by initial geometrical biases, since the azimuthal correlations are constant over the narrow pseudorapidity window of $|\eta| < 0.35$ [104,105].

6.3 Other correlation sources

In this section, following two type of other sources on the correlations will be concerned, which are not related to the density correlations but could affect the measurement of the inclusive charged particle multiplicity fluctuations. The first is charged track pairs from particle decays in flight. The second is background charged track pairs originating from secondary particle interactions in detector materials *e.g.* showers, conversion pairs and so on. These two sources have been estimated as effects of contaminations to the inclusive charged particle multiplicity fluctuations by the GEANT based MC [88] simulations.

6.3.1 Contributions from weak decay particles

The statistically dominant weak decay particles which can contribute to the inclusive charged particle multiplicity are $K_S^0 \to \pi^+ \pi^-$ and $\Lambda (\bar{\Lambda}) \to p (\bar{p}) \pi^- (\pi^+)$. The relative invariant yields of those particles to charged pions are 15% and 5% for K_S^0 and $\Lambda (\bar{\Lambda})$, respectively. It is calculated by using the measured production cross section in Au + Au collisions at $\sqrt{s_{NN}} = 200$ GeV for $\Lambda (\bar{\Lambda})$ [106,107]. The production cross section of K_S^0 is assumed to be same as measured charged kaons [84]. The detection efficiency of the charged track pairs from these weak decay particles in the one arm acceptance of PHENIX detector ($|\eta| < 0.35$,

$\Delta\phi < \pi/2$) are obtained by the GEANT based [88] MC simulation. It is estimated by using the p_T spectra of charged kaons for K_S^0 as the most dominant meson, and by using the p_T spectra of charged pions with transverse mass scaling for Λ ($\bar{\Lambda}$) as the most dominant baryon, which contribute to the inclusive charged particle multiplicity fluctuation. As the result, the ratios of charged track pairs originating from those weak decay particles to the number of produced charged

Figure 6.4: a) Fraction of charged track pairs originated in single K_s^0 (open circle) and $\Lambda + \bar{\Lambda}$ (closed circle) as a function of difference between two tracks in η. b) Relative fraction of the track pairs as compared to charged π yield in each $\delta\eta$ window size. Statistical errors are included in each marker. Solid lines indicate the minimum window size in this analysis. The dashed line and dotted line correspond to the yield with respect to the each parent particles normalized by the charged π yield in the total acceptance.

pions per event are 0.7% and 0.9% for K_S^0 and $\Lambda + \bar{\Lambda}$, respectively.

The effects of those correlations on NBD k were estimated as follows. Suppose two independent NBD's in different windows have the same NBD parameters of μ and k for a given window size of $\delta\eta/2$. If there is no correlation between the two windows, NBD in the $\delta\eta$ window size becomes a convoluted distribution between the two NBD's. This is certainly true, since it is known the correlation length is well below the minimum size of $\delta\eta$ windows as already discussed in Section 6.1. Based on the NBD convolution theorem [65,95], the convoluted NBD parameters, μ_{conv} and k_{conv} are expressed as $\mu_{conv} = 2\mu$ and $k_{conv} = 2k$, respectively, in the case
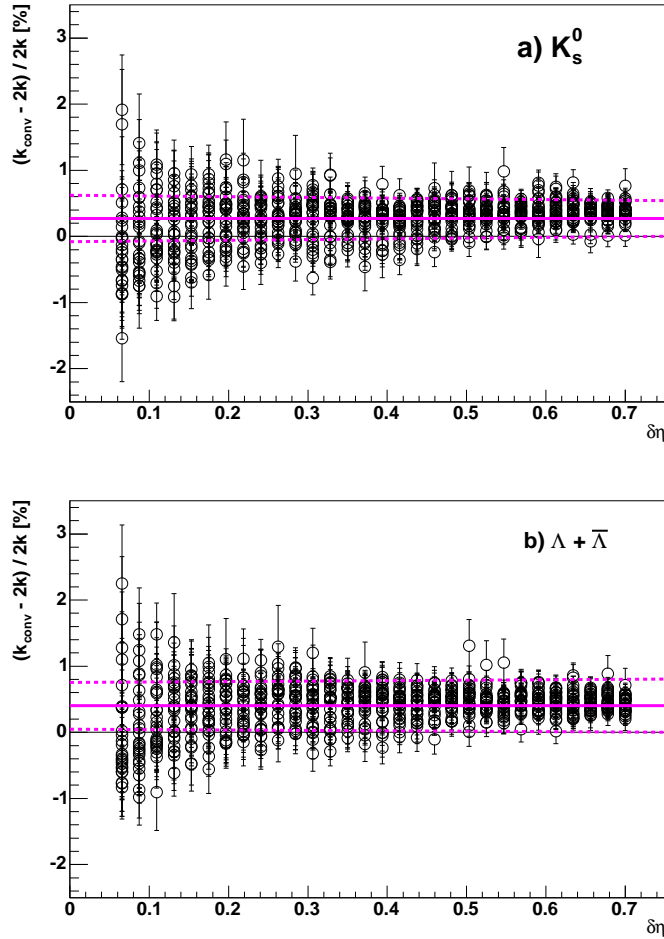
Figure 6.5: Effects in NBD k estimated by $(k_{conv} - 2k)/2k$ as a function of $\delta\eta$ window size from a) K_s^0 and b) $\Lambda + \bar{\Lambda}$. Solid and dashed lines correspond to weighted mean value and corresponding one standard deviation, respectively, for over all $\delta\eta$.

of no correlation. For the case where the correlated pairs are embedded, a fraction f is defined for the number of correlated pairs with respected to μ. Then the mean value before the correlated pairs are embedded is expressed as $\mu(1-f)$ in the $\delta\eta/2$ window. The effect of the embedded correlation on k_{conv} can be estimated by adding the number of correlated pairs to both windows simultaneously with the fraction of f. With $\mu(1-f)$ and k, one can generate NBD with a random number generator in each window of $\delta\eta/2$ and convolute the two NBD's. From the NBD fit to the convoluted distribution, it can be obtained as k_{conv} including the effect of the correlated pairs. The ratio of the deviation of k_{conv} is defined to the independent case, $\Delta k \equiv (k_{conv} - 2k)/2k$ for K_S^0 and $\Lambda + \bar{\Lambda}$, respectively. In this method, the pair fraction f depends on $\delta\eta$ window size, since weak decay particles have their own correlation length due to the kinematical constraint as shown in Figure 6.4 a). Figure 6.4 a) shows the pa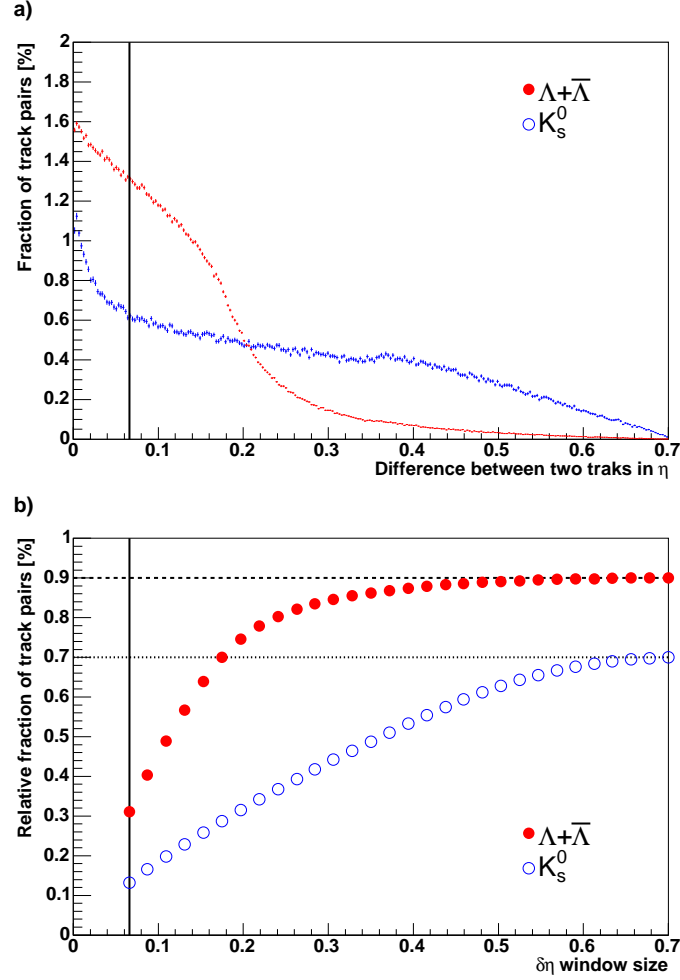ir fraction of charged track pairs originated in single K_s^0 (open circle) and $\Lambda + \bar{\Lambda}$ (closed circle) as a function of difference between two tracks in pseudorapidity η. It is also evaluated from the GEANT based MC simulation with the actual track selection criteria. The fraction f were obtained based on the two particle correlation of decayed pairs as a function of $\delta\eta$ window size. It should be noted that the integrated fractions correspond to the fractions mentioned above as 0.7% and 0.9% for K_S^0 and $\Lambda + \bar{\Lambda}$, respectively. Figure 6.4 b) shows the relative fraction of the track pairs as compared to the charged π yield in each $\delta\eta$ window size. Statistical errors are included in each marker. Solid lines indicate the minimum window size in this analysis. The dashed line and dotted line correspond to the pair yield with respect to the each parent particles normalized by the charged π yield in the total acceptance.

For all observed $(\langle\mu_c\rangle, \langle k_c\rangle)$ values as input values in all $\delta\eta$ windows and in all centrality bins, the Δk have been estimated according to the estimated fraction f for each parent particles. Figure 6.5 a) and Figure 6.5 b) shows the effects in NBD k estimated by the $(k_{conv} - 2k)/2k$ as a function of $\delta\eta$ window size for a) K_s^0 and b) $\Lambda + \bar{\Lambda}$, respectively. As a result, the average values of Δk over all data points were estimated as $+ 0.27\% \pm 0.35\%$ (standard deviation) and $+ 0.40\% \pm 0.35\%$ (standard deviation) for K_S^0 and $\Lambda + \bar{\Lambda}$ decays, respectively. The average values and errors are calculated by taking weighted mean and corresponding one standard deviation, respectively, over all points as shown in solid and dashed lines in Figure 6.5.

Meanwhile, the average value of relative errors, $\delta\langle k_c\rangle(total)/\langle k_c\rangle$ in measured k is $\pm 7.34\% \pm 3.29\%$ (standard deviation). It is confirmed that the estimated Δk values are all included within the range of the relative errors on measured k. Therefore, it can be concluded that the effect of the statistically dominant weak decay pairs with a few percent level on the $\alpha\xi$ product can not exceed the full error sizes of the $\alpha\xi$ products in Table 5.1.

Table 6.1: Summary of detector materials in PHENIX [40] and photon conversion probability in front of EMCal [79] detector. Since TOF is located in front of only PbGl type detector, the total radiation length indicate the different value between the PbSc type and PbGl.

Detector and materials	Total radiation length (%)
Beam pipe + MVD + (He) + DC [75]	1.3
PC1 [77]	1.2
RICH (CO_2) [78]	2.1
TEC [77]	0.8
PC3 [77]	2.4
TOF [78]	0.0 (PbSc) or 6.0 (PbGl)
Total	7.8 (PbSc) or 13.8 (PbGl)
Origin particle	Photon conversion probability (%)
Single γ	5.9 (PbSc) or 10.1 (PbGl)
Decay from π^0 (maximum)	11.8 (PbSc) or 20.2 (PbGl)

6.3.2 Contributions from detector materials

The most significant process originating from the detector materials, which could affect the charged particle multiplicity fluctuation, is photon conversions. Some fraction of photons produces electron-positron pairs in the detector materials *i.e.* $\gamma \to e^+ e^-$, depending on the total amount of the detector materials in front of the tracking detectors for the charged particles. Almost 100% of photons up to 4 GeV/c of p_T in Au + Au collsions at $\sqrt{s_{NN}} = 200$ GeV are produced by decays from π^0 [108,109]. Nevertheless, the same number of π^0 are produced as charged pions at the collisions. Therefore, the effects of the photon conversion process should be considered in the analysis of charged particle multiplicity fluctuation.

The total photon conversion probability in front of the EMCal is estimated based on the corresponding radiation lengths X_0 for each detectors. It can be obtained with respect to single photon γ and neutral pion π^0 as

$$\begin{aligned} P_{conv}(\gamma) &= 1 - e^{-7/9(x/X_0)}, \\ P_{conv}(\pi^0) &= 2P_{conv}(\gamma), \end{aligned} \qquad (6.1)$$

where $P_{conv}(\pi^0)$ is maximum probability assmuming both decay photons convert. Table 6.1 indicates the summary of the radiation length in each section of the detector materials in PHENIX and the total photon conversion probability in front of the two type of the EMCal (see Section 3.4.4). Meanwhile, the

charged tracks used in this analysis are recontacted by the vector information in DC (see Section 3.4.1) mainly, and the information of the PC1, PC3 and EMCal are used only for the tracking association as described in Section 4.2.1. Therefore, only the amount of detector materials before and inside DC is important, and it correspond to 1.3% of a radiation length as indicated in Table 6.1. It produces electron-positron pairs with 1.0% photon conversion probability. The detection efficiency of electron-positron pairs which survive after the requirement of the charged track associations and two track separations in Section 4.2.1 is estimated as 0.22%. It was estimated by the MC simulations with flat p_T distribution of photons. Since the opening angle of the conversion pairs are very small, these conversion electrons are strongly suppressed by the two track separation cuts. Consequently, electron-positron pairs of 2.2×10^{-3}% with respect to the produced charged pions per event contribute to the multiplicity fluctuations.

The efficiency of charged track pairs, which is produced by the materials from single charged hadrons as knock-on electrons (positrons), is estimated as less than 5.8×10^{-5}%. Since the total pair fractions are much smaller than that in weak decays by several orders of magnitude, it can be concluded that the effect of those secondary particles on the $\alpha\xi$ products are negligible.

6.4   Evaluation of the non-monotonic $\alpha\xi$

6.4.1   Significance of local maximum

The $\alpha\xi$ product obtained by Equation (2.29) is related with susceptibility in the long wavelength limit, $\chi_{k=0}$ as described in Section 2.4.2. According to Equation (2.30), if the system temperature T is far from the critical temperature T_c, $\alpha\xi$ is expected to decrease monotonically with increasing T which is a monotonic function of N_{part} as discussed in Section 4.1.4. Therefore, one can assume the monotonically decreasing function as a hypothesis of the baseline in T far from T_c. As the baseline functional forms, following two cases have been considered. The one is a power law function which is naturally expected from Equation (2.30), and the other is a linear function as the simplest assumption. The power law baseline and the linear baseline are parametrized as

$$\alpha\xi(N_{part}) = p_1(N_{part})^{p_2}, \tag{6.2}$$

and

$$\alpha\xi(N_{part}) = p_1 + p_2 N_{part}, \tag{6.3}$$

with fit parameter p_1 and p_2, respectively. As a test hypothesis, a local maximum on the monotonic baselines in $\alpha\xi$ vs. N_{part} is assumed. Although the functional form around the local maximum is not known a priori without introducing a physical model, at least one can discuss the significance of the local maximum from
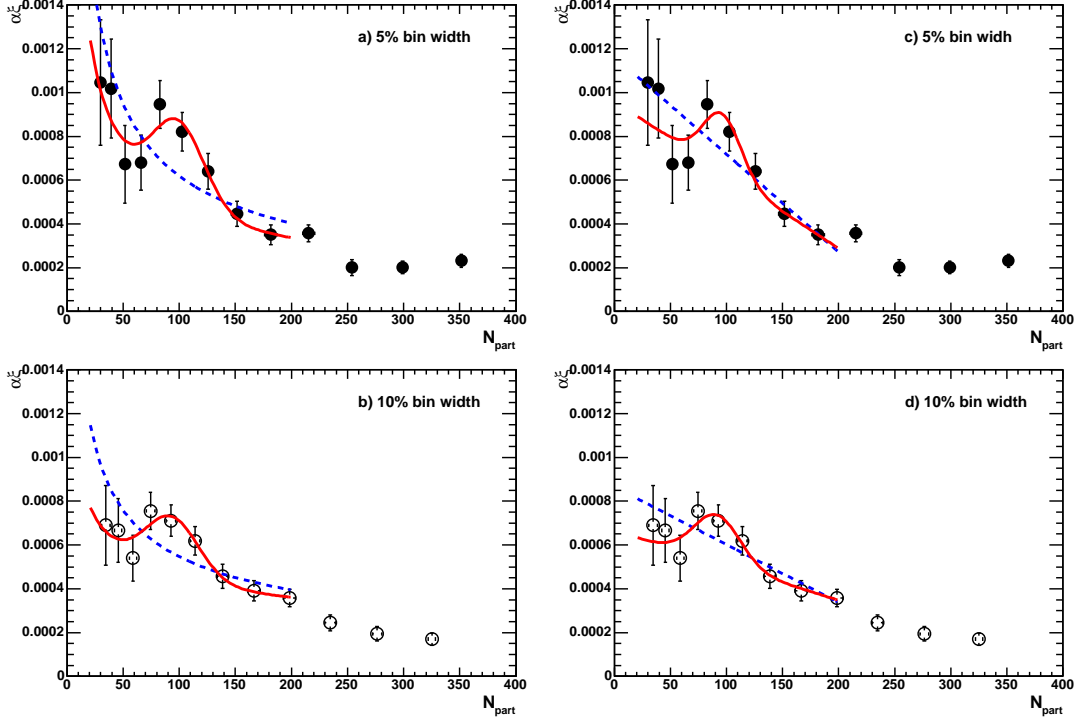
Figure 6.6: $\alpha\xi$ vs. N_{part} in Table 5.1 with fit curves. The dashed and solid curves show the fit results with the baseline functions and with the composite functions, respectively. a) and b) correspond to 5% and 10% bin width cases with the power law baselines, respectively. c) and d) correspond to 5% and 10% bin width cases with the linear baselines, respectively.

the monotonic baseline by introducing a Gaussian distribution. The composite functions are defined as

$$\alpha\xi(N_{part}) = p_1(N_{part})^{p_2} + ae^{-\frac{(N_{part}-m)^2}{2w^2}} \tag{6.4}$$

and

$$\alpha\xi(N_{part}) = p_1 + p_2 N_{part} + ae^{-\frac{(N_{part}-m)^2}{2w^2}}, \tag{6.5}$$

where a, m and w correspond to amplitude, mean and width of the Gaussian component, respectively. Fits with the four functional forms were performed to $\alpha\xi$ vs. N_{part} in $20 < N_{part} < 200$. Figure 6.6 shows $\alpha\xi$ vs. N_{part} in Table 5.1 with those fit curves. The dashed and solid curves show the fit results with the baseline functions and with the composite functions, respectively. Figure 6.6 a) and b) correspond to 5% and 10% bin width cases with the power law baselines, respectively. Figure 6.6 c) and d) correspond to 5% and 10% bin

Table 6.2: The fit parameters in Equation (6.2), Equation (6.3), Equation (6.4) and Equation (6.5).

Functional form	Centrality bin bin width (%)	χ^2/NDF (NDF)	$a \pm \delta a$	Significance $(a/\delta a)$
Power law in Eq. (6.2)	5	2.76 (7)		
Power law + Gaussian in Eq. (6.4)	5	0.60 (4)	$0.37 \times 10^3 \pm 0.09 \times 10^3$	3.98
Linear in Eq. (6.3)	5	1.23 (7)		
Linear + Gaussian in Eq. (6.5)	5	0.79 (4)	$0.27 \times 10^3 \pm 0.21 \times 10^3$	1.24
Power law in Eq. (6.2)	10	2.10 (7)		
Power law + Gaussian in Eq. (6.4)	10	0.38 (4)	$0.27 \times 10^3 \pm 0.08 \times 10^3$	3.21
Linear in Eq. (6.3)	10	1.09 (7)		
Linear + Gaussian in Eq. (6.5)	10	0.43 (4)	$0.22 \times 10^3 \pm 0.13 \times 10^3$	1.69

width cases with the linear baselines, respectively. Table 6.2 summarizes all the fit results by the MINUIT program [94], where functional forms, centrality bin widths, χ^2/NDF (NDF), the Gaussian amplitude a with its error δa and the significance of the amplitude defined by $a/\delta a$. Although the significance of the local maximum with the linear baseline is smaller than that with the power law baseline, it is mainly due to the larger errors on a in Equation (6.5) than errors in Equation (6.4). This is a reflection that the combination of Gaussian distribution with the linear baseline is not as good as that with the power law baseline for the given data points. The difference on the significance between 5% and 10% centrality bin width cases is not attributed to the correlations with β parameter, since β was introduced as a parameter independent of $\delta\eta$. This can be rather understood as smearing effects of a peak-like shape due to the difference of centrality bin widths around the mean N_{part}. In any cases in Table 6.2, χ^2/NDF indicate that all the composite functions are favored compared to the monotonic functions. This result supports the non-monotonicity of $\alpha\xi$ as a function of N_{part}.

6.4.2 Assumption of the one correlation length

Although there is a possibility that more than one correlation length scale is dynamically present, the functional form with one correlation length in Equation (2.29) can reasonably describe the region of $0.066 < \delta\eta < 0.7$ with the average χ^2/NDF of 0.43 over all centrality bins. A further check on the N_{part} dependence of the $\alpha\xi$ products have been performed by limiting the region of fit to $0.066 < \delta\eta < 0.306$ as shown in Figure 6.7. The characteristic behavior of $\alpha\xi$ still present at around $N_{part} \sim 90$.
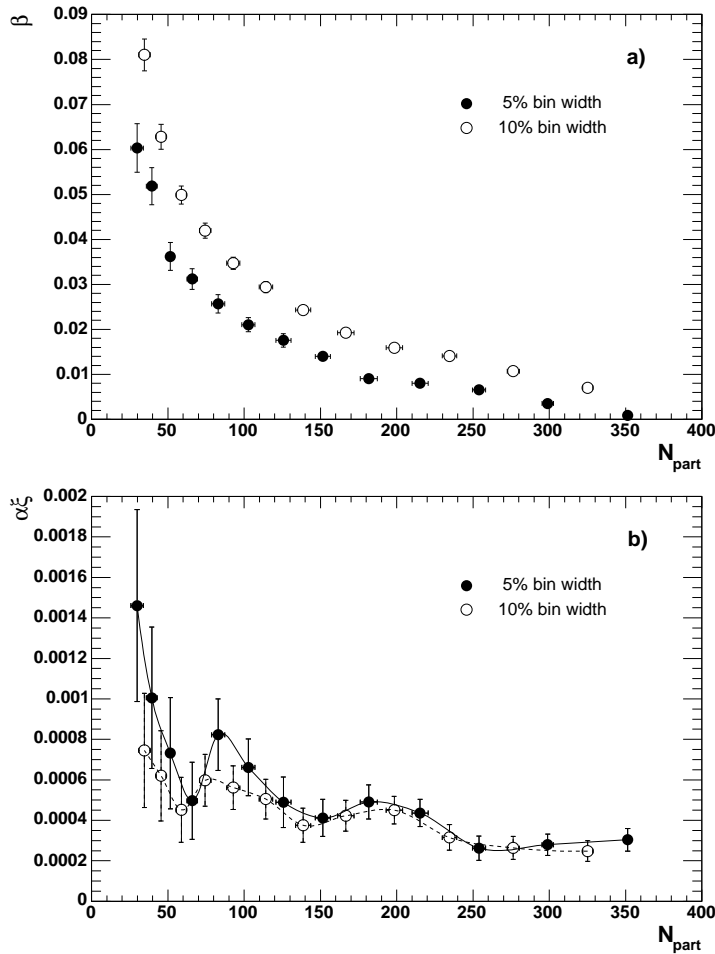
Figure 6.7: Fit results based on Equation (2.29) by limiting the range of $\delta\eta$ from 0.066 to 0.306. a) is β and b) is products of $\alpha\xi$ as a function of N_{part}. The horizontal error bars correspond to ambiguities in the mean value of N_{part} as explained in Section 4.1.3. The vertical error bars are obtained from errors on the fitting parameter.

6.5 Physical interpretation of the results

This analysis is predicated on an application of the most simplest model *i.e.* Ginzburg-Landau thermodynamical theory, for the high-density matter created by the high energy heavy ion collision. Therefore, it is important whether the system reached thermal equilibrium or not. According to the fruitful RHIC results already obtained, it is almost established that a strongly interacting, high density matter has been created in nucleus-nucleus collisions [37]. Especially, strong suppression of hadrons at high transverse momentum (p_T) observed in central Au+Au collisions at $\sqrt{s_{NN}} = 200$GeV at RHIC indicates creation of the

high density partonic matter [86, 112]. Additionally, strong elliptic flow, which is one of the indicative observables on collective motions of the matter, indicates that the matter thermalizes rapidly and behaves like a fluid with very low viscosity [103, 110]. Furthermore, the valence quark number scaling of the elliptic flow suggests that quark-like degrees of freedom are pertinent in the evolution of the flow [111]. Those observations naturally lead us to the expectation that the initial thermalized state of matter is at $T > T_c$ in central Au+Au collisions, and possibly at $T < T_c$ in the most peripheral collisions. Therefore it can be considered that a system with initial $T = T_c$ may exist somewhere between peripheral and central collisions.

One can form a lot of hypothesis on the space-time evolution of the system before and after the thermalizaion. However, it is difficult to conclude the correct path on the phase diagram only by the experimental observables exclusively, because we always observe the final state particles. Even in this case, fluctuation observables have possibilities to keep the information at the phase transition as described in Section 2.3. According to the scenario, a singular behavior on the thermodynamic quantity will be seen at one point of the scanning regions. It corresponds to N_{part} in this analysis case. $\alpha\xi$ obtained by this analysis as a function of N_{part} indicates statistically non-monotonic part at $N_{part} \sim 90$ as shown in Figure 5.4. This behavior is consistent with the scenario of rapid cooling of the system and surviving fluctuations.

Chapter 7

Conclusion

The multiplicity distributions measured in Au+Au collisions at $\sqrt{s_{NN}} = 200$ GeV are found to be well described by negative binomial distributions (NBD) in cases where the collision centrality is greater than 65%.

The longitudinal density correlations have been measured via the functional form for pseudorapidity (η) density fluctuations derived in the Ginzburg-Landau thermodynamical theory, up to the second order term in the free energy, with a scalar order parameter defined as pseudorapidity dependent multiplicity fluctuations around the mean value. The functional form can reasonably fit NBD k parameters as a function of pseudorapidity window sizes $\delta\eta$ in the measured all centrality (0 - 65%) at $|\eta| < 0.35$ region with one correlation length ξ assumption and the constant term β which is independent of $\delta\eta$. The β is found to be necessary to absorb residual effects of finite centrality binning.

The absolute scale of the correlation length ξ depends on the magnitude of the correlation strength at zero distance α within the range of pseudorapidity window sizes available in this analysis. However, according to the free parameter fit results, the upper limit on $\xi < 0.035$ was obtained, and it was confirmed by the accuracy of the fits with approximated integrated correlation function in the limit of the small correlation length ($\xi \ll \delta\eta$).

The $\alpha\xi$ product in the correlation function, which is monotonically related to susceptibility in the long wavelength limit $\chi_{k=0}$, was seen to exhibit a non-monotonic behavior as a function of the number of participant nucleons N_{part}. A possible indication of a local maximum is seen at $N_{part} \sim 90$ and the corresponding energy density based on the Bjorken picture is $\varepsilon_{Bj} \cdot \tau \sim 2.4$ GeV/fm$^2 \cdot c$ with the transverse area size of 60 fm^2.

Trivial particle correlations originating from charged track reconstructions in tracking detectors have been suppressed in this analysis a priori. The ratio of charged particles from statistically dominant weak decays and secondary particles produced in the detector materials, which contribute as correlated pairs, are respectively estimated below $\sim 1\%$ and $\sim 10^{-3}\%$ with respect to the total number of charged pions in the PHENIX acceptance per event. It is estimated that those

effects on measured k values and the deviation due to the effect is well inside the total error size of observed $\delta\langle k_c\rangle$. Therefore, it can be concluded that their contributions are almost negligible to the observed behavior of the $\alpha\xi$ products.

The behavior may be explained by the onset of a mixture of different types of particle production mechanisms which are not necessarily related with temperature nor density correlations. However, interpreted within the Ginzburg-Landau framework, the local maximum of the $\alpha\xi$ product could be an indication of a critical phase boundary.

Acknowledgment

Appendix A

Tables of NBD fit results

NBD fit results in all window sizes in all centrality bins in Figure 5.3. In the following Table A.1 through Table A.12 and Table A.13 through Table A.25 correspond to results in 10% and 5% bin width cases, respectively. $\langle \mu_c \rangle$ and $\langle \mu \rangle$ are weighted means of corrected and uncorrected μ over all window positions, respectively. $\langle k_c \rangle$ and $\langle k \rangle$ are weighted means of corrected and uncorrected k over all window positions, respectively. Statistical errors on weighted means $\delta \langle k_c \rangle$ (stat) are obtained as explained in Section 4.4.2. $\langle \chi^2/NDF \rangle$ is the average of reduced χ^2 of NBD fits over all window positions. $\langle NDF \rangle$ is the average of the degree of freedom of NBD fits over all window positions. Systematic errors $\delta \langle k_c \rangle$ (dead), $\delta \langle k_c \rangle$ (fake) and $\delta \langle k_c \rangle$ (total) are explained in Section 4.4.2.

Table A.1: NBD fit results in centrality 0-10%.

$\delta\eta$	$\langle\mu_c\rangle(\langle\mu\rangle)$	$\langle k_c\rangle(\langle k\rangle)$	$\langle\chi^2/NDF\rangle(\langle NDF\rangle)$	$\delta\langle k_c\rangle(dead)$	$\delta\langle k_c\rangle(fake)$	$\delta\langle k_c\rangle(total)$
0.700	77.535 (60.011) ± 0.108	114.28 (88.45) ± 3.21	0.96 (71.0)	±2.89	±2.28	±4.89
0.678	75.445 (58.445) ± 0.106	113.11 (87.62) ± 3.29	0.89 (69.7)	±4.92	±3.31	±6.78
0.656	72.977 (56.455) ± 0.103	114.40 (88.50) ± 3.38	0.95 (68.2)	±4.33	±3.04	±6.28
0.634	70.485 (54.450) ± 0.101	114.02 (88.08) ± 3.42	0.92 (66.7)	±4.54	±3.01	±6.43
0.613	67.998 (52.489) ± 0.099	114.44 (88.33) ± 3.52	0.94 (65.3)	±3.79	±2.31	±5.66
0.591	65.530 (50.572) ± 0.096	114.28 (88.18) ± 3.60	0.95 (63.9)	±3.59	±2.62	±5.72
0.569	63.050 (48.609) ± 0.094	114.62 (88.35) ± 3.71	0.97 (62.3)	±3.88	±2.80	±6.05
0.547	60.569 (46.624) ± 0.091	114.27 (87.94) ± 3.80	0.96 (60.8)	±3.61	±2.98	±6.03
0.525	58.100 (44.655) ± 0.089	114.38 (87.89) ± 3.92	0.95 (59.7)	±3.79	±2.87	±6.16
0.503	55.637 (42.682) ± 0.086	114.36 (87.70) ± 4.03	0.93 (57.8)	±3.64	±3.17	±6.29
0.481	53.164 (40.688) ± 0.084	114.41 (87.54) ± 4.17	0.94 (56.3)	±4.24	±3.40	±6.85
0.459	50.682 (38.672) ± 0.081	115.19 (87.87) ± 4.35	0.98 (54.2)	±4.10	±3.14	±6.75
0.438	48.209 (36.654) ± 0.079	114.89 (87.33) ± 4.51	0.98 (52.4)	±4.49	±3.72	±7.37
0.416	45.743 (34.645) ± 0.076	115.05 (87.11) ± 4.71	0.98 (50.3)	±4.79	±3.49	±7.57
0.394	43.283 (32.654) ± 0.074	114.86 (86.61) ± 4.90	0.97 (48.3)	±4.37	±4.15	±7.77
0.372	40.838 (30.677) ± 0.071	115.20 (86.46) ± 5.17	1.00 (46.2)	±4.22	±4.10	±7.83
0.350	38.424 (28.782) ± 0.049	115.87 (86.69) ± 3.88	1.04 (44.5)	±3.81	±4.22	±6.88
0.328	36.034 (27.062) ± 0.047	115.35 (86.43) ± 4.04	1.04 (42.9)	±4.04	±4.58	±7.32
0.306	33.665 (25.363) ± 0.045	114.46 (86.00) ± 4.21	1.08 (41.2)	±4.28	±4.89	±7.74
0.284	31.288 (23.638) ± 0.043	113.91 (85.92) ± 4.39	1.09 (39.9)	±3.60	±5.13	±7.65
0.263	28.916 (21.900) ± 0.041	111.53 (84.56) ± 4.51	1.10 (37.9)	±3.75	±5.29	±7.90
0.241	26.542 (20.145) ± 0.039	109.53 (83.35) ± 4.67	1.08 (36.3)	±3.71	±5.40	±8.04
0.219	24.155 (18.360) ± 0.030	107.67 (82.28) ± 4.03	1.11 (34.4)	±3.66	±5.96	±8.07
0.197	21.758 (16.553) ± 0.028	105.84 (80.90) ± 4.29	1.15 (32.4)	±3.17	±6.12	±8.12
0.175	19.355 (14.723) ± 0.023	102.63 (78.59) ± 3.96	1.21 (30.1)	±3.59	±6.85	±8.69
0.153	16.948 (12.880) ± 0.021	97.91 (75.16) ± 4.19	1.25 (27.6)	±3.83	±6.93	±8.96
0.131	14.536 (11.031) ± 0.017	93.93 (72.13) ± 4.01	1.34 (24.9)	±3.77	±7.03	±8.93
0.109	12.119 (9.172) ± 0.014	87.92 (66.93) ± 3.81	1.39 (21.9)	±3.48	±7.30	±8.94
0.087	9.695 (7.305) ± 0.011	78.94 (58.95) ± 3.35	1.34 (18.7)	±3.48	±7.34	±8.79
0.066	7.308 (5.685) ± 0.008	65.53 (49.27) ± 2.87	1.09 (15.4)	±4.05	±6.83	±8.45

Table A.2: NBD fit results in centrality 5-15%.

$\delta\eta$	$\langle\mu_c\rangle(\langle\mu\rangle)$	$\langle k_c\rangle(\langle k\rangle)$	$\langle\chi^2/NDF\rangle(\langle NDF\rangle)$	$\delta\langle k_c\rangle(dead)$	$\delta\langle k_c\rangle(fake)$	$\delta\langle k_c\rangle(total)$
0.700	66.445 (51.428) ± 0.098	80.80 (62.54) ± 1.92	1.20 (68.0)	±2.14	±2.17	±3.60
0.678	64.658 (50.089) ± 0.097	80.40 (62.28) ± 1.95	1.15 (66.4)	±3.40	±1.53	±4.21
0.656	62.535 (48.377) ± 0.094	81.17 (62.79) ± 1.99	1.20 (65.0)	±2.28	±1.11	±3.22
0.634	60.379 (46.644) ± 0.092	81.10 (62.65) ± 2.02	1.23 (64.1)	±2.24	±1.57	±3.40
0.613	58.258 (44.970) ± 0.090	80.61 (62.21) ± 2.06	1.21 (62.4)	±2.75	±1.43	±3.72
0.591	56.156 (43.337) ± 0.088	79.66 (61.47) ± 2.08	1.12 (60.6)	±2.85	±1.50	±3.83
0.569	54.043 (41.665) ± 0.085	79.26 (61.09) ± 2.12	1.07 (59.2)	±2.59	±1.88	±3.83
0.547	51.923 (39.968) ± 0.083	78.98 (60.79) ± 2.17	1.09 (57.4)	±2.90	±1.68	±3.99
0.525	49.809 (38.283) ± 0.081	79.14 (60.81) ± 2.23	1.11 (56.2)	±2.83	±1.88	±4.07
0.503	47.691 (36.586) ± 0.078	79.62 (61.06) ± 2.32	1.13 (54.7)	±2.15	±1.91	±3.69
0.481	45.573 (34.878) ± 0.076	79.66 (60.95) ± 2.39	1.13 (53.0)	±2.35	±1.59	±3.71
0.459	43.446 (33.150) ± 0.073	80.40 (61.33) ± 2.48	1.18 (51.3)	±2.25	±1.70	±3.76
0.438	41.327 (31.420) ± 0.071	79.99 (60.80) ± 2.56	1.15 (49.4)	±2.84	±2.29	±4.46
0.416	39.211 (29.696) ± 0.069	80.34 (60.83) ± 2.67	1.18 (47.7)	±2.98	±2.03	±4.49
0.394	37.107 (27.993) ± 0.067	80.40 (60.62) ± 2.79	1.15 (45.9)	±3.24	±2.36	±4.88
0.372	35.007 (26.295) ± 0.064	80.45 (60.38) ± 2.92	1.18 (43.9)	±3.19	±2.29	±4.89
0.350	32.938 (24.672) ± 0.044	80.58 (60.28) ± 2.17	1.21 (42.1)	±3.22	±2.23	±4.48
0.328	30.889 (23.196) ± 0.042	80.09 (60.08) ± 2.25	1.22 (40.3)	±3.29	±2.71	±4.82
0.306	28.861 (21.741) ± 0.040	79.49 (59.81) ± 2.33	1.22 (38.6)	±3.21	±2.56	±4.73
0.284	26.832 (20.270) ± 0.038	79.11 (59.73) ± 2.44	1.24 (37.0)	±2.85	±2.87	±4.72
0.263	24.795 (18.778) ± 0.036	78.06 (59.22) ± 2.55	1.23 (35.3)	±3.01	±3.26	±5.12
0.241	22.758 (17.270) ± 0.035	77.16 (58.82) ± 2.68	1.22 (33.8)	±2.93	±3.39	±5.22
0.219	20.708 (15.737) ± 0.026	76.33 (58.44) ± 2.32	1.27 (32.1)	±2.56	±3.09	±4.64
0.197	18.654 (14.187) ± 0.025	75.26 (57.80) ± 2.47	1.29 (30.2)	±2.84	±3.67	±5.26
0.175	16.591 (12.614) ± 0.020	73.89 (56.91) ± 2.30	1.36 (28.1)	±2.74	±3.58	±5.06
0.153	14.526 (11.035) ± 0.019	71.68 (55.18) ± 2.44	1.41 (25.9)	±2.84	±3.97	±5.46
0.131	12.458 (9.451) ± 0.015	69.08 (53.03) ± 2.31	1.47 (23.1)	±2.81	±4.10	±5.48
0.109	10.385 (7.857) ± 0.013	65.32 (49.65) ± 2.23	1.46 (20.3)	±2.92	±4.28	±5.64
0.087	8.306 (6.253) ± 0.010	59.45 (44.57) ± 2.03	1.29 (17.4)	±2.58	±4.32	±5.43
0.066	6.262 (4.870) ± 0.007	51.33 (38.86) ± 1.88	0.89 (14.4)	±2.75	±4.18	±5.34

Table A.3: NBD fit results in centrality 10-20%.

$\delta\eta$	$\langle\mu_c\rangle(\langle\mu\rangle)$	$\langle k_c\rangle(\langle k\rangle)$	$\langle\chi^2/NDF\rangle(\langle NDF\rangle)$	$\delta\langle k_c\rangle(dead)$	$\delta\langle k_c\rangle(fake)$	$\delta\langle k_c\rangle(total)$
0.700	55.290 (42.794) ± 0.090	63.58 (49.21) ± 1.47	1.14 (64.0)	±0.37	±0.57	±1.62
0.678	53.832 (41.701) ± 0.089	62.10 (48.11) ± 1.46	0.93 (63.1)	±2.48	±2.60	±3.88
0.656	52.092 (40.299) ± 0.087	61.78 (47.79) ± 1.48	0.88 (62.3)	±2.34	±1.54	±3.17
0.634	50.301 (38.858) ± 0.085	61.91 (47.82) ± 1.51	0.90 (60.3)	±2.06	±1.23	±2.83
0.613	48.533 (37.463) ± 0.082	61.80 (47.70) ± 1.54	0.88 (58.5)	±2.10	±1.09	±2.83
0.591	46.769 (36.093) ± 0.080	62.00 (47.85) ± 1.58	0.90 (57.9)	±1.74	±1.21	±2.64
0.569	45.006 (34.698) ± 0.078	61.89 (47.71) ± 1.61	0.87 (56.6)	±1.77	±1.06	±2.62
0.547	43.255 (33.296) ± 0.076	61.70 (47.49) ± 1.65	0.88 (55.1)	±1.80	±1.34	±2.78
0.525	41.499 (31.895) ± 0.074	61.86 (47.55) ± 1.70	0.89 (53.8)	±1.95	±1.21	±2.86
0.503	39.742 (30.488) ± 0.072	61.94 (47.51) ± 1.75	0.90 (52.4)	±1.89	±1.38	±2.92
0.481	37.976 (29.063) ± 0.070	61.92 (47.38) ± 1.80	0.90 (50.8)	±1.84	±1.26	±2.87
0.459	36.206 (27.625) ± 0.067	61.91 (47.24) ± 1.85	0.91 (48.8)	±1.84	±1.46	±2.99
0.438	34.435 (26.179) ± 0.065	61.83 (47.01) ± 1.91	0.91 (47.2)	±1.91	±1.55	±3.12
0.416	32.667 (24.739) ± 0.063	62.02 (46.98) ± 1.99	0.95 (45.6)	±1.96	±1.63	±3.23
0.394	30.908 (23.315) ± 0.061	62.18 (46.92) ± 2.07	1.00 (43.8)	±2.02	±1.58	±3.30
0.372	29.156 (21.898) ± 0.059	62.35 (46.85) ± 2.16	1.02 (42.1)	±2.14	±1.69	±3.48
0.350	27.434 (20.547) ± 0.040	62.21 (46.61) ± 1.59	1.02 (40.4)	±2.30	±1.77	±3.31
0.328	25.727 (19.316) ± 0.038	61.90 (46.54) ± 1.64	1.06 (38.6)	±2.05	±1.66	±3.11
0.306	24.039 (18.105) ± 0.037	61.43 (46.42) ± 1.71	1.09 (36.8)	±2.09	±1.68	±3.17
0.284	22.347 (16.876) ± 0.035	60.84 (46.18) ± 1.77	1.10 (35.1)	±2.30	±1.84	±3.44
0.263	20.653 (15.635) ± 0.033	60.20 (45.91) ± 1.85	1.12 (33.3)	±2.19	±1.93	±3.45
0.241	18.956 (14.380) ± 0.032	59.81 (45.79) ± 1.95	1.19 (31.6)	±2.27	±1.91	±3.54
0.219	17.251 (13.105) ± 0.024	59.09 (45.44) ± 1.68	1.22 (29.7)	±2.19	±2.04	±3.43
0.197	15.537 (11.813) ± 0.023	58.31 (44.99) ± 1.78	1.25 (27.6)	±2.23	±2.11	±3.55
0.175	13.816 (10.501) ± 0.018	57.38 (44.38) ± 1.65	1.31 (25.5)	±1.84	±2.17	±3.29
0.153	12.090 (9.179) ± 0.017	55.59 (43.04) ± 1.75	1.33 (23.0)	±1.77	±2.18	±3.31
0.131	10.367 (7.858) ± 0.014	52.81 (40.76) ± 1.63	1.27 (20.6)	±1.83	±2.31	±3.36
0.109	8.639 (6.528) ± 0.011	49.83 (38.38) ± 1.57	1.14 (18.2)	±1.85	±2.55	±3.52
0.087	6.909 (5.194) ± 0.009	46.30 (35.28) ± 1.45	0.97 (15.6)	±1.82	±2.85	±3.68
0.066	5.215 (4.052) ± 0.007	42.21 (32.18) ± 1.43	0.75 (13.0)	±2.04	±2.90	±3.82

Table A.4: NBD fit results in centrality 15-25%.

$\delta\eta$	$\langle\mu_c\rangle(\langle\mu\rangle)$	$\langle k_c\rangle(\langle k\rangle)$	$\langle\chi^2/NDF\rangle(\langle NDF\rangle)$	$\delta\langle k_c\rangle(dead)$	$\delta\langle k_c\rangle(fake)$	$\delta\langle k_c\rangle(total)$
0.700	45.868 (35.502) ± 0.082	53.43 (41.35) ± 1.25	1.06 (57.0)	±1.83	±1.78	±2.85
0.678	44.657 (34.594) ± 0.080	53.48 (41.43) ± 1.29	0.95 (55.3)	±1.49	±0.53	±2.04
0.656	43.211 (33.428) ± 0.078	53.45 (41.35) ± 1.31	0.98 (54.2)	±1.53	±0.71	±2.14
0.634	41.737 (32.242) ± 0.076	53.70 (41.48) ± 1.35	0.96 (53.0)	±1.43	±0.58	±2.05
0.613	40.288 (31.098) ± 0.075	53.41 (41.23) ± 1.38	0.92 (51.2)	±1.94	±1.12	±2.63
0.591	38.829 (29.965) ± 0.073	53.66 (41.42) ± 1.42	0.96 (50.3)	±1.71	±0.70	±2.33
0.569	37.368 (28.808) ± 0.071	53.48 (41.23) ± 1.45	0.94 (49.0)	±1.76	±0.82	±2.42
0.547	35.911 (27.642) ± 0.069	53.32 (41.04) ± 1.48	0.91 (47.6)	±1.77	±0.88	±2.47
0.525	34.454 (26.481) ± 0.067	53.41 (41.05) ± 1.52	0.95 (46.1)	±1.75	±0.76	±2.44
0.503	32.995 (25.311) ± 0.065	53.58 (41.11) ± 1.56	1.02 (44.9)	±1.50	±0.81	±2.31
0.481	31.532 (24.131) ± 0.063	53.73 (41.13) ± 1.61	1.02 (44.0)	±1.50	±0.66	±2.29
0.459	30.062 (22.936) ± 0.061	53.65 (40.95) ± 1.65	1.02 (42.8)	±1.57	±0.86	±2.44
0.438	28.591 (21.736) ± 0.059	53.69 (40.84) ± 1.71	1.03 (41.4)	±1.70	±0.87	±2.57
0.416	27.125 (20.541) ± 0.057	53.76 (40.75) ± 1.78	1.04 (40.0)	±1.71	±0.84	±2.61
0.394	25.664 (19.358) ± 0.055	53.81 (40.64) ± 1.84	1.03 (38.5)	±1.78	±1.07	±2.78
0.372	24.206 (18.179) ± 0.053	54.03 (40.64) ± 1.93	1.05 (37.1)	±1.71	±1.02	±2.77
0.350	22.778 (17.058) ± 0.036	54.05 (40.55) ± 1.42	1.09 (35.7)	±1.94	±1.07	±2.63
0.328	21.359 (16.035) ± 0.035	53.79 (40.53) ± 1.48	1.12 (34.5)	±1.74	±1.02	±2.50
0.306	19.955 (15.027) ± 0.033	53.36 (40.43) ± 1.54	1.14 (33.2)	±1.74	±1.09	±2.57
0.284	18.552 (14.008) ± 0.032	52.52 (40.03) ± 1.59	1.16 (31.7)	±1.78	±1.17	±2.66
0.263	17.146 (12.979) ± 0.030	51.86 (39.73) ± 1.66	1.19 (29.9)	±1.63	±1.17	±2.60
0.241	15.736 (11.936) ± 0.029	51.03 (39.31) ± 1.74	1.25 (28.0)	±1.53	±1.28	±2.65
0.219	14.320 (10.876) ± 0.022	49.80 (38.58) ± 1.48	1.26 (26.0)	±1.69	±1.32	±2.60
0.197	12.897 (9.802) ± 0.021	48.78 (37.96) ± 1.57	1.26 (24.1)	±1.43	±1.39	±2.53
0.175	11.465 (8.711) ± 0.017	47.43 (37.04) ± 1.43	1.26 (22.3)	±1.39	±1.30	±2.38
0.153	10.030 (7.612) ± 0.015	45.48 (35.65) ± 1.51	1.21 (20.2)	±1.13	±1.41	±2.36
0.131	8.597 (6.513) ± 0.013	43.13 (33.84) ± 1.41	1.06 (18.1)	±1.27	±1.55	±2.45
0.109	7.163 (5.409) ± 0.011	40.33 (31.64) ± 1.34	0.79 (15.9)	±1.21	±1.67	±2.45
0.087	5.730 (4.304) ± 0.008	37.88 (29.64) ± 1.27	0.64 (13.7)	±1.15	±1.77	±2.47
0.066	4.327 (3.360) ± 0.006	35.48 (27.59) ± 1.28	0.54 (11.6)	±1.20	±1.96	±2.63

Table A.5: NBD fit results in centrality 20-30%.

$\delta\eta$	$\langle\mu_c\rangle(\langle\mu\rangle)$	$\langle k_c\rangle(\langle k\rangle)$	$\langle\chi^2/NDF\rangle(\langle NDF\rangle)$	$\delta\langle k_c\rangle(dead)$	$\delta\langle k_c\rangle(fake)$	$\delta\langle k_c\rangle(total)$
0.700	37.610 (29.110) $\pm$ 0.073	47.51 (36.77) $\pm$ 1.17	0.82 (53.0)	$\pm$1.28	$\pm$0.76	$\pm$1.89
0.678	36.606 (28.358) $\pm$ 0.072	47.66 (36.92) $\pm$ 1.20	0.86 (51.7)	$\pm$1.61	$\pm$0.68	$\pm$2.12
0.656	35.403 (27.388) $\pm$ 0.070	47.76 (36.94) $\pm$ 1.22	0.83 (51.4)	$\pm$1.10	$\pm$0.43	$\pm$1.70
0.634	34.199 (26.419) $\pm$ 0.069	47.45 (36.66) $\pm$ 1.24	0.83 (50.2)	$\pm$1.54	$\pm$0.65	$\pm$2.08
0.613	33.002 (25.474) $\pm$ 0.067	47.80 (36.90) $\pm$ 1.27	0.97 (49.3)	$\pm$0.99	$\pm$0.68	$\pm$1.75
0.591	31.812 (24.550) $\pm$ 0.065	47.37 (36.56) $\pm$ 1.28	0.96 (48.6)	$\pm$1.29	$\pm$0.62	$\pm$1.92
0.569	30.609 (23.598) $\pm$ 0.063	47.42 (36.56) $\pm$ 1.31	0.93 (47.7)	$\pm$1.12	$\pm$0.51	$\pm$1.80
0.547	29.413 (22.641) $\pm$ 0.062	47.14 (36.29) $\pm$ 1.34	0.92 (46.0)	$\pm$1.26	$\pm$0.68	$\pm$1.96
0.525	28.218 (21.688) $\pm$ 0.060	47.13 (36.23) $\pm$ 1.37	0.94 (44.8)	$\pm$1.38	$\pm$0.66	$\pm$2.05
0.503	27.021 (20.729) $\pm$ 0.058	47.16 (36.19) $\pm$ 1.41	0.98 (43.6)	$\pm$1.29	$\pm$0.53	$\pm$1.98
0.481	25.823 (19.762) $\pm$ 0.057	47.14 (36.08) $\pm$ 1.45	0.98 (42.2)	$\pm$1.40	$\pm$0.52	$\pm$2.08
0.459	24.623 (18.787) $\pm$ 0.055	47.14 (35.98) $\pm$ 1.50	0.98 (41.1)	$\pm$1.37	$\pm$0.57	$\pm$2.11
0.438	23.421 (17.806) $\pm$ 0.053	46.88 (35.66) $\pm$ 1.54	0.95 (39.4)	$\pm$1.53	$\pm$0.68	$\pm$2.28
0.416	22.218 (16.826) $\pm$ 0.051	47.13 (35.72) $\pm$ 1.61	1.02 (38.0)	$\pm$1.42	$\pm$0.55	$\pm$2.21
0.394	21.024 (15.858) $\pm$ 0.050	46.86 (35.38) $\pm$ 1.67	0.99 (36.6)	$\pm$1.61	$\pm$0.68	$\pm$2.42
0.372	19.831 (14.894) $\pm$ 0.048	46.92 (35.28) $\pm$ 1.74	1.00 (35.1)	$\pm$1.60	$\pm$0.78	$\pm$2.49
0.350	18.658 (13.973) $\pm$ 0.033	46.79 (35.08) $\pm$ 1.29	1.02 (33.7)	$\pm$1.63	$\pm$0.83	$\pm$2.23
0.328	17.499 (13.138) $\pm$ 0.031	46.40 (34.90) $\pm$ 1.33	1.02 (32.1)	$\pm$1.63	$\pm$0.79	$\pm$2.25
0.306	16.350 (12.314) $\pm$ 0.030	46.22 (34.90) $\pm$ 1.40	1.07 (30.6)	$\pm$1.72	$\pm$0.73	$\pm$2.33
0.284	15.201 (11.480) $\pm$ 0.029	45.61 (34.60) $\pm$ 1.45	1.06 (29.0)	$\pm$1.56	$\pm$0.82	$\pm$2.28
0.263	14.048 (10.636) $\pm$ 0.027	44.99 (34.29) $\pm$ 1.51	1.06 (27.4)	$\pm$1.65	$\pm$0.90	$\pm$2.41
0.241	12.892 (9.781) $\pm$ 0.026	44.22 (33.84) $\pm$ 1.58	1.07 (25.6)	$\pm$1.54	$\pm$0.91	$\pm$2.39
0.219	11.729 (8.913) $\pm$ 0.020	43.26 (33.22) $\pm$ 1.34	1.05 (24.0)	$\pm$1.36	$\pm$0.93	$\pm$2.13
0.197	10.561 (8.032) $\pm$ 0.019	42.28 (32.55) $\pm$ 1.41	1.05 (22.4)	$\pm$1.30	$\pm$0.95	$\pm$2.14
0.175	9.389 (7.139) $\pm$ 0.015	41.04 (31.68) $\pm$ 1.29	0.96 (20.4)	$\pm$1.26	$\pm$0.96	$\pm$2.04
0.153	8.216 (6.239) $\pm$ 0.014	39.50 (30.60) $\pm$ 1.36	0.83 (18.6)	$\pm$1.18	$\pm$1.13	$\pm$2.13
0.131	7.045 (5.342) $\pm$ 0.012	38.08 (29.47) $\pm$ 1.31	0.68 (16.6)	$\pm$1.07	$\pm$1.20	$\pm$2.08
0.109	5.871 (4.439) $\pm$ 0.009	36.53 (28.20) $\pm$ 1.30	0.54 (14.7)	$\pm$1.08	$\pm$1.31	$\pm$2.14
0.087	4.697 (3.532) $\pm$ 0.007	35.06 (27.06) $\pm$ 1.31	0.51 (12.4)	$\pm$1.03	$\pm$1.57	$\pm$2.29
0.066	3.547 (2.756) $\pm$ 0.005	32.64 (25.34) $\pm$ 1.37	0.46 (10.4)	$\pm$1.02	$\pm$1.72	$\pm$2.42

Table A.6: NBD fit results in centrality 25-35%.

$\delta\eta$	$\langle\mu_c\rangle(\langle\mu\rangle)$	$\langle k_c\rangle(\langle k\rangle)$	$\langle\chi^2/NDF\rangle(\langle NDF\rangle)$	$\delta\langle k_c\rangle(dead)$	$\delta\langle k_c\rangle(fake)$	$\delta\langle k_c\rangle(total)$
0.700	30.796 (23.836) $\pm$ 0.065	41.09 (31.80) $\pm$ 1.05	0.77 (48.0)	$\pm$1.99	$\pm$0.38	$\pm$2.28
0.678	29.940 (23.193) $\pm$ 0.063	41.40 (32.07) $\pm$ 1.06	0.83 (48.9)	$\pm$1.53	$\pm$0.13	$\pm$1.87
0.656	28.970 (22.412) $\pm$ 0.062	41.18 (31.85) $\pm$ 1.07	0.81 (47.9)	$\pm$1.52	$\pm$0.55	$\pm$1.94
0.634	27.967 (21.605) $\pm$ 0.060	41.07 (31.73) $\pm$ 1.09	0.84 (46.8)	$\pm$1.36	$\pm$0.47	$\pm$1.81
0.613	26.977 (20.823) $\pm$ 0.059	40.97 (31.62) $\pm$ 1.11	0.85 (45.4)	$\pm$1.15	$\pm$0.55	$\pm$1.69
0.591	26.003 (20.068) $\pm$ 0.058	40.72 (31.42) $\pm$ 1.12	0.88 (44.1)	$\pm$1.23	$\pm$0.36	$\pm$1.71
0.569	25.020 (19.289) $\pm$ 0.056	40.64 (31.33) $\pm$ 1.15	0.89 (42.6)	$\pm$1.43	$\pm$0.53	$\pm$1.91
0.547	24.036 (18.502) $\pm$ 0.055	40.41 (31.11) $\pm$ 1.17	0.91 (41.1)	$\pm$1.35	$\pm$0.55	$\pm$1.87
0.525	23.058 (17.722) $\pm$ 0.053	40.37 (31.03) $\pm$ 1.20	0.91 (40.0)	$\pm$1.37	$\pm$0.44	$\pm$1.87
0.503	22.086 (16.943) $\pm$ 0.052	40.25 (30.88) $\pm$ 1.23	0.90 (38.8)	$\pm$1.54	$\pm$0.55	$\pm$2.05
0.481	21.108 (16.155) $\pm$ 0.050	40.05 (30.66) $\pm$ 1.26	0.91 (37.2)	$\pm$1.56	$\pm$0.48	$\pm$2.07
0.459	20.126 (15.356) $\pm$ 0.049	40.00 (30.53) $\pm$ 1.30	0.92 (35.9)	$\pm$1.59	$\pm$0.39	$\pm$2.09
0.438	19.143 (14.554) $\pm$ 0.047	39.77 (30.26) $\pm$ 1.34	0.92 (34.6)	$\pm$1.62	$\pm$0.42	$\pm$2.15
0.416	18.163 (13.755) $\pm$ 0.046	39.51 (29.96) $\pm$ 1.38	0.88 (33.3)	$\pm$1.70	$\pm$0.52	$\pm$2.25
0.394	17.184 (12.962) $\pm$ 0.044	39.36 (29.73) $\pm$ 1.44	0.91 (31.8)	$\pm$1.72	$\pm$0.50	$\pm$2.29
0.372	16.206 (12.172) $\pm$ 0.043	39.43 (29.67) $\pm$ 1.50	0.95 (30.6)	$\pm$1.64	$\pm$0.43	$\pm$2.27
0.350	15.249 (11.420) $\pm$ 0.029	39.31 (29.50) $\pm$ 1.11	0.98 (29.2)	$\pm$1.63	$\pm$0.51	$\pm$2.04
0.328	14.299 (10.736) $\pm$ 0.028	38.92 (29.31) $\pm$ 1.14	1.00 (27.9)	$\pm$1.55	$\pm$0.53	$\pm$2.00
0.306	13.362 (10.063) $\pm$ 0.027	38.24 (28.93) $\pm$ 1.18	0.97 (26.5)	$\pm$1.56	$\pm$0.56	$\pm$2.04
0.284	12.422 (9.381) $\pm$ 0.026	37.66 (28.62) $\pm$ 1.22	0.95 (25.2)	$\pm$1.48	$\pm$0.63	$\pm$2.02
0.263	11.476 (8.689) $\pm$ 0.024	37.27 (28.42) $\pm$ 1.28	0.97 (23.9)	$\pm$1.35	$\pm$0.59	$\pm$1.95
0.241	10.531 (7.990) $\pm$ 0.023	36.55 (27.96) $\pm$ 1.33	0.91 (22.4)	$\pm$1.35	$\pm$0.60	$\pm$1.99
0.219	9.581 (7.281) $\pm$ 0.018	35.75 (27.42) $\pm$ 1.13	0.78 (21.0)	$\pm$1.21	$\pm$0.67	$\pm$1.78
0.197	8.626 (6.560) $\pm$ 0.017	35.01 (26.95) $\pm$ 1.19	0.73 (19.3)	$\pm$1.15	$\pm$0.74	$\pm$1.81
0.175	7.670 (5.832) $\pm$ 0.013	34.26 (26.41) $\pm$ 1.09	0.63 (17.6)	$\pm$1.20	$\pm$0.74	$\pm$1.78
0.153	6.712 (5.099) $\pm$ 0.013	33.65 (25.96) $\pm$ 1.19	0.59 (16.0)	$\pm$1.12	$\pm$0.82	$\pm$1.82
0.131	5.756 (4.365) $\pm$ 0.010	32.98 (25.42) $\pm$ 1.16	0.53 (14.3)	$\pm$0.98	$\pm$0.85	$\pm$1.74
0.109	4.800 (3.629) $\pm$ 0.009	31.80 (24.50) $\pm$ 1.17	0.48 (12.4)	$\pm$1.01	$\pm$0.95	$\pm$1.82
0.087	3.841 (2.888) $\pm$ 0.006	30.92 (23.78) $\pm$ 1.17	0.54 (10.7)	$\pm$0.94	$\pm$1.11	$\pm$1.87
0.066	2.902 (2.255) $\pm$ 0.005	28.55 (22.23) $\pm$ 1.20	0.47 (9.0)	$\pm$0.98	$\pm$1.24	$\pm$1.98

Table A.7: NBD fit results in centrality 30-40%.

$\delta\eta$	$\langle\mu_c\rangle(\langle\mu\rangle)$	$\langle k_c\rangle(\langle k\rangle)$	$\langle\chi^2/NDF\rangle(\langle NDF\rangle)$	$\delta\langle k_c\rangle(dead)$	$\delta\langle k_c\rangle(fake)$	$\delta\langle k_c\rangle(total)$
0.700	24.860 (19.241) ± 0.058	34.21 (26.48) ± 0.88	0.75 (47.0)	±1.14	±0.33	±1.47
0.678	24.177 (18.729) ± 0.057	34.00 (26.34) ± 0.88	0.77 (45.9)	±1.12	±0.30	±1.46
0.656	23.382 (18.088) ± 0.055	33.88 (26.21) ± 0.90	0.81 (44.2)	±0.91	±0.29	±1.31
0.634	22.573 (17.438) ± 0.054	33.73 (26.06) ± 0.91	0.90 (42.5)	±1.10	±0.25	±1.45
0.613	21.776 (16.808) ± 0.053	33.63 (25.96) ± 0.93	0.94 (40.9)	±1.08	±0.27	±1.44
0.591	20.986 (16.195) ± 0.051	33.54 (25.89) ± 0.94	0.92 (39.8)	±0.97	±0.25	±1.38
0.569	20.198 (15.571) ± 0.050	33.46 (25.80) ± 0.97	0.97 (38.4)	±1.04	±0.26	±1.44
0.547	19.406 (14.937) ± 0.049	33.43 (25.74) ± 0.99	1.01 (37.2)	±1.04	±0.24	±1.45
0.525	18.616 (14.307) ± 0.048	33.48 (25.74) ± 1.02	1.03 (36.0)	±1.04	±0.25	±1.48
0.503	17.830 (13.678) ± 0.046	33.37 (25.61) ± 1.05	1.06 (34.7)	±1.07	±0.28	±1.52
0.481	17.040 (13.040) ± 0.045	33.31 (25.51) ± 1.08	1.03 (33.4)	±1.11	±0.28	±1.58
0.459	16.246 (12.395) ± 0.043	33.30 (25.43) ± 1.12	1.04 (32.2)	±1.03	±0.28	±1.55
0.438	15.451 (11.746) ± 0.042	33.14 (25.23) ± 1.16	1.03 (31.0)	±1.09	±0.34	±1.63
0.416	14.662 (11.103) ± 0.041	32.95 (24.99) ± 1.20	0.97 (29.7)	±1.18	±0.38	±1.73
0.394	13.869 (10.461) ± 0.040	32.84 (24.83) ± 1.25	0.99 (28.4)	±1.21	±0.33	±1.77
0.372	13.081 (9.824) ± 0.038	32.69 (24.61) ± 1.30	1.00 (26.8)	±1.08	±0.36	±1.73
0.350	12.306 (9.216) ± 0.026	32.49 (24.40) ± 0.95	1.00 (25.5)	±1.05	±0.35	±1.46
0.328	11.540 (8.663) ± 0.025	31.92 (24.08) ± 0.98	0.99 (24.2)	±1.05	±0.36	±1.48
0.306	10.781 (8.119) ± 0.024	31.35 (23.78) ± 1.00	0.94 (23.1)	±1.05	±0.36	±1.49
0.284	10.020 (7.565) ± 0.023	30.76 (23.49) ± 1.04	0.91 (22.0)	±1.01	±0.35	±1.49
0.263	9.258 (7.008) ± 0.022	30.22 (23.20) ± 1.07	0.83 (20.8)	±0.93	±0.36	±1.46
0.241	8.494 (6.443) ± 0.021	29.75 (22.94) ± 1.12	0.77 (19.5)	±0.91	±0.39	±1.49
0.219	7.727 (5.870) ± 0.016	29.20 (22.62) ± 0.95	0.70 (18.3)	±0.85	±0.37	±1.33
0.197	6.958 (5.290) ± 0.015	28.62 (22.29) ± 1.01	0.65 (17.0)	±0.76	±0.38	±1.32
0.175	6.187 (4.702) ± 0.012	27.94 (21.88) ± 0.93	0.59 (15.5)	±0.83	±0.46	±1.33
0.153	5.416 (4.112) ± 0.011	27.29 (21.40) ± 1.00	0.50 (14.0)	±0.84	±0.56	±1.42
0.131	4.645 (3.520) ± 0.009	26.74 (20.98) ± 0.99	0.50 (12.5)	±0.81	±0.60	±1.41
0.109	3.873 (2.926) ± 0.008	25.80 (20.22) ± 1.01	0.50 (10.9)	±0.86	±0.66	±1.48
0.087	3.098 (2.328) ± 0.006	24.72 (19.40) ± 1.02	0.54 (9.4)	±0.75	±0.74	±1.46
0.066	2.341 (1.819) ± 0.004	22.77 (17.95) ± 1.02	0.49 (8.0)	±0.64	±0.81	±1.45

Table A.8: NBD fit results in centrality 35-45%.

$\delta\eta$	$\langle\mu_c\rangle(\langle\mu\rangle)$	$\langle k_c\rangle(\langle k\rangle)$	$\langle\chi^2/NDF\rangle(\langle NDF\rangle)$	$\delta\langle k_c\rangle(dead)$	$\delta\langle k_c\rangle(fake)$	$\delta\langle k_c\rangle(total)$
0.700	19.726 (15.268) ± 0.051	29.23 (22.62) ± 0.80	1.12 (40.0)	±0.69	±0.09	±1.06
0.678	19.191 (14.867) ± 0.050	29.24 (22.65) ± 0.81	1.02 (39.0)	±0.58	±0.17	±1.01
0.656	18.568 (14.364) ± 0.049	29.05 (22.47) ± 0.82	0.98 (38.2)	±0.76	±0.16	±1.13
0.634	17.920 (13.844) ± 0.048	29.04 (22.43) ± 0.83	1.09 (37.1)	±0.73	±0.13	±1.12
0.613	17.291 (13.348) ± 0.046	28.91 (22.31) ± 0.85	1.06 (36.2)	±0.77	±0.10	±1.15
0.591	16.672 (12.867) ± 0.045	28.64 (22.10) ± 0.86	1.04 (35.3)	±0.86	±0.20	±1.23
0.569	16.044 (12.369) ± 0.044	28.57 (22.02) ± 0.88	1.06 (34.2)	±0.79	±0.18	±1.20
0.547	15.417 (11.867) ± 0.043	28.48 (21.92) ± 0.90	1.07 (33.3)	±0.91	±0.24	±1.30
0.525	14.789 (11.366) ± 0.042	28.48 (21.89) ± 0.92	1.12 (32.2)	±0.88	±0.21	±1.29
0.503	14.165 (10.866) ± 0.041	28.36 (21.76) ± 0.94	1.10 (31.2)	±0.82	±0.21	±1.26
0.481	13.537 (10.360) ± 0.040	28.27 (21.64) ± 0.97	1.11 (29.9)	±0.85	±0.20	±1.31
0.459	12.908 (9.849) ± 0.039	28.14 (21.47) ± 1.00	1.11 (28.8)	±0.92	±0.21	±1.38
0.438	12.276 (9.334) ± 0.037	28.00 (21.28) ± 1.03	1.10 (27.7)	±0.88	±0.23	±1.37
0.416	11.648 (8.822) ± 0.036	27.82 (21.07) ± 1.06	1.08 (26.6)	±0.89	±0.23	±1.40
0.394	11.019 (8.313) ± 0.035	27.61 (20.83) ± 1.09	1.04 (25.5)	±0.96	±0.26	±1.47
0.372	10.391 (7.805) ± 0.034	27.49 (20.65) ± 1.13	0.98 (24.5)	±0.85	±0.26	±1.44
0.350	9.774 (7.322) ± 0.023	27.32 (20.46) ± 0.83	0.92 (23.4)	±0.81	±0.21	±1.18
0.328	9.165 (6.883) ± 0.022	26.94 (20.23) ± 0.85	0.89 (22.4)	±0.75	±0.21	±1.15
0.306	8.562 (6.451) ± 0.021	26.60 (20.05) ± 0.87	0.86 (21.4)	±0.72	±0.16	±1.14
0.284	7.959 (6.013) ± 0.020	26.19 (19.83) ± 0.90	0.82 (20.2)	±0.73	±0.21	±1.18
0.263	7.353 (5.569) ± 0.019	25.80 (19.62) ± 0.93	0.75 (19.3)	±0.73	±0.22	±1.21
0.241	6.748 (5.122) ± 0.018	25.24 (19.28) ± 0.97	0.65 (18.3)	±0.80	±0.29	±1.29
0.219	6.138 (4.666) ± 0.014	24.84 (19.05) ± 0.83	0.63 (17.1)	±0.61	±0.29	±1.07
0.197	5.527 (4.205) ± 0.013	24.45 (18.82) ± 0.88	0.61 (15.9)	±0.62	±0.28	±1.11
0.175	4.915 (3.739) ± 0.011	24.05 (18.53) ± 0.81	0.62 (14.7)	±0.55	±0.30	±1.03
0.153	4.303 (3.270) ± 0.010	23.55 (18.15) ± 0.88	0.57 (13.3)	±0.60	±0.37	±1.13
0.131	3.691 (2.801) ± 0.008	22.88 (17.57) ± 0.85	0.53 (11.8)	±0.59	±0.38	±1.11
0.109	3.076 (2.328) ± 0.007	22.21 (16.99) ± 0.88	0.56 (10.4)	±0.51	±0.41	±1.10
0.087	2.461 (1.851) ± 0.005	21.27 (16.15) ± 0.89	0.61 (8.9)	±0.56	±0.47	±1.16
0.066	1.859 (1.445) ± 0.004	19.60 (14.74) ± 0.92	0.59 (7.4)	±0.70	±0.52	±1.27

Table A.9: NBD fit results in centrality 40-50%.

$\delta\eta$	$\langle\mu_c\rangle(\langle\mu\rangle)$	$\langle k_c\rangle(\langle k\rangle)$	$\langle\chi^2/NDF\rangle(\langle NDF\rangle)$	$\delta\langle k_c\rangle(dead)$	$\delta\langle k_c\rangle(fake)$	$\delta\langle k_c\rangle(total)$
0.700	15.446 (11.955) ± 0.044	23.99 (18.57) ± 0.65	1.07 (36.0)	±1.02	±0.17	±1.22
0.678	15.032 (11.644) ± 0.043	23.87 (18.49) ± 0.66	1.08 (35.1)	±0.64	±0.18	±0.93
0.656	14.534 (11.243) ± 0.042	24.03 (18.59) ± 0.68	1.24 (34.0)	±0.61	±0.06	±0.91
0.634	14.033 (10.841) ± 0.041	24.11 (18.63) ± 0.69	1.25 (33.2)	±0.78	±0.16	±1.06
0.613	13.547 (10.457) ± 0.041	23.98 (18.51) ± 0.71	1.18 (32.4)	±0.77	±0.17	±1.06
0.591	13.055 (10.075) ± 0.040	23.97 (18.50) ± 0.73	1.15 (31.6)	±0.80	±0.16	±1.09
0.569	12.561 (9.684) ± 0.038	23.89 (18.42) ± 0.74	1.16 (30.8)	±0.68	±0.14	±1.02
0.547	12.072 (9.293) ± 0.037	23.70 (18.24) ± 0.76	1.09 (30.2)	±0.74	±0.14	±1.07
0.525	11.583 (8.903) ± 0.037	23.65 (18.17) ± 0.78	1.02 (29.3)	±0.63	±0.12	±1.01
0.503	11.093 (8.510) ± 0.036	23.66 (18.15) ± 0.81	1.05 (28.1)	±0.65	±0.15	±1.05
0.481	10.600 (8.112) ± 0.035	23.64 (18.09) ± 0.83	1.00 (27.3)	±0.66	±0.17	±1.08
0.459	10.106 (7.711) ± 0.034	23.56 (17.98) ± 0.86	0.95 (26.2)	±0.58	±0.16	±1.05
0.438	9.610 (7.306) ± 0.033	23.42 (17.81) ± 0.89	0.86 (25.2)	±0.60	±0.14	±1.08
0.416	9.116 (6.904) ± 0.032	23.27 (17.62) ± 0.92	0.80 (23.9)	±0.67	±0.18	±1.15
0.394	8.620 (6.503) ± 0.030	23.36 (17.62) ± 0.96	0.81 (22.9)	±0.55	±0.17	±1.12
0.372	8.131 (6.107) ± 0.029	23.21 (17.44) ± 1.00	0.72 (22.0)	±0.62	±0.18	±1.19
0.350	7.652 (5.731) ± 0.020	22.92 (17.18) ± 0.73	0.64 (20.9)	±0.77	±0.24	±1.08
0.328	7.176 (5.388) ± 0.019	22.61 (17.05) ± 0.76	0.63 (19.8)	±0.74	±0.21	±1.08
0.306	6.706 (5.050) ± 0.018	22.30 (16.92) ± 0.78	0.62 (18.8)	±0.70	±0.20	±1.07
0.284	6.235 (4.708) ± 0.018	22.05 (16.82) ± 0.81	0.60 (18.0)	±0.65	±0.20	±1.06
0.263	5.762 (4.362) ± 0.017	21.72 (16.65) ± 0.85	0.59 (17.0)	±0.61	±0.22	±1.06
0.241	5.287 (4.011) ± 0.016	21.38 (16.47) ± 0.89	0.60 (16.0)	±0.55	±0.23	±1.07
0.219	4.811 (3.656) ± 0.012	20.89 (16.16) ± 0.76	0.57 (14.9)	±0.58	±0.24	±0.98
0.197	4.333 (3.295) ± 0.012	20.52 (15.95) ± 0.81	0.53 (13.9)	±0.51	±0.25	±0.99
0.175	3.852 (2.929) ± 0.009	20.17 (15.72) ± 0.76	0.54 (12.8)	±0.49	±0.28	±0.94
0.153	3.372 (2.561) ± 0.009	19.78 (15.44) ± 0.82	0.51 (11.6)	±0.45	±0.28	±0.98
0.131	2.891 (2.192) ± 0.007	19.34 (15.10) ± 0.81	0.49 (10.6)	±0.43	±0.28	±0.96
0.109	2.410 (1.821) ± 0.006	18.81 (14.69) ± 0.85	0.46 (9.3)	±0.36	±0.33	±0.98
0.087	1.928 (1.449) ± 0.004	18.14 (14.19) ± 0.87	0.48 (7.9)	±0.38	±0.35	±1.01
0.066	1.456 (1.131) ± 0.004	17.03 (13.51) ± 0.91	0.48 (6.6)	±0.32	±0.35	±1.03

Table A.10: NBD fit results in centrality 45-55%.

$\delta\eta$	$\langle\mu_c\rangle(\langle\mu\rangle)$	$\langle k_c\rangle(\langle k\rangle)$	$\langle\chi^2/NDF\rangle(\langle NDF\rangle)$	$\delta\langle k_c\rangle(dead)$	$\delta\langle k_c\rangle(fake)$	$\delta\langle k_c\rangle(total)$
0.700	11.838 (9.163) ± 0.038	20.15 (15.59) ± 0.61	1.14 (28.0)	±0.71	±0.06	±0.94
0.678	11.517 (8.922) ± 0.037	20.06 (15.54) ± 0.61	1.10 (27.9)	±0.60	±0.03	±0.86
0.656	11.142 (8.620) ± 0.036	19.94 (15.43) ± 0.62	1.10 (26.6)	±0.48	±0.08	±0.79
0.634	10.759 (8.311) ± 0.035	19.94 (15.40) ± 0.64	1.08 (25.8)	±0.47	±0.11	±0.80
0.613	10.380 (8.013) ± 0.035	19.99 (15.43) ± 0.65	1.06 (24.9)	±0.51	±0.08	±0.83
0.591	10.005 (7.721) ± 0.034	19.95 (15.39) ± 0.67	1.06 (24.1)	±0.41	±0.11	±0.79
0.569	9.629 (7.424) ± 0.033	19.85 (15.30) ± 0.68	1.05 (23.2)	±0.44	±0.10	±0.82
0.547	9.254 (7.123) ± 0.032	19.76 (15.21) ± 0.70	1.04 (22.5)	±0.47	±0.12	±0.85
0.525	8.879 (6.824) ± 0.031	19.73 (15.16) ± 0.72	1.02 (21.8)	±0.42	±0.11	±0.84
0.503	8.505 (6.525) ± 0.030	19.69 (15.10) ± 0.74	0.96 (21.4)	±0.42	±0.13	±0.86
0.481	8.130 (6.222) ± 0.030	19.63 (15.02) ± 0.76	0.89 (20.7)	±0.44	±0.14	±0.89
0.459	7.751 (5.915) ± 0.029	19.62 (14.97) ± 0.79	0.77 (20.1)	±0.49	±0.14	±0.94
0.438	7.370 (5.604) ± 0.028	19.66 (14.95) ± 0.82	0.66 (19.6)	±0.49	±0.14	±0.96
0.416	6.991 (5.295) ± 0.027	19.74 (14.95) ± 0.85	0.63 (18.8)	±0.49	±0.16	±1.00
0.394	6.612 (4.988) ± 0.026	19.80 (14.94) ± 0.89	0.62 (18.1)	±0.55	±0.17	±1.06
0.372	6.236 (4.684) ± 0.025	19.79 (14.86) ± 0.93	0.58 (17.3)	±0.56	±0.17	±1.10
0.350	5.868 (4.395) ± 0.017	19.74 (14.79) ± 0.69	0.58 (16.7)	±0.55	±0.20	±0.91
0.328	5.502 (4.131) ± 0.017	19.58 (14.75) ± 0.72	0.62 (16.1)	±0.52	±0.21	±0.91
0.306	5.141 (3.872) ± 0.016	19.30 (14.66) ± 0.74	0.62 (15.5)	±0.51	±0.19	±0.92
0.284	4.780 (3.610) ± 0.015	18.97 (14.51) ± 0.78	0.59 (14.9)	±0.47	±0.17	±0.93
0.263	4.418 (3.345) ± 0.015	18.76 (14.44) ± 0.82	0.61 (14.2)	±0.48	±0.21	±0.97
0.241	4.056 (3.077) ± 0.014	18.53 (14.33) ± 0.87	0.59 (13.6)	±0.48	±0.19	±1.01
0.219	3.689 (2.803) ± 0.011	18.38 (14.30) ± 0.76	0.61 (13.0)	±0.49	±0.19	±0.93
0.197	3.321 (2.526) ± 0.010	18.29 (14.30) ± 0.83	0.60 (12.2)	±0.44	±0.20	±0.96
0.175	2.953 (2.244) ± 0.008	18.03 (14.17) ± 0.79	0.56 (11.4)	±0.52	±0.20	±0.97
0.153	2.583 (1.962) ± 0.007	17.80 (14.06) ± 0.89	0.55 (10.4)	±0.46	±0.22	±1.02
0.131	2.215 (1.678) ± 0.006	17.55 (13.94) ± 0.92	0.57 (9.3)	±0.34	±0.24	±1.00
0.109	1.846 (1.394) ± 0.005	17.10 (13.66) ± 0.98	0.56 (8.2)	±0.34	±0.29	±1.08
0.087	1.477 (1.109) ± 0.004	16.55 (13.29) ± 1.05	0.51 (7.0)	±0.29	±0.27	±1.12
0.066	1.117 (0.875) ± 0.003	16.05 (12.98) ± 1.09	0.51 (5.8)	±0.26	±0.34	±1.17

Table A.11: NBD fit results in centrality 50-60%.

$\delta\eta$	$\langle\mu_c\rangle(\langle\mu\rangle)$	$\langle k_c\rangle(\langle k\rangle)$	$\langle\chi^2/NDF\rangle(\langle NDF\rangle)$	$\delta\langle k_c\rangle(dead)$	$\delta\langle k_c\rangle(fake)$	$\delta\langle k_c\rangle(total)$
0.700	4.508 (3.489) ± 0.023	8.89 (6.88) ± 0.29	0.90 (15.0)	±0.21	±0.01	±0.35
0.678	4.387 (3.398) ± 0.022	8.85 (6.85) ± 0.29	0.90 (14.8)	±0.23	±0.01	±0.37
0.656	4.248 (3.286) ± 0.022	8.78 (6.79) ± 0.29	0.76 (14.2)	±0.25	±0.01	±0.39
0.634	4.102 (3.169) ± 0.021	8.74 (6.75) ± 0.30	0.76 (13.9)	±0.26	±0.01	±0.39
0.613	3.954 (3.052) ± 0.021	8.81 (6.80) ± 0.31	1.14 (13.4)	±0.23	±0.01	±0.38
0.591	3.813 (2.942) ± 0.020	8.67 (6.69) ± 0.31	0.91 (13.1)	±0.24	±0.01	±0.39
0.569	3.666 (2.827) ± 0.020	8.66 (6.67) ± 0.32	0.96 (12.9)	±0.27	±0.02	±0.42
0.547	3.518 (2.708) ± 0.019	8.78 (6.76) ± 0.33	1.19 (12.5)	±0.21	±0.01	±0.40
0.525	3.378 (2.596) ± 0.019	8.67 (6.66) ± 0.34	0.93 (12.0)	±0.21	±0.01	±0.40
0.503	3.236 (2.482) ± 0.018	8.67 (6.65) ± 0.35	0.86 (11.8)	±0.25	±0.01	±0.43
0.481	3.091 (2.366) ± 0.018	8.71 (6.67) ± 0.36	0.88 (11.6)	±0.23	±0.02	±0.43
0.459	2.949 (2.250) ± 0.017	8.67 (6.62) ± 0.37	0.80 (11.1)	±0.20	±0.02	±0.42
0.438	2.806 (2.133) ± 0.017	8.63 (6.56) ± 0.39	0.76 (10.5)	±0.20	±0.03	±0.44
0.416	2.664 (2.017) ± 0.017	8.58 (6.50) ± 0.40	0.65 (9.9)	±0.24	±0.03	±0.47
0.394	2.520 (1.901) ± 0.016	8.60 (6.49) ± 0.42	0.64 (9.5)	±0.23	±0.02	±0.48
0.372	2.376 (1.785) ± 0.015	8.69 (6.54) ± 0.45	0.75 (8.9)	±0.26	±0.02	±0.52
0.350	2.236 (1.675) ± 0.011	8.77 (6.57) ± 0.34	0.73 (8.5)	±0.25	±0.02	±0.43
0.328	2.097 (1.575) ± 0.010	8.75 (6.58) ± 0.36	0.69 (8.1)	±0.25	±0.02	±0.44
0.306	1.960 (1.476) ± 0.010	8.74 (6.61) ± 0.38	0.74 (7.6)	±0.22	±0.03	±0.44
0.284	1.822 (1.376) ± 0.009	8.71 (6.63) ± 0.41	0.75 (7.1)	±0.23	±0.03	±0.47
0.263	1.683 (1.274) ± 0.009	8.70 (6.67) ± 0.44	0.78 (6.7)	±0.21	±0.03	±0.49
0.241	1.545 (1.172) ± 0.008	8.66 (6.67) ± 0.47	0.75 (6.3)	±0.19	±0.03	±0.51
0.219	1.407 (1.069) ± 0.006	8.55 (6.62) ± 0.41	0.70 (5.9)	±0.18	±0.03	±0.45
0.197	1.267 (0.963) ± 0.006	8.45 (6.57) ± 0.45	0.59 (5.5)	±0.18	±0.03	±0.48
0.175	1.126 (0.856) ± 0.005	8.41 (6.59) ± 0.44	0.59 (5.2)	±0.15	±0.04	±0.47
0.153	0.986 (0.749) ± 0.005	8.31 (6.54) ± 0.50	0.58 (4.8)	±0.14	±0.05	±0.52
0.131	0.846 (0.641) ± 0.004	8.07 (6.36) ± 0.52	0.52 (4.4)	±0.16	±0.06	±0.55
0.109	0.706 (0.534) ± 0.003	7.85 (6.21) ± 0.54	0.40 (3.8)	±0.08	±0.07	±0.55
0.087	0.565 (0.424) ± 0.002	7.86 (6.23) ± 0.64	0.58 (3.3)	±0.06	±0.09	±0.65
0.066	0.428 (0.339) ± 0.002	7.22 (5.77) ± 0.64	0.44 (2.9)	±0.06	±0.07	±0.65

Table A.12: NBD fit results in centrality 55-65%.

$\delta\eta$	$\langle\mu_c\rangle(\langle\mu\rangle)$	$\langle k_c\rangle(\langle k\rangle)$	$\langle\chi^2/NDF\rangle(\langle NDF\rangle)$	$\delta\langle k_c\rangle(dead)$	$\delta\langle k_c\rangle(fake)$	$\delta\langle k_c\rangle(total)$
0.700	3.086 (2.389) ± 0.019	5.90 (4.56) ± 0.20	0.76 (13.0)	±0.25	±0.01	±0.32
0.678	3.000 (2.324) ± 0.019	5.88 (4.56) ± 0.20	0.79 (12.7)	±0.13	±0.01	±0.24
0.656	2.902 (2.245) ± 0.018	5.85 (4.52) ± 0.20	0.76 (12.5)	±0.14	±0.02	±0.24
0.634	2.803 (2.166) ± 0.018	5.78 (4.46) ± 0.20	0.69 (12.2)	±0.14	±0.02	±0.25
0.613	2.703 (2.086) ± 0.017	5.80 (4.48) ± 0.21	0.78 (12.1)	±0.07	±0.02	±0.22
0.591	2.607 (2.012) ± 0.017	5.76 (4.45) ± 0.21	0.70 (11.3)	±0.14	±0.02	±0.25
0.569	2.508 (1.934) ± 0.017	5.76 (4.44) ± 0.22	0.62 (10.9)	±0.13	±0.02	±0.25
0.547	2.410 (1.855) ± 0.016	5.75 (4.43) ± 0.23	0.55 (10.3)	±0.12	±0.04	±0.26
0.525	2.313 (1.777) ± 0.016	5.75 (4.42) ± 0.23	0.50 (9.9)	±0.16	±0.04	±0.28
0.503	2.215 (1.699) ± 0.015	5.76 (4.42) ± 0.24	0.47 (9.6)	±0.16	±0.01	±0.29
0.481	2.117 (1.620) ± 0.015	5.79 (4.43) ± 0.25	0.49 (9.2)	±0.16	±0.01	±0.30
0.459	2.018 (1.540) ± 0.015	5.78 (4.41) ± 0.26	0.49 (8.9)	±0.16	±0.01	±0.30
0.438	1.919 (1.459) ± 0.014	5.79 (4.40) ± 0.27	0.50 (8.8)	±0.17	±0.02	±0.32
0.416	1.820 (1.378) ± 0.014	5.81 (4.40) ± 0.28	0.52 (8.6)	±0.20	±0.03	±0.34
0.394	1.721 (1.298) ± 0.013	5.84 (4.41) ± 0.30	0.53 (8.4)	±0.15	±0.02	±0.34
0.372	1.623 (1.219) ± 0.013	5.84 (4.39) ± 0.32	0.54 (7.8)	±0.18	±0.01	±0.36
0.350	1.527 (1.144) ± 0.009	5.87 (4.41) ± 0.24	0.52 (7.6)	±0.21	±0.01	±0.32
0.328	1.432 (1.075) ± 0.008	5.86 (4.42) ± 0.25	0.49 (7.4)	±0.24	±0.02	±0.34
0.306	1.339 (1.008) ± 0.008	5.85 (4.43) ± 0.27	0.48 (7.2)	±0.21	±0.02	±0.34
0.284	1.244 (0.940) ± 0.008	5.85 (4.45) ± 0.28	0.52 (6.9)	±0.21	±0.02	±0.35
0.263	1.150 (0.871) ± 0.007	5.85 (4.48) ± 0.31	0.59 (6.5)	±0.14	±0.02	±0.34
0.241	1.056 (0.801) ± 0.007	5.83 (4.49) ± 0.33	0.59 (6.2)	±0.11	±0.02	±0.35
0.219	0.961 (0.730) ± 0.005	5.81 (4.50) ± 0.29	0.62 (5.9)	±0.10	±0.03	±0.31
0.197	0.866 (0.658) ± 0.005	5.73 (4.46) ± 0.32	0.57 (5.5)	±0.10	±0.03	±0.34
0.175	0.770 (0.585) ± 0.004	5.72 (4.46) ± 0.32	0.54 (5.2)	±0.10	±0.04	±0.33
0.153	0.674 (0.511) ± 0.004	5.67 (4.44) ± 0.36	0.53 (4.8)	±0.09	±0.06	±0.38
0.131	0.578 (0.438) ± 0.003	5.50 (4.32) ± 0.36	0.40 (4.5)	±0.05	±0.07	±0.37
0.109	0.482 (0.364) ± 0.003	5.31 (4.18) ± 0.39	0.51 (4.0)	±0.05	±0.10	±0.41
0.087	0.386 (0.292) ± 0.002	4.90 (3.89) ± 0.43	0.54 (3.6)	±0.05	±0.02	±0.43
0.066	0.292 (0.232) ± 0.002	4.56 (3.63) ± 0.44	0.57 (3.1)	±0.05	±0.05	±0.45

Table A.13: NBD fit results in centrality 0-5%.

$\delta\eta$	$\langle\mu_c\rangle(\langle\mu\rangle)$	$\langle k_c\rangle(\langle k\rangle)$	$\langle\chi^2/NDF\rangle(\langle NDF\rangle)$	$\delta\langle k_c\rangle(dead)$	$\delta\langle k_c\rangle(fake)$	$\delta\langle k_c\rangle(total)$
0.700	84.371 (65.303) ± 0.148	341.22 (264.10) ± 31.75	0.54 (58.0)	±54.10	±6.72	±63.09
0.678	82.149 (63.638) ± 0.144	359.73 (278.66) ± 35.51	0.58 (57.8)	±29.67	±26.46	±53.31
0.656	79.451 (61.463) ± 0.141	369.96 (286.25) ± 37.82	0.66 (56.4)	±13.85	±14.18	±42.69
0.634	76.740 (59.282) ± 0.138	370.46 (286.18) ± 38.62	0.63 (55.4)	±19.09	±14.98	±45.61
0.613	74.027 (57.142) ± 0.135	372.37 (287.35) ± 40.79	0.62 (54.7)	±13.54	±15.22	±45.60
0.591	71.331 (55.050) ± 0.133	374.07 (288.55) ± 42.84	0.64 (53.6)	±13.41	±17.15	±48.06
0.569	68.629 (52.910) ± 0.130	374.10 (288.36) ± 44.31	0.64 (52.7)	±18.44	±19.49	±51.80
0.547	65.925 (50.747) ± 0.127	367.65 (282.90) ± 44.42	0.64 (52.2)	±16.76	±24.95	±53.63
0.525	63.249 (48.612) ± 0.124	368.12 (282.88) ± 46.12	0.68 (51.2)	±16.19	±24.02	±54.46
0.503	60.566 (46.465) ± 0.121	364.03 (279.07) ± 46.64	0.65 (50.2)	±15.42	±23.48	±54.45
0.481	57.877 (44.295) ± 0.118	362.25 (277.19) ± 48.15	0.65 (49.0)	±12.93	±24.16	±55.40
0.459	55.171 (42.098) ± 0.115	363.40 (277.12) ± 50.80	0.66 (47.9)	±13.82	±20.65	±56.55
0.438	52.479 (39.900) ± 0.112	355.07 (269.86) ± 51.95	0.64 (46.5)	±9.95	±25.57	±58.75
0.416	49.791 (37.710) ± 0.109	352.80 (267.18) ± 54.68	0.66 (45.2)	±14.68	±26.89	±62.68
0.394	47.118 (35.547) ± 0.106	349.73 (263.69) ± 57.42	0.64 (43.6)	±13.29	±32.16	±67.14
0.372	44.456 (33.395) ± 0.103	347.01 (260.24) ± 64.15	0.65 (42.1)	±3.82	±30.09	±70.96
0.350	41.832 (31.335) ± 0.070	340.53 (254.77) ± 52.65	0.67 (40.6)	±11.74	±34.67	±64.13
0.328	39.229 (29.465) ± 0.068	340.79 (254.20) ± 55.01	0.65 (39.4)	±2.10	±27.89	±61.72
0.306	36.653 (27.626) ± 0.065	332.14 (246.66) ± 60.16	0.68 (37.9)	±12.90	±31.13	±68.95
0.284	34.073 (25.755) ± 0.062	333.98 (247.30) ± 64.64	0.69 (37.0)	±1.38	±33.33	±72.74
0.263	31.493 (23.870) ± 0.060	313.43 (230.73) ± 62.92	0.69 (35.2)	±1.26	±26.90	±68.44
0.241	28.903 (21.959) ± 0.057	294.86 (214.95) ± 59.84	0.68 (33.5)	±2.22	±32.24	±68.01
0.219	26.305 (20.020) ± 0.044	278.11 (200.81) ± 51.12	0.69 (31.9)	±3.21	±29.02	±58.87
0.197	23.677 (18.009) ± 0.042	253.36 (181.02) ± 56.29	0.71 (30.2)	±6.54	±23.20	±61.24
0.175	21.066 (16.025) ± 0.034	232.35 (165.72) ± 50.48	0.73 (28.3)	±3.92	±24.00	±56.04
0.153	18.425 (13.948) ± 0.032	199.21 (140.84) ± 48.99	0.75 (26.2)	±8.99	±17.20	±52.70
0.131	15.807 (11.964) ± 0.026	181.55 (126.91) ± 37.35	0.80 (24.2)	±10.43	±17.64	±42.61
0.109	13.174 (9.949) ± 0.022	157.69 (108.85) ± 28.73	0.83 (21.4)	±3.79	±14.86	±32.57
0.087	10.522 (7.808) ± 0.017	125.65 (86.76) ± 21.21	0.80 (18.2)	±3.14	±11.02	±24.10
0.066	7.947 (6.122) ± 0.013	97.74 (67.60) ± 13.55	0.73 (15.1)	±8.30	±9.98	±18.77

Table A.14: NBD fit results in centrality 5-10%.

$\delta\eta$	$\langle\mu_c\rangle(\langle\mu\rangle)$	$\langle k_c\rangle(\langle k\rangle)$	$\langle\chi^2/NDF\rangle(\langle NDF\rangle)$	$\delta\langle k_c\rangle(dead)$	$\delta\langle k_c\rangle(fake)$	$\delta\langle k_c\rangle(total)$
0.700	72.246 (55.918) ± 0.126	187.62 (145.22) ± 10.56	0.80 (61.0)	±1.88	±9.61	±14.40
0.678	70.291 (54.452) ± 0.124	185.02 (143.32) ± 10.61	0.68 (61.3)	±10.46	±6.69	±16.33
0.656	67.996 (52.602) ± 0.121	188.09 (145.50) ± 11.00	0.71 (59.8)	±4.99	±4.56	±12.91
0.634	65.656 (50.720) ± 0.119	188.72 (145.76) ± 11.29	0.76 (59.0)	±2.81	±6.48	±13.32
0.613	63.346 (48.897) ± 0.116	186.50 (143.95) ± 11.39	0.79 (57.0)	±4.55	±6.31	±13.79
0.591	61.055 (47.118) ± 0.114	185.01 (142.75) ± 11.53	0.76 (55.6)	±6.00	±5.32	±14.04
0.569	58.752 (45.296) ± 0.111	184.61 (142.29) ± 11.90	0.76 (54.0)	±4.96	±7.98	±15.16
0.547	56.443 (43.447) ± 0.108	183.38 (141.14) ± 12.28	0.78 (52.2)	±5.40	±8.57	±15.92
0.525	54.144 (41.614) ± 0.106	183.73 (141.18) ± 12.87	0.78 (51.2)	±5.90	±8.41	±16.47
0.503	51.839 (39.768) ± 0.103	186.84 (143.32) ± 13.65	0.81 (49.4)	±3.47	±7.23	±15.83
0.481	49.534 (37.909) ± 0.100	187.11 (143.19) ± 14.16	0.84 (47.9)	±3.90	±7.38	±16.44
0.459	47.220 (36.030) ± 0.097	189.72 (144.71) ± 15.07	0.88 (46.3)	±2.39	±7.36	±16.94
0.438	44.921 (34.153) ± 0.095	187.66 (142.61) ± 15.56	0.85 (44.6)	±8.12	±10.08	±20.24
0.416	42.618 (32.277) ± 0.092	188.72 (142.85) ± 16.50	0.86 (43.1)	±7.80	±7.74	±19.83
0.394	40.328 (30.425) ± 0.089	186.94 (140.87) ± 17.11	0.82 (41.6)	±5.86	±9.43	±20.40
0.372	38.053 (28.585) ± 0.086	186.28 (139.66) ± 18.10	0.85 (39.9)	±7.17	±9.93	±21.86
0.350	35.798 (26.815) ± 0.059	187.25 (139.96) ± 13.64	0.89 (38.5)	±5.58	±9.02	±17.28
0.328	33.572 (25.212) ± 0.057	184.92 (138.46) ± 14.19	0.89 (37.3)	±5.46	±12.28	±19.55
0.306	31.368 (23.631) ± 0.055	182.12 (136.56) ± 14.59	0.91 (36.0)	±5.25	±11.88	±19.53
0.284	29.158 (22.030) ± 0.052	178.29 (134.27) ± 14.70	0.89 (34.6)	±4.86	±13.82	±20.75
0.263	26.943 (20.408) ± 0.050	173.07 (131.50) ± 15.26	0.91 (33.1)	±5.84	±15.75	±22.69
0.241	24.731 (18.770) ± 0.048	169.01 (129.45) ± 15.73	0.88 (32.1)	±6.53	±15.73	±23.19
0.219	22.501 (17.102) ± 0.037	167.76 (129.28) ± 13.97	0.94 (30.7)	±3.27	±12.91	±19.31
0.197	20.271 (15.421) ± 0.035	160.25 (123.65) ± 14.29	0.94 (29.1)	±5.43	±15.13	±21.52
0.175	18.030 (13.713) ± 0.028	152.49 (118.31) ± 13.95	0.99 (27.4)	±5.87	±13.32	±20.16
0.153	15.787 (11.998) ± 0.026	144.71 (112.06) ± 13.58	1.00 (25.4)	±5.81	±15.35	±21.30
0.131	13.540 (10.276) ± 0.022	137.12 (106.29) ± 12.40	1.05 (22.9)	±5.42	±14.45	±19.80
0.109	11.289 (8.548) ± 0.018	122.24 (92.30) ± 10.92	1.09 (20.3)	±6.77	±14.31	±19.23
0.087	9.029 (6.805) ± 0.014	99.52 (72.96) ± 9.30	1.03 (17.2)	±5.46	±10.51	±15.06
0.066	6.807 (5.296) ± 0.011	75.37 (54.94) ± 6.89	0.81 (14.2)	±6.29	±8.08	±12.34

Table A.15: NBD fit results in centrality 10-15%.

$\delta\eta$	$\langle\mu_c\rangle(\langle\mu\rangle)$	$\langle k_c\rangle(\langle k\rangle)$	$\langle\chi^2/NDF\rangle(\langle NDF\rangle)$	$\delta\langle k_c\rangle(dead)$	$\delta\langle k_c\rangle(fake)$	$\delta\langle k_c\rangle(total)$
0.700	60.607 (46.909) ± 0.119	129.59 (100.31) ± 6.29	0.80 (58.0)	±1.29	±1.51	±6.60
0.678	59.026 (45.725) ± 0.118	123.34 (95.54) ± 6.09	0.76 (56.6)	±4.71	±9.77	±12.44
0.656	57.108 (44.179) ± 0.116	121.44 (93.94) ± 6.08	0.70 (55.3)	±5.55	±4.90	±9.58
0.634	55.139 (42.596) ± 0.113	121.88 (94.14) ± 6.24	0.70 (54.2)	±4.92	±3.01	±8.50
0.613	53.198 (41.064) ± 0.111	120.98 (93.37) ± 6.33	0.69 (52.9)	±5.23	±2.63	±8.62
0.591	51.256 (39.556) ± 0.108	120.49 (92.96) ± 6.46	0.71 (52.2)	±3.80	±3.87	±8.44
0.569	49.321 (38.025) ± 0.106	119.78 (92.31) ± 6.58	0.70 (51.3)	±3.61	±2.65	±7.95
0.547	47.393 (36.482) ± 0.103	117.86 (90.68) ± 6.62	0.71 (50.1)	±3.12	±3.60	±8.15
0.525	45.463 (34.943) ± 0.101	117.65 (90.38) ± 6.79	0.71 (49.2)	±3.77	±3.44	±8.49
0.503	43.535 (33.398) ± 0.098	117.79 (90.32) ± 7.03	0.71 (48.2)	±3.47	±4.14	±8.87
0.481	41.602 (31.839) ± 0.095	118.04 (90.30) ± 7.29	0.71 (46.9)	±3.18	±3.55	±8.71
0.459	39.668 (30.267) ± 0.092	118.96 (90.76) ± 7.64	0.73 (45.2)	±3.46	±4.65	±9.59
0.438	37.729 (28.684) ± 0.090	118.41 (90.03) ± 7.87	0.72 (44.0)	±3.52	±4.95	±9.94
0.416	35.787 (27.104) ± 0.087	118.19 (89.52) ± 8.24	0.74 (42.5)	±4.23	±5.06	±10.56
0.394	33.864 (25.547) ± 0.084	118.35 (89.25) ± 8.67	0.76 (41.1)	±4.60	±4.92	±10.98
0.372	31.943 (23.994) ± 0.082	118.19 (88.71) ± 9.20	0.75 (39.6)	±4.92	±5.31	±11.70
0.350	30.061 (22.517) ± 0.056	117.56 (87.92) ± 6.85	0.75 (38.1)	±4.91	±5.85	±10.26
0.328	28.191 (21.172) ± 0.053	117.37 (87.84) ± 7.21	0.78 (36.3)	±5.14	±5.41	±10.38
0.306	26.340 (19.845) ± 0.051	117.25 (87.95) ± 7.59	0.78 (34.7)	±4.90	±5.07	±10.36
0.284	24.493 (18.509) ± 0.049	117.01 (87.82) ± 8.16	0.82 (33.5)	±4.41	±5.83	±10.96
0.263	22.636 (17.150) ± 0.047	114.86 (86.40) ± 8.44	0.80 (31.8)	±5.74	±5.96	±11.82
0.241	20.776 (15.774) ± 0.044	114.37 (86.11) ± 8.95	0.82 (30.3)	±5.34	±6.20	±12.13
0.219	18.905 (14.375) ± 0.034	112.39 (84.83) ± 7.68	0.82 (28.8)	±5.37	±7.32	±11.89
0.197	17.029 (12.958) ± 0.033	111.32 (84.34) ± 8.15	0.83 (26.9)	±6.15	±7.47	±12.66
0.175	15.142 (11.519) ± 0.026	109.44 (83.15) ± 7.72	0.88 (25.1)	±5.22	±7.32	±11.85
0.153	13.253 (10.073) ± 0.024	106.03 (80.26) ± 8.35	0.94 (23.0)	±4.18	±6.94	±11.64
0.131	11.367 (8.626) ± 0.020	96.68 (72.34) ± 7.60	0.94 (20.5)	±4.30	±7.09	±11.25
0.109	9.474 (7.170) ± 0.017	88.58 (65.38) ± 7.20	0.87 (18.1)	±3.97	±8.10	±11.54
0.087	7.575 (5.704) ± 0.013	77.55 (55.69) ± 6.79	0.81 (15.6)	±3.54	±7.64	±10.82
0.066	5.714 (4.443) ± 0.010	64.41 (47.02) ± 6.22	0.63 (12.8)	±4.49	±6.13	±9.82

Table A.16: NBD fit results in centrality 15-20%.

$\delta\eta$	$\langle\mu_c\rangle(\langle\mu\rangle)$	$\langle k_c\rangle(\langle k\rangle)$	$\langle\chi^2/NDF\rangle(\langle NDF\rangle)$	$\delta\langle k_c\rangle(dead)$	$\delta\langle k_c\rangle(fake)$	$\delta\langle k_c\rangle(total)$
0.700	50.243 (38.888) ± 0.109	95.08 (73.59) ± 4.42	0.79 (53.0)	±4.84	±6.50	±9.23
0.678	48.892 (37.875) ± 0.106	95.76 (74.18) ± 4.54	0.67 (52.4)	±3.20	±1.41	±5.73
0.656	47.301 (36.592) ± 0.104	95.63 (73.98) ± 4.65	0.75 (51.2)	±2.80	±1.66	±5.68
0.634	45.685 (35.292) ± 0.102	95.70 (73.94) ± 4.78	0.71 (49.2)	±2.09	±1.96	±5.57
0.613	44.087 (34.031) ± 0.100	94.78 (73.17) ± 4.87	0.71 (47.7)	±3.79	±3.17	±6.94
0.591	42.483 (32.785) ± 0.097	95.97 (74.07) ± 5.05	0.70 (47.1)	±2.95	±1.99	±6.18
0.569	40.884 (31.519) ± 0.095	96.10 (74.10) ± 5.22	0.69 (46.1)	±2.66	±2.10	±6.22
0.547	39.301 (30.251) ± 0.092	95.92 (73.85) ± 5.36	0.70 (44.8)	±3.31	±2.60	±6.82
0.525	37.708 (28.981) ± 0.090	96.52 (74.20) ± 5.57	0.71 (43.6)	±3.47	±1.98	±6.85
0.503	36.108 (27.700) ± 0.088	96.81 (74.28) ± 5.77	0.75 (42.5)	±2.84	±2.39	±6.86
0.481	34.505 (26.406) ± 0.085	96.51 (73.88) ± 5.92	0.73 (41.4)	±2.38	±1.88	±6.65
0.459	32.897 (25.100) ± 0.083	95.50 (72.89) ± 6.03	0.73 (40.1)	±2.67	±2.54	±7.07
0.438	31.285 (23.784) ± 0.081	95.28 (72.47) ± 6.24	0.77 (38.6)	±2.78	±2.27	±7.19
0.416	29.677 (22.474) ± 0.078	95.11 (72.09) ± 6.45	0.78 (37.3)	±3.02	±2.26	±7.47
0.394	28.079 (21.180) ± 0.076	94.76 (71.57) ± 6.69	0.78 (35.9)	±2.98	±3.07	±7.94
0.372	26.483 (19.889) ± 0.073	95.08 (71.55) ± 7.04	0.81 (34.6)	±2.59	±2.66	±7.96
0.350	24.918 (18.661) ± 0.050	94.28 (70.78) ± 5.11	0.80 (33.3)	±3.11	±2.66	±6.55
0.328	23.365 (17.541) ± 0.048	92.98 (70.16) ± 5.28	0.82 (32.3)	±2.56	±2.78	±6.50
0.306	21.831 (16.441) ± 0.046	91.68 (69.59) ± 5.47	0.84 (31.2)	±2.32	±3.06	±6.69
0.284	20.294 (15.325) ± 0.044	89.06 (68.15) ± 5.60	0.85 (29.8)	±2.62	±3.13	±6.93
0.263	18.754 (14.199) ± 0.042	87.46 (67.23) ± 5.76	0.85 (28.5)	±2.47	±2.87	±6.90
0.241	17.215 (13.060) ± 0.040	86.16 (66.47) ± 6.04	0.88 (27.0)	±2.30	±3.25	±7.23
0.219	15.665 (11.902) ± 0.031	83.50 (64.86) ± 5.15	0.90 (25.4)	±3.27	±3.46	±7.01
0.197	14.110 (10.728) ± 0.029	81.20 (63.31) ± 5.36	0.88 (23.7)	±2.47	±3.88	±7.06
0.175	12.547 (9.540) ± 0.024	79.16 (61.58) ± 4.86	0.93 (21.9)	±2.06	±3.41	±6.28
0.153	10.977 (8.337) ± 0.022	73.67 (57.42) ± 4.99	0.91 (19.8)	±1.63	±3.89	±6.53
0.131	9.409 (7.133) ± 0.018	67.77 (52.73) ± 4.44	0.83 (17.8)	±2.00	±3.98	±6.29
0.109	7.840 (5.924) ± 0.015	61.02 (47.54) ± 4.01	0.74 (15.6)	±1.99	±4.09	±6.06
0.087	6.271 (4.713) ± 0.012	54.47 (42.05) ± 3.54	0.63 (13.4)	±1.64	±3.81	±5.46
0.066	4.734 (3.678) ± 0.009	47.73 (35.64) ± 3.59	0.58 (11.3)	±2.06	±3.33	±5.31

Table A.17: NBD fit results in centrality 20-25%.

$\delta\eta$	$\langle\mu_c\rangle(\langle\mu\rangle)$	$\langle k_c\rangle(\langle k\rangle)$	$\langle\chi^2/NDF\rangle(\langle NDF\rangle)$	$\delta\langle k_c\rangle(dead)$	$\delta\langle k_c\rangle(fake)$	$\delta\langle k_c\rangle(total)$
0.700	41.340 (31.997) ± 0.101	80.17 (62.05) ± 3.85	0.71 (48.0)	±1.34	±1.27	±4.27
0.678	40.233 (31.167) ± 0.099	80.14 (62.08) ± 3.92	0.67 (47.2)	±3.19	±1.69	±5.33
0.656	38.920 (30.109) ± 0.096	81.43 (63.00) ± 4.07	0.68 (46.9)	±1.52	±0.92	±4.44
0.634	37.606 (29.051) ± 0.094	81.18 (62.71) ± 4.17	0.68 (45.8)	±3.68	±1.51	±5.76
0.613	36.282 (28.006) ± 0.092	82.48 (63.67) ± 4.38	0.78 (44.7)	±1.90	±1.68	±5.07
0.591	34.986 (27.000) ± 0.090	81.78 (63.12) ± 4.43	0.76 (44.2)	±2.76	±1.37	±5.39
0.569	33.656 (25.947) ± 0.088	81.76 (63.04) ± 4.53	0.75 (43.4)	±1.38	±1.07	±4.86
0.547	32.342 (24.895) ± 0.086	81.09 (62.42) ± 4.60	0.68 (42.5)	±1.91	±1.56	±5.22
0.525	31.029 (23.848) ± 0.083	81.53 (62.67) ± 4.76	0.72 (41.5)	±1.98	±1.63	±5.40
0.503	29.714 (22.794) ± 0.081	81.92 (62.85) ± 4.93	0.77 (40.5)	±1.94	±1.10	±5.41
0.481	28.395 (21.731) ± 0.079	82.20 (62.93) ± 5.11	0.77 (39.3)	±2.21	±1.08	±5.67
0.459	27.071 (20.654) ± 0.077	82.39 (62.89) ± 5.33	0.79 (38.3)	±2.25	±1.31	±5.93
0.438	25.754 (19.579) ± 0.074	81.71 (62.18) ± 5.47	0.78 (37.1)	±2.79	±1.73	±6.38
0.416	24.428 (18.499) ± 0.072	82.61 (62.66) ± 5.83	0.82 (35.8)	±2.05	±1.10	±6.28
0.394	23.116 (17.436) ± 0.070	81.91 (61.93) ± 6.04	0.78 (34.6)	±2.84	±1.75	±6.90
0.372	21.803 (16.374) ± 0.068	82.06 (61.77) ± 6.34	0.78 (33.3)	±2.84	±1.94	±7.21
0.350	20.516 (15.364) ± 0.046	82.29 (61.74) ± 4.77	0.82 (32.1)	±3.10	±2.13	±6.08
0.328	19.244 (14.448) ± 0.044	81.98 (61.71) ± 4.99	0.82 (30.8)	±2.85	±2.02	±6.09
0.306	17.979 (13.542) ± 0.043	81.64 (61.65) ± 5.26	0.82 (29.7)	±3.02	±1.98	±6.38
0.284	16.715 (12.625) ± 0.041	80.08 (60.81) ± 5.43	0.83 (28.4)	±2.99	±2.30	±6.61
0.263	15.448 (11.697) ± 0.039	78.84 (60.25) ± 5.73	0.84 (26.9)	±3.19	±2.34	±6.96
0.241	14.177 (10.756) ± 0.037	77.06 (59.22) ± 5.98	0.86 (25.2)	±2.73	±2.06	±6.89
0.219	12.899 (9.802) ± 0.029	74.63 (57.61) ± 5.08	0.88 (23.8)	±2.84	±2.57	±6.36
0.197	11.616 (8.833) ± 0.027	72.40 (56.12) ± 5.38	0.92 (22.1)	±2.12	±2.05	±6.13
0.175	10.327 (7.850) ± 0.022	68.48 (53.34) ± 4.75	0.88 (20.2)	±2.15	±2.18	±5.65
0.153	9.035 (6.859) ± 0.021	62.87 (49.41) ± 4.84	0.82 (18.3)	±2.09	±2.55	±5.85
0.131	7.744 (5.870) ± 0.017	58.29 (45.68) ± 4.29	0.71 (16.3)	±2.05	±2.65	±5.45
0.109	6.452 (4.877) ± 0.014	54.02 (41.89) ± 4.10	0.58 (14.5)	±1.91	±2.54	±5.19
0.087	5.160 (3.881) ± 0.011	49.72 (38.24) ± 4.19	0.49 (12.2)	±1.74	±2.92	±5.40
0.066	3.895 (3.027) ± 0.008	44.74 (34.54) ± 4.38	0.49 (10.2)	±1.45	±3.09	±5.55

Table A.18: NBD fit results in centrality 25-30%.

$\delta\eta$	$\langle\mu_c\rangle(\langle\mu\rangle)$	$\langle k_c\rangle(\langle k\rangle)$	$\langle\chi^2/NDF\rangle(\langle NDF\rangle)$	$\delta\langle k_c\rangle(dead)$	$\delta\langle k_c\rangle(fake)$	$\delta\langle k_c\rangle(total)$
0.700	33.991 (26.309) ± 0.090	67.99 (52.63) ± 3.18	0.56 (44.0)	±2.58	±0.80	±4.17
0.678	33.067 (25.615) ± 0.088	68.77 (53.27) ± 3.29	0.61 (44.0)	±2.56	±0.05	±4.17
0.656	31.992 (24.750) ± 0.086	67.53 (52.23) ± 3.30	0.56 (43.6)	±3.20	±1.31	±4.78
0.634	30.890 (23.863) ± 0.084	67.26 (51.95) ± 3.34	0.58 (42.8)	±2.31	±1.01	±4.19
0.613	29.811 (23.012) ± 0.082	67.40 (52.02) ± 3.41	0.64 (41.9)	±1.64	±1.27	±3.99
0.591	28.732 (22.173) ± 0.081	66.18 (51.07) ± 3.41	0.65 (41.3)	±2.18	±0.79	±4.12
0.569	27.643 (21.312) ± 0.079	66.17 (51.01) ± 3.50	0.62 (40.2)	±2.87	±1.24	±4.69
0.547	26.558 (20.443) ± 0.077	65.89 (50.72) ± 3.57	0.65 (38.9)	±2.32	±1.30	±4.45
0.525	25.479 (19.583) ± 0.075	65.64 (50.44) ± 3.66	0.66 (37.9)	±2.53	±0.86	±4.53
0.503	24.403 (18.721) ± 0.073	65.21 (50.01) ± 3.75	0.66 (37.1)	±3.12	±1.03	±4.99
0.481	23.325 (17.852) ± 0.071	64.30 (49.19) ± 3.80	0.64 (35.9)	±3.10	±0.97	±5.00
0.459	22.243 (16.972) ± 0.069	64.65 (49.31) ± 3.94	0.67 (35.0)	±2.62	±0.71	±4.78
0.438	21.155 (16.084) ± 0.067	63.75 (48.45) ± 4.03	0.68 (33.4)	±2.73	±0.89	±4.95
0.416	20.074 (15.204) ± 0.065	63.34 (47.95) ± 4.15	0.70 (32.4)	±2.72	±1.01	±5.06
0.394	18.991 (14.327) ± 0.063	62.47 (47.09) ± 4.26	0.69 (31.0)	±2.95	±1.01	±5.28
0.372	17.912 (13.455) ± 0.061	62.61 (47.00) ± 4.49	0.71 (29.9)	±2.80	±0.83	±5.35
0.350	16.855 (12.625) ± 0.042	62.05 (46.45) ± 3.30	0.72 (28.7)	±2.34	±0.81	±4.12
0.328	15.805 (11.868) ± 0.040	61.38 (46.04) ± 3.39	0.72 (27.5)	±2.67	±1.02	±4.43
0.306	14.769 (11.126) ± 0.038	60.26 (45.34) ± 3.48	0.72 (26.3)	±2.88	±1.01	±4.63
0.284	13.731 (10.376) ± 0.037	59.70 (44.97) ± 3.62	0.71 (25.1)	±2.44	±1.21	±4.54
0.263	12.685 (9.610) ± 0.035	59.20 (44.67) ± 3.84	0.74 (23.7)	±2.61	±1.06	±4.76
0.241	11.640 (8.838) ± 0.033	57.91 (43.73) ± 4.00	0.71 (22.3)	±2.54	±1.09	±4.86
0.219	10.591 (8.054) ± 0.026	56.00 (42.22) ± 3.34	0.64 (21.0)	±2.38	±1.26	±4.29
0.197	9.535 (7.258) ± 0.024	54.60 (41.11) ± 3.51	0.67 (19.3)	±2.10	±1.43	±4.33
0.175	8.479 (6.455) ± 0.020	52.59 (39.35) ± 3.21	0.64 (17.6)	±2.49	±1.42	±4.30
0.153	7.420 (5.643) ± 0.018	51.06 (38.08) ± 3.48	0.62 (16.0)	±1.76	±1.53	±4.19
0.131	6.363 (4.832) ± 0.015	49.16 (36.41) ± 3.38	0.56 (14.3)	±1.61	±1.59	±4.07
0.109	5.306 (4.017) ± 0.013	45.94 (33.94) ± 3.32	0.49 (12.3)	±1.57	±1.75	±4.07
0.087	4.245 (3.196) ± 0.010	43.38 (31.95) ± 3.30	0.49 (10.5)	±1.68	±2.00	±4.21
0.066	3.205 (2.492) ± 0.007	38.41 (28.81) ± 3.58	0.47 (8.8)	±1.46	±2.20	±4.45

Table A.19: NBD fit results in centrality 30-35%.

$\delta\eta$	$\langle\mu_c\rangle(\langle\mu\rangle)$	$\langle k_c\rangle(\langle k\rangle)$	$\langle\chi^2/NDF\rangle(\langle NDF\rangle)$	$\delta\langle k_c\rangle(dead)$	$\delta\langle k_c\rangle(fake)$	$\delta\langle k_c\rangle(total)$
0.700	27.652 (21.402) ± 0.079	58.33 (45.15) ± 2.86	0.67 (41.0)	±3.24	±0.86	±4.41
0.678	26.900 (20.838) ± 0.078	57.89 (44.85) ± 2.86	0.60 (40.9)	±2.95	±0.85	±4.20
0.656	26.016 (20.126) ± 0.076	57.99 (44.86) ± 2.94	0.63 (39.6)	±2.17	±0.88	±3.75
0.634	25.115 (19.401) ± 0.074	57.51 (44.43) ± 2.98	0.66 (38.4)	±2.60	±0.72	±4.02
0.613	24.225 (18.699) ± 0.073	56.95 (43.97) ± 3.03	0.67 (37.0)	±2.60	±0.86	±4.09
0.591	23.345 (18.015) ± 0.071	56.94 (43.95) ± 3.10	0.70 (36.3)	±2.27	±0.77	±3.92
0.569	22.464 (17.318) ± 0.070	56.67 (43.71) ± 3.17	0.74 (35.0)	±1.78	±0.77	±3.72
0.547	21.583 (16.613) ± 0.068	55.99 (43.12) ± 3.22	0.71 (33.9)	±2.04	±0.69	±3.87
0.525	20.702 (15.911) ± 0.066	56.01 (43.07) ± 3.34	0.73 (33.0)	±2.00	±0.70	±3.96
0.503	19.828 (15.210) ± 0.065	55.63 (42.71) ± 3.44	0.76 (31.8)	±1.94	±0.84	±4.03
0.481	18.948 (14.500) ± 0.063	55.29 (42.37) ± 3.57	0.72 (30.9)	±2.25	±0.85	±4.30
0.459	18.064 (13.781) ± 0.061	55.70 (42.57) ± 3.73	0.77 (30.1)	±1.76	±0.78	±4.20
0.438	17.181 (13.060) ± 0.059	54.86 (41.80) ± 3.89	0.79 (29.1)	±2.03	±1.04	±4.51
0.416	16.302 (12.344) ± 0.058	53.65 (40.75) ± 3.97	0.68 (28.0)	±2.50	±1.08	±4.82
0.394	15.419 (11.629) ± 0.056	53.33 (40.40) ± 4.19	0.74 (26.8)	±2.48	±0.99	±4.97
0.372	14.543 (10.920) ± 0.054	52.71 (39.80) ± 4.38	0.75 (25.4)	±2.14	±0.93	±4.96
0.350	13.684 (10.246) ± 0.037	52.57 (39.60) ± 3.27	0.78 (24.3)	±2.15	±0.93	±4.02
0.328	12.833 (9.633) ± 0.035	51.53 (38.93) ± 3.35	0.81 (23.0)	±2.25	±0.95	±4.14
0.306	11.991 (9.029) ± 0.034	49.87 (37.95) ± 3.43	0.77 (22.0)	±2.29	±0.94	±4.23
0.284	11.146 (8.415) ± 0.033	48.20 (36.98) ± 3.59	0.76 (20.9)	±2.06	±0.89	±4.23
0.263	10.299 (7.796) ± 0.031	47.05 (36.22) ± 3.67	0.71 (19.7)	±1.60	±0.93	±4.11
0.241	9.450 (7.169) ± 0.030	45.91 (35.45) ± 3.79	0.69 (18.6)	±1.51	±0.93	±4.18
0.219	8.597 (6.532) ± 0.023	44.64 (34.66) ± 3.18	0.62 (17.5)	±1.43	±1.00	±3.62
0.197	7.740 (5.885) ± 0.022	43.61 (34.05) ± 3.30	0.57 (16.3)	±1.22	±1.01	±3.66
0.175	6.881 (5.231) ± 0.018	42.44 (33.32) ± 3.04	0.50 (14.9)	±1.36	±1.10	±3.51
0.153	6.023 (4.574) ± 0.016	41.28 (32.47) ± 3.26	0.45 (13.6)	±1.39	±1.27	±3.76
0.131	5.165 (3.914) ± 0.013	40.29 (31.79) ± 3.21	0.45 (12.2)	±1.33	±1.30	±3.71
0.109	4.306 (3.253) ± 0.011	38.26 (30.17) ± 3.27	0.46 (10.7)	±1.62	±1.28	±3.87
0.087	3.445 (2.587) ± 0.009	35.11 (27.79) ± 3.39	0.51 (9.2)	±1.18	±1.41	±3.86
0.066	2.606 (2.037) ± 0.006	30.96 (24.26) ± 3.44	0.54 (7.9)	±1.25	±1.14	±3.83

Table A.20: NBD fit results in centrality 35-40%.

$\delta\eta$	$\langle\mu_c\rangle(\langle\mu\rangle)$	$\langle k_c\rangle(\langle k\rangle)$	$\langle\chi^2/NDF\rangle(\langle NDF\rangle)$	$\delta\langle k_c\rangle(dead)$	$\delta\langle k_c\rangle(fake)$	$\delta\langle k_c\rangle(total)$
0.700	21.970 (17.005) ± 0.071	47.25 (36.57) ± 2.31	0.79 (38.0)	±0.68	±0.60	±2.48
0.678	21.372 (16.556) ± 0.070	47.47 (36.77) ± 2.32	0.69 (37.7)	±0.44	±0.02	±2.36
0.656	20.684 (16.001) ± 0.068	46.97 (36.33) ± 2.33	0.71 (37.1)	±0.92	±0.23	±2.51
0.634	19.964 (15.423) ± 0.067	46.50 (35.92) ± 2.35	0.79 (36.0)	±0.86	±0.30	±2.52
0.613	19.253 (14.862) ± 0.065	46.36 (35.78) ± 2.40	0.86 (34.6)	±0.91	±0.15	±2.57
0.591	18.572 (14.333) ± 0.064	45.46 (35.08) ± 2.41	0.82 (33.4)	±1.16	±0.36	±2.70
0.569	17.877 (13.783) ± 0.063	45.55 (35.11) ± 2.48	0.83 (32.5)	±1.22	±0.37	±2.79
0.547	17.176 (13.221) ± 0.061	45.52 (35.05) ± 2.54	0.83 (31.7)	±1.26	±0.44	±2.87
0.525	16.475 (12.662) ± 0.059	45.45 (34.94) ± 2.63	0.87 (30.7)	±1.09	±0.34	±2.87
0.503	15.778 (12.104) ± 0.058	45.41 (34.85) ± 2.70	0.87 (29.8)	±0.92	±0.22	±2.86
0.481	15.082 (11.542) ± 0.057	44.90 (34.38) ± 2.77	0.84 (28.6)	±1.02	±0.36	±2.97
0.459	14.380 (10.972) ± 0.055	44.50 (33.97) ± 2.83	0.81 (27.6)	±1.03	±0.31	±3.03
0.438	13.678 (10.399) ± 0.053	43.95 (33.42) ± 2.91	0.82 (26.3)	±1.15	±0.39	±3.15
0.416	12.978 (9.829) ± 0.052	43.68 (33.09) ± 2.99	0.81 (25.4)	±1.16	±0.33	±3.22
0.394	12.280 (9.264) ± 0.050	43.03 (32.45) ± 3.06	0.79 (24.2)	±1.23	±0.41	±3.32
0.372	11.582 (8.700) ± 0.049	42.60 (31.98) ± 3.17	0.77 (23.1)	±1.08	±0.45	±3.38
0.350	10.894 (8.161) ± 0.033	42.04 (31.45) ± 2.30	0.74 (22.0)	±1.00	±0.34	±2.53
0.328	10.213 (7.670) ± 0.032	41.13 (30.87) ± 2.34	0.72 (21.0)	±0.90	±0.35	±2.54
0.306	9.540 (7.188) ± 0.031	40.19 (30.29) ± 2.39	0.70 (20.0)	±0.86	±0.19	±2.55
0.284	8.867 (6.699) ± 0.029	39.08 (29.61) ± 2.46	0.69 (18.9)	±0.92	±0.28	±2.64
0.263	8.191 (6.204) ± 0.028	38.50 (29.35) ± 2.57	0.67 (18.0)	±0.97	±0.34	±2.77
0.241	7.517 (5.707) ± 0.027	37.29 (28.54) ± 2.64	0.57 (17.1)	±1.25	±0.50	±2.97
0.219	6.837 (5.198) ± 0.021	36.65 (28.17) ± 2.29	0.55 (16.1)	±0.92	±0.47	±2.51
0.197	6.155 (4.685) ± 0.019	35.93 (27.66) ± 2.40	0.55 (15.0)	±0.77	±0.51	±2.58
0.175	5.474 (4.166) ± 0.016	34.69 (26.74) ± 2.20	0.52 (13.7)	±0.77	±0.65	±2.43
0.153	4.792 (3.644) ± 0.015	33.23 (25.56) ± 2.37	0.50 (12.4)	±0.86	±0.72	±2.62
0.131	4.111 (3.122) ± 0.012	31.76 (24.13) ± 2.33	0.48 (11.1)	±0.88	±0.72	±2.59
0.109	3.426 (2.594) ± 0.010	30.11 (22.76) ± 2.52	0.54 (9.8)	±0.65	±0.72	±2.69
0.087	2.742 (2.069) ± 0.008	28.05 (20.82) ± 2.59	0.55 (8.3)	±0.86	±0.84	±2.85
0.066	2.070 (1.609) ± 0.006	24.89 (18.20) ± 2.64	0.54 (7.0)	±0.94	±0.95	±2.96

Table A.21: NBD fit results in centrality 40-45%.

$\delta\eta$	$\langle\mu_c\rangle(\langle\mu\rangle)$	$\langle k_c\rangle(\langle k\rangle)$	$\langle\chi^2/NDF\rangle(\langle NDF\rangle)$	$\delta\langle k_c\rangle(dead)$	$\delta\langle k_c\rangle(fake)$	$\delta\langle k_c\rangle(total)$
0.700	17.453 (13.508) ± 0.063	37.64 (29.13) ± 1.83	0.74 (35.0)	±0.40	±0.98	±2.12
0.678	16.988 (13.160) ± 0.062	37.36 (28.94) ± 1.85	0.74 (34.1)	±1.08	±0.27	±2.16
0.656	16.429 (12.709) ± 0.061	37.57 (29.06) ± 1.91	0.83 (33.0)	±0.91	±0.00	±2.12
0.634	15.863 (12.255) ± 0.059	37.55 (29.01) ± 1.96	0.82 (32.2)	±1.54	±0.31	±2.51
0.613	15.315 (11.822) ± 0.058	36.88 (28.47) ± 1.96	0.76 (31.4)	±1.75	±0.34	±2.65
0.591	14.758 (11.389) ± 0.057	36.84 (28.43) ± 1.97	0.83 (30.6)	±1.76	±0.32	±2.68
0.569	14.201 (10.948) ± 0.056	36.74 (28.32) ± 2.04	0.88 (29.8)	±1.32	±0.26	±2.45
0.547	13.652 (10.508) ± 0.054	36.19 (27.85) ± 2.07	0.85 (29.2)	±1.54	±0.32	±2.60
0.525	13.096 (10.065) ± 0.053	36.01 (27.67) ± 2.12	0.83 (28.3)	±1.30	±0.22	±2.50
0.503	12.537 (9.618) ± 0.051	36.07 (27.66) ± 2.21	0.89 (27.1)	±1.25	±0.28	±2.55
0.481	11.980 (9.169) ± 0.050	35.96 (27.51) ± 2.28	0.91 (26.3)	±1.27	±0.33	±2.63
0.459	11.422 (8.715) ± 0.049	35.74 (27.26) ± 2.36	0.91 (25.2)	±1.12	±0.33	±2.63
0.438	10.861 (8.258) ± 0.048	35.46 (26.95) ± 2.43	0.87 (24.2)	±1.08	±0.28	±2.67
0.416	10.302 (7.803) ± 0.046	35.19 (26.64) ± 2.51	0.89 (22.9)	±1.10	±0.38	±2.77
0.394	9.742 (7.349) ± 0.045	35.42 (26.71) ± 2.63	0.92 (22.0)	±0.69	±0.34	±2.74
0.372	9.189 (6.902) ± 0.043	35.02 (26.31) ± 2.70	0.83 (21.1)	±0.86	±0.36	±2.86
0.350	8.649 (6.478) ± 0.030	34.15 (25.59) ± 1.94	0.73 (19.9)	±1.22	±0.51	±2.35
0.328	8.110 (6.090) ± 0.029	33.55 (25.21) ± 1.99	0.71 (19.0)	±1.19	±0.45	±2.36
0.306	7.578 (5.708) ± 0.027	33.04 (24.89) ± 2.06	0.70 (18.0)	±1.22	±0.41	±2.43
0.284	7.044 (5.321) ± 0.026	32.48 (24.52) ± 2.12	0.67 (17.0)	±1.18	±0.43	±2.47
0.263	6.509 (4.930) ± 0.025	31.66 (23.97) ± 2.17	0.63 (16.1)	±1.12	±0.45	±2.48
0.241	5.973 (4.533) ± 0.024	30.82 (23.44) ± 2.22	0.61 (15.1)	±1.00	±0.46	±2.48
0.219	5.435 (4.131) ± 0.018	29.59 (22.59) ± 1.88	0.58 (14.0)	±1.09	±0.45	±2.23
0.197	4.894 (3.723) ± 0.017	28.75 (22.00) ± 2.00	0.54 (13.1)	±0.83	±0.49	±2.22
0.175	4.353 (3.311) ± 0.014	28.04 (21.41) ± 1.89	0.56 (12.1)	±0.90	±0.54	±2.16
0.153	3.811 (2.896) ± 0.013	26.88 (20.50) ± 2.02	0.50 (10.9)	±0.74	±0.51	±2.21
0.131	3.267 (2.478) ± 0.011	25.91 (19.73) ± 2.01	0.52 (9.9)	±0.63	±0.54	±2.18
0.109	2.724 (2.060) ± 0.009	24.44 (18.61) ± 2.05	0.47 (8.7)	±0.38	±0.61	±2.18
0.087	2.179 (1.639) ± 0.007	22.93 (17.48) ± 2.12	0.55 (7.4)	±0.38	±0.55	±2.22
0.066	1.646 (1.279) ± 0.005	20.46 (15.59) ± 2.26	0.54 (6.3)	±0.59	±0.51	±2.39

Table A.22: NBD fit results in centrality 45-50%.

$\delta\eta$	$\langle\mu_c\rangle(\langle\mu\rangle)$	$\langle k_c\rangle(\langle k\rangle)$	$\langle\chi^2/NDF\rangle(\langle NDF\rangle)$	$\delta\langle k_c\rangle(dead)$	$\delta\langle k_c\rangle(fake)$	$\delta\langle k_c\rangle(total)$
0.700	13.493 (10.444) ± 0.054	32.22 (24.94) ± 1.72	0.77 (27.0)	±1.57	±0.13	±2.34
0.678	13.123 (10.166) ± 0.053	32.44 (25.13) ± 1.74	0.79 (26.9)	±1.12	±0.09	±2.07
0.656	12.698 (9.823) ± 0.052	32.30 (24.99) ± 1.77	0.81 (25.6)	±0.70	±0.22	±1.92
0.634	12.261 (9.472) ± 0.051	32.54 (25.14) ± 1.85	0.89 (24.6)	±0.78	±0.32	±2.04
0.613	11.829 (9.131) ± 0.050	32.98 (25.46) ± 1.94	0.89 (23.9)	±0.81	±0.20	±2.11
0.591	11.403 (8.800) ± 0.049	33.01 (25.47) ± 2.00	0.88 (23.1)	±0.56	±0.28	±2.10
0.569	10.976 (8.462) ± 0.048	32.73 (25.23) ± 2.04	0.84 (22.3)	±0.56	±0.24	±2.13
0.547	10.547 (8.119) ± 0.046	32.55 (25.05) ± 2.09	0.84 (21.7)	±0.52	±0.29	±2.18
0.525	10.120 (7.778) ± 0.045	32.54 (25.00) ± 2.16	0.80 (21.0)	±0.30	±0.28	±2.20
0.503	9.694 (7.437) ± 0.044	32.48 (24.91) ± 2.23	0.76 (20.5)	±0.39	±0.31	±2.28
0.481	9.267 (7.093) ± 0.043	32.14 (24.60) ± 2.28	0.67 (19.8)	±0.44	±0.30	±2.34
0.459	8.836 (6.742) ± 0.042	31.98 (24.40) ± 2.37	0.60 (19.1)	±0.57	±0.34	±2.46
0.438	8.403 (6.389) ± 0.041	31.90 (24.26) ± 2.46	0.55 (18.5)	±0.56	±0.36	±2.54
0.416	7.970 (6.037) ± 0.039	31.80 (24.10) ± 2.56	0.52 (17.7)	±0.58	±0.38	±2.65
0.394	7.537 (5.686) ± 0.038	31.73 (23.97) ± 2.67	0.54 (17.1)	±0.79	±0.42	±2.82
0.372	7.108 (5.339) ± 0.037	31.47 (23.68) ± 2.78	0.53 (16.4)	±0.83	±0.37	±2.92
0.350	6.688 (5.009) ± 0.025	31.14 (23.38) ± 2.05	0.54 (15.6)	±0.84	±0.38	±2.25
0.328	6.271 (4.709) ± 0.024	30.59 (23.16) ± 2.12	0.55 (15.0)	±0.77	±0.37	±2.29
0.306	5.860 (4.413) ± 0.023	29.82 (22.83) ± 2.20	0.55 (14.4)	±0.72	±0.35	±2.34
0.284	5.450 (4.115) ± 0.022	29.04 (22.41) ± 2.27	0.54 (13.7)	±0.57	±0.36	±2.37
0.263	5.037 (3.813) ± 0.021	28.60 (22.23) ± 2.41	0.57 (13.1)	±0.44	±0.43	±2.49
0.241	4.623 (3.508) ± 0.020	28.11 (21.89) ± 2.48	0.55 (12.4)	±0.47	±0.42	±2.56
0.219	4.205 (3.196) ± 0.016	27.55 (21.51) ± 2.15	0.55 (11.8)	±0.45	±0.38	±2.23
0.197	3.785 (2.879) ± 0.015	27.20 (21.34) ± 2.35	0.56 (11.0)	±0.42	±0.41	±2.42
0.175	3.364 (2.558) ± 0.012	26.76 (21.15) ± 2.25	0.58 (10.3)	±0.45	±0.40	±2.33
0.153	2.943 (2.236) ± 0.011	26.24 (20.74) ± 2.47	0.57 (9.4)	±0.16	±0.40	±2.50
0.131	2.523 (1.913) ± 0.009	25.81 (20.49) ± 2.54	0.53 (8.5)	±0.12	±0.42	±2.57
0.109	2.104 (1.592) ± 0.008	25.12 (19.94) ± 2.71	0.48 (7.6)	±0.09	±0.52	±2.76
0.087	1.692 (1.306) ± 0.006	23.73 (18.71) ± 2.55	0.45 (6.6)	±0.14	±0.38	±2.58
0.066	1.277 (1.014) ± 0.004	21.69 (16.94) ± 2.72	0.49 (5.4)	±0.51	±0.45	±2.80

Table A.23: NBD fit results in centrality 50-55%.

$\delta\eta$	$\langle\mu_c\rangle(\langle\mu\rangle)$	$\langle k_c\rangle(\langle k\rangle)$	$\langle\chi^2/NDF\rangle(\langle NDF\rangle)$	$\delta\langle k_c\rangle(dead)$	$\delta\langle k_c\rangle(fake)$	$\delta\langle k_c\rangle(total)$
0.700	10.177 (7.877) ± 0.046	27.08 (20.96) ± 1.52	1.18 (24.0)	±1.23	±0.17	±1.96
0.678	9.898 (7.667) ± 0.045	26.98 (20.90) ± 1.53	1.14 (23.0)	±0.62	±0.26	±1.67
0.656	9.584 (7.414) ± 0.044	26.02 (20.12) ± 1.50	1.07 (21.9)	±0.94	±0.23	±1.79
0.634	9.257 (7.151) ± 0.044	25.65 (19.81) ± 1.51	0.97 (21.2)	±0.43	±0.21	±1.58
0.613	8.935 (6.897) ± 0.043	25.16 (19.42) ± 1.52	0.85 (20.8)	±0.63	±0.16	±1.66
0.591	8.613 (6.647) ± 0.042	24.75 (19.10) ± 1.53	0.82 (20.0)	±0.77	±0.21	±1.73
0.569	8.287 (6.389) ± 0.041	24.69 (19.03) ± 1.58	0.80 (19.6)	±0.54	±0.10	±1.68
0.547	7.964 (6.130) ± 0.040	24.46 (18.82) ± 1.62	0.79 (19.1)	±0.70	±0.22	±1.77
0.525	7.640 (5.872) ± 0.039	24.42 (18.76) ± 1.67	0.79 (18.5)	±0.67	±0.28	±1.81
0.503	7.318 (5.614) ± 0.038	24.25 (18.59) ± 1.72	0.74 (18.0)	±0.67	±0.25	±1.86
0.481	6.991 (5.351) ± 0.037	24.35 (18.62) ± 1.80	0.74 (17.5)	±0.57	±0.26	±1.91
0.459	6.664 (5.085) ± 0.036	24.37 (18.58) ± 1.89	0.70 (16.9)	±0.79	±0.24	±2.06
0.438	6.338 (4.818) ± 0.035	24.32 (18.48) ± 1.96	0.61 (16.3)	±0.93	±0.26	±2.19
0.416	6.013 (4.554) ± 0.034	24.34 (18.42) ± 2.05	0.55 (15.7)	±0.93	±0.39	±2.28
0.394	5.689 (4.292) ± 0.033	24.43 (18.41) ± 2.14	0.52 (15.0)	±1.01	±0.22	±2.38
0.372	5.365 (4.031) ± 0.032	24.59 (18.43) ± 2.28	0.52 (14.3)	±0.85	±0.35	±2.46
0.350	5.047 (3.781) ± 0.022	24.82 (18.54) ± 1.71	0.54 (13.8)	±0.85	±0.37	±1.94
0.328	4.731 (3.554) ± 0.021	24.90 (18.65) ± 1.81	0.62 (13.4)	±0.58	±0.26	±1.92
0.306	4.421 (3.331) ± 0.020	24.53 (18.49) ± 1.90	0.62 (12.9)	±0.47	±0.35	±1.99
0.284	4.110 (3.106) ± 0.019	24.09 (18.29) ± 2.00	0.58 (12.3)	±0.62	±0.20	±2.10
0.263	3.798 (2.877) ± 0.018	23.76 (18.20) ± 2.19	0.61 (11.6)	±0.57	±0.11	±2.27
0.241	3.487 (2.646) ± 0.018	23.58 (18.20) ± 2.34	0.59 (11.1)	±0.59	±0.23	±2.43
0.219	3.173 (2.412) ± 0.013	23.10 (17.98) ± 2.13	0.56 (10.5)	±0.77	±0.24	±2.28
0.197	2.858 (2.174) ± 0.013	22.73 (17.85) ± 2.36	0.53 (9.8)	±0.74	±0.25	±2.49
0.175	2.541 (1.932) ± 0.010	22.47 (17.74) ± 2.36	0.54 (9.0)	±0.95	±0.27	±2.56
0.153	2.224 (1.691) ± 0.010	22.22 (17.61) ± 2.64	0.57 (8.2)	±0.89	±0.29	±2.80
0.131	1.906 (1.447) ± 0.008	21.76 (17.39) ± 2.93	0.64 (7.4)	±0.75	±0.36	±3.05
0.109	1.593 (1.215) ± 0.006	20.48 (16.47) ± 3.02	0.59 (6.6)	±0.69	±0.35	±3.11
0.087	1.279 (0.982) ± 0.005	19.00 (15.26) ± 2.67	0.54 (5.5)	±0.67	±0.47	±2.80
0.066	0.969 (0.770) ± 0.004	16.64 (13.48) ± 2.31	0.52 (4.5)	±0.59	±0.54	±2.45

Table A.24: NBD fit results in centrality 55-60%.

$\delta\eta$	$\langle\mu_c\rangle(\langle\mu\rangle)$	$\langle k_c\rangle(\langle k\rangle)$	$\langle\chi^2/NDF\rangle(\langle NDF\rangle)$	$\delta\langle k_c\rangle(dead)$	$\delta\langle k_c\rangle(fake)$	$\delta\langle k_c\rangle(total)$
0.700	7.465 (5.778) ± 0.041	18.75 (14.52) ± 1.12	0.71 (16.0)	±0.59	±0.13	±1.27
0.678	7.258 (5.622) ± 0.040	19.02 (14.74) ± 1.14	0.76 (16.0)	±0.60	±0.08	±1.29
0.656	7.021 (5.431) ± 0.039	18.80 (14.54) ± 1.14	0.73 (15.8)	±0.61	±0.09	±1.29
0.634	6.781 (5.238) ± 0.038	18.41 (14.22) ± 1.14	0.57 (15.4)	±0.57	±0.09	±1.28
0.613	6.547 (5.054) ± 0.038	18.01 (13.89) ± 1.13	0.51 (14.7)	±0.70	±0.07	±1.33
0.591	6.307 (4.867) ± 0.037	17.98 (13.87) ± 1.15	0.56 (14.4)	±0.70	±0.07	±1.34
0.569	6.070 (4.680) ± 0.036	17.84 (13.75) ± 1.15	0.51 (14.1)	±0.69	±0.07	±1.35
0.547	5.833 (4.490) ± 0.035	17.66 (13.59) ± 1.17	0.47 (13.7)	±0.63	±0.07	±1.33
0.525	5.596 (4.301) ± 0.034	17.52 (13.46) ± 1.19	0.44 (13.4)	±0.60	±0.08	±1.34
0.503	5.360 (4.112) ± 0.033	17.52 (13.43) ± 1.22	0.43 (13.2)	±0.67	±0.09	±1.40
0.481	5.122 (3.920) ± 0.033	17.49 (13.38) ± 1.26	0.47 (13.1)	±0.66	±0.09	±1.43
0.459	4.885 (3.728) ± 0.032	17.37 (13.24) ± 1.30	0.49 (12.6)	±0.69	±0.09	±1.47
0.438	4.648 (3.534) ± 0.031	17.22 (13.08) ± 1.33	0.51 (12.1)	±0.74	±0.10	±1.53
0.416	4.411 (3.340) ± 0.030	17.20 (13.01) ± 1.39	0.58 (11.5)	±0.62	±0.10	±1.52
0.394	4.173 (3.148) ± 0.029	17.18 (12.95) ± 1.44	0.62 (10.9)	±0.78	±0.12	±1.64
0.372	3.935 (2.955) ± 0.028	17.34 (13.00) ± 1.54	0.63 (10.4)	±0.84	±0.13	±1.76
0.350	3.701 (2.772) ± 0.019	17.31 (12.94) ± 1.15	0.65 (9.9)	±0.67	±0.08	±1.33
0.328	3.472 (2.607) ± 0.018	17.17 (12.87) ± 1.19	0.66 (9.5)	±0.71	±0.10	±1.39
0.306	3.244 (2.444) ± 0.018	17.09 (12.85) ± 1.25	0.68 (9.2)	±0.64	±0.09	±1.41
0.284	3.016 (2.279) ± 0.017	16.91 (12.74) ± 1.32	0.67 (8.6)	±0.53	±0.08	±1.42
0.263	2.787 (2.111) ± 0.016	16.61 (12.58) ± 1.40	0.62 (8.1)	±0.56	±0.09	±1.51
0.241	2.558 (1.942) ± 0.015	16.53 (12.57) ± 1.50	0.61 (7.6)	±0.52	±0.11	±1.59
0.219	2.326 (1.769) ± 0.012	16.34 (12.46) ± 1.35	0.66 (7.1)	±0.49	±0.10	±1.44
0.197	2.095 (1.595) ± 0.011	16.13 (12.30) ± 1.44	0.62 (6.7)	±0.48	±0.11	±1.52
0.175	1.861 (1.417) ± 0.009	16.07 (12.24) ± 1.45	0.72 (6.3)	±0.34	±0.12	±1.49
0.153	1.630 (1.240) ± 0.009	15.67 (11.91) ± 1.54	0.59 (5.7)	±0.17	±0.13	±1.56
0.131	1.399 (1.062) ± 0.007	14.90 (11.39) ± 1.50	0.47 (5.1)	±0.35	±0.15	±1.54
0.109	1.166 (0.882) ± 0.006	14.25 (10.82) ± 1.56	0.42 (4.5)	±0.37	±0.17	±1.61
0.087	0.935 (0.714) ± 0.004	13.41 (10.20) ± 1.63	0.46 (4.0)	±0.30	±0.15	±1.66
0.066	0.703 (0.548) ± 0.003	11.85 (9.19) ± 1.63	0.53 (3.3)	±0.35	±0.17	±1.67

Table A.25: NBD fit results in centrality 60-65%.

$\delta\eta$	$\langle\mu_c\rangle(\langle\mu\rangle)$	$\langle k_c\rangle(\langle k\rangle)$	$\langle\chi^2/NDF\rangle(\langle NDF\rangle)$	$\delta\langle k_c\rangle(dead)$	$\delta\langle k_c\rangle(fake)$	$\delta\langle k_c\rangle(total)$
0.700	5.337 (4.131) ± 0.033	14.40 (11.14) ± 0.81	0.79 (15.0)	±0.33	±0.04	±0.88
0.678	5.197 (4.026) ± 0.033	14.25 (11.04) ± 0.82	0.77 (14.8)	±0.45	±0.04	±0.94
0.656	5.031 (3.892) ± 0.032	14.37 (11.12) ± 0.86	0.61 (14.2)	±0.46	±0.03	±0.97
0.634	4.861 (3.755) ± 0.032	14.35 (11.09) ± 0.88	0.53 (13.8)	±0.47	±0.04	±0.99
0.613	4.686 (3.617) ± 0.031	14.41 (11.13) ± 0.93	0.78 (13.1)	±0.44	±0.04	±1.03
0.591	4.519 (3.487) ± 0.030	13.99 (10.80) ± 0.90	0.63 (12.9)	±0.53	±0.04	±1.05
0.569	4.344 (3.349) ± 0.029	14.01 (10.80) ± 0.92	0.73 (12.7)	±0.51	±0.05	±1.06
0.547	4.169 (3.209) ± 0.029	14.23 (10.96) ± 0.97	0.82 (12.5)	±0.41	±0.04	±1.05
0.525	4.003 (3.077) ± 0.028	13.97 (10.74) ± 0.97	0.64 (12.0)	±0.41	±0.04	±1.06
0.503	3.835 (2.942) ± 0.027	13.88 (10.65) ± 1.00	0.59 (11.8)	±0.45	±0.04	±1.10
0.481	3.665 (2.805) ± 0.027	13.89 (10.63) ± 1.04	0.60 (11.6)	±0.43	±0.04	±1.12
0.459	3.495 (2.667) ± 0.026	13.85 (10.57) ± 1.07	0.59 (11.1)	±0.34	±0.05	±1.12
0.438	3.326 (2.529) ± 0.025	13.78 (10.48) ± 1.11	0.56 (10.5)	±0.33	±0.06	±1.16
0.416	3.159 (2.393) ± 0.025	13.65 (10.35) ± 1.15	0.48 (9.9)	±0.38	±0.06	±1.22
0.394	2.989 (2.255) ± 0.024	13.71 (10.35) ± 1.23	0.46 (9.5)	±0.37	±0.05	±1.28
0.372	2.818 (2.117) ± 0.023	13.95 (10.48) ± 1.33	0.52 (8.9)	±0.40	±0.05	±1.39
0.350	2.652 (1.986) ± 0.016	14.10 (10.57) ± 1.00	0.54 (8.5)	±0.41	±0.06	±1.09
0.328	2.487 (1.867) ± 0.015	14.06 (10.58) ± 1.06	0.56 (8.1)	±0.41	±0.06	±1.15
0.306	2.324 (1.750) ± 0.015	14.16 (10.71) ± 1.14	0.66 (7.6)	±0.34	±0.06	±1.19
0.284	2.160 (1.631) ± 0.014	14.12 (10.76) ± 1.22	0.66 (7.1)	±0.38	±0.06	±1.28
0.263	1.996 (1.511) ± 0.013	14.01 (10.76) ± 1.31	0.63 (6.6)	±0.36	±0.06	±1.36
0.241	1.832 (1.390) ± 0.013	13.79 (10.64) ± 1.39	0.53 (6.3)	±0.40	±0.06	±1.45
0.219	1.667 (1.267) ± 0.010	13.49 (10.50) ± 1.24	0.51 (5.9)	±0.40	±0.07	±1.30
0.197	1.502 (1.143) ± 0.009	13.23 (10.37) ± 1.35	0.47 (5.5)	±0.46	±0.07	±1.43
0.175	1.335 (1.015) ± 0.007	13.17 (10.38) ± 1.32	0.50 (5.1)	±0.47	±0.08	±1.40
0.153	1.168 (0.888) ± 0.007	12.96 (10.25) ± 1.55	0.56 (4.7)	±0.38	±0.10	±1.60
0.131	1.005 (0.768) ± 0.006	12.13 (9.56) ± 1.46	0.45 (4.3)	±0.29	±0.10	±1.50
0.109	0.838 (0.639) ± 0.005	11.68 (9.21) ± 1.66	0.44 (3.8)	±0.15	±0.12	±1.67
0.087	0.673 (0.524) ± 0.004	10.96 (8.64) ± 1.65	0.54 (3.3)	±0.14	±0.14	±1.66
0.066	0.507 (0.405) ± 0.003	9.15 (7.32) ± 1.29	0.41 (2.7)	±0.16	±0.09	±1.31

Bibliography

[1] See, e.g. J. A. Peacock, *"Cosmological physics,"* Cambridge, Univ. Pr. (1999).

[2] See, e.g. W. N. Cottingham and D. A. Greenwood, *"AN INTRODUCTION TO NUCLEAR PHYSICS,"* Cambridge Univ. Pr. (1986).

[3] See, e.g. Y. Nagashima, *"PROGRESSIONS OF HIGH ENERGY PHYSICS,"* Asakura Shoten (1999).

[4] See, e.g. W. Gebhardt and U. Krey, *"Phase transition and critical phenomena,"* Friedr. Vieweg & Shon, Braunschweig/Wiesbaden (1980). S. Komura, Yoshioka Shoten (1992).

[5] V. L. Ginzburg and L. D. Landau, Zh. Eksp. Teor. Fiz. **20**, 1064 (1950).

[6] See, e.g. T. Muta, *"Foundations of quantum chromodynamics. Second edition,"* World Sci. Lect. Notes Phys. **57**, 1 (1998).

[7] Y. Nambu and G. Jona-Lasinio, Phys. Rev. **122**, 345 (1961).

[8] Y. Nambu and G. Jona-Lasinio, Phys. Rev. **124**, 246 (1961).

[9] See, e.g. C. Y. Wong, *"Introduction to high-energy heavy ion collisions,"* Singapore, World Sci. (1994).

[10] See, e.g. T. Kanki, *"Quark Gluon Plasma,"* Maruzen (1992).

[11] See, e.g. K. Yagi, T. Hatsuda and Y. Miake, *"Quark-Gluon Plasma: From Big Bang To Little Bang,"* Cambridge, Univ. Pr. (2005).

[12] N. Cabibbo and G. Parisi, Phys. Lett. B **59**, 67 (1975).

[13] A. Chodos, R. L. Jaffe, K. Johnson, C. B. Thorn and V. F. Weisskopf, Phys. Rev. D **9**, 3471 (1974).

[14] K. Rajagopal, Acta Phys. Polon. B **31**, 3021 (2000).

[15] F. Karsch, Lect. Notes Phys. **583**, 209 (2002).

[16] J. B. Kogut, M. Stone, H. W. Wyld, W. R. Gibbs, J. Shigemitsu, S. H. Shenker and D. K. Sinclair, Phys. Rev. Lett. **50**, 393 (1983).

[17] S. Muroya, A. Nakamura, C. Nonaka and T. Takaishi, Prog. Theor. Phys. **110**, 615 (2003).

[18] H. Fujii, Phys. Rev. D **67**, 094018 (2003).

[19] F. R. Brown *et al.*, Phys. Rev. Lett. **65**, 2491 (1990).

[20] Y. Aoki, Z. Fodor, S. D. Katz and K. K. Szabo, Phys. Lett. B **643**, 46 (2006).

[21] M. A. Stephanov, K. Rajagopal and E. V. Shuryak, Phys. Rev. Lett. **81**, 4816 (1998).

[22] M. A. Stephanov, Prog. Theor. Phys. Suppl. **153**, 139 (2004) [Int. J. Mod. Phys. A **20**, 4387 (2005)].

[23] Z. Fodor and S. D. Katz, JHEP **0203**, 014 (2002).

[24] S. Ejiri, C. R. Allton, S. J. Hands, O. Kaczmarek, F. Karsch, E. Laermann and C. Schmidt, Prog. Theor. Phys. Suppl. **153**, 118 (2004).

[25] O. Scavenius, A. Mocsy, I. N. Mishustin and D. H. Rischke, Phys. Rev. C **64**, 045202 (2001).

[26] M. Asakawa and K. Yazaki, Nucl. Phys. A **504**, 668 (1989).

[27] J. Berges and K. Rajagopal, Nucl. Phys. B **538**, 215 (1999).

[28] A. Barducci, R. Casalbuoni, S. De Curtis, R. Gatto and G. Pettini, Phys. Rev. D **41**, 1610 (1990).

[29] M. A. Halasz, A. D. Jackson, R. E. Shrock, M. A. Stephanov and J. J. M. Verbaarschot, Phys. Rev. D **58**, 096007 (1998).

[30] Y. Hatta and T. Ikeda, Phys. Rev. D **67**, 014028 (2003).

[31] N. G. Antoniou and A. S. Kapoyannis, Phys. Lett. B **563**, 165 (2003).

[32] J. D. Bjorken, Phys. Rev. D **27**, 140 (1983).

[33] L. Ahle *et al.* [E-802 Collaboration], Phys. Lett. B **332**, 258 (1994).

[34] K. Adcox *et al.* [PHENIX Collaboration], Phys. Rev. Lett. **87**, 052301 (2001).

[35] S. S. Adler *et al.* [PHENIX Collaboration], Phys. Rev. C **71**, 034908 (2005).

[36] S. Margetis *et al.* [NA49 Collaboration], Phys. Rev. Lett. **75** (1995) 3814.

[37] K. Adcox *et al.* [PHENIX Collaboration], Nucl. Phys. A **757**, 184 (2005).

[38] R. S. Hayano and T. Hatsuda, arXiv:0812.1702 [nucl-ex].

[39] T. Matsui and H. Satz, Phys. Lett. B **178**, 416 (1986).

[40] K. Adcox *et al.* [PHENIX Collaboration], Nucl. Instrum. Meth. A **499**, 469 (2003).

[41] A. Adare *et al.* [PHENIX Collaboration], Phys. Rev. C **78**, 044902 (2008).

[42] J. H. Vignos and H. A. Fairbank, Phys. Rev. Lett. **6**, 265 (1961).

[43] W. M. Fairbank, M. J. Buckingam, Int. Conf. on Low Temp. Phys. (1957).

[44] See, e.g. W. M. Fairbank, C. K. Kellers, *"Critical Phenimena,"* National Bureau of Standards, Washington D. C. (1965).

[45] M. E. Fisher, Phys. Rev. Lett. **16**, 11 (1966).

[46] R. B. Griffiths, Phys. Rev. Lett. **23**, 17 (1969).

[47] R. B. Griffiths, Phys. Rev. Lett. **24**, 1479 (1970).

[48] K. G. Wilson, Phys. Rev. B **4**, 3174 (1971).

[49] K. G. Wilson, Phys. Rev. B **4**, 3184 (1971).

[50] See, e.g. L. D. Landau, E. M. Lifshitz, *"Vol. 5, Statisitical Physics, Third edition, Part 1,"* Pegamon Press, Oxford (1980).

[51] L. S. Ornstein and F. Zernike, Proc. Akad. Sci. **15**, 54 (1912).

[52] L. S. Ornstein and F. Zernike, Proc. Akad. Sci. **17**, 793 (1914).

[53] See, e.g. H. Nishimori, *"Statistical phycsics of phase transition and critical phenomena,"* Baifukan, (2005).

[54] D. J. Scalapino and R. L. Sugar, Phys. Rev. D **8**, 2284 (1973).

[55] N. G. Antoniou, Y. F. Contoyiannis, F. K. Diakonos, A. I. Karanikas and C. N. Ktorides, Nucl. Phys. A **693**, 799 (2001).

[56] N. G. Antoniou, F. K. Diakonos, A. S. Kapoyannis and K. S. Kousouris, Phys. Rev. Lett. **97**, 032002 (2006).

[57] N. G. Antoniou, C. N. Ktorides, I. S. Mistakidis and F. K. Diakonos, Eur. Phys. J. C **4**, 513 (1998).

[58] N. Sasaki, O. Miyamura, S. Muroya and C. Nonaka, Europhys. Lett. **54**, 38 (2001).

[59] M. A. Stephanov, K. Rajagopal and E. V. Shuryak, Phys. Rev. D **60**, 114028 (1999).

[60] C. Nonaka and M. Asakawa, Phys. Rev. C **71**, 044904 (2005).

[61] E. A. De Wolf, I. M. Dremin and W. Kittel, Phys. Rept. **270**, 1 (1996).

[62] G. J. Alner *et al.* [UA5 Collaboration], Phys. Lett. B **160**, 193 (1985).

[63] T. Abbott *et al.* [E-802 Collaboration], Phys. Rev. C **52**, 2663 (1995).

[64] P. Abreu *et al.* [DELPHI Collaboration], Z. Phys. C **56**, 63 (1992).

[65] P. Carruthers and C. C. Shih, Phys. Lett. B **165**, 209 (1985).

[66] A. Bialas and R. Peschanski, Nucl. Phys. B **273**, 703 (1986).

[67] W. A. Zajc, Phys. Lett. B **175**, 219 (1986).

[68] A. Bialas and R. Peschanski, Nucl. Phys. B **308**, 857 (1988).

[69] P. Carruthers, E. M. Friedlander, C. C. Shih and R. M. Weiner, Phys. Lett. B **222**, 487 (1989).

[70] P. Carruthers and I. Sarcevic, Phys. Rev. Lett. **63**, 1562 (1989).

[71] P. Carruthers, H. C. Eggers and I. Sarcevic, Phys. Rev. C **44**, 1629 (1991).

[72] A. Giovannini and L. Van Hove, Z. Phys. C **30**, 391 (1986).

[73] M. J. Tannenbaum and J. Kang [E802 Collaboration.], Nucl. Phys. A **566**, 423C (1994).

[74] H. Nakamura and R. Seki, Phys. Rev. C **66**, 024902 (2002).

[75] M. Allen *et al.* [PHENIX Collaboration], Nucl. Instrum. Meth. A **499**, 549 (2003).

[76] S. H. Aronson *et al.* [PHENIX Collaboration], Nucl. Instrum. Meth. A **499**, 480 (2003).

[77] K. Adcox *et al.* [PHENIX Collaboration], Nucl. Instrum. Meth. A **499**, 489 (2003).

[78] M. Aizawa *et al.* [PHENIX Collaboration], Nucl. Instrum. Meth. A **499**, 508 (2003).

[79] L. Aphecetche *et al.* [PHENIX Collaboration], Nucl. Instrum. Meth. A **499**, 521 (2003).

[80] S. S. Adler *et al.* [PHENIX Collaboration], Nucl. Instrum. Meth. A **499**, 560 (2003).

[81] S. S. Adler *et al.* [PHENIX Collaboration], Nucl. Instrum. Meth. A **499**, 593 (2003).

[82] C. Adler, A. Denisov, E. Garcia, M. J. Murray, H. Strobele and S. White, Nucl. Instrum. Meth. A **470**, 488 (2001).

[83] K. Ikematsu *et al.*, Nucl. Instrum. Meth. A **411**, 238 (1998)

[84] S. S. Adler *et al.* [PHENIX Collaboration], Phys. Rev. C **69**, 034909 (2004).

[85] A. Kiyomichi, Ph. D. thesis, Department of Physics, University of Tsukuba (2005).

[86] S. S. Adler *et al.* [PHENIX Collaboration], Phys. Rev. Lett. **91**, 072301 (2003).

[87] H. Torii, Ph. D. thesis, Department of Physics, Kyoto University (2004).

[88] Computer code GEANT 3.21, CERN, Genva, (1993).

[89] X. N. Wang and M. Gyulassy, Phys. Rev. D **44**, 3501 (1991).

[90] H. R. Collard, L. R. B. Elton, R. Hofstadter, *"Nuclear Radii"* Landolt-Brnstein, Vol. 2, Springer-Verlag, (1967).

[91] M. Chiu, A. Denisov, E. Garcia, J. Katzy and S. White, Phys. Rev. Lett. **89**, 12302 (2002).

[92] K. Tokushuku *et al.*, Phys. Lett. B **235**, 245 (1990).

[93] H. Pi, Comput. Phys. Commun. **71**, 173 (1992).

[94] F. James and M. Roos, Comput. Phys. Commun. **10**, 343 (1975).

[95] M. J. Tannenbaum, E802 Internal Rept. No. E-802-MEM-58 (1993).

[96] G. Baym, B. Blattel, L. L. Frankfurt, H. Heiselberg and M. Strikman, Phys. Rev. C **52**, 1604 (1995).

[97] Y. Akiba *et al.* [E802 Collaboration], Phys. Rev. C **56**, 1544 (1997).

[98] S. S. Adler *et al.* [PHENIX Collaboration], Phys. Rev. Lett. **93**, 152302 (2004).

[99] A. Enokizono, Ph. D. thesis, Department of Physical Science, Hiroshima University (2004).

[100] M. Rybczynski *et al.* [NA49 Collaboration], J. Phys. Conf. Ser. **5**, 74 (2005).

[101] C. Alt *et al.* [NA49 Collaboration], Phys. Rev. C **75**, 064904 (2007).

[102] V. P. Konchakovski, S. Haussler, M. I. Gorenstein, E. L. Bratkovskaya, M. Bleicher and H. Stoecker, Phys. Rev. C **73**, 034902 (2006).

[103] S. S. Adler *et al.* [PHENIX Collaboration], Phys. Rev. Lett. **91**, 182301 (2003).

[104] B. B. Back *et al.* [PHOBOS Collaboration], Phys. Rev. C **72**, 051901 (2005).

[105] E. B. Johnson, AIP Conf. Proc. **842**, 137 (2006).

[106] J. Adams *et al.* [STAR Collaboration], Phys. Rev. Lett. **98**, 062301 (2007).

[107] J. Adams *et al.* [STAR Collaborations], arXiv:nucl-ex/0601042.

[108] S. S. Adler *et al.* [PHENIX Collaboration], Phys. Rev. Lett. **94**, 232301 (2005).

[109] S. S. Adler *et al.* [PHENIX Collaboration], Phys. Rev. Lett. **96**, 032301 (2006).

[110] A. Adare *et al.* [PHENIX Collaboration], Phys. Rev. Lett. **98**, 172301 (2007).

[111] A. Adare *et al.* [PHENIX Collaboration], Phys. Rev. Lett. **98**, 162301 (2007).

[112] S. S. Adler *et al.* [PHENIX Collaboration], Phys. Rev. C **69**, 034910 (2004).

公表論文

(1) Measurement of density correlations in pseudorapidity via charged particle multiplicity fluctuations in Au+Au collisions at $\sqrt{s_{NN}}$ =200 GeV
S. S. Adler et al., (別紙、共著者リスト①参照)
Physical Review C 76, 034903 (2007).

Letter of Acceptance

We approve that Mr. Tomoaki Nakamura preferentially applies following article as the main part of his doctoral dissertation at Hiroshima University.

Article: Physical Review C76, 034903 (2007)
Title: Measurement of density correlations in pseudorapidity via charged particle multiplicity fluctuations in Au+Au collisions at $\sqrt{s_{NN}}$ = 200GeV

Spokesperson of the PHENIX Collaboration:
Barbara V. Jacak
Professor of Physics and Astronomy at SUNY Stony Brook University

Date: _____November 24, 2008_____

Signature: _____

参考論文

(1) Systematic studies of the centrality and $\sqrt{s_{NN}}$ dependence of the $dE_T/d\eta$ and $dN_{ch}/d\eta$ in heavy ion collisions at midrapidity
S. S. Adler et al, (別紙、共著者リスト②参照)
Physical Review C 71, 034908 (2005).

(2) Charged hadron multiplicity fluctuations in Au+Au and Cu+Cu collisions from $\sqrt{s_{NN}}$ =22.5 to 200GeV
A. Adare et al, (別紙、共著者リスト③参照)
Physical Review C 78, 044902 (2008).

(3) PHENIX inner detectors
M. Allen et al., (別紙、共著者リスト④参照)
Nuclear Instruments and Methods in Physics Research A 499, 549 (2003).